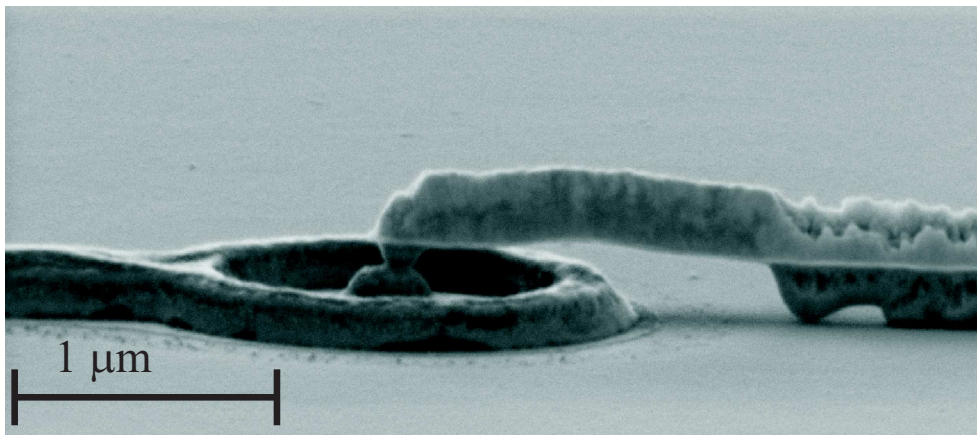
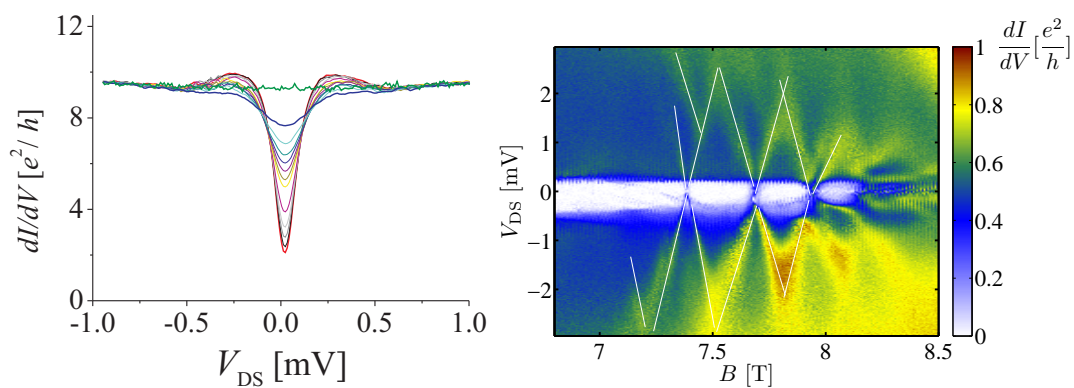


Small alloyed ohmic contacts to 2DES and submicron scale Corbino devices in strong magnetic fields: observation of a zero bias anomaly and single-electron charging



Oktay Göktaş

Max-Planck-Institut für Festkörperforschung

Stuttgart, 2009

**Small alloyed ohmic contacts to 2DES and
submicron scale corbino devices in strong
magnetic fields: Observation of a zero bias
anomaly and single electron charging**

Von der Fakultät Mathematik und Physik der Universität Stuttgart zur
Erlangung der Würde eines Doktors der Naturwissenschaften
(Dr. rer. nat.) genehmigte Abhandlung

Vorgelegt von

Oktay Göktaş

aus Hozat, Tunceli/Turkey

Hauptberichter:	Prof. Dr. Klaus von Klitzing
Mitberichter:	Prof. Dr. Peter Michler
Tag der Einreichung:	5.3.2009
Tag der mündlichen Prüfung:	7.4.2009

Max-Planck-Institut für Festkörperforschung
Stuttgart, 2009

Contents

Symbols	v
1 Introduction	1
2 Microscopic understanding of the Quantum Hall Effect in terms of compressible and incompressible stripes	5
2.1 The two-dimensional electron system	6
2.1.1 Realization of the two-dimensional electron system	6
2.1.2 2DES in a perpendicular magnetic field: Classical picture and Hall bar geometry	7
2.2 The Quantum Hall Effect(QHE)	9
2.2.1 2DES in strong magnetic field: Landau quantization and effect of disorder	11
2.2.2 The edge state picture	14
2.2.3 Electrostatic of edge channels and formation of compressible and incompressible stripes	16
2.2.4 Self-consistent calculation of edge channels	18
2.3 Scanning probe experiments on potential profiles of quantum Hall samples	21
2.3.1 Hall potential profile in Hall bar samples	21
2.3.2 Potential profile in Corbino samples	23
2.4 The present understanding of microscopic picture of QHE based on compressible and incompressible stripes.	26
2.5 The link between microscopic picture of the QHE and the goal of the thesis	29
3 Proposal of a new type of single-electron charging device based on the submicron Corbino devices in strong magnetic field	31
3.1 Single-electron charging effect and quantum dot systems	31
3.1.1 Concept of single-electron charging and Coulomb blockade effect	32

3.1.2	Transport spectroscopy under finite bias	35
3.2	Quantum dot systems	36
3.2.1	The Fock-Darwin spectrum	39
3.3	Proposal of a new type of single-electron charging device: Submicron Corbino devices in strong magnetic fields	40
3.4	Quantum rings and quantum antidots	42
3.4.1	Quantum rings	42
3.4.2	Quantum antidots	43
3.4.3	Aharonov-Bohm effect	44
4	Ohmic Contacts to 2DES in GaAs/Al_δGa_{1-δ}As heterostructures	47
4.1	Alloyed Au/Ge/Ni contacts	48
4.1.1	The recipe	49
4.2	Electrical characterization of the alloyed contacts to the 2DES	52
4.2.1	Determining the contact resistance: the transmission line method (TLM)	52
4.2.2	Anisotropy of contact resistance on the crystal orientation	54
4.2.3	Scaling properties of contact resistance in good contacting direction	58
4.2.4	Temperature dependence of the contact resistance	61
4.2.5	The role of the contact resistance in QHE measurements	62
4.3	Structural properties of alloyed Au/Ge/Ni contacts to 2DES	66
4.3.1	SEM studies	67
4.3.2	TOF-SIMS studies	71
4.3.3	STEM studies	75
4.3.4	EDX studies	83
4.3.5	Discussion of the result of the structural investigations	88
4.4	A model for the current injection between alloyed contacts and 2DES	90
4.5	Summary	92
5	Alloyed contacts to 2DES on submicron scale	95
5.1	The sample	95
5.2	Alloyed contacts to 2DES on submicron scale at liquid He and room temperature	99
5.3	Submicron scale ohmic contacts at very low temperatures and strong magnetic fields	104
5.4	SEM study of submicron scale ohmic contacts	107
5.5	Summary	109

6	Observation of a zero bias anomaly and positive magneto conductance increase at small magnetic fields on submicron Corbino devices	111
6.1	The device and measurement setup	112
6.2	Submicron scale Corbino devices at low temperatures and small magnetic field	115
6.2.1	Theoretical predictions due to the ballistic motion of single electrons	116
6.2.2	Transport experiments at low temperatures and observation of a zero bias anomaly	118
6.2.3	Zero bias anomaly at finite magnetic field: observation of a positive magneto conductance	125
6.2.4	Temperature dependence of magneto-conductance dip	132
6.3	Discussion of zero bias anomaly and interference effects as a possible source of the phenomenon	134
6.3.1	1-D weak localization as a possible source of the interference in submicron Corbino devices ?	135
6.3.2	Weak localization in ballistic cavities as a possible source of the interference in submicron Corbino devices ?	136
6.4	Asymmetric zero bias anomaly	142
6.5	Induced difference in the electrochemical potential difference between the contact of the Corbino device with sweeping magnetic field	144
6.6	Summary	144
7	Experiments on submicron GaAs/Al_δGa_{1-δ}As Corbino devices at high magnetic fields: observation of single-electron charging	147
7.1	Submicron scale Corbino devices under strong magnetic fields	147
7.2	Observation of single-electron charging in Corbino devices	153
7.3	Reproducing the experimental results after cycling the device to room temperature.	159
7.4	Third cool down of the Corbino device s#1 and effect of back gate	163
7.5	Comparison of single-electron charging effect on different Corbino devices	168
7.6	Discussion of the asymmetry of the breakdown of QHE	175
7.7	Summary	178
8	Conclusion and outlook	181
9	Zusammenfassung	185

Appendices	189
A Clean room process for ohmic contacts by optical lithography	191
B List of chemicals and equipment	195
C Additional TLM experiments on alloyed ohmic contacts	197
D Additional SEM images of the alloyed contacts	207
E Additional TOF-SIMS images of the alloyed contacts	213
F Additional TEM images of the alloyed contacts	215
G Clean room process for the ohmic contacts using EBL lithography	221
H Additional SEM images of small alloyed contacts	227
I Clean room process for the Corbino devices	231
J Additional transport data for zero bias anomaly	235
K Additional transport data of submicron Corbino devices under high magnetic field	243
Bibliography	258

Symbols and notations

Abbreviations

AAS	Altshuler-Aronov-Spivak, Ref. [58]
CBO	Coulomb Blockade Oscillations
CSG	D.B. Chklovskii, B.I. Shklovskii, L.I. Glazman, Ref. [11]
EBL	Electron Beam Lithography
EDX	Energy Dispersive X-Ray
FQHE	Fractional Quantum Hall Effect
MBE	Molecular Beam Epitaxy
QD	Quantum Dot
QHE	Quantum Hall Effect
SEM	Scanning Electron Microscope
SET	Single-Electron Transistor
TEM	Transmission Electron Microscope
TOF-SIMS	Time of Flight-Secondary Ion Mass Spectrometry

Symbols

a_B	Effective Bohr radius
a_k	The width of the k^{th} incompressible stripe
a_ν	The width of the incompressible stripe with local filling factor ν
A_{cl}	Area enclosed by a typical classical trajectory of electrons
A_C	Area of the Corbino device
α_{cl}	Inverse of the area enclosed by a typical classical trajectory
\mathbf{B}	Magnetic field
$C_i, \quad i = \{S,D,G\}$	The capacitance of i^{th} electrode to the island
C_Σ	The total capacitance between the island and the rest of the system
d_0	Voltage dependent depletion width of 2DES
d_i	Distance between two contacts pair
D_{2DES}	Depth of GaAs/Al $_\delta$ Ga $_{1-\delta}$ As heterojunction where 2DES form
D	Diameter of circular contacts
Δr	The width of the Corbino device (r_o-r_i)
ε_F	Fermi energy
\mathbf{E}	Electric field
$E_C = e^2/2C_\Sigma$	Charging energy
$E^{Critical}$	Critical value of Hall field for the breakdown of QHE
ε_i	Single particle energies in a quantum dot

g^*	Landé g-factor
g_s	Spin degeneracy factor; 1 for a non degenerate and 2 for a degenerate case
G	Conductance
I	Current
j_r	Current density
k_B	Boltzmann-constant
$k = (k_x, k_y)$	Wave vector
l	The angular quantum number
l_B	Magnetic length
l_{cycl}	Cyclotron radius
l_e	Mean free path
l_ϕ	Phase coherence length
L	Length between the two potential probes in x direction
m^*	Effective mass of electrons in the conduction band of GaAs
μ	Electron mobility
μ_{ch}	Chemical potential
μ_{elch}	Electrochemical potential
n	Radial quantum number
n_L	Density of flux quantum
n_s	Electron density of a 2DES
N_e	Number of electrons in the Corbino
ν	Filling factor
ν_l	Local filling factor
r_c	Unity length contact resistance
r_i	Radius of inner contact of the Corbino device
r_o	Inner radius of the outer contact of the Corbino device
R_c	Contact resistance
R_t	Total resistance between two contacts pair
R_w	Resistance of the measurement apparatus
R_{xx}	Longitudinal resistance
R_{xy}, R_H	Hall resistance
ρ_s	Sheet resistivity of a semiconductor (or a 2DES)
ρ_{xx}	Longitudinal resistivity
ρ_{xy}	Hall resistivity
S	Area enclosed by an electron in a closed path
σ_{xx}	Longitudinal conductivity in cartesian coordinates
σ_{xy}	Hall conductivity in cartesian coordinates
τ_e	Elastic scattering time
τ_ϕ	Phase coherence time

V_{DS}	Drain-source voltage
v_{F}	Fermi velocity of electrons
v_{D}	Drift velocity of an electron
$V_{\text{DS}}^{\text{Critical}}$	Critical value of V_{DS} where a finite differential conductance is measured in plateau regime
w	The width of the mesa stripe
w_c	Cyclotron frequency
W	The width of a Hall bar
y_{ν}	Position of the incompressible stripe with local filling factor ν

Physical constants

e	Elementary charge
$-e$	Electron charge
h	Planck constant
k_{B}	Boltzmann constant
m_e	Mass of electron
μ_{B}	Bohr magneton
Φ_0	Magnetic flux quantum

Chapter 1

Introduction

The Quantum Hall Effect (QHE) was a big surprise discovered on a two-dimensional electron system (2DES) in 1980 [1]. The surprising result was that the Hall resistance develops plateaus with simultaneously vanishing longitudinal resistance for a certain range of magnetic field. The value of Hall resistance is quantized at $h/(ie^2)$ where i is an integer number. The accuracy of the quantization made the possibility of defining an international resistance standard. Klaus von Klitzing was honored by the physics Nobel prize in 1985 for his discovery. The original discovery was made on a 2DES at the Si-SiO₂ interface in a metal-oxide-semiconductor field effect transistor. However, 2DES realized in molecular beam epitaxy grown modulation doped GaAs/Al_δGa_{1-δ}As heterostructures become the base system for the investigation of the QHE due to their superior electron mobility.

The 2DES forms at the GaAs/Al_δGa_{1-δ}As heterojunction which lies typically 35 nm to 200 nm below the surface. Making a reliable, reproducible and low resistive ohmic contacts to the 2DES in these heterostructures is an important issue. Alloyed Indium ohmic contacts have been used to contact the 2DES on these heterostructures. Since, Indium is not a suitable material for lithographic purposes - it is hard to evaporate- Au/Ge/Ni contacts, which are used to contact n-GaAs, have been adopted to contact the 2DES in GaAs/Al_δGa_{1-δ}As heterostructures. However, every group developed and used its own recipe and there are not much systematic studies available in the literature. A detailed study of alloyed ohmic contacts to 2DES is necessary since they become an important ingredient of the QHE for the microscopic understanding of the phenomena.

The present understanding of Quantum Hall Effect is still under debate. Several theories has been developed to explain the effect. Of them the edge state picture was very successful to account for most of the experimental findings. However, recent experiments on the Hall potential profiles in quantum Hall samples by scanning force microscopes reveal convincing evidences for the existence of compressible and incompressible stripes in the depletion region at the sample edges

supporting the theories that take screening effects into account. Moreover, these experiments have shown that compressible and incompressible stripes also exist at the border between ohmic contacts and the 2DES. Based on the fact that incompressible stripes have insulating properties, we propose a submicron Corbino devices as a new type of single electron-charging device in this work.

Single-electron charging is a phenomena that is observable when the electrostatic charging energy for adding an electron to a conducting island becomes larger than the thermal energy. The effect is observable for the devices in micron or submicron size at temperatures in the range of one Kelvin or below. The basic ingredients of a single-electron charging device is a small island coupled to the leads via tunneling barriers. When Fermi wavelength of electrons become comparable to the island size, which is the case for electrons in a 2DES in GaAs/Al_δGa_{1-δ}As heterostructures with a few hundred nanometer device size, the effect of the size confinement starts to play a role and one speaks of quantum dot systems. In a Corbino device, at low temperatures and under strong magnetic field, there are incompressible stripes isolating the main compressible bulk from the ohmic contacts for certain magnetic field range. When the size of Corbino device is small enough - in submicron scale - single-electron charging should be observable. This makes the base of our proposal.

During this work we have investigated electrical and structural properties of alloyed Au/Ge/Ni contacts to the 2DES in GaAs/Al_δGa_{1-δ}As heterostructures in great detail and developed a model for the ohmic contact formation on these systems based on the experimental findings. We have focused on contacting the 2DES in GaAs/Al_δGa_{1-δ}As heterostructures on submicron scale and succeeded to make successfully working contacts down to a diameter of 0.2 μm. Using these small contacts we have prepared successfully working Corbino devices in submicron scale. As characterizing the devices at low temperatures we have observed a zero bias anomaly - a differential conductance dip at zero bias. Applying a small magnetic field partly suppress the zero bias anomaly. This zero bias anomaly seems to be an interference effect with some unusual properties. Under strong magnetic field we have observed magnetic field periodic oscillations and signature of single-electron charging. We propose models for the explanation of the observed phenomena based on compressible and incompressible stripes.

The thesis is organized in the following way: In Chapter 2 we will focus on the microscopic understanding of the QHE. In Chapter 3 we will present the basics of single-electron charging effect and present different kind of single-electron charging devices relevant for this study. Alloyed ohmic contacts to the 2DES in the GaAs/Al_δGa_{1-δ}As heterostructures are basic ingredients of the proposed devices and will be the subject of Chapter 4. In Chapter 5 we will present the electrical and structural properties of small ohmic contacts. The experimental results and

discussion of the observed zero bias anomaly on submicron scale Corbino devices will be shown in Chapter 6. In Chapter 7 we will present experimental results for single-electron charging obtained in Corbino devices under strong magnetic field. Experimental results for magnetic field periodic oscillation and breakdown of QHE on submicron scale Corbinos device will be discussed also in Chapter 7. Finally the conclusion of the present work will be given in Chapter 8. In the appendices the sample processing steps are described in detail. The supportive experiments for the main chapters are also presented in appendices and refereed from the main text.

Chapter 2

Microscopic understanding of the Quantum Hall Effect in terms of compressible and incompressible stripes

The Quantum Hall Effect has been intensively investigated in the last three decades, both theoretically and experimentally. The focus of this chapter is the microscopic understanding of the QHE. The high mobility two-dimensional electron system (2DES) in GaAs/Al_δGa_{1-δ}As heterostructures is an ideal system for investigation of the QHE and will be discussed in section 2.1. Then the Quantum Hall Effect will be discussed in section 2.2. First a general introduction will be given. Then Landau quantization and effect of disorder will be introduced in chapter 2.2.1. The edge state picture is the subject of section 2.2.2. Electrostatic model as well as a self-consistent model which results in formation of compressible and incompressible stripes are discussed in section 2.2.3. Experiments on the Hall potential profile in Quantum Hall Effect samples will be presented in section 2.3. The experimental evidences of formation of compressible and incompressible stripes in front of the ohmic contacts are presented in the same section. Then we will present potential profile experiments on the Corbino samples in section 2.3.2. Finally, a summary of the present understanding of microscopic picture of QHE is given in section 2.4. At the end of the chapter, the link between the goal of the present thesis and the microscopic understanding of QHE is discussed in section 2.5.

2.1 The two-dimensional electron system

2.1.1 Realization of the two-dimensional electron system

The QHE was originally discovered in a 2DES formed at the Si-SiO₂ interface in a metal-oxide-semiconductor field effect transistor (MOSFET). However the development of modulation doped GaAs/Al_δGa_{1-δ}As heterostructures [2] grown by Molecular Beam Epitaxy (MBE) made it possible to realize higher electron mobility 2DES. The main advantage of the modulation doped method is the separation of donors, which provide electrons for the 2DES, by a spacer layer from the 2DES. Thus, scattering of electrons in the 2DES due to the ionized-donor potential is reduced. Therefore these heterostructures become the most commonly used material for the investigation of the QHE. A schematic layer sequence of a modulation doped heterostructure is shown in Fig. 2.1. The silicon doped AlGaAs layer provides electrons. Electrons are confined at the GaAs/Al_δGa_{1-δ}As interface due to the conduction band offset between GaAs and AlGaAs and the attractive potential of the ionized donors in the silicon doped AlGaAs layer. The sketch of the conduction band bending of the modulation doped heterostructure is shown in the right side of Fig. 2.1. Electrons are free to move in the xy plane. The electron eigenenergies are quantized in z direction. The total energy is therefore

$$\varepsilon(i, k_x, k_y) = \varepsilon_i + \frac{\hbar^2 k_x^2}{2m^*} + \frac{\hbar^2 k_y^2}{2m^*} , \quad i = \{0, 1, 2, \dots\}. \quad (2.1)$$

Here ε_i are the quantized eigenenergies in the z direction; k_x and k_y are the momentum components in x and y directions and m^* is the effective electron mass in the conduction band of GaAs. Due to the quantized energy ε_i , the energy of electrons arrange into subbands. The spatial extension of the wave function (in z direction) in the lowest subband (ε_0) is usually less than 10 nm [3]. For small electron concentrations only the lowest subband is populated. Therefore at low temperatures electrons at the GaAs/Al_δGa_{1-δ}As interface form a perfect 2DES. The density-of-state in the 2DES is constant and reads as

$$D(\varepsilon) = \frac{g_s m^*}{\pi \hbar^2} . \quad (2.2)$$

Here g_s accounts for the spin degeneracy. The Fermi level has a linear dependence on the electron density,

$$\varepsilon_F = \frac{\pi \hbar^2}{g_s m^*} n_s , \quad (2.3)$$

where n_s is the sheet density of the 2DES. The electron density ranges typically from $8 \times 10^{14} \text{ m}^{-2}$ to $6 \times 10^{15} \text{ m}^{-2}$ and the Fermi energy ranges from 2.8 meV to 21.7 meV, respectively.

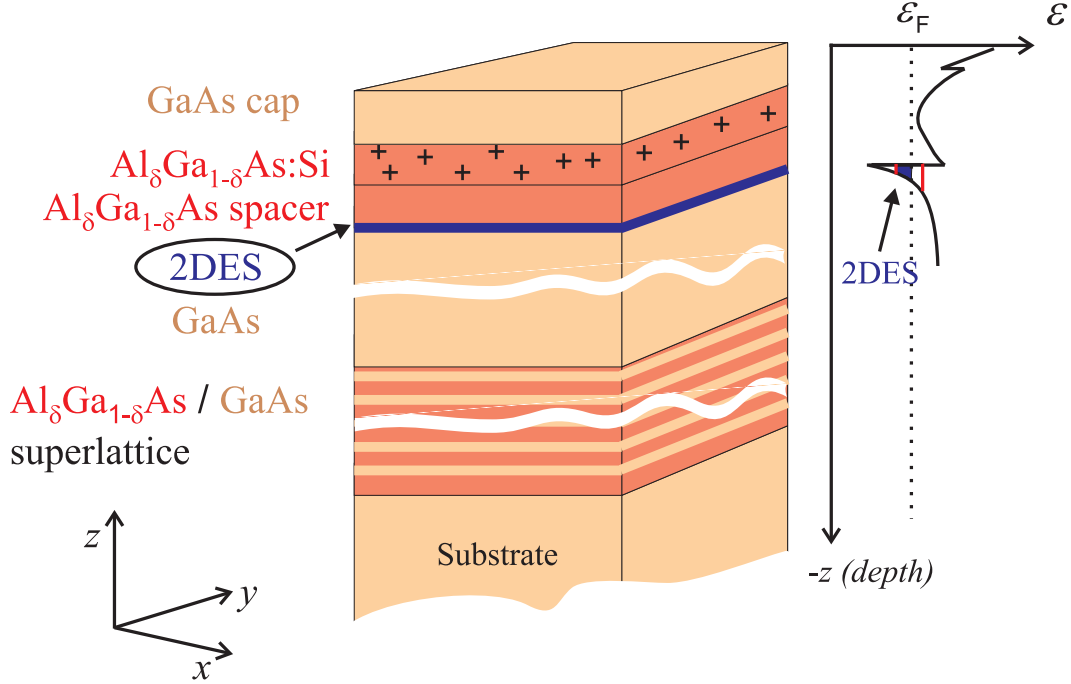


Figure 2.1: Scheme of the layers sequence of a GaAs/ $\text{Al}_\delta\text{Ga}_{1-\delta}\text{As}$ heterostructure and sketch of the conduction band minima in growth direction. Electrons are provided by the Si donors. Electrons are confined at the interface of the GaAs/ $\text{Al}_\delta\text{Ga}_{1-\delta}\text{As}$ due to the conduction band offset at the interface and attractive potential of ionized donors at the silicon doped AlGaAs layer. Electrons move freely in the xy plane. In z direction the electron eigenenergies are quantized due to the confinement. The spacer separates ionized donors from the 2DES. The cap layer is for avoiding oxidization.

2.1.2 2DES in a perpendicular magnetic field: Classical picture and Hall bar geometry

The properties of a 2DES under low magnetic field can be described by the Drude model. In the presence of a perpendicular magnetic field electrons are subject to a Lorentz force. The equation of motion is a classical Newton equation with a constant scattering relaxation time τ and reads as

$$m^* \frac{d\mathbf{v}_D}{dt} + m^* \frac{\mathbf{v}_D}{\tau} = -e[\mathbf{E} + (\mathbf{v}_D \times \mathbf{B})] \quad , \quad (2.4)$$

where \mathbf{v}_D is the drift velocity of electrons in the 2DES, \mathbf{E} is the electric field and \mathbf{B} is the applied magnetic field perpendicular to the 2DES. In the stationary case the first term in the equation vanishes and the equation (2.4) can be written in

cartesian coordinates as

$$\begin{pmatrix} j_x \\ j_y \end{pmatrix} = \begin{pmatrix} \sigma_{xx} & \sigma_{xy} \\ \sigma_{xy} & \sigma_{xx} \end{pmatrix} \begin{pmatrix} E_x \\ E_y \end{pmatrix} = \frac{\sigma_0}{1 + (\mu B)^2} \begin{pmatrix} 1 & \mu B \\ -\mu B & 1 \end{pmatrix} \begin{pmatrix} E_x \\ E_y \end{pmatrix} , \quad (2.5)$$

where we have used the current density $\mathbf{j} = -en_s \mathbf{v}_D$ and the conductivity tensor $\tilde{\sigma}$ which relates the local current density to the local electric field as $\mathbf{j} = \tilde{\sigma} \mathbf{E}$ [4]. Here

$$\mu = e\tau/m^* \quad (2.6)$$

is the electron mobility and

$$\sigma_0 = en_s \mu \quad (2.7)$$

is the Drude conductivity at zero magnetic field. The mobility depends on the scattering time τ and can be used as a measure of the sample quality. Another parameter used for a measure of the sample quality is the mean free path $l_e = v_F \tau$ where $v_F = \sqrt{2\varepsilon_F/m^*}$.

The longitudinal and Hall resistivities are related to the longitudinal and Hall conductivities as follows,

$$\rho_{xx} = \frac{\sigma_{xx}}{(\sigma_{xx}^2 + \sigma_{xy}^2)} , \quad \rho_{xy} = \frac{-\sigma_{xy}}{(\sigma_{xx}^2 + \sigma_{xy}^2)} . \quad (2.8)$$

The most common geometry to investigate the 2DES is the Hall bar geometry. A sketch of the Hall bar geometry is shown in the inset of Fig. 2.2. A current I flows in the 2DES and the longitudinal voltage V_x and the transverse voltage V_y are measured simultaneously. For a constant field and a homogenous current distribution, we have $j_x = I/W$ and $j_y = 0$, where W is the width of the Hall bar and L is the distance between the contacts (contact 5 and 6 in the inset of Fig. 2.2). R_{xx} and R_{xy} are longitudinal and Hall resistances, respectively. For a homogeneous current distribution in the sample, the longitudinal resistivity and resistance are related to each other by

$$\rho_{xx} = E_x/j_x = (V_x/L) \cdot (W/I) = (W/L)R_{xx} ; \quad (2.9)$$

and the Hall resistivity is equal to the Hall resistance in a two-dimensional system,

$$\rho_{xy} = E_y/j_x = (V_y/W) \cdot (W/I) = R_{xy} . \quad (2.10)$$

At high temperatures the behavior is the classical Hall effect. The Hall resistance varies linearly with the magnetic field

$$R_{xy} = \rho_{xy} = \frac{B}{|-e|n_s} \quad (2.11)$$

and the longitudinal resistivity remains for small magnetic field to that of zero magnetic field [5],

$$\rho_{xx} = \frac{1}{|-e|n_s\mu} . \quad (2.12)$$

However, the behavior at low temperature and high magnetic field is a big surprise. A typical data is shown in Fig. 2.2 [6]. There are a series of well developed plateaus with vanishing longitudinal resistance. This phenomenon is known as the Quantum Hall Effect (QHE) and will be the subject of the following section.

2.2 The Quantum Hall Effect(QHE)

Electrons in a 2DES show a surprising behavior at low temperatures and high magnetic fields. The Hall resistance is constant at $h/(ie^2)$ for a certain range of magnetic field, where i is a integer number. The longitudinal resistance vanishes in parallel as shown in Fig. 2.2. The exactness of quantization made the possibility of defining a resistance standard. This phenomena is known as Quantum Hall Effect (QHE) and the value $R_K = h/e^2$ is now denoted as von-Klitzing constant [1, 6]. The quantization is independent of sample details and is related to universal physical constants h and e , where h is the Planck constant and e is the elementary charge. The Comité Consultatif d'Électricité (CCE) suggested the value of 25812.807 Ω as conventional von-Klitzing constant with the notation R_{K-90} . The conventional von-Klitzing constant, accepted as the reference value for the resistance calibrations since 1990. A very nice review of the QHE and its application in metrology is given by B. Jeckelmann and B. Jeanneret in Ref. [7].

Being such an important phenomenon, the QHE has attracted a considerable research both theoretically and experimentally. However, the microscopic picture is still controversial. Several theories have been put forward. Laughlin proposed that the effect is due to the gauge invariance and existence of a mobility gap [8]. Existence of localized and extended states due to disorder was discussed by Prange [9]. A very popular theory is the edge state picture [10]. This picture is a single-electron picture and have been extensively used to explain the experimental observations very successfully. In 1993, an electrostatic theory of the edge states, taking screening effects into account, was developed [11]. This has shown that screening effects result in formation of compressible and incompressible stripes in the depletion region of the 2DES at the edges, later on extended by the numerical self-consistent calculations [12]. Experimental observations with a scanning force microscope investigating the local Hall potential distribution in 2DES under quantum Hall conditions supports the existence of compressible and incompressible stripes [13]. In the following sections the Landau quantization, the

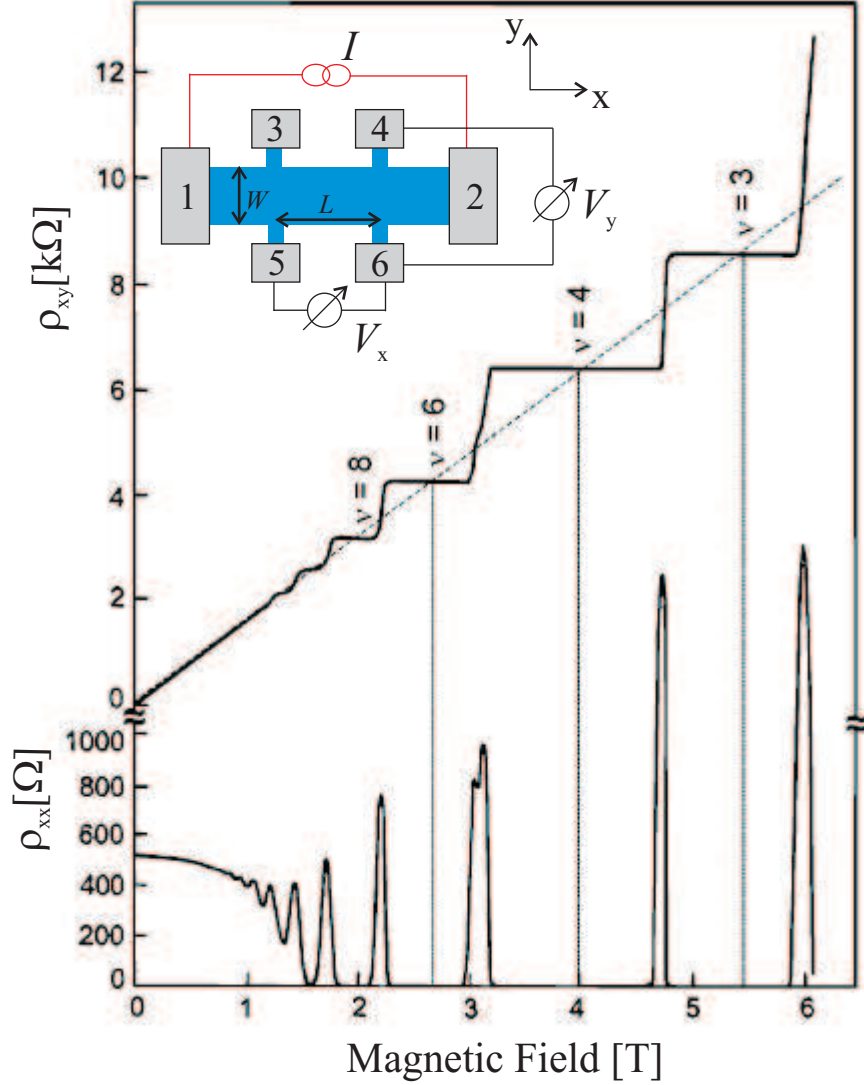


Figure 2.2: Typical magneto transport data observed on a 2DES in a GaAs/Al_δGa_{1-δ}As heterostructure at low temperatures, adopted from the Nobel lecture of Klaus von Klitzing [6]. Inset: A typical sample geometry, known as Hall bar, used in experiments. The blue part contains 2DES and the gray areas are alloyed ohmic contacts. V_x and V_y are measured longitudinal and transverse (Hall) voltages, respectively. ρ_{xx} is the longitudinal resistivity, $\rho_{xx} = (W/L) \cdot (V_x/I)$ and ρ_{xy} is the transverse (Hall) resistivity, $\rho_{xy} = V_y/I$. The width of sample W and distance between the side contacts L is also indicated.

effect of disorder in the Landau quantization, the edge states picture and finally the electrostatic theories of the edge states will be discussed.

2.2.1 2DES in strong magnetic field: Landau quantization and effect of disorder

The energy spectrum of electrons in a 2DES in the presence of the perpendicular magnetic field is discrete. The single particle Hamiltonian in an external magnetic field $\mathbf{B} = \nabla \times \mathbf{A}$ in the Landau gauge $A = (By, 0, 0)$ reads as

$$\frac{1}{2m^*} [(\hat{p}_x - eBy)^2 + \hat{p}_y^2] \phi(x, y) = \varepsilon \phi(x, y) \quad , \quad (2.13)$$

where \hat{p}_x and \hat{p}_y are canonical momentum operators. Energy eigenvalues are called Landau levels and are given by

$$\varepsilon_n = (n + \frac{1}{2})\hbar\omega_c \quad , \quad n = \{0, 1, 2, \dots\} \quad , \quad (2.14)$$

where ω_c is the cyclotron frequency,

$$\omega_c = eB/m^* \quad . \quad (2.15)$$

The eigenwave functions are product of a plane wave function in the x direction and the eigenstates of a harmonic oscillator in y direction,

$$\phi(x, y) = e^{ik_x x} H_n\left(\frac{y - y_0}{l_B}\right) \exp\left[-\frac{(y - y_0)^2}{2l_B^2}\right] \quad , \quad (2.16)$$

where H_n is the n th Hermite polynomial, k_x is the wave vector in x direction and l_B is the magnetic length defined as

$$l_B = \sqrt{\frac{\hbar}{eB}} \quad . \quad (2.17)$$

The magnetic length l_B is the new length scale introduced by the magnetic field and is 26 nm at 1 Tesla. The harmonic oscillator eigenstates are centered around the center coordinate $y_0 = -l_B^2 k_x$ and have a width of $\Delta y = l_B^2 2\pi/L_x$, where L_x is the length of the system in x direction. The Landau eigenenergies are independent of the center coordinate, therefore highly degenerate. The number of the states per unit area is

$$n_L = \frac{eB}{h} \quad . \quad (2.18)$$

Total number of states N_L is

$$N_L = n_L S = \frac{SB}{h/e} = \frac{\Phi}{\Phi_0} \quad , \quad (2.19)$$

where Φ is the total magnetic flux through the area of the sample, S (area of the 2DES) and $\Phi_0 = h/e$ is the magnetic flux quantum. Finally, a very useful quantity, the filling factor, is defined as the ratio of the electron density n_s to the flux density n_L ,

$$\nu = \frac{n_s}{n_L} = \frac{h}{eB} n_s \quad . \quad (2.20)$$

If we take the spin and confinement in z direction into account, there are additional terms and the full energy eigenvalues are

$$\varepsilon_n = \varepsilon_0 + \left(n + \frac{1}{2}\right)\hbar\omega_c \pm \frac{1}{2}g^*\mu_B B \quad , \quad n = \{0, 1, 2, \dots\} \quad , \quad (2.21)$$

where μ_B is the Bohr magneton, g^* is Landé g -factor for the electrons in the conduction band of bulk GaAs and ε_0 is the quantization energy due to confinement in the z direction (the lowest subband).

Clearly there is a gap of $\hbar\omega_c$ between consequent Landau levels and each Landau level splits into two sub levels depending on the spin orientation. The density of states is discrete and highly degenerate as shown in Fig. 2.3. That means whenever a level is completely full, decreasing magnetic field for a constant density of electrons or increasing electron density for a fixed magnetic field will cause a jump in the chemical potential of the system. The magnitude of the energy gap is $\hbar\omega_c - g^*\mu_B B$ for populating the next Landau level and $g^*\mu_B B$ for the next spin sublevel. When the Landau levels are completely full the filling factor $\nu = n_s/n_L$ is an integer and the Hall resistance is quantized as

$$R_H = \frac{B}{en_s} = \frac{h}{\nu e^2} \quad , \quad \nu = \{1, 2, 3, \dots\} \quad . \quad (2.22)$$

However the existence of the gap itself is not enough to explain the observed behavior shown in Fig. 2.2. The plateaus have a finite width and the quantized values $h/(\nu e^2)$ hold over a broad range of magnetic field. Longitudinal resistance is zero, indicating that the current flows without dissipation. The quantized values do not depend on the sample details. The above facts can be explained if effect of the disorder is taken into account.

In real samples there are impurities and point defects which create a disorder potential acting as scattering centers. The disorder lifts the degeneracy of the Landau levels and broadens the levels with a finite width as shown in Fig. 2.3 (c). States in the gap are localized and carry no current at zero temperature [5].

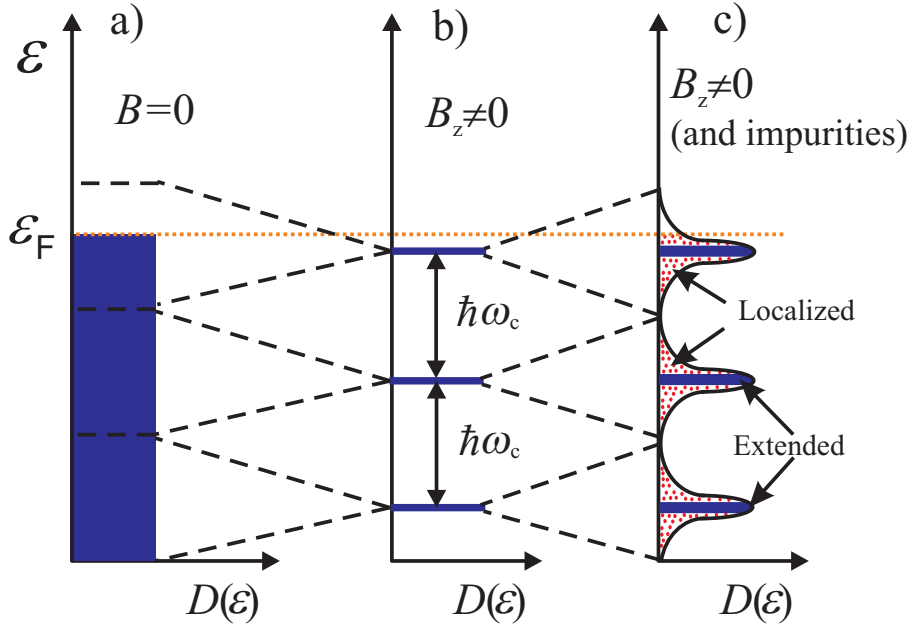


Figure 2.3: Density of states of a 2DES ignoring the spin degree-of-freedom. (a) Density of states at zero magnetic field. Each state accommodate only one electron because of Pauli principle, and states are filled up to Fermi level. (b) Density of states in the presence of strong perpendicular magnetic field. The energy spectrum is discrete and energy levels are highly degenerate. The gap is $\hbar\omega_c$. (c) Broadening of Landau levels due to disorder. Blue areas represent extended states and red dotted areas represent localized states.

The diagonal elements $\sigma_{xx} = \sigma_{yy}$ of the conductivity tensor are determined by the states at the Fermi level. When the Fermi energy is in the gap, the states at the Fermi level are localized and the longitudinal conductivity σ_{xx} vanishes. On the other hand, the off-diagonal elements $\sigma_{xy} = \sigma_{yx}$ of the conductivity tensor depends on all the states below the Fermi level. Therefore, as long as a portion of states below the Fermi level is extended, the Hall conductivity is finite [5]. The finite value of the Hall resistance R_H is shown to be precisely quantized Hall value given by (2.22) for a delta function impurity model [9]. A more general argument given by Laughlin considering a Gauge invariance [8] and proves the quantized value of Hall resistance. However, all of these models are far from describing transport in a real device (like that of the inset of Fig. 2.2) with current and voltage contacts. Description of the transport in a real device is developed in the context of the edge states and is the subject of the following chapter.

2.2.2 The edge state picture

The existence of current carrying edge states was discussed by Halperin [14] shortly after the discovery of QHE, following the general explanation of the QHE by Laughlin [8]. However here contacts were not included in the discussion. This was finally done by Büttiker [10] in 1988. This approach describes electrical transport by transmission and reflection at the contacts and uses the Landauer approach of transport [15]. A detailed review of the edge state picture was given by R. J. Haug in [16].

The edge states arise due to the fact that in a real sample there exist boundaries. Along the boundaries the electron density goes to zero (depletion). As a consequence, the potential rises near to the edges and Landau levels bend upward and cross the Fermi level. The Landau levels that are below the Fermi level at the bulk have occupied edge states at the Fermi level as shown in the Fig. 2.4. Carriers at the edges acquire a longitudinal velocity proportional to the slope of Landau level bending which is in opposite direction at opposite edges (upper and lower edges in the figure). Therefore these states form one dimensional edge channels along the boundary as shown in Fig. 2.4 and are assumed, from a single particle point of view, to be responsible for the electrical transport. A schematic diagram of one dimensional edge channels along the boundary of a Hall bar is shown in the right side of Fig. 2.4. The amount of the current that flows into i^{th} contact in a multi contact sample is formulated as

$$I_i = \frac{e}{h}(N - R_i) \cdot \mu_i - \sum_j T_{ij} \mu_j \quad . \quad (2.23)$$

Here N is the number of channels, R_i is the reflection coefficient at the contact i , T_{ij} is the sum of transmission coefficient from contact j to contact i and μ_i is the electrochemical potential ¹.

In equilibrium no net current flows through the device. Under non equilibrium conditions the amount of current fed into a channel is proportional to the electrochemical potential difference between contacts (contact 1 and 2 in Fig. 2.4) and reads as follows,

$$I = \frac{e}{h}(\mu_1 - \mu_2) = \frac{e}{h}\Delta\mu \quad . \quad (2.24)$$

The total current is

$$I = N \frac{e}{h} \Delta\mu \quad . \quad (2.25)$$

¹In the original paper of Büttiker the term chemical potential was used. However, since the contribution of the electrostatic potential has to be included the term electrochemical potential has to be used.

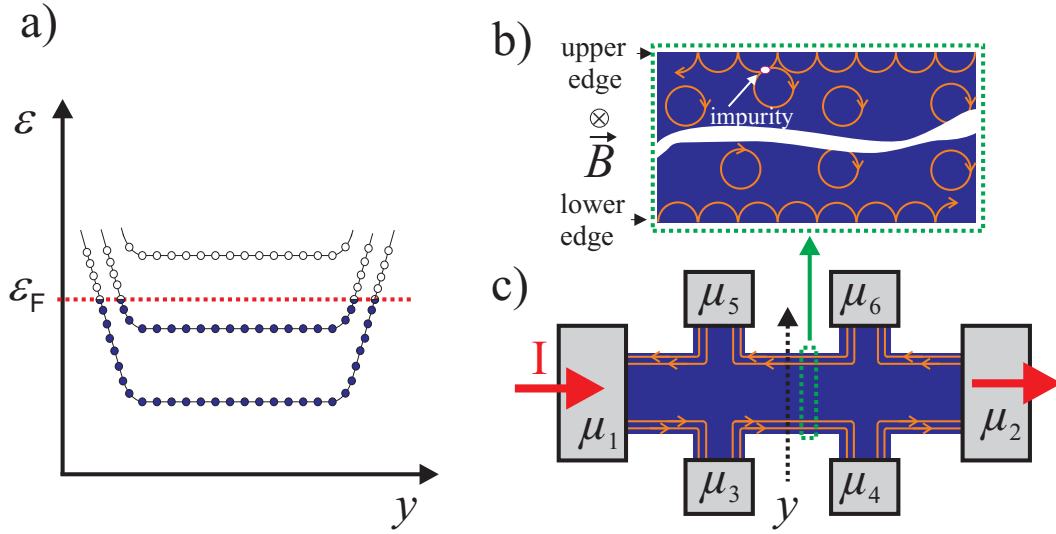


Figure 2.4: (a) Landau levels bending at the edges of sample (in equilibrium). Edge states exist at the intersection of Landau levels with the Fermi level. (b) A typical sample geometry, Hall bar, which is used to measure the QHE in 2DES. Two occupied Landau levels below the Fermi energy are assumed. Therefore, there are two occupied edge channels at the Fermi level at the edges of the sample. The edge channels are indicated as orange lines and arrows indicate the direction of drift velocity for electrons. A portion of the sample is highlighted (green frame) to show quasiclassical skipping orbit at the edges of the sample. An impurity near the edges does not cause back scattering as long as the cyclotron radius is smaller than the sample width and distance between scatterers. Adopted from Büttiker [10].

Finally, since the voltage drop between contacts is $eV = \Delta\mu$ the two terminal resistance between contact is expressed as

$$R = \frac{h}{e^2} \frac{1}{N} . \quad (2.26)$$

In the quantum Hall regime (at the Hall plateau), the Fermi energy lies in the middle of the gap, there are no extended states at the bulk, back scattering is suppressed and dissipation takes place only at the contacts. The voltage contacts, (see Fig. 2.4), are in equilibrium with the edge channels along the edge, thus $\mu_3 = \mu_4 = \mu_1$ and $\mu_5 = \mu_6 = \mu_2$. The longitudinal resistance is zero since $V_{34} = V_{56} = 0$ and Hall resistance is quantized as given in (2.26). The accuracy of the quantized Hall resistance is related to the degree of suppression of back scattering [10, 16]. Even in the presence of many impurities backscattering is suppressed at high magnetic fields as long as the mean distance between scatterers is large compared to the cyclotron radius [10]. Quantization is lost when the Fermi

level lies in the middle of a Landau level since in that case extended states that exist in the bulk allow backscattering between edges in the opposite side. The electrostatics of the edge channels has been analyzed and solved analytically by D.B. Chklovskii, B.I. Shklovskii, L.I. Glazman [11](CSG) [11]. The focus of the next section will be on this model.

2.2.3 Electrostatic of edge channels and formation of compressible and incompressible stripes

The edge state picture does not account for the electrostatic screening effects of 2DES. A qualitative description of the screening effects on the edge channels, leading to the presence of alternating compressible and incompressible stripes, was discussed by Beenakker [17] and Chang [18]. However, these two models lack a quantitative description and do not give any information about width and position of these stripes. Moreover, both papers contradict to each other in the prediction in which stripe the current flows. A quantitative description of edge channels was given by D.B. Chklovskii, B.I. Shklovskii, L.I. Glazman [11](CSG). In the CSG model, a half plane of 2DES is considered to be depleted via a metallic gate on the other half plane with the boundary at $y = -l$. The system is translational invariant in x direction. The boundary of the 2DES is obtained via a negative voltage applied to the gate electrode. A perfect screening is assumed in the 2DES. Solving the Poisson equation with the boundary conditions gives the analytical solution of the problem. At zero magnetic field, the density profile of electrons at the edge towards the bulk reads as follows,

$$n = \left[\frac{y - l}{y + l} \right]^{1/2} n_0 \quad , \quad (2.27)$$

where $2l$ is the gate voltage dependent depletion length and n_0 is the density of electrons in the bulk (far from the gate). As it is clear, the gate dependent depletion length $2l$ is the only relevant scale that determines the density profile. Density is zero for $y < l$ and smoothly increases towards to the bulk. If a finite magnetic field is applied perpendicularly to the plane of the 2DES the situation is different, as depicted in Fig. 2.5. On the left side of the figure, the single-electron picture is shown. The self-consistent electrostatic picture is shown on the right side. The drawback of the single-electron picture is that whenever a Landau level crosses the Fermi level, the density of electrons shows a step-like increase and stays constant over a large length scale. However, the electron density distribution can not be very different from the zero field profile since it costs huge amount of electrostatic energy. The effect of the magnetic field is the dependence of screening properties of the 2DES on the local filling factor ν_l : no screening at

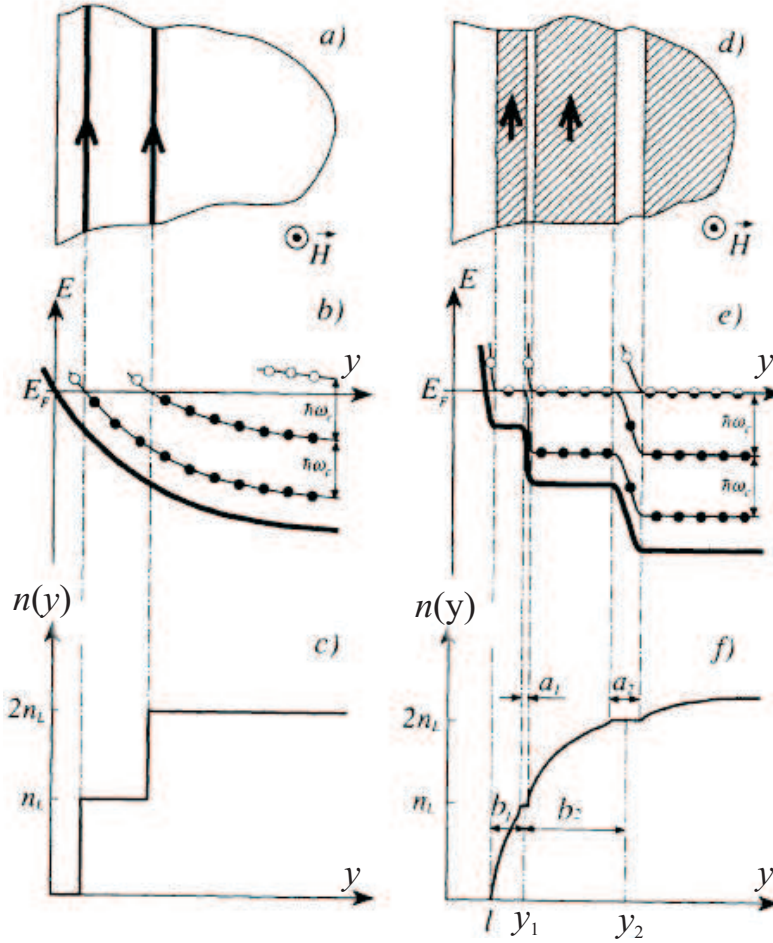


Figure 2.5: Edge state picture versus self-consistent electrostatic picture. (a)-(c) the single-particle picture is depicted. a) Top view of 2DES near the edge. Arrows indicate the direction of the electron flow in the two edge channels. b) The bending of Landau levels near the edge due to the confining potential. Circles represents local filling of the Landau levels: \circ , empty ; \bullet occupied. c) Electron density from the edge towards the bulk. (d)-(f) Self consistent electrostatic picture. d) Top view of the 2DES near the edge; shaded regions represent compressible regions and unshaded regions represent incompressible regions. Arrows show the direction of the electron flow. e) Bending of the electrostatic potential and Landau levels near the edge. f) Electron density as a function of distance from the edge. $2l$ is the gate voltage dependent depletion region. The gate is located at $y = -l$. Adopted from Ref [11].

the integer values of local filling factor and very good screening at non integer values. This leads to the formation of alternating stripes. The region with integer

local filling factor are called incompressible stripes. Within the incompressible stripes there are no states available at the Fermi level. Rearrangement of electrons in the incompressible region is not possible therefore electrostatic potential is not screened. In the incompressible stripes electron concentration is constant. The incompressible region behave insulator like. On the other hand, in the compressible regions there are states available at the Fermi level, rearrangement of electrons in the region or adding on more electron to the region is possible [11, 18]. Therefore in the compressible stripes the confinement potential is screened, thus within the compressible stripes electrostatic potential is constant.

The position of the k^{th} incompressible stripe from this self-consistent electrostatic theory is given as

$$y_n = l \frac{\nu^2 + k^2}{\nu^2 - k^2}. \quad (2.28)$$

Here ν is the bulk filling factor defined as $h n_s / eB$, n_s is the bulk density of electrons. The width of the k^{th} incompressible stripe is

$$a_k^2 = \frac{8\epsilon\epsilon_0 \hbar \omega_c}{\pi e^2 dn/dy|_{x=x_k}}, \quad (2.29)$$

where ω_c is the cyclotron frequency $\omega_c = eB/m^*$, m^* being electron effective mass on GaAs. For a given bulk filling factor value, the innermost incompressible stripe (if there exist several) is the widest. While CSG theory gives very valuable information about the formation of compressible and incompressible stripes, it lacks two important properties. The analytical solution is a zero temperature solution and electrochemical equilibrium is not satisfied [19]. Self-consistent numerical solutions for nonzero temperatures satisfying electrochemical equilibrium came out from R. R. Gerhardts and his group [12, 19–21], confirming the validity of (2.28) and (2.29).

2.2.4 Self-consistent calculation of edge channels

The numerical self-consistent calculations of R.R. Gerhardts group confirms the existence of alternating stripes of compressible and incompressible regions and support the CSG theory [19]. R. R. Gerhardts group treats a similar geometry considered in the work of CSG model. This model uses the electrostatic approach of CSG to solve the Poisson equation for calculating the potential for a given charge density at zero magnetic field. Then a self-consistent schema is followed: (1) electron density is determined, in the thermodynamical equilibrium, within the self-consistent Thomas-Fermi approximation, with the boundary condition that the electrochemical potential μ_{elch} , the local chemical potential $\mu_{\text{ch}}(\mathbf{r})$ plus the local electrostatic energy $-e\phi(\mathbf{r})$, is constant in the whole 2DES,

$$\mu_{\text{elch}} = \mu_{\text{ch}}(\mathbf{r}) - e\phi(\mathbf{r}) = \text{const}; \quad (2.30)$$

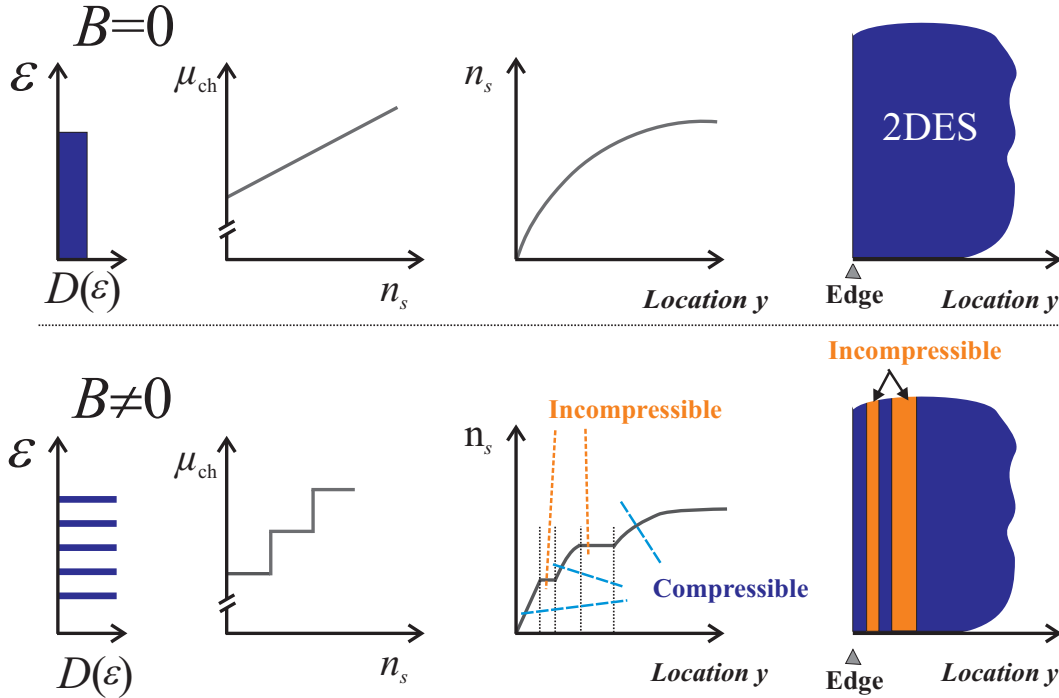


Figure 2.6: Sketch of the density of states $D(\epsilon)$ as a function of single-particle energy ϵ , the chemical potential μ_{ch} versus electron concentration n_s , and the electron concentration in the absence and presence of perpendicular magnetic field in 2DES. Right bottom: compressible and incompressible stripes at the edge of 2DES.

and (2) the local electrostatic potential $\phi(\mathbf{r})$ is related to local electron concentration $n_s(\mathbf{r})$ via Poisson equation with the appropriate boundary condition of the sample. At zero magnetic field for an ideal 2DES the density of states is a constant of energy as depicted in Fig. 2.6. The chemical potential increases linearly with increasing electron concentration; the electron concentration is a smoothly increasing function and reaches its bulk value far from the edge. At a perpendicular magnetic field the density of states is discrete and degenerate due to Landau quantization. The chemical potential is a step-like function of the electron concentration. Thus, whenever a level is completely occupied, increasing the electron concentration towards bulk requires a large amount of chemical energy; instead it is energetically more favorable to keep electron concentration constant for a region of finite width and pay a smaller amount of electrostatic energy. That leads to the formation of alternating region of constant electrostatic potential and constant electron concentration in the edge region of 2DES, compressible and incompressible stripes, as sketched in Fig. 2.6 [22].

The result of the self-consistent calculation of Lier *et al.* is presented in Fig. 2.7

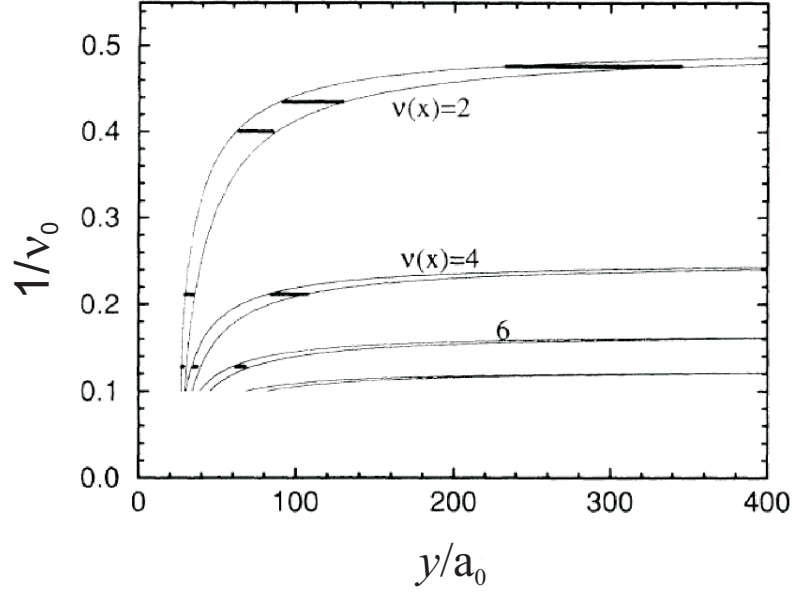


Figure 2.7: Magnetic field dependence of the position and width of incompressible stripes for corresponding local filling factor $\nu(y) = \{2, 4, 6, 8\}$ at different magnetic fields, measured by the inverse bulk filling factor (vertical axis). The thin solid lines represent analytical result of CSG theory for the stripe edges. The thick horizontal bars are numerical results of self-consistent theory of Lier and Gerhardtts. $a_0 = a_B^*/2$ is the screening length and is around 5 nm. Taken from Lier *et al.* [19].

compared with the analytical solution of theory of CSG. The thin solid lines indicates the position of the edges of innermost incompressible stripes according to CSG. The center position $y_\nu = |y - y_{edge}|$ of the incompressible stripes from CSG is reformulated by Lier and Gerhardtts [19] as

$$y_\nu = \frac{d_0}{1 - \left[\frac{\text{int}(\nu)}{\nu} \right]^2} \quad (2.31)$$

where $\text{int}(\nu)$ is the integer part of the bulk filling factor, ν , and d_0 is the gate voltage dependent depletion width,

$$d_0 = \frac{4\epsilon_0\epsilon_{\text{GaAs}} V_g}{\pi e n_s} . \quad (2.32)$$

Here V_g is the gate voltage. The width of the incompressible stripe, a_ν , is also reformulated

$$a_\nu = \frac{4y_\nu}{\nu} \sqrt{\frac{\text{int}(\nu)a_B^*}{\pi d_0}} , \quad (2.33)$$

where $a_B = 4\pi\epsilon_0\epsilon_{\text{GaAs}}\hbar^2/(e^2m^*)$ is the effective Bohr radius. The horizontal thick lines indicate the position and width of the incompressible stripes from Lier et al. Both theories agree very well in the predicted position of incompressible stripes. At half integer filling factor, away from a plateau, the bulk is mainly compressible and the width of innermost incompressible stripe is small. As the magnetic field is increased, the incompressible stripes move towards the middle of the 2DES and gets wider. Towards the middle of the plateau the incompressible stripe becomes wider and in the middle of the plateau the whole bulk of the 2DES is incompressible. The numerical self-consistent theories give information about compressible and incompressible stripes at finite temperatures as well. With increasing temperatures the width of incompressible stripes becomes thinner than zero temperature width. The potential in the compressible stripe is not exactly flat; total variation is of the order of thermal energy $k_B T$ which becomes zero at zero temperature. However the plateaus of electron density in the incompressible stripe is absolutely flat within the numerical accuracy [19]. An important implication of the self-consistent calculations is that the current is confined in the incompressible stripes [12]. Several experimental studies have been reported where the findings cannot be explained from the single-particle picture of the edge channels but imply existence of alternating compressible and incompressible stripes [22–25]. Experimental studies of current distribution on the QHE reveal more convincing evidences for the existence of region of compressible and incompressible stripes in the samples. In the following section the experimental findings of the current distribution on the QHE will be discussed.

2.3 Scanning probe experiments on potential profiles of quantum Hall samples

2.3.1 Hall potential profile in Hall bar samples

Experiments on the current distribution of the QHE samples have been very useful for the understanding of the microscopic nature of the QHE [13, 26]. Here the experiment that has been performed in our group will be discussed [13, 27–29]. A scanning force microscope has been used to probe the local potential landscape in 2DES at low temperatures and high magnetic fields. Experiments have been performed at a temperature of 1.4 K. The resonant frequency shift of the cantilever which is sensitive to the electrostatics of the sample is used as a signal. A calibration technique is used to eliminate contributions from the surface and donor layer of the sample. For this, a trace (trace α) is taken at the equilibrium when no current flows in the device; then another trace (trace β) is taken while current flows in the device. The Hall potential is obtained via dividing the trace β to trace

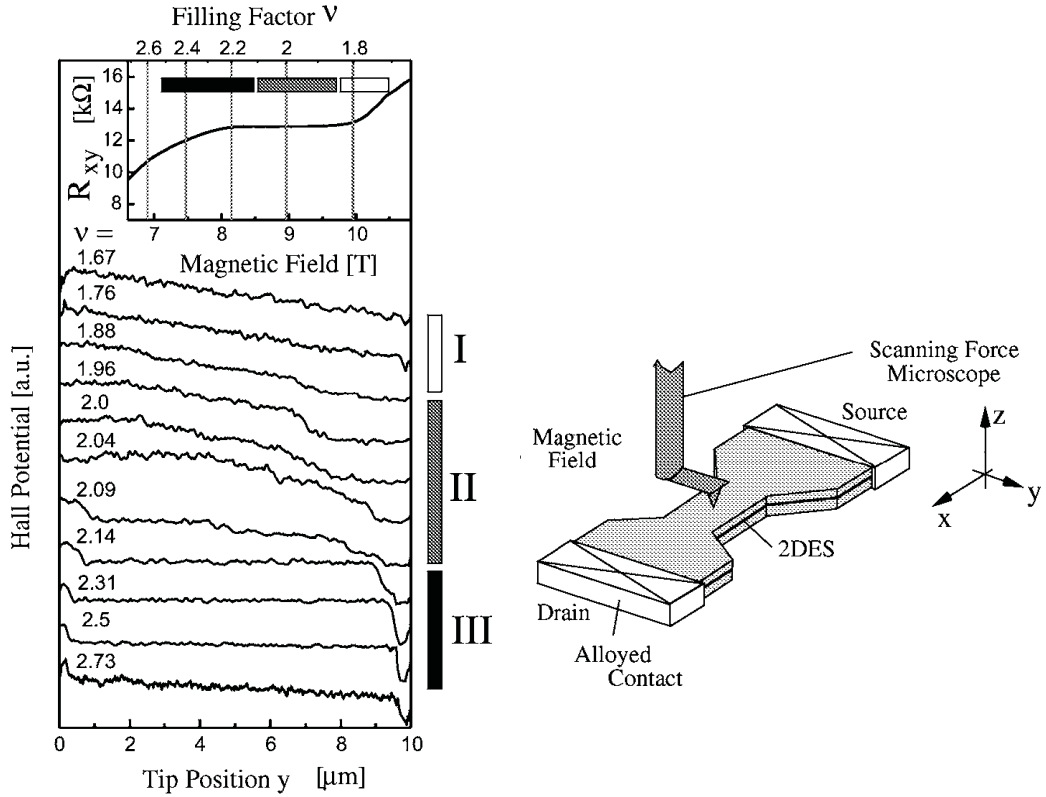


Figure 2.8: Left: Hall potential profile measured on a Hall bar with a scanning probe microscope for different magnetic field values around filling factor $\nu = 2$. The width of sample is $10 \mu\text{m}$ with a mobility of $50 \text{ m}^2/\text{Vs}$. Shown in the inset is the corresponding Hall resistance data around $\nu = 2$ quantum Hall plateau. Right: Sketch of measurement setup and sample; the scanning direction y is indicated [13, 27].

α [13, 27–29].

The measured Hall potential profiles are shown in Fig. 2.8. The scan direction on the sample is shown on the right side on the same figure. The line scans are taken for the different magnetic field values around filling factor $\nu=2$ but along the same line on the sample. Three different types of profiles can be identified clearly. Approaching to the quantum Hall plateau from the higher values of magnetic field (from lower values of filling factor) the Hall voltage drops linearly as is the case for classical Hall effect; this is labeled as type I profile. The type II profile is faced between the filling factor values of $\nu = 1.96$ and $\nu = 2.04$. Here the Hall potential profile is rather flat in the edges and has a drop at the inner region of the

sample. Above $\nu = 2.10$ (lower magnetic field side of plateau) the Hall potential profile is flat in the bulk and has step like drops at the both edges of the sample (type III). In Fig. 2.9 (a), the measured Hall potential profiles for a wide range of magnetic field is shown in color scale [27, 29]. As clearly seen the previously discussed three type of profiles repeat for consequent integer filling factors. The results of CSG [11, 19] calculations are compared with the experimental data in Fig. 2.9 (b). The position of the incompressible stripe from the theory and the position of the drop on the measured Hall potential profile agree very well.

Another example of such Hall potential profile is shown in Fig. 2.10 for $\nu = 2.0$ and $\nu = 2.1$. The sketch of the sample and scan direction are shown in Fig. 2.10 (a). In Fig. 2.10 (b) scans were taken at $\nu = 2.0$ which corresponds to type II Hall profile in previous discussion. As clearly visible, the Hall potential drops at the inner region of the sample whereas at the edges potential profile is rather flat. Fig. 2.10 (c) on the other hand is an example of the type-III Hall potential profile. Here a sharp drop occurs at the both edges of the sample which implies an incompressible stripe running along the 2DES boundary (mesa edge). What is more interesting is that the same sharp drop exists in front of the ohmic contacts as well.

The drop in front of the ohmic contacts implies that there is an incompressible stripe between the bulk of the 2DES and ohmic contacts border, which in turn means that bulk and contact are not at the same electrochemical potential. Such an incompressible stripe can be expected if electron density profile is not flat from contact to 2DES. Indeed a variation in the electron concentration (a partial depletion) in front of the contact can be expected since the contact metals and semiconductor structure have different work functions [30]. As we have discussed in previous chapters, a varying electron concentration results in the formation of compressible and incompressible stripes at low temperatures and high magnetic fields. It is necessary at this point to say that these are very good quality alloyed ohmic contacts that can be found in literature [31].

2.3.2 Potential profile in Corbino samples

Another very interesting experiment is the measurement of the potential profile under high magnetic field in Corbino devices [32]. A Corbino disc is a special sample geometry and consists of concentric circular conductor (2DES in this case) between a circular inner contact and a circular outer contact. A sketch of the device is shown in the inset of Fig. 2.11 (b); the gray areas are ohmic contacts and white area is 2DES. In the Corbino geometry, 2DES is surrounded by contacts everywhere. No Hall voltage arises due to the special symmetry of the geometry, i.e. the edges are shorted. In Fig. 2.11(a) the potential profile measured on a Corbino disk at filling factor $\nu = 2.2$ is shown. The sharp drop at both sides is

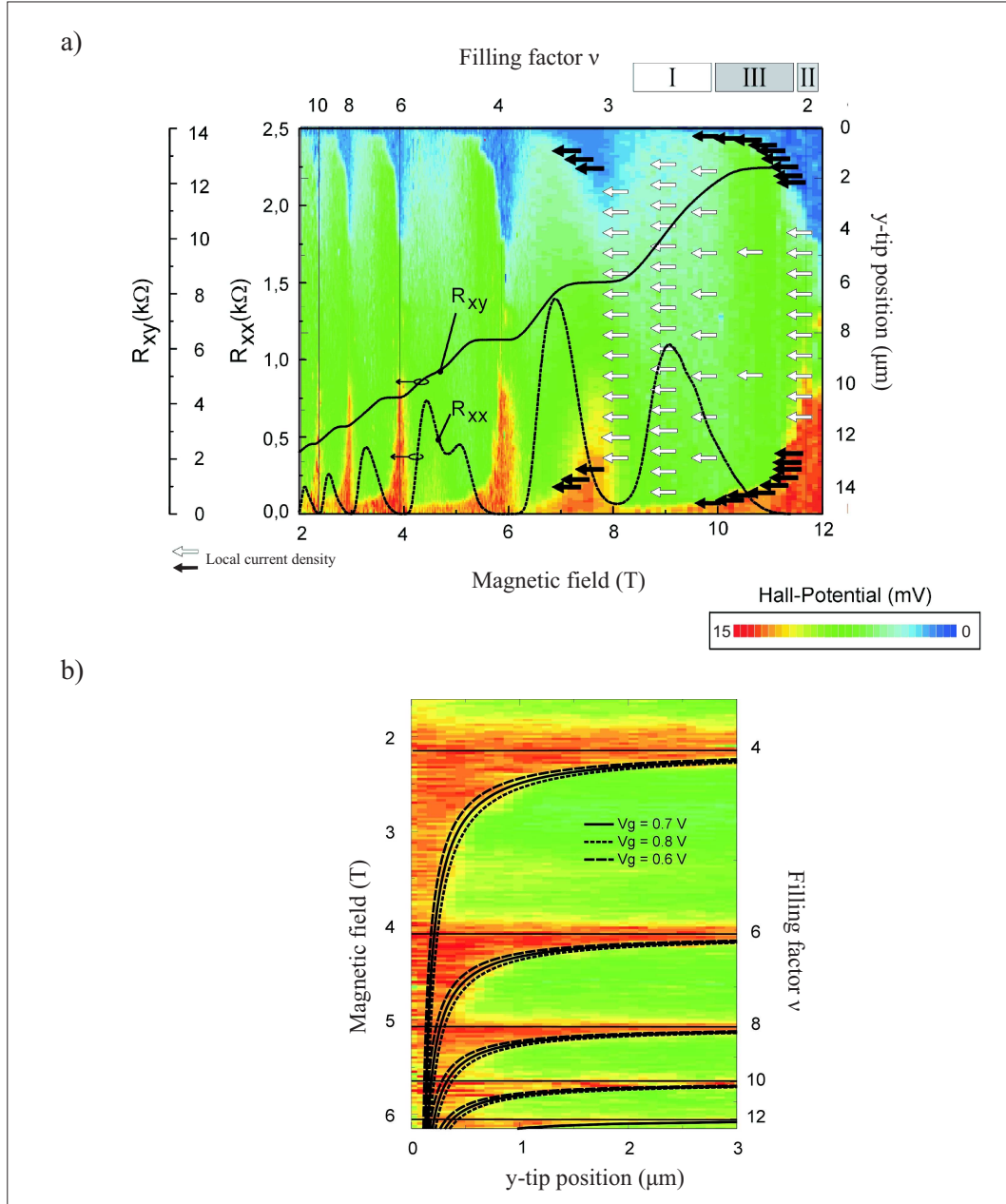


Figure 2.9: (a) Hall potential profile measured for a wide range of magnetic field (filling factor). Red is for high and blue is low potential as indicated on the color bar. The Hall resistance R_{xy} and longitudinal resistances R_{xx} are superimposed to the plot. Arrows indicate the local current distribution on the sample for certain magnetic field values. (b) Data from (a) for a limited filling factor range and position. Solid lines indicate the position of the incompressible stripes from the theory of CSG; the formula is given in (2.31) in its reformulated form by Lier and Gerhardt [19]. Theory is in perfect agreement with experiment. After reference [27, 29].

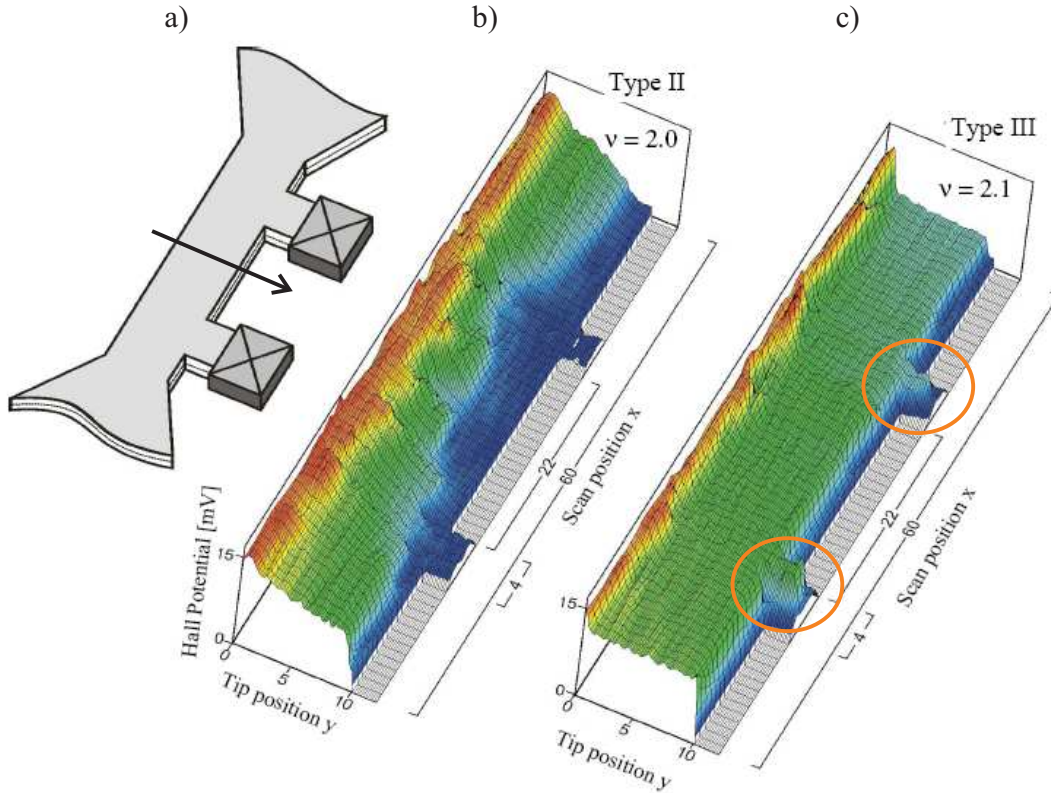


Figure 2.10: Hall potential landscape measured for two filling factors values $\nu = 2.0$ and $\nu = 2.1$. a) Sketch of the sample; scan direction is indicated. b) $\nu = 2.0$; Hall potential drop is in the inner region of sample. c) $\nu = 2.1$; Hall potential drops at edges of the sample. Note that this drop does not occur only at mesa edge but also at the 2DES/ohmic contact interface. From PhD thesis of Erik Ahlswede [27].

very clear. This profile is quite similar to the one measured in the Hall bar devices for the same filling factor value. The measured potential profile for a wide range of magnetic field near the inner contact is presented in Fig. 2.11(b). The position of the drop is close to the contact at $\nu = 2.5$ and moves away from the contact as filling factor decreases towards to integer value of $\nu = 2$. This is also similar to what has been observed in Hall bar samples. These findings clearly demonstrate that electron concentration in front of the contact is varying towards to bulk. Such a variation leads to the formation of compressible and incompressible stripes along the contacts.

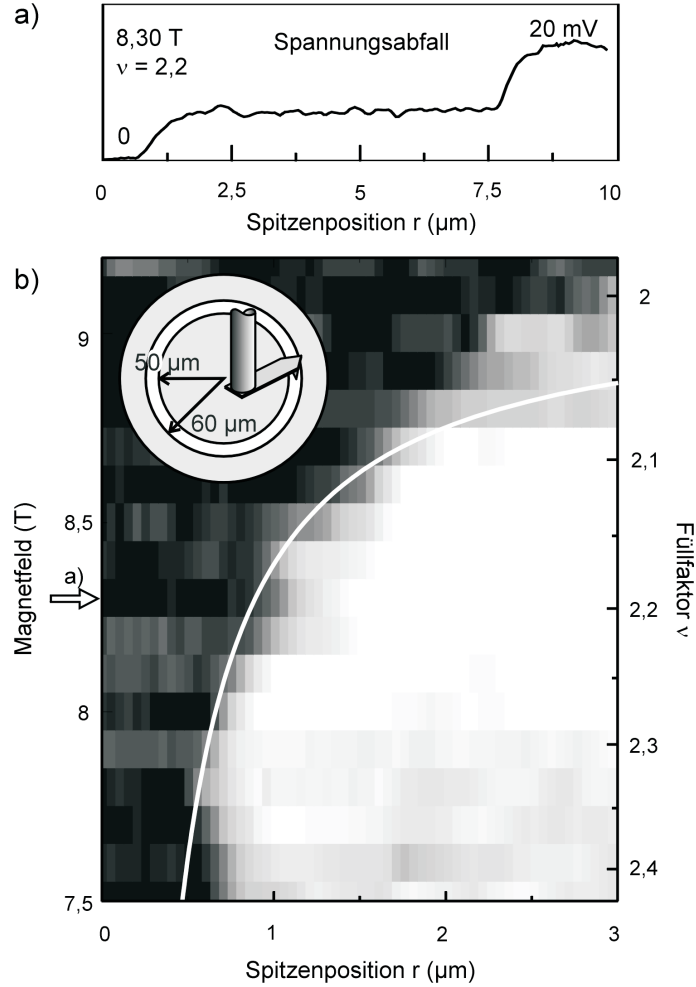


Figure 2.11: Potential profile measurements on a Corbino disk. (a) Line scan across the Corbino at a bulk filling factor of $\nu = 2.2$. The position r is measured from the inner contact. The sharp potential drops on both sides near the inner and outer contacts are very clear. (b) Color plot of line scans for a wide range of the magnetic field. White(black) indicates high(low) potential. Incompressible stripe moves towards inner part of the sample with increasing magnetic field. The white line indicates the position of incompressible stripes calculated from (2.31) for a gate voltage value $V_g = -0.7$ V. The device dimension is indicated in the inset. From PhD thesis of Erik Ahlswede [32].

2.4 The present understanding of microscopic picture of QHE based on compressible and incompressible stripes.

In this section we would like to summarize the present microscopic understanding of the QHE based on compressible and incompressible stripes. A quantum Hall

plateau for the filling factor, $\nu = i$, is shown in Fig. 2.12, where i is an integer [33]. The development of the compressible and the innermost incompressible stripes in a Hall bar is also shown. White represents compressible and gray represents incompressible regions. The stripes exist not only along the boundaries of 2DES but also along the contact/2DES borderline. There is yet no theory modeling compressible and incompressible stripes in front of the contacts. However, as we have seen in the previous sections, the Hall potential profile experiments on the Hall bar and Corbino devices clearly reveal the existence of the compressible and incompressible stripes along the contact/ 2DES border.

Away from plateau the whole bulk and edge are compressible. Current runs in the bulk and at the edges, as shown in sketch Fig. 2.12 (a). As magnetic field increased, at the lower edge of the plateau, incompressible stripes appear at the edges of the sample (b). The incompressible stripe hinders equilibration between the compressible bulk and compressible edges. Current flows in the incompressible stripe along the edges of the sample. In the middle of the plateau bulk is mainly incompressible (c). There are compressible islands due to the disorder potential fluctuations. Towards the upper edge of the plateau the incompressible bulk becomes narrower and disappears at the upper edge of the plateau (d). Then the situation that is shown in (a) is recovered as shown in (e). The whole bulk and edges become compressible.

To understand the origin of the quantized Hall resistance and vanishing longitudinal resistance the Hall bar is depicted with the electrochemical potential of the source (S) and drain (D) contacts in Fig. 2.12 (d). The electrochemical potential of the source is carried by the compressible region along one edge and the electrochemical potential of the drain is carried by the compressible region along the other edge. The incompressible stripe, when it is wide enough, hinders the equilibration between the compressible regions around it. Therefore whenever there exists a well developed incompressible stripe in the sample the Hall voltage drops across the incompressible stripe and the quantized value of the Hall resistance, $R_H = h/(ie^2)$, is measured. Dissipation takes place at the opposite corners of the contacts, indicated as hot spots, which has been experimentally confirmed [34,35]. The longitudinal resistance R_{xx} vanishes since the voltage contacts at the same edge are at the same electrochemical potential. The landscape of the compressible and incompressible stripes change strongly as the magnetic field swept in the quantum Hall plateau. Therefore the current distribution varies as well; mainly at the edges at the lower side of the plateau and mainly in the bulk in the upper side of the plateau. However, the quantized value of the Hall resistance remains the same since the compressible regions with different electrochemical potential are separated from each other by the incompressible stripe, which hinders the equilibration between them. Outside of the Hall plateau there is no incompressible

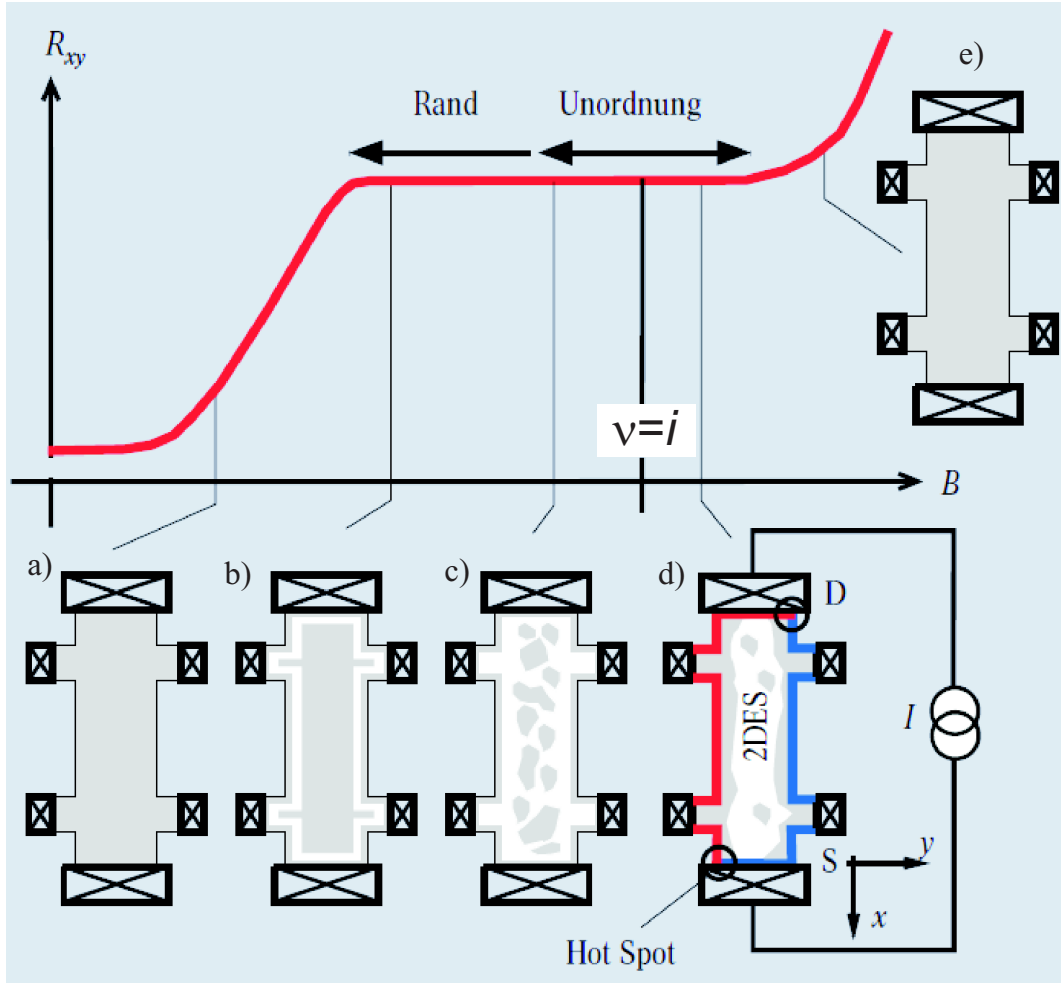


Figure 2.12: Sketch of the development of the compressible (grey) and innermost incompressible (white) regions in a real, inhomogeneous 2DES during a sweep of the magnetic field over a quantized Hall plateau. At lower B side of the plateau, the plateau is stabilized by incompressible stripes. At the higher B side of plateau the plateau is stabilized by disorder and inhomogeneities. In the plateau region a dissipationless current runs in the incompressible stripes, dissipation takes place at the opposite corner of the Hall bar as indicated as hot spots. Outside of the plateau, bulk and edges are mainly compressible and current runs in the compressible region with dissipation. R_{xx} is no longer zero and R_{xy} deviates from the quantized value. After [33]

stripe in the sample or it is not wide enough to isolate; the bulk and edge are compressible. Dissipation takes place everywhere in the sample. The edges of the sample are no longer equipotential, therefore the longitudinal resistance is no longer zero. The Hall resistance deviates from the quantized values [33].

As we have seen, the result of the Hall potential profile experiments are consistent with the CSG theory and self-consistent theory of R .R .Gerhardts group, as discussed previously. However there are a couple of open questions to be explored. The theory of R .R .Gerhardts et al. does not give any answer to the question: how can one put non equilibrium current from contact into the incompressible stripe. There is no existing theory that models density profile and compressible and incompressible stripes in front of the ohmic contacts in the QHE conditions. However the experimental observations are quite clear that there exist compressible and incompressible stripes around contacts. The interesting results of these experiments, revealing existence of compressible and incompressible stripes at the 2DES/contact border, and poor understanding of alloyed ohmic contacts on the QHE conditions give the motivation of the present work.

2.5 The link between microscopic picture of the QHE and the goal of the thesis

The goal of the present work is two-folded. One is to deepen the understanding of the ohmic contacts to 2DES under QHE conditions. This will be discussed in Chapter 4. The second one is to make use of our present knowledge about ohmic contacts to prepare new devices. Having known the existence of incompressible stripes in front of the ohmic contacts and keeping in mind that these stripes have insulating properties, we propose a new type of single-electron charging device. Before discussing the proposal of the new device, the single-electron charging effect and quantum dots will be explained in the next chapter. Then the proposed device will be presented in the same chapter.

Chapter 3

Proposal of a new type of single-electron charging device based on the submicron Corbino devices in strong magnetic field

In the previous chapter we have seen that Hall potential profile experiments suggest that compressible and incompressible stripes form in front of the ohmic contacts. Compressible stripes have metallic properties and incompressible stripes have insulating properties. Motivated by these findings we will propose a new single-electron charging device in this chapter. The device is a submicron Corbino device in the quantum Hall conditions. Under these conditions, for certain filling factor values, incompressible stripes form around the contact and are wide enough to isolate the inner compressible region from the contacts. That mimics a single-electron charging device, when the size of the island is small enough, in submicron scale, and temperature is low enough, in miliKelvin range. In this chapter a brief introduction of single-electron charging effect will be given in section 3.1. In section 3.2 the concept of quantum dots will be given. Then the proposal of a new type of single-electron charging device will be presented in section 3.3. The similarities of the proposed device to other type of single-electron charging devices will be discussed in section 3.4.

3.1 Single-electron charging effect and quantum dot systems

The single-electron charging effect arises due to the discrete nature of the electron charge. The effect is not observable at the large scale and high temperatures.

However as the device dimension gets smaller and temperature gets lower, the effect becomes observable and even becomes the dominant effect determining device properties. A series of excellent reviews exist in literature [36–39]. In this chapter the concept of single-electron charging and quantum dots (QDs) will be explained.

3.1.1 Concept of single-electron charging and Coulomb blockade effect

Let us consider the configuration shown in Fig. 3.1(a). The source and drain electrode are coupled to a metal island via tunneling barriers. The term island is commonly used since it is surrounded by an insulator [36]. Electron can tunnel in and out of the island. The island and leads can be made, for instance, of aluminum (Al) and tunneling barriers can be a thin layer of aluminum oxide. The gate electrode has a capacitive coupling to the island; no tunneling process can take place between the gate and the island. The equivalent circuit is shown in Fig. 3.1 (b). Transferring a single-electron between the island and electrodes costs an electrostatic *charging energy*¹

$$E_C = \frac{e^2}{2C_\Sigma} \quad , \quad (3.1)$$

where C_Σ is the total capacitance between the island and the rest of the system. The charging energy is usually negligibly small at room temperature compared to the thermal energy $k_B T$. However the charging energy exceeds the thermal energy at 1 K if the island size is about 1 micron or smaller. In this case, charge fluctuations, due to the thermal energy, between the island and leads are suppressed, assuming the bias voltage V_{DS} is small. The charge on the island is a well defined integer. In order to put one more electron on the island, a finite amount of energy has to be paid as depicted in Fig. 3.1(c).

The electrostatic energy stored in the configuration with N electrons in the island when the surrounding electrodes are at the potential V_i is

$$E(N) = \frac{(-Ne)^2}{2C_\Sigma} - Ne \sum_i \frac{C_i}{C_\Sigma} V_i \quad . \quad (3.2)$$

Here

$$C_\Sigma = \sum_i C_i \quad (3.3)$$

is the total capacitance of the island with respect to the rest of the system (all the leads and gates), C_i is the capacitance of the i^{th} electrode to the island and

¹In the literature different definition exist. e^2/C_Σ is also called as charging energy.

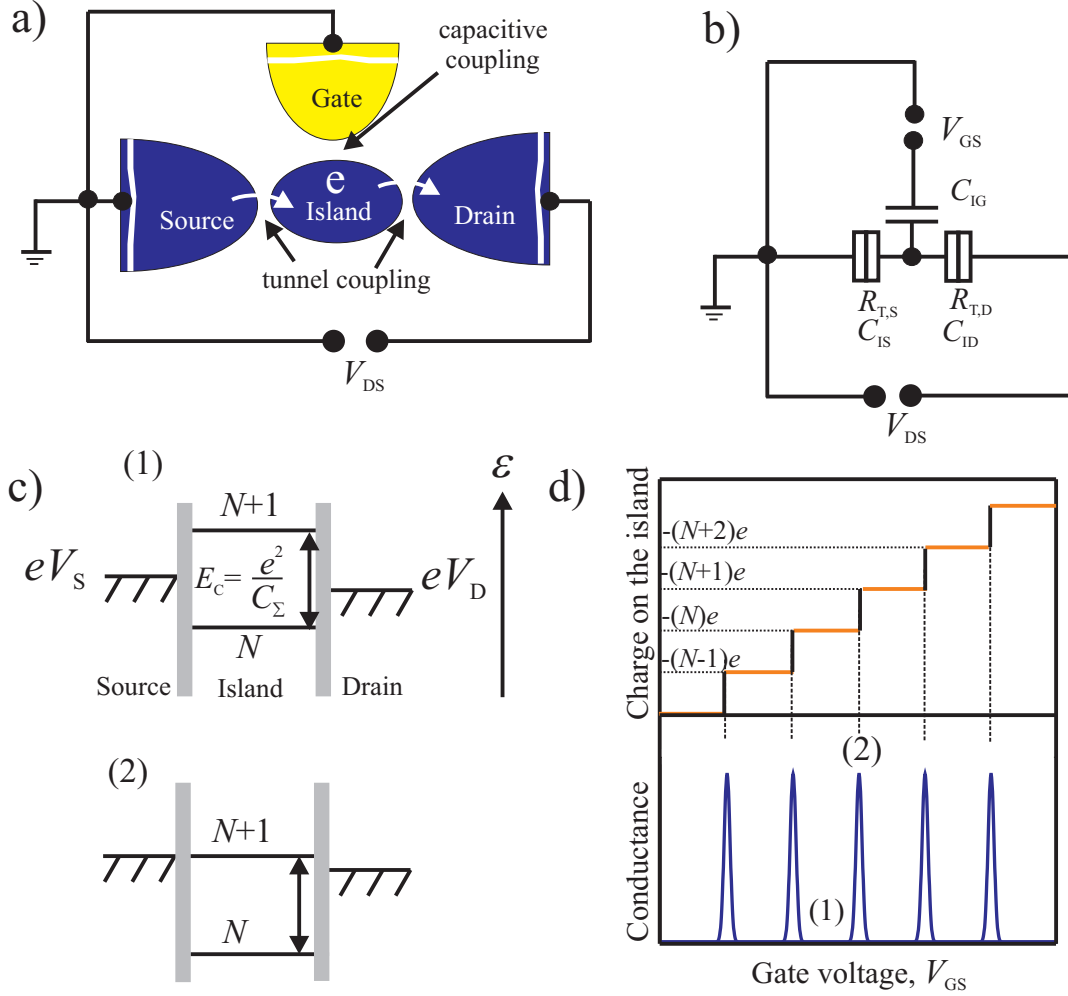


Figure 3.1: Single-electron charging effect and Coulomb blockade effect. (a) A mesoscopic metal island is coupled to leads via tunneling barriers and capacitively coupled to a nearby gate electrode. (b) Equivalent circuit. (c) Energy scheme representing the charging energies for two distinct gate-source voltages: (1) Coulomb blockade regime, i.e. no tunneling occurs. (2) charge degeneracy regime, i.e. sequential tunneling of electrons is possible. (d) The amount of the charge in the island (starting counting from the electrically uncharged island) is increased one by one with increasing gate voltage. Conductance oscillates as a function of gate voltage.

V_i is the voltage of i^{th} electrode where i labels source, drain and all gates in the system. The first term in this expression is the electrostatic charging energy stored in the capacitor (island and all the other electrodes) due to separation of charge ($-Ne$) from the surrounding electrodes. The second one is the electrostatic

potential energy of the N electron in the island due to the electrostatic potential of surrounding electrodes. The energy required to put the N^{th} electron onto the island when $N - 1$ electron are present on the island is

$$\Delta E = E(N) - E(N - 1) = (N - \frac{1}{2}) \frac{e^2}{C_\Sigma} - e \sum_i \frac{C_i}{C_\Sigma} V_i . \quad (3.4)$$

This addition energy is discrete due to the discrete nature of the charge, with an energy gap of

$$\frac{e^2}{C_\Sigma} = 2E_C . \quad (3.5)$$

The equation (3.4) suggests an energy ladder whose levels are separated by $2E_C$ for different number of electrons on the island for a fixed gate voltage as depicted in Fig. 3.1 (c). In situation (1) transport is blocked since electrons on the leads have not enough energy to charge the island (Coulomb blockade). The electrostatic potential of the island can be shifted by changing the voltage of the gate electrode. By increasing the gate voltage, the energy levels of the island are lowered. Finally when $eV_S \leq E(N+1) \leq eV_D$ is fulfilled, a charge degeneracy point is reached. At this point the electrostatic energy defined in (3.2) is degenerate for having N electrons or $N+1$ on the island. Thus, the charge of island can fluctuate between N and $N+1$ as shown in Fig. 3.1 (c)(2). Transport is no longer blocked and electron can tunnel in and out of the island sequentially. The conductance is not zero as depicted in Fig. 3.1 (d). Increasing the gate voltage more and more, lowers the energy levels of island and a similar situation to that depicted in (1) is reached having $N+1$ electrons on the island. The transport is blocked again. Thus, the conductance peaks are observed with sweeping the gate voltage with a period of

$$\Delta V_G = \frac{e}{C_G} . \quad (3.6)$$

These are called Coulomb blockade oscillations. The whole system is called single-electron transistor (SET).

As we have discussed at the beginning, the observation of the Coulomb blockade is a direct result of the isolation of a small island from the leads. But the leads and the island are coupled via tunneling barriers. The tunnel barriers should be transparent enough to allow tunneling. On the other hand, the transparency should be such that electrons are either localized on the island or in the leads. An estimate for the resistance of the tunneling barriers, R_T , fulfilling localization of the electrons in the island, is usually made following Heisenberg uncertainty relation, $\Delta E \Delta \tau \geq \hbar$. The energy uncertainty associated to the lifetime, $\tau = R_T C_\Sigma$ of electrons on the charge state of the island should be smaller than the charging

energy, $\Delta E \leq E_C$. The island is usually considered as isolated if

$$R_T \geq h/e^2 \approx 25.8 \text{ k}\Omega \quad . \quad (3.7)$$

However, this number should be taken as an order of magnitude measure not as a critical well-defined value.

3.1.2 Transport spectroscopy under finite bias

In the previous section the applied bias voltage was small, practically zero. One can apply a finite bias voltage V_{DS} and investigate transport properties of the single-electron transistor. Away from the charge degeneracy point, as depicted in Fig. 3.2 (a), transport is blocked. The threshold level for charging the island can

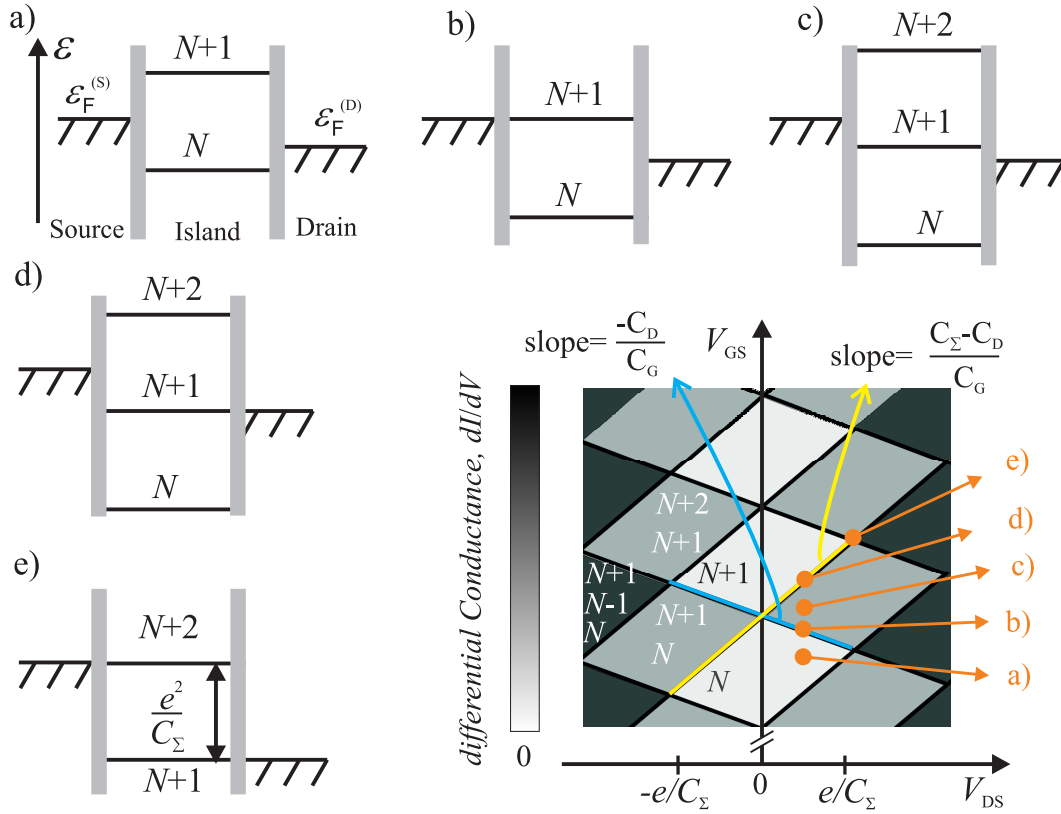


Figure 3.2: (a)-(e) Energy scheme of a few special cases in the charge-stability diagram. (f) Charge-stability diagram of a SET. White regions are Coulomb blockade regions of transport. On the nearby gray areas, sequential tunneling of single-electrons takes place. In the more darker regions, tunneling of multi electrons are allowed. The slope of the red and blue indicated lines give the capacitance ratio of the electrodes.

be lowered as defined in (3.2). As the threshold level of $N + 1$ electrons is aligned to the Fermi level of one of the leads transport is allowed. A finite conductance is measurable as long as the threshold level stays in the transport window of the leads as depicted in (c). Increasing the gate voltage brings the threshold level of $N + 1$ electrons aligned to the Fermi level of the drain electrode as shown in (d). Tunneling of two electrons at same time is also possible if the bias voltage is large enough as shown in (e)². Here the multi electron transport takes place and the current is larger than that of the situation depicted in (c). Indicating the transport regions of a SET in the (V_{DS}, V_{GS}) plane as shown in (e) is named charge-stability diagram. In the central white diamonds transport is blocked. In the gray areas single-electron tunneling takes place. The more darker areas are the region of the multi-electron tunneling.

The charging energy and the capacitance ratios can be derived from the charge-stability diagram. The maximum value of the bias voltage at which Coulomb blockade ends is $V_{DS} = 2E_C/e = e^2/C_\Sigma$, as indicated in the V_{DS} axis. The capacitance ratio of the drain and source electrode to the gate electrode can be derived from slope of the red and blue indicated line [37]. When source electrode is the reference electrode, the slope of the blue line is

$$\frac{dV_{GS}}{dV_{DS}} = -\frac{C_D}{C_G} \quad , \quad (3.8)$$

and the slope of the yellow line is

$$\frac{dV_{GS}}{dV_{DS}} = \frac{C_\Sigma - C_D}{C_G} \quad . \quad (3.9)$$

3.2 Quantum dot systems

Up to here the discussion was about a metal island which ranges from a few ten nanometers to a micron. In a metal the Fermi wavelength is very small compared to the dimension of the island. If the island is made of a semiconductor the situation is different due to smaller density of electrons. The Fermi energy is small therefore the Fermi wavelength is larger. In GaAs the typical Fermi wavelength λ_F is 46 nm for a typical Fermi energy of 10 meV. For a single-electron transistor realized in GaAs structures the Fermi wavelength becomes comparable to the size of the island. Therefore the confinement energy, due to the quantum mechanical nature of the particles, is large and becomes equal to the charging energy for an island having a diameter of 40 nm in GaAs [40]. This modifies

²If the tunneling barriers are strongly asymmetric this situation might alter the transport and a single-electron transport is observed instead of a multi electron transport.

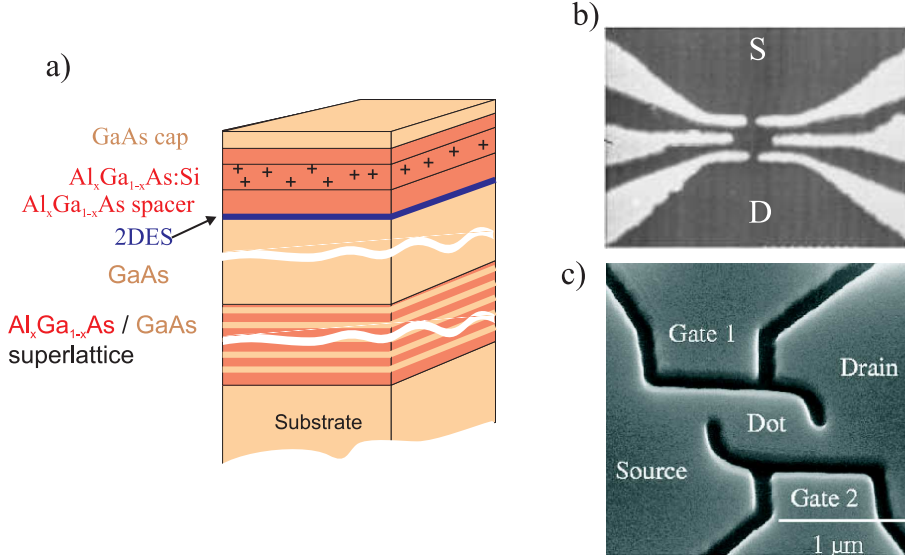


Figure 3.3: (a) 2DES in the GaAs/ $\text{Al}_\delta\text{Ga}_{1-\delta}\text{As}$ heterostructures. (b) A split gate QD defined in GaAs/ $\text{Al}_\delta\text{Ga}_{1-\delta}\text{As}$ heterostructure (top view). By applying voltage to the gates, the 2DES underneath the surface can be divided into regions. The small droplet of electrons is formed between gates separated from the large 2DES regions. The tunneling in and out of the island is possible. The large areas indicated as S and D act as source and drain and are contacted via alloyed ohmic contacts at the edge of the heterostructure [41]. (c) A QD defined by etching (top view). The dark traces are etched regions, dividing the 2DES in the respective regions [42].

the energy gap for adding an electron into the island. Now the system is called quantum dot (QD). A phenomenological model for describing a many-electron quantum dot is widely used and called constant interaction (CI) model. It assumes that discrete electronic levels are independent of the electron number in the dot. Furthermore, the interaction of electrons in the dot and leads or gates are described via capacitances. To put one more electron in the island requires not only the electrostatic charging energy but also energy required to get into next unoccupied discrete single-particle level.

$$\Delta E = \frac{e^2}{2C_\Sigma} + (\varepsilon_i - \varepsilon_{i-1}) \quad , \quad (3.10)$$

where ε_i are single-particle energies. The set of the discrete levels, described by (3.10), is called addition spectrum of the quantum dot. Two example of experimental realization of QD in GaAs/ $\text{Al}_\delta\text{Ga}_{1-\delta}\text{As}$ heterostructure are shown in Fig. 3.3.

The transport spectroscopy of a QD is similar to that of a SET. However, now

there are some additional features due to the confinement. The tunneling rate does not depend only on the transparency or height of the tunnel barriers but also overlap of the wave function of electrons on the dot to the leads. This overlap can be different for the different states. Thus, the height of the zero bias conductance peaks are no longer equal. As long as single-particle levels ε_i are not equally spaced or degenerate, the conductance peaks are not periodic. Another important difference is that now there might be additional excited states of the N electrons in the QD. These excited states manifest themselves as shown in Fig. 3.4 (b). Whenever an excited state is in the transport window of source and drain as shown in Fig. 3.4 (1) and (2), there will be two available states to charge and discharge the QD. However, two electrons can not tunnel in parallel. Therefore the process is still sequential tunneling. But the existence of the additional state increases the probability of electrons to tunnel into the island and therefore generally leads to

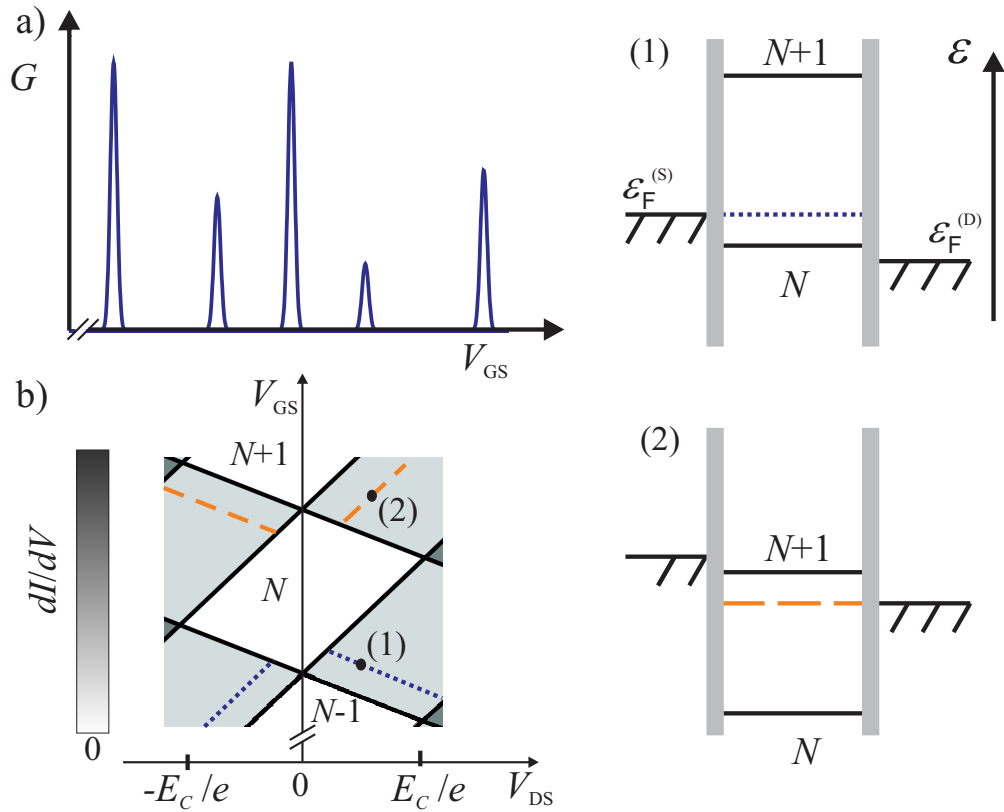


Figure 3.4: (a) Conductance of a QD as a function of gate voltage. (b) Charge-stability diagram of a QD. Two example of excited states are shown as orange and blue lines. (1), (2) Energy level schemes of the selected points on (b).

an increase in the current. There are also cases where the existence of an excited state results in a decrease of current if the lifetime of the excited states is longer (lower tunnel coupling). There have been several experimental studies of addition and excitation spectrum of QDs [37, 43].

3.2.1 The Fock-Darwin spectrum

The single-particle energy spectrum of a QD in a parabolic confinement, for non-interacting electrons, in the presence of magnetic field was given by Fock and Darwin [44, 45] and called Fock-Darwin spectrum. The eigenenergies $E_{n,l}$ as a function of magnetic field B in a parabolic confining potential $V(r) = m\omega_0^2 r^2/2$ are

$$E_{n,l} = (2n + |l| + 1) \frac{\hbar}{2} \sqrt{(4\omega_0^2 + \omega_c^2)} + \frac{1}{2} l \hbar \omega_c , \quad (3.11)$$

where n is the radial quantum number, l is the angular quantum number, $\hbar\omega_0$ is the electrostatic confinement energy and $\hbar\omega_c$ is the cyclotron energy. Each level has a two-fold spin degeneracy. Experimental observation in vertical few electron QDs are in good agreement with the Fock-Darwin spectrum [43].

In the intermediate magnetic fields, one can rewrite the Fock-Darwin spectrum in a new way using the following transformations [46],

$$p = n + \frac{1}{2}(|l| + l) , \quad (3.12)$$

and

$$m = n + \frac{1}{2}(|l| - l) + 1 . \quad (3.13)$$

Then the new form of the Fock-Darwin spectrum, neglecting spin splitting, is

$$E_{m,p} = \hbar(m + p) \sqrt{\omega_0^2 + \frac{1}{4}\omega_c^2} + \frac{1}{2} \hbar(m - p - 1) \omega_c . \quad (3.14)$$

Between filling factor $2 < \nu < 4$, the electrochemical potential of the quantum dot has a zigzag behavior with magnetic field for a constant electron number in the dot. The magnetic field periodicity ΔB is

$$\Delta B \approx \left(\frac{\omega_0}{\omega_c}\right)^2 B . \quad (3.15)$$

The energy levels are approximatively equally spaced,

$$\Delta E = E_{m,p+1} - E_{m,p} \approx \hbar \frac{\omega_0^2}{\omega_c} . \quad (3.16)$$

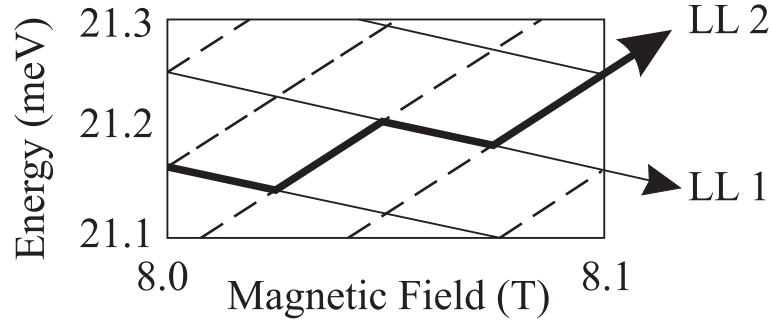


Figure 3.5: A section of energy spectrum of a quantum dot at the intermediate magnetic field for $2 < \nu < 4$. The spectrum is calculated for a circular quantum dot with parabolic confinement of $\hbar\omega_0 = 1$ meV. From [46].

3.3 Proposal of a new type of single-electron charging device: Submicron Corbino devices in strong magnetic fields

We have seen that the main ingredient of a single-electron charging device is an island of electrons isolated from the leads via tunneling barriers. In case of a metal SET, the island is a small metal island and tunneling barriers are formed by a thin oxide layer. In case of a QD, the island is a small region of electron in a 2DES separated from the rest of 2DES via gate or etching defined depletion. The depleted regions act as tunneling barriers. Several realization method for single-electron charging devices have been demonstrated. For instance single electron charging devices realized with carbon nanotubes [47], QDs defined in vertical pillars of GaAs/Al_δGa_{1-δ}As heterostructures [43] or quantum antidots [48]. In this section a proposal for a new type of single-electron charging device will be presented as a main goal of this thesis.

The scheme of device is shown in Fig. 3.6(b). The device is a Corbino device on submicron length scale. That is, there is a circular inner contact and a circular concentric outer contacts. Contacts are alloyed Au/Ge/Ni contacts and the contacts recipe and quality will be discussed in Chapter 4. With alloying, contact material sink into heterostructure and make electrical contact to 2DES which is 40 nm or 50 nm below the surface. That is, we have two metallic contacts (inner and outer) and in between 2DES. Details of fabrication process will be discussed in Chapter 6.1. If the device is a macroscopic one, usually more than a few ten micron, there is nothing interesting at zero magnetic field. At high magnetic field usual QHE features are measured. However, if the device dimension is small, say in the range of a micron or smaller, the behavior is expected to change drastically:

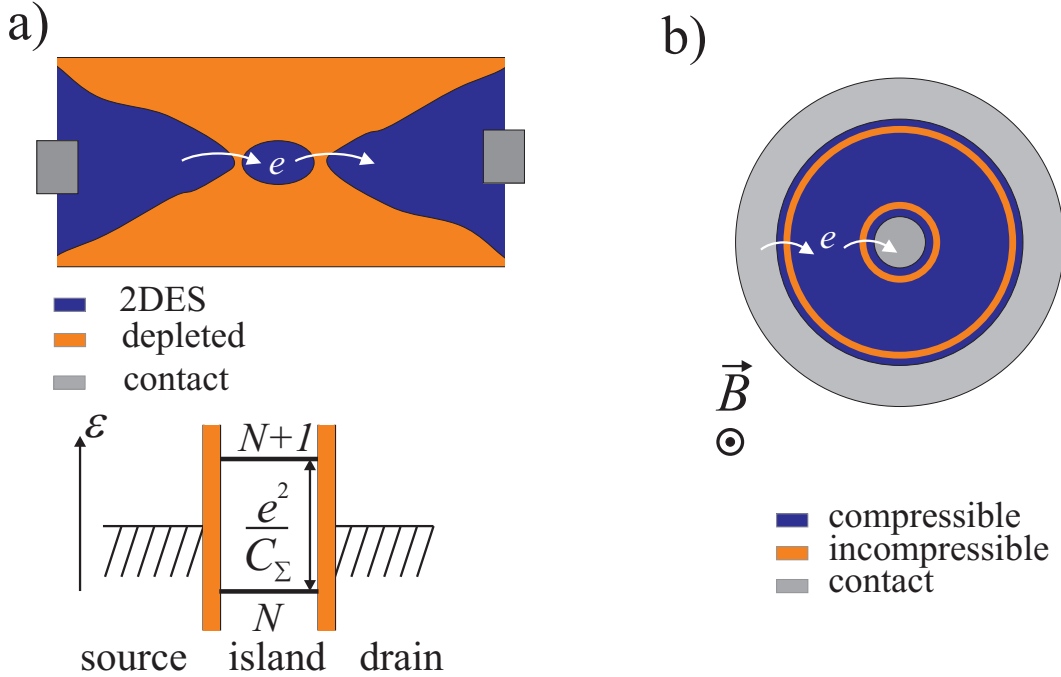


Figure 3.6: (a) A single-electron charging device defined in a 2DES. The orange areas are depleted region of 2DES. Depletion can be achieved by split gates at top of the heterostructure or by etching. (b) Sketch of a Corbino device (top view) on submicron length scale in the QHE conditions; compressible and incompressible stripes are indicated. The incompressible stripes isolate the middle compressible region from the contacts. Electron transport is possible via quantum mechanical tunneling.

The existence of compressible and incompressible strips in front of the contacts in high magnetic fields due to the variation of the local electron concentration was discussed in previous section. Driving the system into the quantum Hall regime, the compressible and incompressible rings are formed as depicted in Fig. 3.6(b). We have seen that incompressible stripes have insulating properties. The innermost (outermost) incompressible strip can act as a tunneling barrier between the inner contact (outer contact) and the compressible region in the middle. In this configuration, one has a confined circular compressible island coupled to metallic leads. This is similar to the single-electron charging devices as shown in Fig. 3.6(a). The transport features at high magnetic field is therefore expected to be modified by single-electron charging. The transport experiments in various devices and detailed discussion of the results will be presented in Chapter 7.

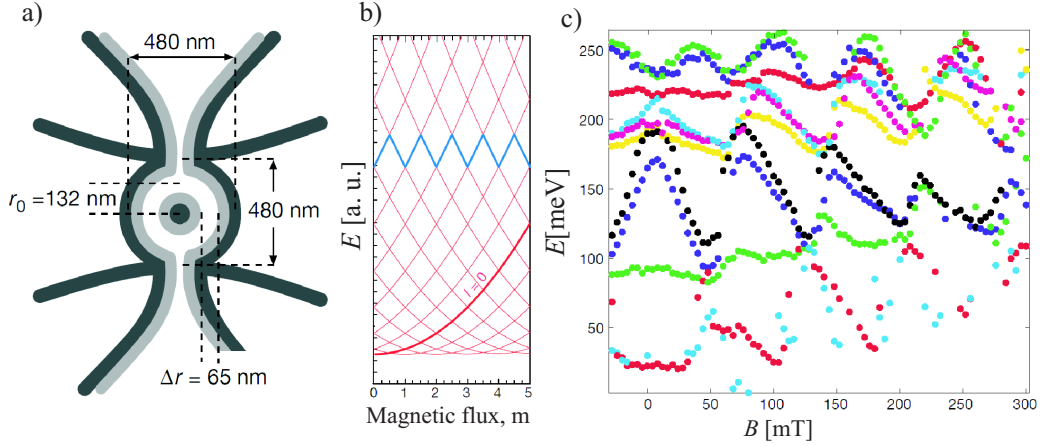


Figure 3.7: After Ref. [49]. (a) A sketch of a quantum ring. The white regions represents regions of 2DES. The gray area is depleted. (b) Energy spectrum of a ring as a function of flux piercing the ring. (c) Reconstructed energy spectrum of a ring from the experiments of Ref. [49]

3.4 Quantum rings and quantum antidots

Here we will discuss quantum rings and quantum antidots due to the similarities to the proposed device. It is similar to a quantum ring since we naturally have a ring structure when the compressible and incompressible stripes are well developed. The similarity with quantum antidots is mainly due to the measurements technique. In quantum antidots, the magnetic field plays the role of the gate voltage in quantum dots as we will see in section 3.4.3.

3.4.1 Quantum rings

A sketch of a quantum ring is shown in Fig. 3.7 (a) [49, 50]. A ring-like region of 2DES is coupled to the leads. The white regions represents the regions of 2DES and the gray region is depleted. The single-particle energy spectrum of one dimensional quantum ring is given as [50, 51],

$$E_{l,m} = \frac{\hbar^2}{2m^*r_0^2}(m+l)^2 \quad . \quad (3.17)$$

Here l is the angular momentum quantum number and $m = \Phi/\Phi_0$ is the number of flux quanta threading the ring. This spectrum is a set of parabolas as shown in Fig. 3.7 (b). With the constant number of electron in the ring the energy of the topmost states changes in a zig-zag way (blue curve in the figure Fig. 3.7 (b)).

Fig. 3.7 (c) shows the reconstructed energy spectrum of a quantum ring [49]. The reconstructed energy spectrum shows deviations from the ideal situation. More realistic calculations [49, 52] taking non ideal shape of the ring and asymmetric confining potentials shows a better agreement with the experimental observations.

3.4.2 Quantum antidots

A quantum antidot [53–56] is formed around a small potential hill in the 2DES in the perpendicular magnetic field. The potential hill can be created by a top gate with applied negative voltages, or it can be created by a small etched region in the heterostructure depleting 2DES around it. A sketch of an antidot is shown in Fig. 3.8(a). In the perpendicular magnetic field, from a single-particle point of view, the kinetic energy of the electrons quantizes into Landau levels. As we already discussed in the Chapter 2.2.2, one-dimensional edge channels form at the boundaries of 2DES. As shown in the Fig. 3.8 (b) electrons are trapped in the bound states around the potential hill. Electrons travel phase coherently in these localized states and encloses an integer number of flux quanta. Area of the each state is quantized as

$$BS_m = m\Phi_0 \quad , \quad (3.18)$$

where m is the orbital quantum number of the m th state [54, 55]. The m th state encloses m flux quanta. As the magnetic field increases the area of the each state shrinks in order to keep the enclosed flux constant. As states move towards the center of the dot a net negative charge is accumulated. State at the Fermi level are depopulated whenever a net charge of $e/2$ is accumulated. The period of this process is

$$\Delta B = \frac{h}{eS} \quad , \quad (3.19)$$

where S is the area of the states at the Fermi level. This is similar to quantum dots. Here magnetic field plays the role of the gate voltage in the quantum dots. The diamond like charge stability diagram is measured [54, 56]. The total energy needed to add one more electron into antidot is

$$\Delta\varepsilon_{tot} = \frac{e^2}{2C} + \delta\varepsilon \quad , \quad (3.20)$$

where $e^2/2C$ is the electrostatic charging energy and $\delta\varepsilon$ is the level spacing of single particle states. In the experiment of Ref. [56] charging energy is $e^2/2C \sim 60 \mu\text{eV}$ at 1.4 T where the width of antidot is around $0.45 \mu\text{m}$ and the single particle energy spacing $\delta\varepsilon$ is around $100 \mu\text{eV}$.

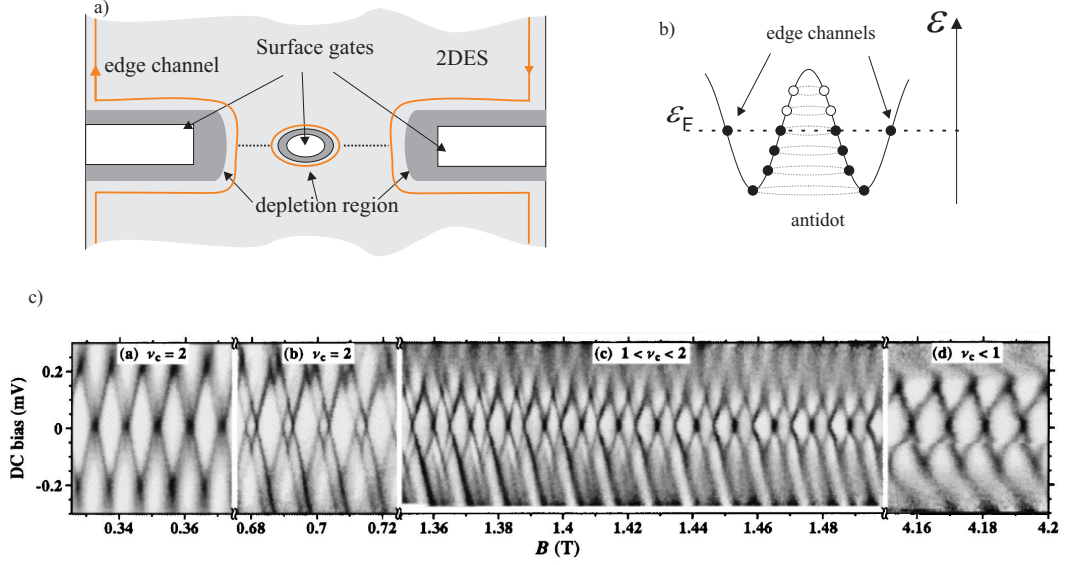


Figure 3.8: (a) Sketch of a quantum antidot. (b) Localized states forms around the potential hill. States are filled up to Fermi level (filled circles); States above Fermi level are empty (empty circles). Tunneling from the edge channels into antidot states is possible. (c) Gray scale plot of differential conductance as a function of dc-bias and magnetic field in the different filling factor regime. ν_c is the filling factor in the antidot constriction. The region of single-electron charging is visible [54, 56].

3.4.3 Aharonov-Bohm effect

Aharonov-Bohm effect is a truly quantum mechanical interference effect and is frequently observed in mesoscopic system where the electron phase coherence persists over a distance comparable to device size [57]. When a charged particle is subjected to the magnetic vector potential, the electron wave function acquires a phase which depends on the path that the particle moves along. For the trajectories along the upper arm and lower arm of the ring as shown in Fig. 3.9 (a) the total phase shift difference is

$$\Delta\phi = \frac{BS}{\Phi_0} \quad , \quad (3.21)$$

where S is the area enclosed by trajectories, B is the magnetic field and $\Phi_0 = h/e$ is the magnetic flux quantum. As magnetic field is changed the phase shift will change electrons interfere destructively or constructively depending of the phase shift. Conductance will oscillate as a function of magnetic field with a period of

$$\Delta B = \frac{\Phi_0}{S} = \frac{h}{eS} \quad . \quad (3.22)$$

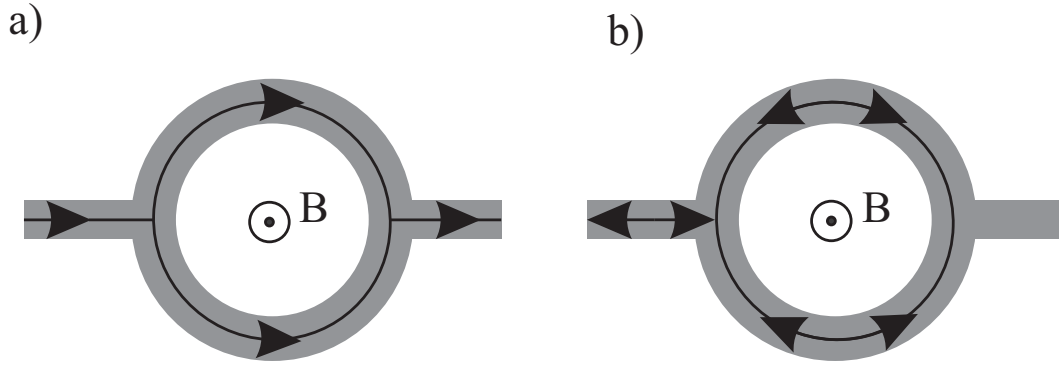


Figure 3.9: (a) Aharonov-Bohm oscillations and (b) Altshuler-Aronov-Spivak (AAS) oscillations.

For the case where electrons propagate both arms of the ring one clockwise and one anticlockwise as shown in Fig. 3.9 (b), which is known as *Altshuler-Aronov-Spivak* (AAS) oscillations [46, 58], the period of oscillation will be half of the Aharonov-Bohm period,

$$\Delta B = \frac{\Phi_0}{2S} = \frac{h}{2eS} \quad . \quad (3.23)$$

Chapter 4

Ohmic Contacts to 2DES in GaAs/ $\text{Al}_\delta\text{Ga}_{1-\delta}\text{As}$ heterostructures

Ohmic contacts are the first ingredient that is needed to get information out of a system which is investigated by means of electrical measurements. To study 2DES in the GaAs/ $\text{Al}_\delta\text{Ga}_{1-\delta}\text{As}$ heterostructures, Au/Ge/Ni alloyed ohmic contacts are widely used [59, 60]. These contacts originally have been developed to contact n-doped GaAs and later on have been used to contact 2DES in GaAs/ $\text{Al}_\delta\text{Ga}_{1-\delta}\text{As}$ heterostructures. In case of 2DES, systematic investigations are rarely reported in literature [61–63], especially for contacts of small size. As we have seen in the previous section, ohmic contacts play an important role in understanding the QHE. Incompressible stripes are experimentally observed in front of the ohmic contacts as discussed in Chapter 2, indicating a partial depletion in front of the contacts. Scanning probe measurements shows adiabatic features due to the missing equilibration between edge and bulk at the contacts [29]. Therefore a better understanding of how the ohmic contacts are working is necessary.

In this chapter electrical and structural properties of alloyed Au/Ge/Ni contacts to 2DES will be discussed. A recipe that has been investigated and optimized in our group [31, 64] to make good ohmic contacts even down to the submicron length scale will be presented in section 4.1. Then the transmission line method (TLM) will be introduced in section 4.2.1 as a method to obtain the value of the contact resistance. There exists a strong dependence on the crystal orientation in the properties of these contacts, so one can speak about good contacting and bad contacting direction. Contact resistance and its anisotropy depending on crystal orientation will be discussed in section 4.2.2. In good contacting direction the contact resistance depends on the border length between contact and 2DES. Scaling properties of the contact resistance on the good contacting direction will

be presented in section 4.2.3. The anisotropy in the contact resistance turn out to be very important in the QHE measurement. It effects the accuracy and position of QHE plateaus. The effect of the alloyed contacts in QHE experiments is presented in section 4.2.5. In order to understand the contacting mechanism and the origin of the anisotropy in the contact resistance we investigated structural and chemical properties of the alloyed contacts. The results from scanning electron microscope (SEM), transmission electron microscope (TEM), scanning transmission electron microscope (STEM) and energy-dispersive X-ray (EDX) spectroscopy will be presented in section 4.3.

4.1 Alloyed Au/Ge/Ni contacts

The recipe of alloyed Au/Ge/Ni to n-GaAs has been introduced by Braslau in 1966 [59]. The underlying idea was that depositing Au/Ge at its eutectic composition allows to anneal contacts at moderate low temperature, i.e slightly above the eutectic temperature. Au has its melting point at 1064 °C and Ge has its melting point at 938 °C. However when both metals are mixed together, that is an alloy of Au and Ge, the melting point depends on the proportion of the metals in the alloy. The eutectic point is the lowest achievable melting temperature. For Au and Ge alloys, the eutectic point is 361 °C for a weight ratio of 88% Au: 12% Ge. Above the eutectic temperature Au/Ge melts and forms complex chemical phases with the substrate thereby diffusing and penetrating into the substrate. The structural studies reveals a complex grainy morphology with different chemical composition.

A transmission electron microscope (TEM) image from one of the earlier studies of Kuan *et al.* is shown in Fig. 4.1 (a) [65]. The corresponding sketch of the chemical composition obtained via X-ray diffraction (XRD) analysis is shown in Fig. 4.1 (b). Mainly two different phases are identified: A gold (Au) rich phase containing also Ga and As and a nickel (Ni) rich phase identified as Ni₂GeAs. The early studies showed that the presence of Ni is crucial. It improves diffusion of Ge into the GaAs substrate, forming Ge rich Ni₂GeAs, making good electrical contact to GaAs [65–67]. The diffusion of Ge into GaAs is low at the Au rich regions; however, it is higher at the Ni₂GeAs/GaAs interface. The low resistivity of good contacts have been related to the distribution of Ni₂GeAs regions at the GaAs interface [65]. The role of Ni was also identified as providing good surface morphology, edge shape and avoiding formation of separate islands of contact materials, called balling-up process [60]. Later on this recipe was adapted to contact 2DES in GaAs/Al_δGa_{1-δ}As heterostructures. However every group has used and developed its own recipe and there was not much systematic studies in case of 2DES [61–63, 68, 69].

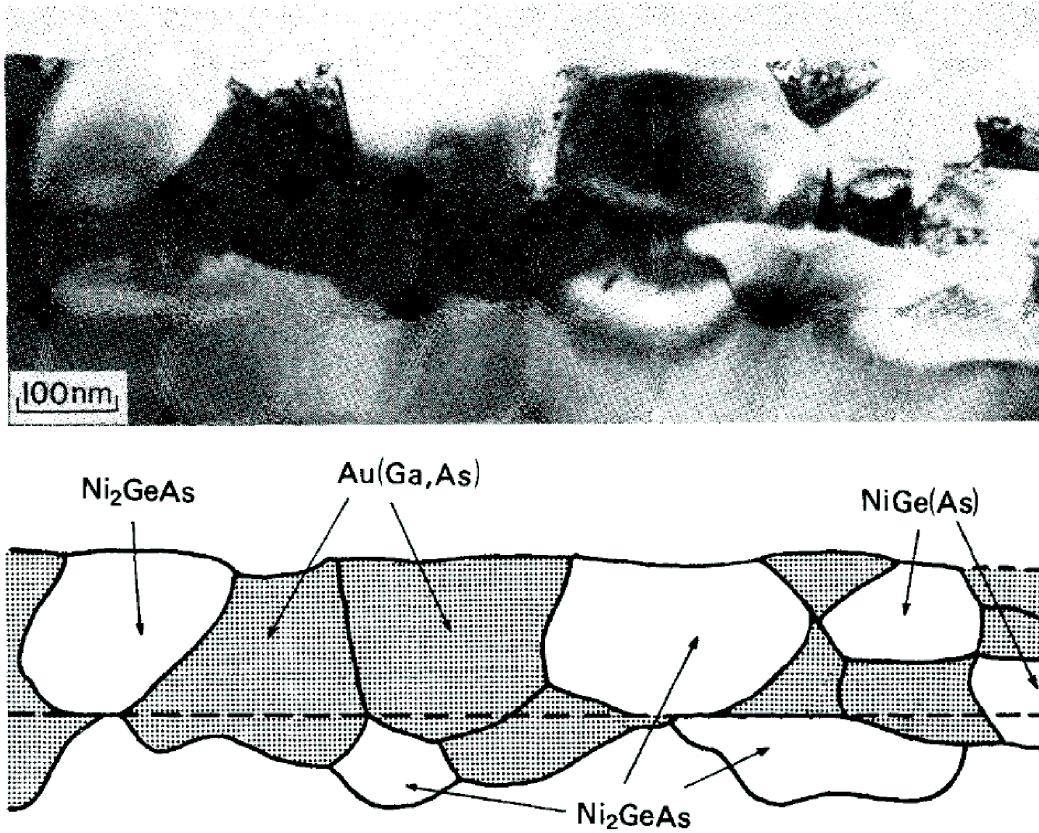


Figure 4.1: A cross-sectional bright-field TEM image of an alloyed Au/Ge/Ni contact defined on n-GaAs. The distribution of phases and their chemical composition are indicated in the sketch below the image. After Kuan et al. [65].

4.1.1 The recipe

In this study a contact recipe is used which was optimized by U. Graumann, J. Schmid and J. Weis in 1998 to have reliable, reproducible and low-resistive ohmic contacts to 2DES in GaAs/Al_δGa_{1-δ}As heterostructures [64]. The complete detailed recipe is given in Appendix A. The list of used technology, chemicals and materials are given in Appendix B. The summary of the contacting process is shown in Fig. 4.2. The sample is a GaAs/Al_δGa_{1-δ}As heterostructure having a 2DES at the GaAs/Al_δGa_{1-δ}As interface as shown in Fig. 4.2(a). The growth sequences and layer thicknesses for the heterostructures which are used in this work are given in Table C.1 in Appendix C. Contact areas were defined by optical lithography. As an important step, a post-cleaning process using Semico Clean 23 (for details of the chemicals see Appendix A) and HCl is performed. Au, Ge and

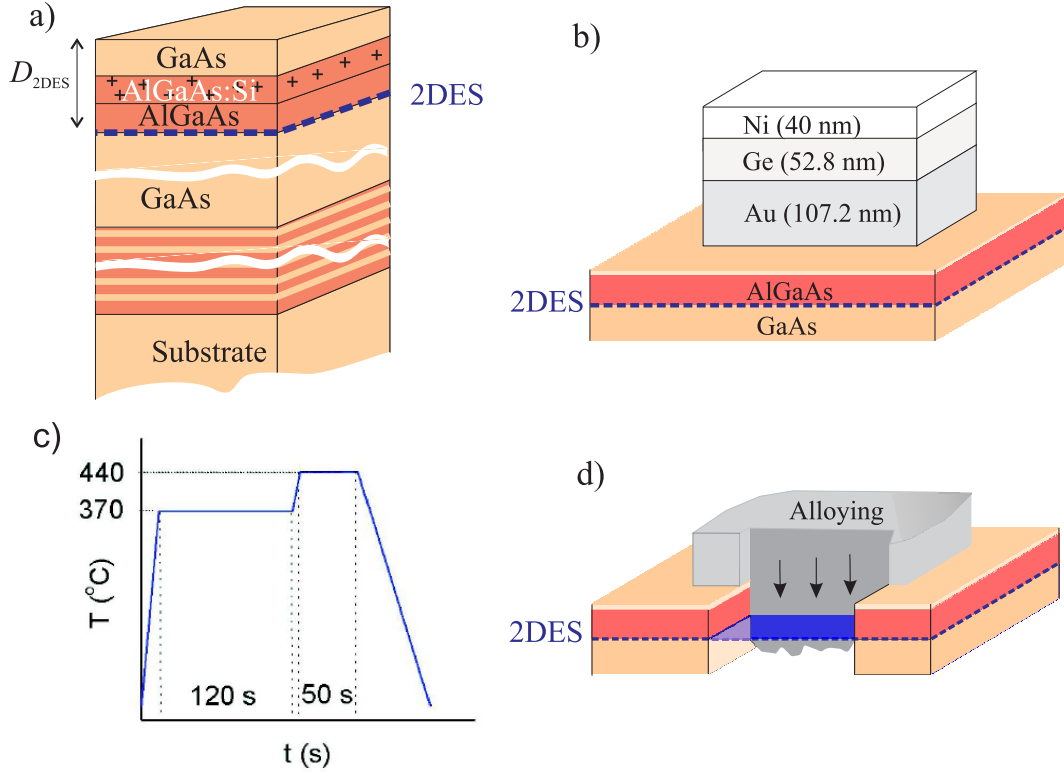


Figure 4.2: a) Sketch of a heterostructure used on this study. A 2DES forms at the GaAs/Al_δGa_{1-δ}As heterojunction interface. b) Evaporated layers of Au, Ge and Ni metals. The thicknesses of the metals are indicated (for a heterojunction interface depth more than 86 nm, a scaling factor is used. See Appendix A). c) Allying sequence. Allying is done in a N₂/H₂ gas atmosphere d) During alloying, Au/Ge/Ni forms an alloy and dissolves the underlying heterostructure.

Ni metals are evaporated in a high vacuum chamber. Then a lift-off procedure is applied. The metal layers and thicknesses are shown in Fig. 4.2(b). The alloying procedure consists of the following steps: (1) rapidly heating to 370 °C and holding at this temperature for 120 s, (2) then for 50 s at 440 °C, and then rapidly cooling down to room temperature as schematically shown in Fig. 4.2(c). Alloying was done under N₂/H₂ gas atmosphere (volume ratio 80% : 20%) at a pressure of 300 mbar. The first two steps are under a static gas overpressure and the last step is under a gas flow with constant pressure to allow a faster cooling as shown in Fig. 4.2(c).

The alloyed contact have usually a grainy morphology similar to that in Fig. 4.1. The grain size depends on several parameters like the metal thickness ratios and

alloying temperature. After alloying one can make an early estimation about the contact quality by just having a look at the contacts under the light microscope. Here we present two optical images to show this. A dark field optical image of a contact in top view is shown in Fig. 4.3(a). This is a $100\ \mu\text{m}$ by $100\ \mu\text{m}$ contact defined on a heterostructure. This is an example of a low-resistive very good quality ohmic contact. The surface morphology is quite good, i.e. there are no large grains visible. In the bright field optical images one sees a smooth surface. An example of a bad quality ohmic contact is shown in Fig. 4.3(b). The surface morphology is very bad, i.e. the contact materials split into separate regions. In this specific example the evaporation of the Ni layer was not successful: i.e. not enough Ni was present for alloying the contact. The exact amount of Ni could not be measured due to some problems in the apparatus but it was definitely less than normal amount. The lack of Ni causes a bad surface morphology and a poor contact quality.

In Fig. 4.3(c) an SE2 detector scanning electron microscope (SEM) image of a good quality contact is shown. The acceleration voltage was 20 kV. Electrons penetrate deep into the contact. This detector detects the secondary electrons which are excited by the backscattered electrons. The amount of the backscattered and secondary electrons depends on the atomic number of the materials. Therefore the region with different contrast in this image can be used to get a rough idea of the grainy structure of the contacts with different chemical composition. The white regions are Au rich regions. The dark regions¹ are Ni and Ge rich grains. The grain size is small in the range of micron or even less. The Ni-Ge rich grains are mainly surrounded by Au rich regions. In Fig. 4.3(d), an SE2 detector SEM image of a bad quality contact is shown (the same contact which is shown in Fig. 4.3(b)). The larger grains with different morphology are visible. This shows the importance of the nickel layer for the contact morphology. However, a good morphology and small grain size does not guarantee low resistive contacts. To have a look in the contact quality, i.e. reproducibility and low contact resistance, we need to perform transport experiments as will be discussed in the next section.

¹Grains with white and dark contrasts have been identified by EDX as will be discussed in Chapter 4.3.

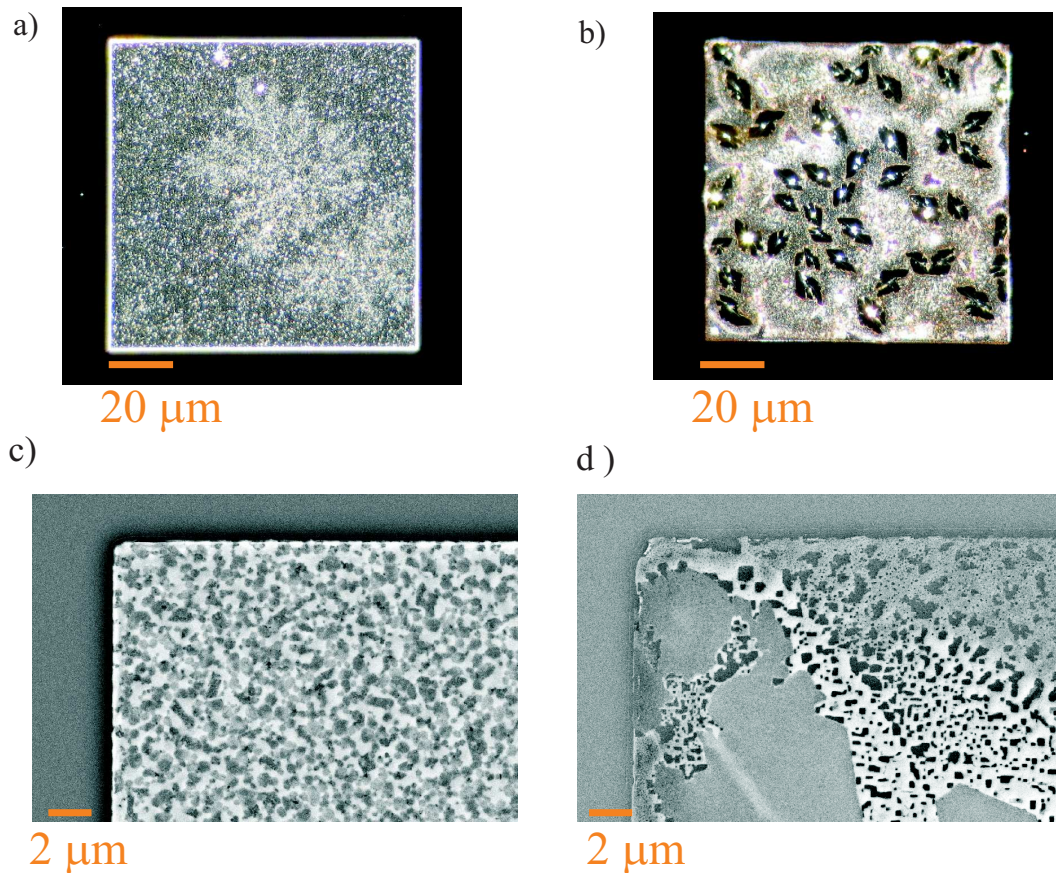


Figure 4.3: a) A dark field optical image of a good quality alloyed contact (top view). Surface morphology is smooth. No large grains are present. (b) A dark field optical image of a bad quality alloyed contact (top view). The very poor surface morphology is visible. Grain size is very large. (c) An SE2 SEM image of a good quality contact. The grains with different contrast are visible. Grain size is in the range of micron or even smaller. (d) An SE2 SEM image of a bad quality contact. Surface morphology is poor, the contact separates into different regions. A phase with smooth uniform contrast and a phase with small micron size grains with different contrast is visible. The problem for this contact was that not enough Ni was evaporated.

4.2 Electrical characterization of the alloyed contacts to the 2DES

4.2.1 Determining the contact resistance: the transmission line method (TLM)

The transmission line method (TLM) is widely used to obtain contact resistance values [70,71]. The principle of the method is explained with Fig. 4.4: a number of

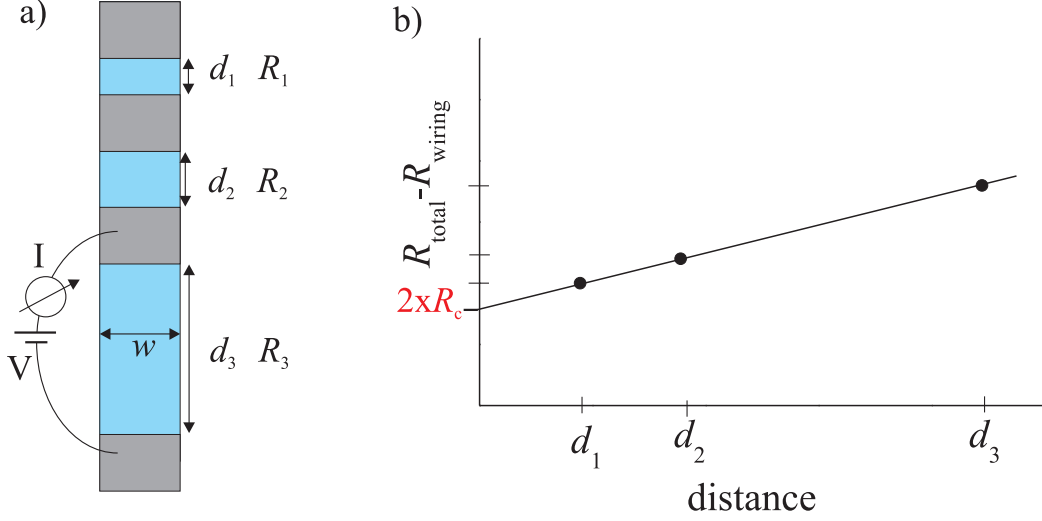


Figure 4.4: (a) The sketch of the TLM sample for the measurement of the contact resistance. Gray represents the contacts and blue represents a (semi)conductor stripe. d_i is the distance between the contacts, R_i is the total resistance measured between the contact pairs and w is the width of the (semi)conductor. (b) The resistance versus distance d plot is shown. The wiring resistance of the measurement apparatus is subtracted. The best fit line to the data gives twice the contact resistance R_c at $d = 0$.

contacts with varying distance are defined along a stripe of the semiconductor of interest. Then a voltage is applied to consequent contacts and the current is measured. The resistance for each pair is calculated via the slope of the corresponding I-V curve. Under assumption that the contact resistances are approximately the same for all the contact/semiconductor interfaces, the measured resistance R_t for a contact pair can be expressed as

$$R_t = 2R_c + R_w + \frac{\rho_s d_i}{w} . \quad (4.1)$$

Here R_c is the contact resistance of interest, R_w is the resistance of the measurement apparatus (for instance wires of the sample holder), d_i is the distance between the contact pairs, w is the width of the semiconductor and ρ_s is the sheet resistivity of the semiconductor. The contact resistance R_c is counted twice since there are two metal/semiconductor interfaces for each contact pair. The measured resistance, after subtracting R_w , is usually a linear function of the distance d as shown in Fig. 4.4(b). The extrapolated value of the best fit line at $d = 0$ gives twice the contact resistance R_c of the metal/semiconductor interface.

4.2.2 Anisotropy of contact resistance on the crystal orientation

Here we will use TLM to obtain the contact resistance between alloyed ohmic contacts and 2DES. Alloyed contacts are defined following the recipe discussed in section 4.1.1. To apply the TLM, mesa stripes were etched out of the heterostructure and a series of contacts of varying distance d were alloyed along the mesa stripes as shown in Fig. 4.5 (a). Mesa stripes are elongated in $[011]$ crystal direction and in $[01\bar{1}]$ crystal direction. The crystal directions are also indicated in Fig. 4.5 (a). The width of mesa stripe for this sample is $10\ \mu\text{m}$. However, we have also used samples with mesa stripe width varying between $1\ \mu\text{m}$ and $100\ \mu\text{m}$. The TLM measurements on these samples will be discussed in the next section. The wafer is #81758 and has a 2DES 50 nm below the surface.

The two-terminal resistance between consequent pair of contacts was determined by measuring the current-voltage characteristics at liquid Helium temperature. The current-voltage characteristics for a few pairs of contacts are shown in Fig. 4.5 (b). In Fig. 4.5 (c) the two-terminal resistance is plotted as a function of the distance d between the contacts. The series resistance due to the wiring in the measurement setup is already subtracted. The measured resistances are grouped by color with respect to crystal directions. Blue is for contacts defined on the mesa stripes along $[011]$ direction and red is for the contacts defined on the mesa stripes along $[01\bar{1}]$. As clearly seen in the Fig. 4.5 (c), resistance values of contacts defined on the $[011]$ elongated mesa stripe, that is the metal/2DES interface is perpendicular to $[011]$ direction, has a linear dependence with distance and the deviation from the linearity is small. However resistance values of contacts that are defined on the $[01\bar{1}]$ elongated mesa stripe do not scale with distance and have high values with a large spread. That means, contacts which have the metal/2DES interface line perpendicular to the $[011]$ direction have approximately the same contact resistance values. However, for the contacts that have the metal/2DES interface line perpendicular to the $[01\bar{1}]$ direction the contact resistance varies very much from one contact to another. Furthermore for the contacts that have the metal/2DES interface line perpendicular to the $[01\bar{1}]$ direction it is not just a matter of high contact resistance but also contact failure is unavoidable in most cases. From now on, we will use *good contacting* direction and *bad contacting* direction to distinguish between these directions. When the metal/2DES interface line is perpendicular to the $[011]$ crystal direction as shown in Fig. 4.5 (a), we will use the notation *good contacting* direction. If the metal/2DES interface line is perpendicular to $[01\bar{1}]$ crystal direction we will use the notation *bad contacting* direction. The observed dependence on the crystal orientation is similar to that observed in literature for alloyed Au/Ge/Ni contacts to 2DES in GaAs/Al_δGa_{1-δ}As heterostructures [61, 64]. It is important to note that at room temperature there is

no clear difference for the contact resistance between both directions. Some room temperature TLM experiments are shown in Fig. C.1 in Appendix C.

The list of wafers with the 2DES parameters, thickness of evaporated contact metals (Au:Ge:Ni) and measured values of contact resistances are given in Table 4.1. The given values of contact resistances are measured on the samples with 10 μm mesa stripe width and normalized to 100 μm width except the wafer #81744. For this wafer the given value is calculated from the sample with 50 μm mesa stripe width and normalized to 100 μm width. The reason that we give the contact resistance values for 100 μm width is that this length scale is the typical length which is used to define contacts on heterostructures for transport measurements. All the contact values which are given in Table 4.1 are extracted from TLM measurements. A typical example of TLM measurements for one of the wafer (#81758) was already shown in Fig. 4.5. The TLM data for the rest of the wafers which are listed in Table 4.1 can be found in Fig. C.2, Fig. C.3, Fig. C.4 in Appendix C.

In bad direction, as shown in Fig. 4.5(c), the contacts are highly resistive or do not work. When we say a contact is not working we mean we could not measure any current in the sensitivity limit of the measurement apparatus which imply a resistance larger than 10 M Ω . The difference between good contacting and bad

Wafer	D_{2DES}	n_s	μ	(Au:Ge:Ni)	R_c in good direction	R_c in bad direction
#	[nm]	[cm^{-2}]	[$\text{cm}^2\text{V}^{-1}\text{s}^{-1}$]	[nm]	[Ω]	[Ω]
8963	120	$1.9 \cdot 10^{11}$	$9.7 \cdot 10^5$	146:72:54	6.3 ± 0.3	—
81744	120	$1.9 \cdot 10^{11}$	$7.8 \cdot 10^5$	146:73:54	6.8 ± 2.3	—
81763	86	-	-	107.2:52.8:40	3.2 ± 6.0	—
81758	50	$3.8 \cdot 10^{11}$	$8.1 \cdot 10^5$	107.2:52.8:40	3.4 ± 0.3	—
81757	40	$6.3 \cdot 10^{11}$	$2.6 \cdot 10^5$	107.2:52.8:40	8.3 ± 0.6	44 ± 7
81628	40	$5.6 \cdot 10^{11}$	$5.7 \cdot 10^5$	107.2:52.8:40	6.5 ± 0.5	5.4 ± 0.4

Table 4.1: The list of wafers characterized in this work. D_{2DES} is the depth of GaAs/GaAs/ $\text{Al}_\delta\text{Ga}_{1-\delta}\text{As}$ heterojunction, n_s is the 2DES electron density, μ is the electron mobility and R_c is the contact resistance for a 100 μm length of the contact/2DES border. The given value of n_s , μ and R_c are measured at 4 K. The thickness of evaporated metals Au/Ge/Ni is also given. For the wafer that have D_{2DES} less than 86 nm the standard recipe is used. For D_{2DES} larger than 86 nm, a scaling factor after [64] is used as described in the Appendix A. The growth details, i.e. thicknesses and sequences of the layers, for the heterostructures listed here are given in Table C.1 in Appendix C.

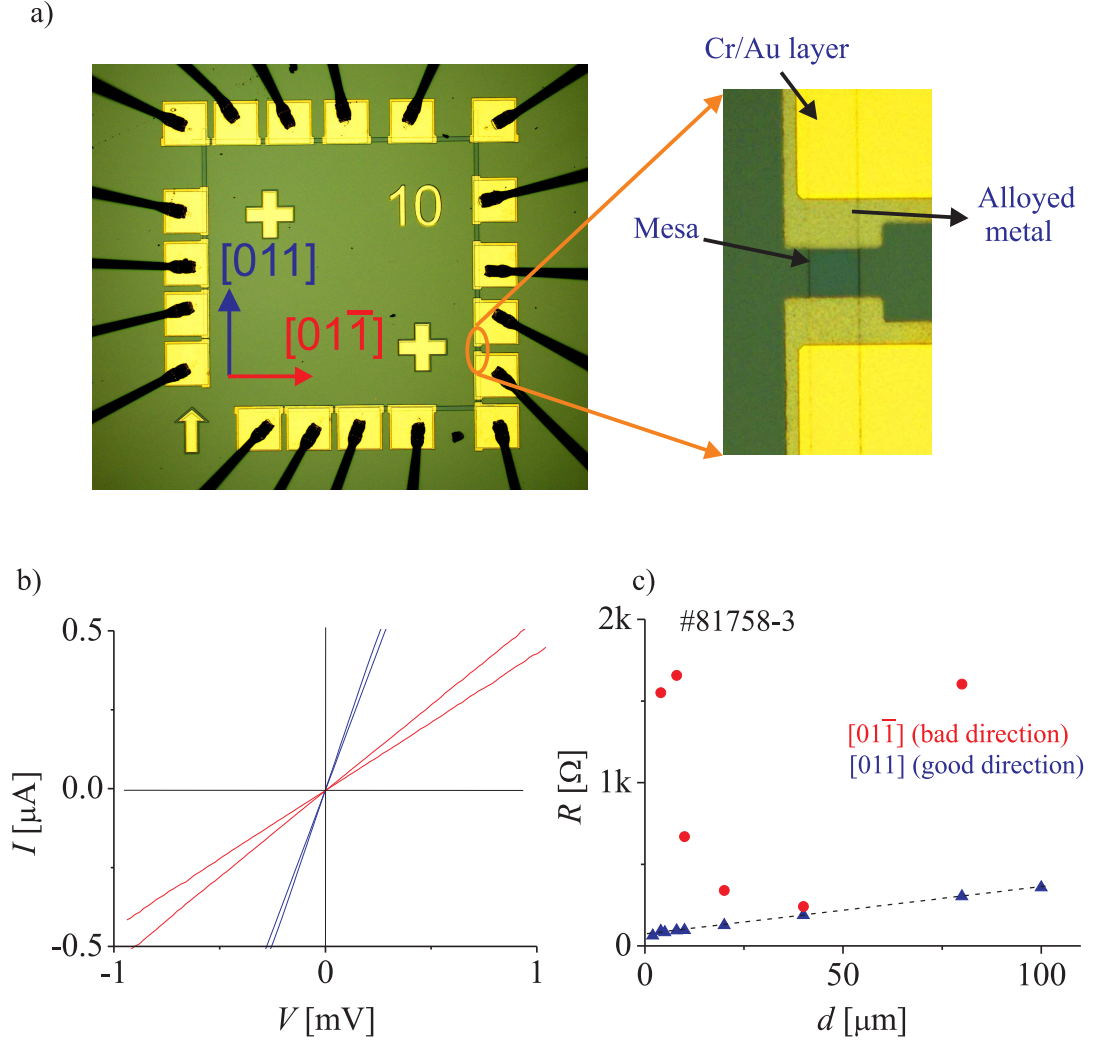


Figure 4.5: (a) An optical image of a TLM sample (top view). The heterostructure is #81758 and has a 2DES 50 nm below the surface. Mesa width is $w = 10 \mu\text{m}$. The crystal directions are indicated. Alloyed Au/Ge/Ni contacts are defined on the mesa stripes elongated in $[011]$ and $[01\bar{1}]$ direction, respectively. The term *good contacting* direction is used when the contact/2DES interface line is perpendicular to $[011]$. When contact/2DES interface line is perpendicular to $[01\bar{1}]$ the term *bad contacting* direction is used. Distance between consequent contacts varies from $2 \mu\text{m}$ to $100 \mu\text{m}$. (b) Current-voltage data for some of the contact pairs. Blue curves are for contacts in good contacting direction and red curves are for contacts in bad contacting direction. Here in both directions, contacts have a linear ohmic behavior. (c) TLM measurement on the sample shown in (a). Triangular (circular) data points correspond to contacts defined on the mesa along the *good contacting* (*bad contacting*) direction. The best fit to data intercepts with the R axis at the value of $2R_c$.

contacting direction is well pronounced for heterostructures that have deeper lying 2DES. First, as we already discussed the contact resistance is higher and have a large spread. Second, the percentage of the working contacts is very low. As the width of mesa stripes get smaller the percentage of working contacts is even less. This has been observed for wafer #8963 and #81763, where the depth of GaAs/GaAs/Al_δGa_{1-δ}As heterojunction is 120 nm and 86 nm, respectively. The TLM measurements in good contacting and bad contacting direction for these wafers are shown in Fig. C.2 in Appendix C. Since the TLM data in bad contacting direction cannot be fitted to a line there are no contact resistance values given in Table 4.1 for these heterostructures for bad contacting direction. However, for the wafers that have shallow lying 2DES, the difference between good contacting and bad contacting direction is less pronounced. For the 2DES depth of 50 nm (wafer #81758) the percentage of working contacts in bad direction is also high. However, the contact resistance in bad direction still have higher values and large spread. The TLM measurements for this wafer are presented in Fig. C.3 (a) and (b) in Appendix C.

The difference between good and bad direction becomes even less pronounced if the depth of the 2DES is 40 nm. The percentage of the working contacts in bad contacting direction is as good as in good contacting direction. This is valid for contacts defined in small mesa stripes as well. For instance the contact resistance values in bad direction becomes comparable to the contact resistance in good direction for the wafer #81628 as given in Table 4.1. Although reported in literature [61, 64], the origin of the contact resistance anisotropy – for instance, due to an anisotropy in diffusion, strain or piezoelectricity - has not been clarified. However, if the thicknesses of the Au/Ge/Ni metal layers are scaled up, the observed anisotropic behavior of contact resistance is recovered for this heterostructures. We have increased the thicknesses of metal layers for a factor of 1.35 and alloyed the contacts. Then we performed the TLM measurements. In the good contacting direction the usual behavior is observed: the data fit a line. The extracted value of the contact resistance in this case is $(18 \pm 3) \Omega$. This value is higher than the value obtained for the standard recipe. However, the TLM data fit a line well, implying a reproducible contact resistance at the contact/2DES interface. In the bad contacting direction the contacts mostly do not work. Few contacts work with a resistance value larger than 10 k Ω . The result for this experiment is presented in Fig. C.5 in Appendix C. This observation implies that the observed anisotropy of contact resistance depends strongly on the overall thickness of the metal layers. The Ni is a important parameter to control the contact resistance quality. To show the critical role of Ni, TLM measurements for the contacts with and without Ni layer is presented in Fig. C.6 in Appendix C. If there is no Ni present in the alloyed metal contact resistance quality is bad for both directions.

4.2.3 Scaling properties of contact resistance in good contacting direction

As we have seen in the previous section, the contact resistance of the alloyed Au/Ge/Ni contacts depends on the crystal direction. In this section we will concentrate on the good contacting direction and have a look on the properties of these contact on small scale. In Fig. 4.6 (a), R versus d for the different mesa stripe width of w is shown. The heterostructure is #81758 and the 2DES depth² is 50 nm. The prepared and measured mesa stripe width is ranging from 100 μm down to 1 μm . As clearly visible, the measured two-terminal resistance shows a linear dependence on the distance between contacts. That holds down to 1 μm of mesa stripe width. All the structures whose TLM measurements are shown in Fig. 4.6 (a) are prepared in the same sample. To make it clear all of these structures have seen exactly the same preparation process, i.e. lithography, cleaning, evaporation, lift-off and alloying. The normalized (unity length) contact resistance r_c for different mesa stripe width w – from 100 μm down to 1 μm – are shown in Fig. 4.6 (b). The normalization has been done by multiplying the contact resistance value R_c with the respective mesa stripe width w

$$r_c = R_c \cdot w \quad . \quad (4.2)$$

Error bars for r_c are according to the error in determining the respective contact resistance R_c via the TLM and error in determining the mesa width w because of depletion at the edges (about 200 nm).

The value for r_c is around 250 Ω and is almost constant for all mesa widths except $w = 100 \mu\text{m}$. The obtained value of r_c is comparable to the reported value of $r_c = 0.2 \Omega\text{mm}$ [68] where however no orientation for the 2DES/alloyed metal borderline is given. All the r_c values shown in Fig. 4.6(b) are derived from TLM measurements shown in the Fig. 4.6(a) except the samples with 50 μm width of mesa stripe. The r_c value obtained from TLM structure with mesa stripe width $w = 100 \mu\text{m}$ is higher than expected value. We have had a look on the contact morphology of this TLM structure with an SEM. The contact morphology and grainy texture was similar to one shown in Fig. 4.3(c) which is a usual picture for the good quality low resistive ohmic contacts. The origin of higher r_c on this sample could not be clarified. A similar behavior has been observed for wafer #81757 as shown in Fig. 4.7(c). The data point for 50 μm width of mesa stripe in Fig. 4.6 (b) corresponds to samples which were prepared by electron beam lithography (EBL). The unity length contact resistance obtained for EBL prepared samples is similar to the values obtained from the samples prepared by optical lithography.

²By 2DES depth we mean the depth of GaAs/Al_δGa_{1-δ}As heterojunction where 2DES lies.

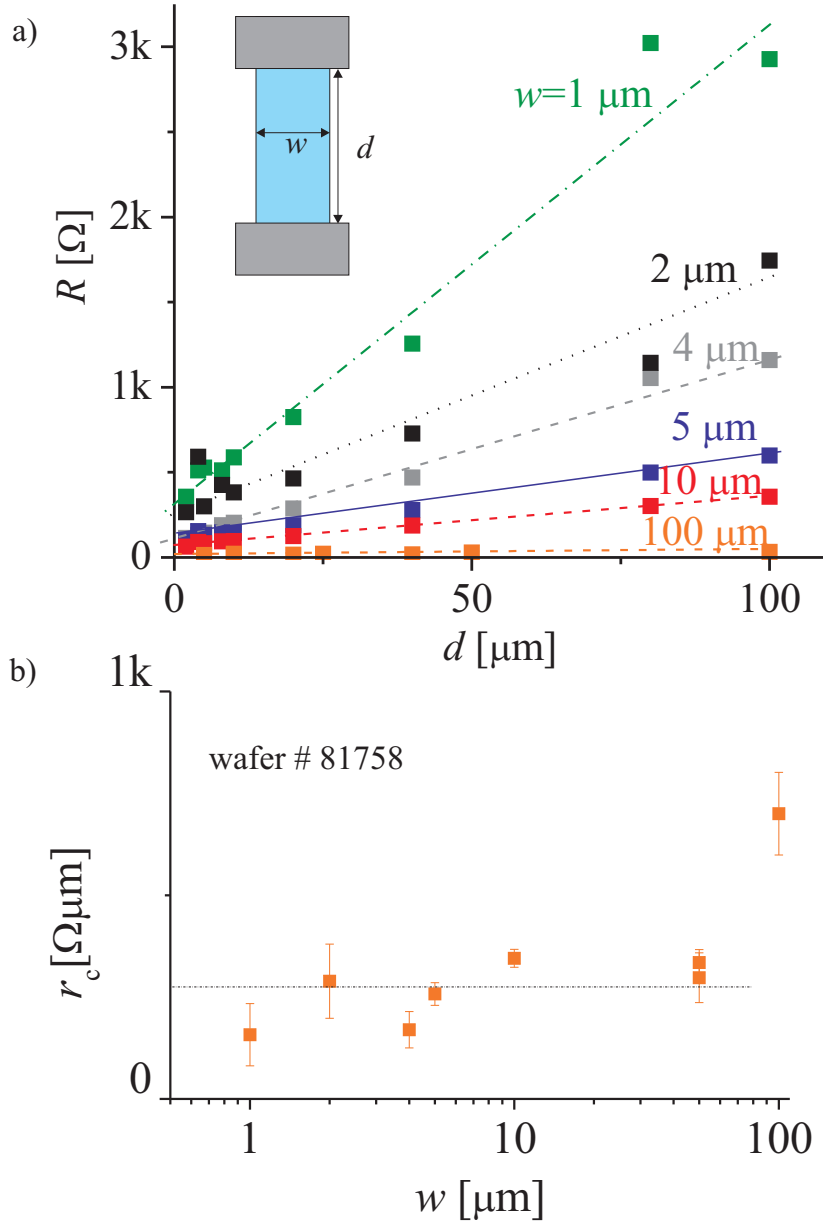


Figure 4.6: (a) TLM measurements on the wafer # 81758 for different width of mesa stripes. The width of the mesa is indicated next to data for each data set. (b) Unity length contact resistance $r_c = R_c \cdot w$ as a function of mesa width w . The error bar consist of error arising from the fitting and also the uncertainty in the width of 2DES due to the depletion at the edges of mesa. The samples with $w = 50 \mu\text{m}$ were prepared with electron beam lithography. The rest of data points corresponds to TLM structures which are shown in (a) and were prepared in the same sample, that is, all the ohmic contact process, i.e. cleaning, evaporation, lift-off and alloying, is common for these TLM structures.

There are two important outcomes from the data presented in Fig. 4.6(a) and (b). Firstly, the unity length contact resistance scales with the border length between alloyed metal/2DES and this holds down to 1 μm of mesa width stripe. Secondly there is no contact failure, i.e. all the contacts which are defined in TLM mesa stripes works even for the TLM structure with 1 μm mesa stripe width. We have also seen that SEM images reveal a grainy contact morphology with grain sizes from 0.1 μm to 1 μm . Now if we assume that some of the grains at the contact/2DES border have no contact or high contact resistivity to 2DES and some have low contact resistivity, we can make some estimation for the electrical properties of these grains according to above mentioned two findings from TLM measurements. We can estimate that the grains which have no contact to 2DES are smaller than 1 μm since there is no contact failure on TLM structures even in 1 μm mesa stripe width. This is consistent with the grainy appearance of the contact as shown in Fig. 4.3 (c). Grain size is generally in submicron size. The distribution of the dark grains is dense so there are almost always dark grains (NiGe rich) and light grains (Au rich) in a micron range. Since the deviation from the TLM line is not large one can estimate that the contact resistance from one grain to an other one is more or less the same. The deviation in the TLM data from the line is not necessarily due to the deviation on the contact resistance of the grains. It can also be due to the deviation of the fractions of the contacting and not contacting grains at the contact/2DES border. These estimations are valid for the good contacting direction. In bad contacting direction the contact failure happens even on large scale for the deeper lying 2DES and become less drastic as the 2DES depth becomes smaller as already discussed in the previous section. However, there is no evidence of any anisotropy in the distribution or alignment of the grains on the alloyed contacts as shown in Fig. 4.3 (c).

In Fig. 4.7 the unity length contact resistance, in good contacting direction, as a function of mesa width is shown for the rest of the heterostructures which are listed in Table 4.1. The unity length contact resistance seems to decrease for the heterostructures #8963 and #81628 as the width of mesa gets smaller. For the heterostructures #81763 and #81757 tendency is just opposite. The slope of the TLM line depends on the sheet resistivity as given in (4.1). The sheet resistivity ρ_s of the 2DES depends on the cooling process since the electron density is not always the same for all the cooling processes. ρ_s can be extracted from the TLM measurements according to (4.1). No correlation between the sheet resistivity of 2DES and the contact resistance has been found. The extracted value of ρ_s for all the TLM measurements are presented in Fig. C.7 in Appendix C.

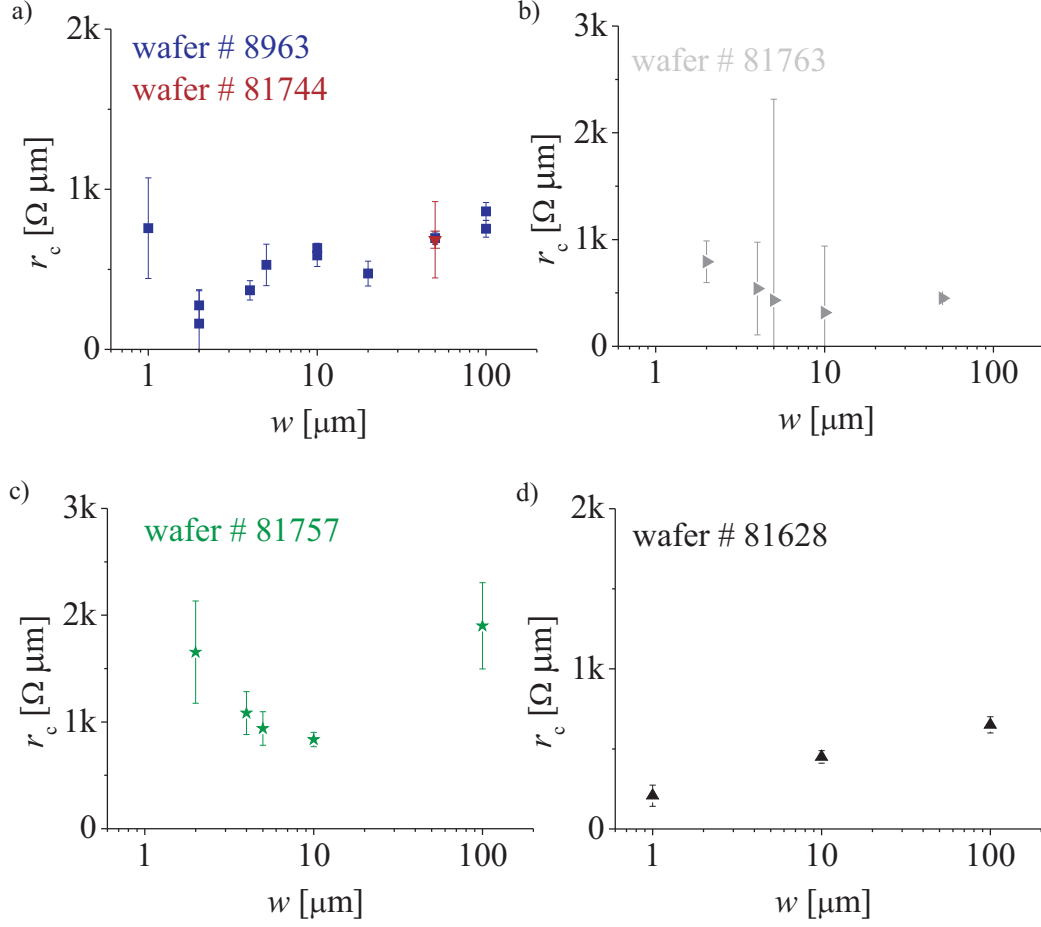


Figure 4.7: The unity length contact resistance r_c for the heterostructures #8963 (a), #81763 (b), #81757 (c), and #81628 (d) as a function of mesa width w . The depth of the 2DES and the other parameters of these heterostructures are given in Table 4.1.

4.2.4 Temperature dependence of the contact resistance

To investigate the temperature dependence of the contact resistance we have performed some temperature dependent TLM measurements. Result of this measurements are shown in Fig. 4.8 (a) for good contacting direction and in Fig. 4.8 (b) for bad contacting direction. The TLM structure has a mesa width of $50 \mu\text{m}$. TLM measurements are performed at 1.5 K and 25 mK. In good contacting direction the extracted value of contact resistance is $R_c = (6.8 \pm 0.5) \Omega$ at 1.5 K and at 25 mK $R_c = (7.5 \pm 0.3) \Omega$. The contact resistance values are given for a $100 \mu\text{m}$ border length in order to be consistent with the values given in Table 4.1. The temperature changes almost two orders of magnitude but the change in the

contact resistance is very weak. A very weak temperature dependence of contact resistance for the same temperature range was also reported by Heiblum *et al.* for alloyed Au/Ge/Ni contacts to n^+ -GaAs [72]. Hawksworth *et al.* also report a weak temperature dependence of contact resistance at low temperature (from room temperature to 4K) for Au/Ge/Ni contacts to GaAs/Al_δGa_{1-δ}As heterostructures [69]. However in their study they observed a relatively unmodified 2DES under the contact area which is not the case for our contacts. The layer sequence and thicknesses in their study is quite different which might have resulted in a low penetration of the contact material into the heterostructure, thereby allowing an intact 2DES under the contact area. Bühlmann *et al.* observe a decrease (a factor of two) in the contact resistance from room temperatures to 77 K, but below 77 K contact resistance stays constant [62]. The weak dependence of the contact resistance on the temperature implies that current injection process is via a tunneling process. In bad contacting direction one can not extract a contact resistance value since the data do not fit to a line as shown in Fig. 4.8 (b). In Fig. 4.8 (c) the increase in the resistance ΔR is shown for bad contacting direction. The very weak temperature dependence can imply that the current injection is via a tunneling process [30, 72]. If there is a tunneling barrier, it must be very high since temperature does not effect contact resistance very much and must be very thin since the contact resistance is usually low. Similar measurements for another TLM structure is presented in Fig. C.9 in Appendix C.

4.2.5 The role of the contact resistance in QHE measurements

As we have seen in this chapter there exist a significant difference for contacts defined in good contacting direction and for contacts in bad contacting direction in terms of contact resistance, especially for the heterostructures which have deeper lying 2DES. Now we will have a look whether this affects the QHE measurements. Here a simple but a rather explanatory experiment will be presented which proves the role of contact in the study of QHE. In Fig. 4.9, the two-terminal magneto resistances of 2DES for the contacts in good contacting direction and in bad contacting direction are presented. The heterostructure is #8963. The sample is a TLM structure with a mesa stripe width of 50 μm . Two pairs of contacts were chosen in good contacting and bad contacting direction. The distance d between pairs were 100 μm and 10 μm . The extracted value of contact resistance in good contacting direction is $R_c = (7.5 \pm 0.4) \Omega$. In the bad contacting direction the contact resistance values are approximately 130 Ω for one of the contact pairs ($d = 100 \mu\text{m}$) and 200 Ω for the other contact pairs ($d = 10 \mu\text{m}$). The contact resistance values for the contact pairs in bad direction are calculated by subtracting

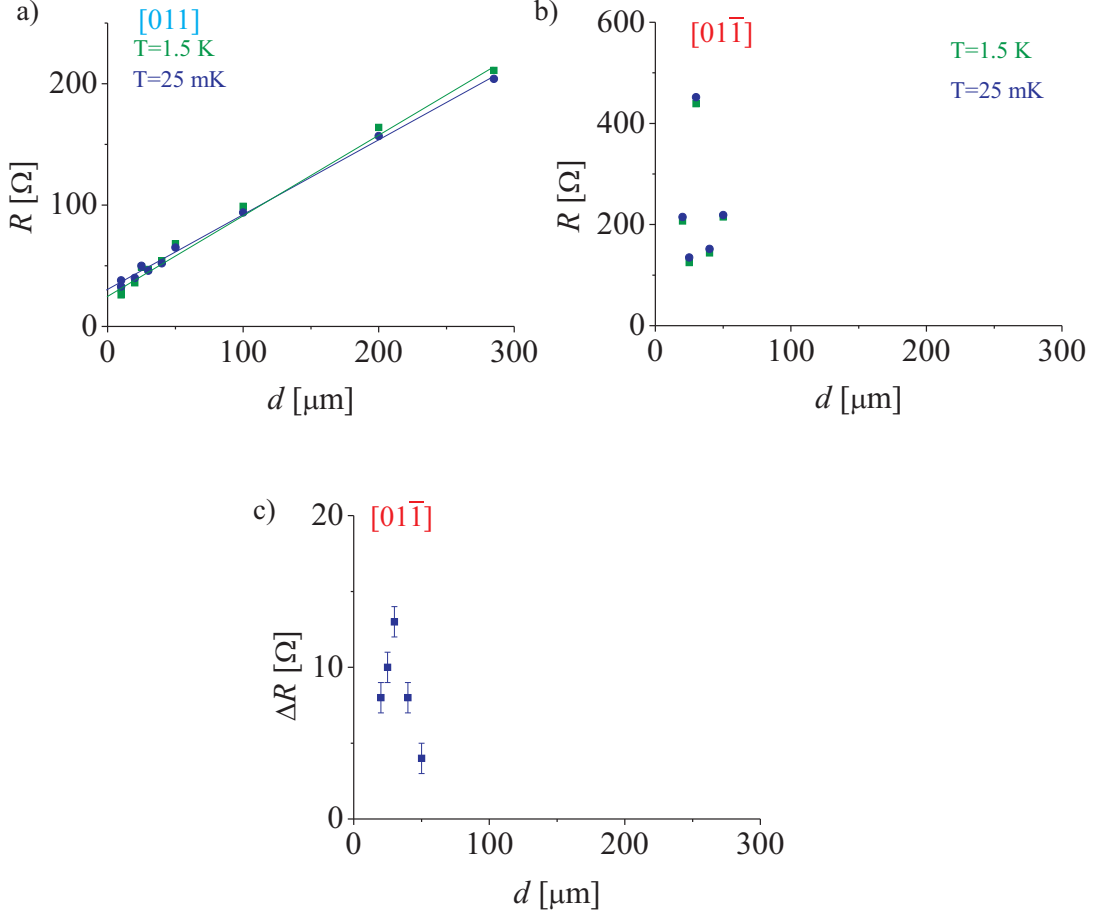


Figure 4.8: TLM measurements at 1.5 K and 25 mK. The width of the mesa is $50 \mu\text{m}$. The heterostructure is #8963. (a) In good contacting direction. The value of contact resistance at 1.5 K and 25 mK are $R_c = (6.8 \pm 0.5) \Omega$ and $R_c = (7.5 \pm 0.3) \Omega$, respectively (The contact resistance values are given for a $100 \mu\text{m}$ border length of mesa). The lower slope at 25 mK is probably due to the increase in the mobility since the mobility at low temperatures is slightly higher. (b) TLM measurements in bad contacting direction. (c) The change in the resistance $\Delta R = R(25 \text{ mK}) - R(1.5 \text{ K})$ for bad contacting direction.

the sheet resistance values from the measured total resistance. As clearly seen, for the contacts in good contacting direction, quantum Hall plateaus are flat and well defined. Contrary for the contacts in bad contacting direction, the quantum Hall plateaus are not well developed. This is neither a coincidence nor an experimental artifact, it is reproducible with any samples.

A detailed study of how the contact/2DES orientation affects the QHE measurements has been done in the PhD work of F. Dahlem [29]. To be more con-

vincing, some of experimental findings from F. Dahlem's thesis are presented in Fig. 4.10. Two Hall bar mesas are oriented along good contacting and bad contacting directions, respectively. Due to the geometry, each Hall bar has some contacts oriented in good and in bad directions. In Fig. 4.10(a) and Fig. 4.10(b) the Hall bar mesas are oriented in two different directions. However, the two terminal magneto resistance between the contacts in the bad contacting direction show the same behavior: the plateaus are shifted to lower magnetic field values with respect to bulk filling factor and have some humps and are at higher resistance values. In Fig. 4.10(c) and Fig. 4.10(d), two terminal magneto resistance are shown having contacts in good contacting directions: the plateaus are at the expected bulk filling factor values. This shows that the effect is due to contacts not due to the anisotropy in the 2DES. Now the remaining question is what causes this anisotropy. The next section will try to give some insights to this issue. The structural properties of the alloyed Au/Ge/Ni contacts will be discussed.

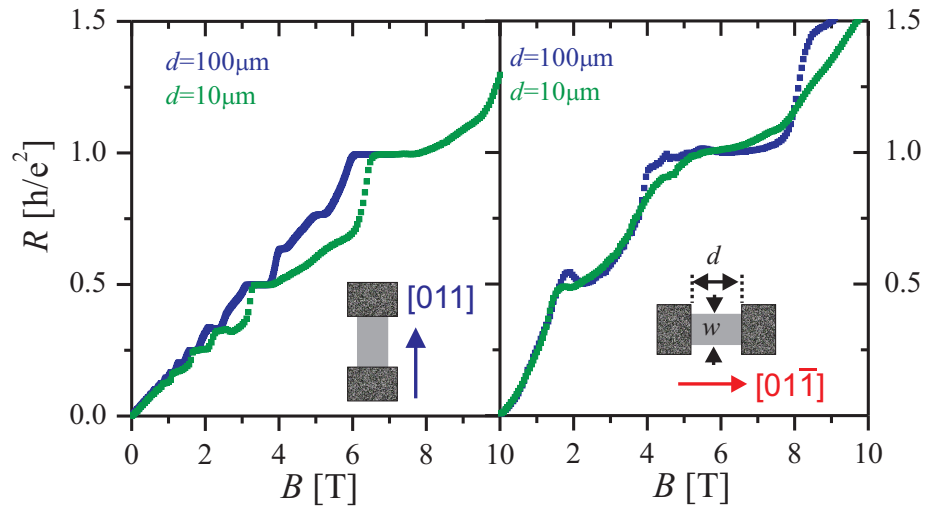


Figure 4.9: Two-terminal magneto resistance measurements on a 2DES for contacts defined in good contacting and bad contacting directions. d is the distance between the contact pairs. Sample is a TLM structure with a mesa stripe width $w = 50 \mu\text{m}$. In good contacting direction the quantum Hall plateaus are well developed. However, the quantum Hall plateau is not well developed for the bad contacting direction. The schema of measured contact pairs and mesa stripe are shown in the inset and the respective crystal directions are indicated.

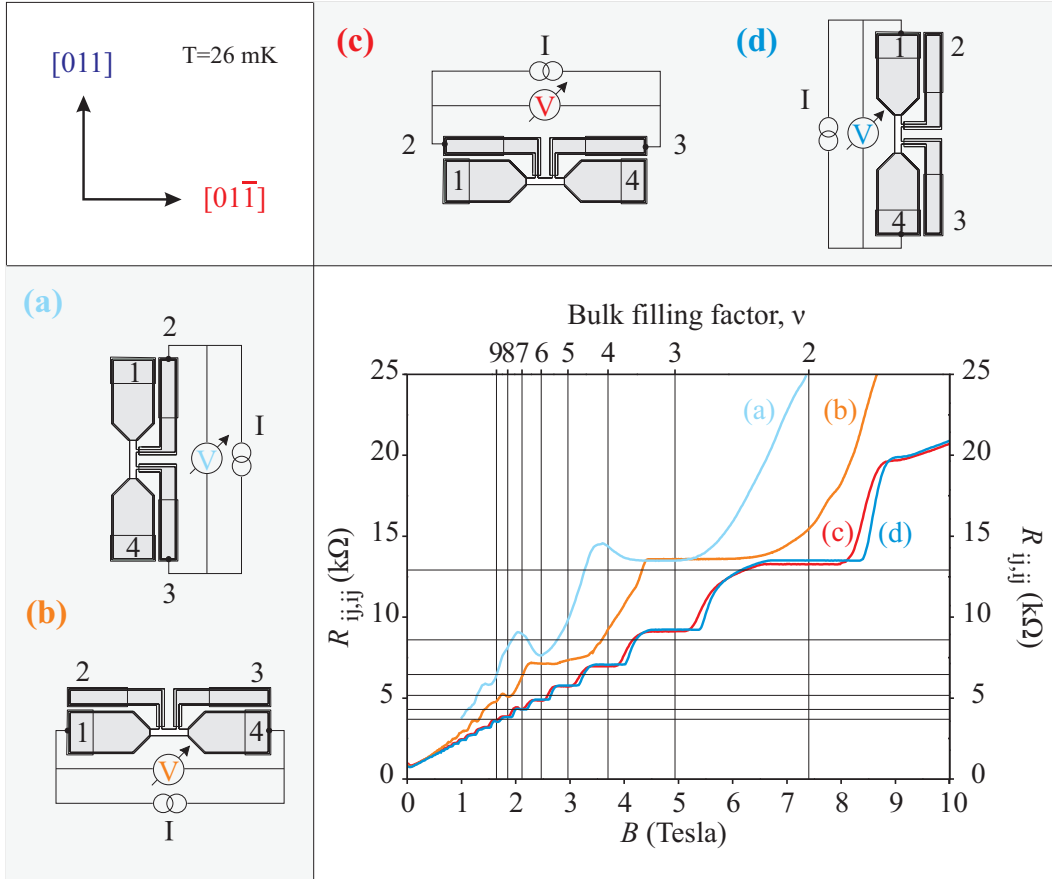


Figure 4.10: From PhD thesis of F. Dahlem [29]. Two-terminal measurements on Hall bars oriented in good contacting and bad contacting direction of the heterostructure. The position of the Hall plateaus are at the lower magnetic field values if current is injected in the bad contacting direction, (Curve (a) and (b)). As current is injected and ejected along good contacting direction, plateaus are at expected bulk filling factor values, (Curve (c) and (d)).

4.3 Structural properties of alloyed Au/Ge/Ni contacts to 2DES

The micro-structure of alloyed Au/Ge/Ni contacts is extremely complicated. The formation of an ohmic contact between the alloyed Au/Ge/Ni metals and the 2DES is not well understood. For the formation of an ohmic contact between alloyed Au/Ge/Ni and n^+ -GaAs, a highly Ge doped region in front of the NiGe rich grains is cited [60, 66, 72]. For the formation of the ohmic contact to the 2DES at the GaAs/Al_δGa_{1-δ}As interface the penetration of spikes into the 2DES is cited [73]. A similar contacting mechanism was reported by Hawksworth *et al.* [69] where a relatively unmodified 2DES under the contact area is also reported to exist. Lumpkin *et al.* reports about the role of Ni for the diffusion of Ge into GaAs. [67]. However, different recipes lead to different morphology and therefore probably different contacting mechanisms. We observed a difference between contacts defined in good contacting and bad contacting directions for deeper lying 2DES. Such an anisotropy of contacting 2DES has also been reported by Kamada *et al.* [61]. The recipe used by Kamada *et al.* is quite similar to one that we use. Here we discuss structural and morphological studies of our contact recipe. We will try to understand how a three-dimensional contact is contacting a 2DES.

The wafer # 8963 with the 2DES 120 nm below the surface is used for the structural investigations. The value of the contact resistance and details for this wafer were already given in Table 4.1. Since the 2DES depth is more than 86 nm, the Au/Ge/Ni layer thicknesses have been scaled up according to the scaling rule, that is, 146.0 nm of Au, 72.0 nm of Ge and 54.0 nm Ni were evaporated and then alloyed. The samples which are used for the SEM, TEM, STEM and EDX investigations is from the TLM structures which have been measured at liquid He temperatures prior to structural investigations. The contact resistance values for these TLM structures are presented in Fig. 4.7 in Chapter 4.2.3 and the TLM measurements are presented in Fig. C.2 in Appendix C. In bad contacting direction contacts mostly do not work, that is, no current is measurable in the sensitivity of measurements apparatus (a contact resistance larger than 10 MΩ). In good contacting direction contacts work very well. For the TOF-SIMS investigations two heterostructures are used. One of the samples is from the wafer #81744 where the 2DES depth is 120 nm. The second sample is prepared for wafer #81763 where the 2DES depth is 86 nm.

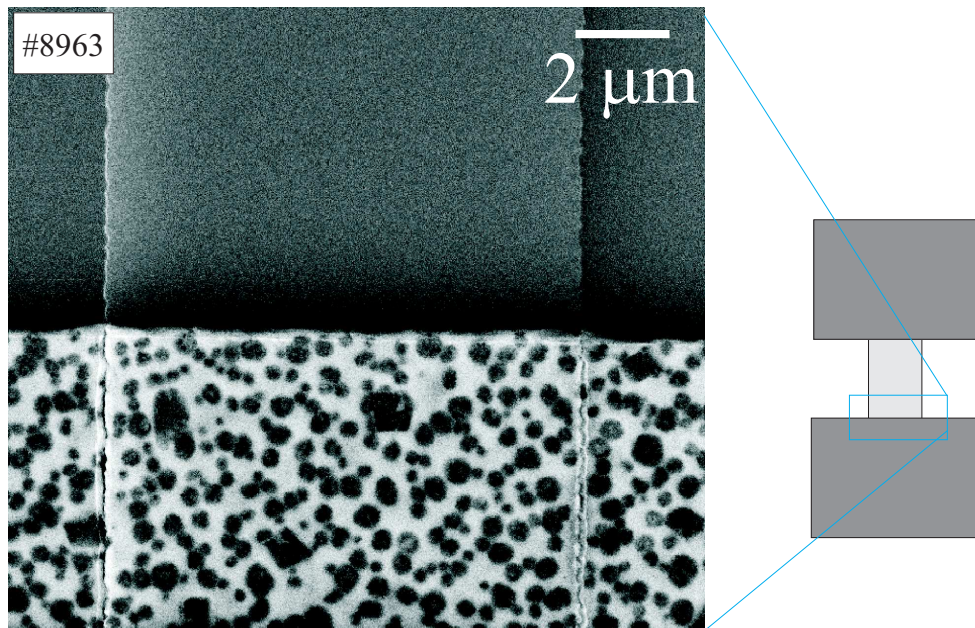
4.3.1 SEM studies

Two examples of SEM images of alloyed contacts are shown in Fig. 4.11. Images are taken at the contact mesa border. The SEM image in Fig. 4.11 (a) is taken at the good interface. The SEM image in Fig. 4.11 (b) is taken at the bad interface. The edge of the contact is very well defined in the range of $0.1 \mu\text{m}$. The grain size is quite small, mostly in submicron scale. The dark regions are Ge and Ni rich phases. The white regions are Au rich. These two images do not exhibit any orientation dependent features, such as a poor edge in one direction or elongated grains in a preferred direction. To have a deeper look we have had cross sectional SEM image of contacts. A TLM structure was used for the cross-sectional SEM investigations. The width of mesa is $5 \mu\text{m}$. The sample is mounted into a ZEISS CrossBeam machine that has a Focused Ion Beam (FIB) and a scanning electron microscope. A rectangular region at the contact/mesa interface is etched away by using FIB (Ga is used as ion source). The place of the etched region is sketched in the inset of Fig. 4.12 (a) as blue rectangle.

A couple of contacts are investigated. Representative scanning electron microscope images are shown in Fig. 4.12 (a) and (b) for good contacting direction and in Fig. 4.13 (a) and (b) for bad contacting direction. There is no apparent difference between both directions. The grainy structure is the same. What is also clear from SEM micrographs is that the modulation in the penetration depth is not large. Therefore for our contact recipe we cannot speak about the spike formation reported by Taylor *et al.* [73]. The visible down-going spiky regions are due to the milling process since the etching rate is different for the different grains. For slower milling rates, the effect is less.

The grainy morphology looks similar to that reported in literature [65] as shown in Fig. 4.1. However, the contrast in Fig. 4.1 is just opposite to that of Fig. 4.12 and Fig. 4.13. Here the dark regions are Ge and Ni rich, the white regions are Au rich. The grains are mostly smaller than $1 \mu\text{m}$ which is already visible in the top view SEM image which is shown in Fig. 4.11. As it is in the high magnification SEM images Fig. 4.12 (b) and Fig. 4.13 (b), the contacts in both orientation look similar at the metal/heterostructure interface. Similar images can be found in Fig. C.8, Fig. D.1, Fig. D.2, Fig. D.3, Fig. D.4, Fig. D.5 in Appendix D. The GaAs/ $\text{Al}_\delta\text{Ga}_{1-\delta}\text{As}$ layer under the contact is mainly consumed during alloying. Therefore, one cannot speak about a 2DES under the contacts. But this will be very clearly demonstrated in the later sections by the TEM investigations.

a) good direction



b) bad direction

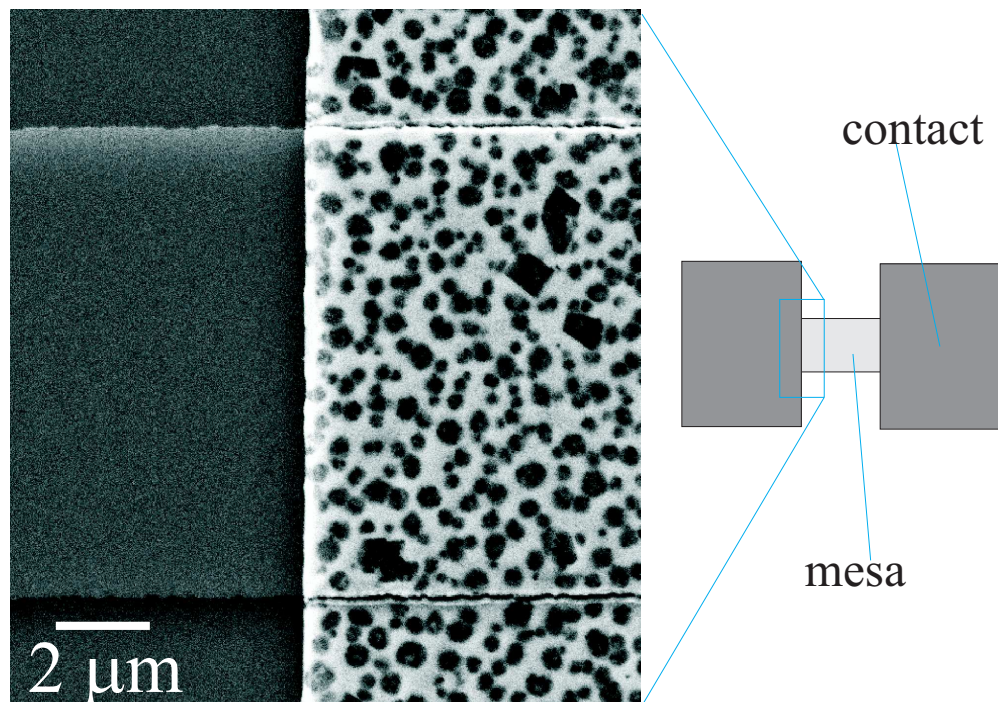


Figure 4.11: Top view SEM images of the alloyed contacts focusing on the metal/2DES border line good contacting and bad contacting direction.

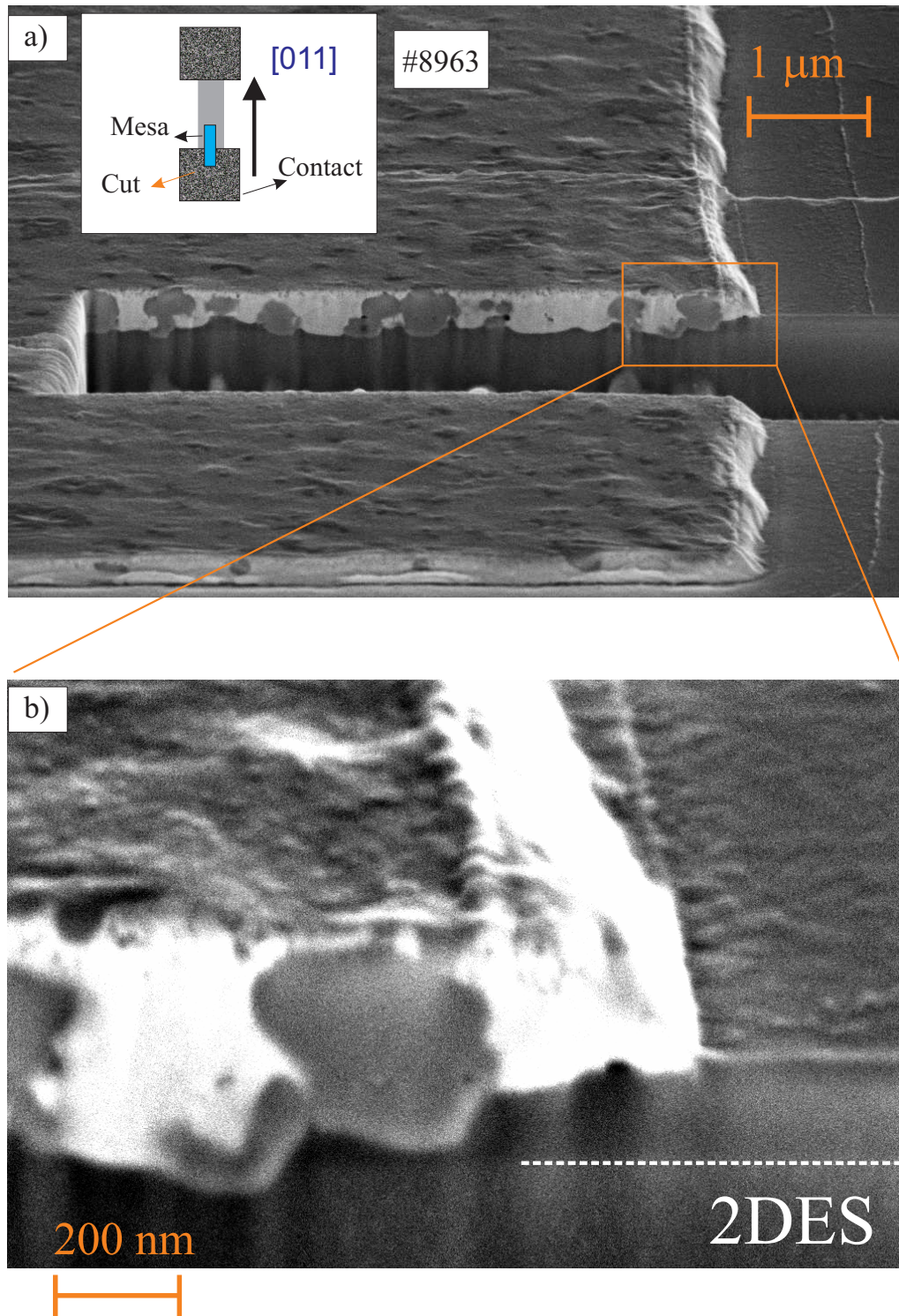


Figure 4.12: SEM image of the alloyed contacts in bad contacting orientation (see text)

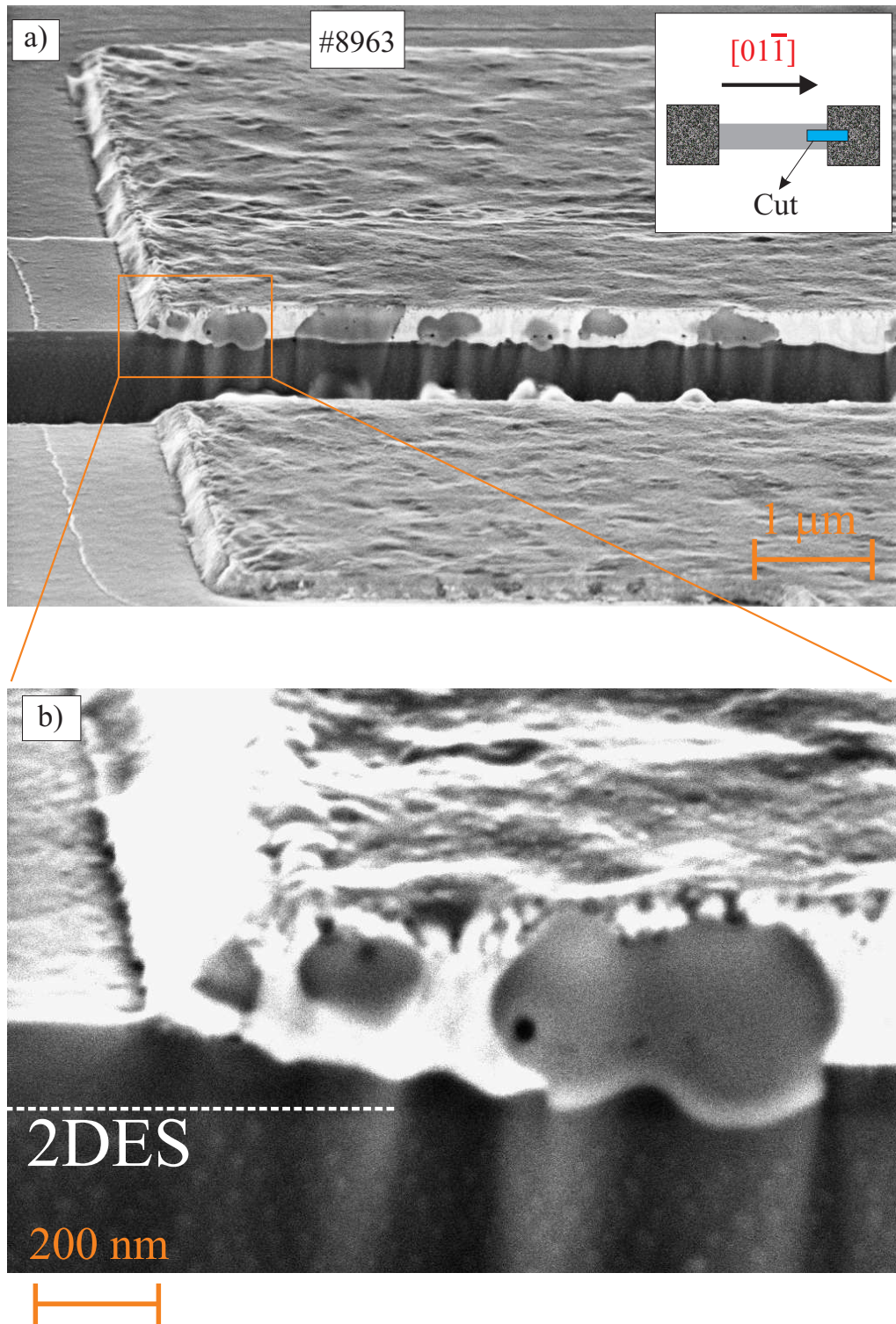


Figure 4.13: SEM image of the alloyed contacts in bad contacting orientation(see text).

4.3.2 TOF-SIMS studies

To obtain a more detailed picture of the structural properties of the alloyed contacts we have performed Time of Flight-Secondary Ion Mass Spectrometry (TOF-SIMS) investigations. The experiments are performed by Tolga Acartürk in the interface analysis group of Dr. Ulrich Starke at the MPI-FKF. Two samples have been investigated. One of the samples is from the wafer #81744 which have the 2DES 120 nm below the surface. The second sample is prepared from wafer #81763 and has the 2DES 86 nm below the surface. Several square contacts with $25 \mu\text{m}$ by $25 \mu\text{m}$ size are prepared on the sample. A TLM structure was prepared on the same sample and characterized at 4 K. TLM measurements exhibit typical behavior: A homogeneous contact resistance is found in the good contacting direction, that is, the TLM data fit a line very well, and the contact resistance is low ($0.6 \Omega\cdot\text{mm}$ for #81763 and $0.4 \Omega\cdot\text{mm}$ for #81744). In the bad contacting direction the TLM data do not fit a line, have a wide spread and contacts are highly resistive. The TLM measurements for the heterostructure #81744 is presented in Fig. C.4 in Appendix C.

In Fig. 4.14 (a) the experimental apparatus is sketched. The sample geometry is shown in Fig. 4.14 (b). Ga is used as a primary ion source that excites secondary ions by scanning across a region of $7.8 \mu\text{m} \times 7.8 \mu\text{m}$ on the contact/heterostructure interface. The analyzed areas are indicated in Fig. 4.14 (b). The secondary ions which are emitted from the surface due to the collision of the primary ions are collected and detected. The ions are then identified by their mass to charge ratio by a Time of flight Mass detector. By scanning the pulsed primary beam across the analysis area a lateral map can be obtained. A second ion beam is used to sputter the surface and successively analyse the deeper layers of the sample in order to generate a 3D cross section of the sample. In Fig. 4.14 (c)-(e) cross-

Caption for Fig. 4.14 (Figure on the next page). Secondary Ion Mass Spectrometry (TOF-SIMS) investigations on the alloyed contacts. (a) Sketch of TOF-SIMS apparatus. A pulsed and focused ion beam generates the secondary ions that are accelerated and collected into the detector by an electric field. The primary beam is rastered across the scan area in order to achieve the spatial resolution. (b) Sketch of the contacts on the sample. The analyzed area in good and bad direction is shown. (c)-(g) Cross-sectional intensity images for Al, Ge and Ni in good contacting direction and in bad contacting direction. White means high intensity and black means low intensity of investigated material is found. Respective material in each image is indicated. The width of scanning area is $7.8 \mu\text{m}$. Note that Al is accumulated on top of contacts (white on top). The z-position in the images corresponds to the depth below the the surface. Therefore, the GaAs signal appears lower under the contact due to the height of the contact and correspondingly a longer sputter time to reach the GaAs layer.

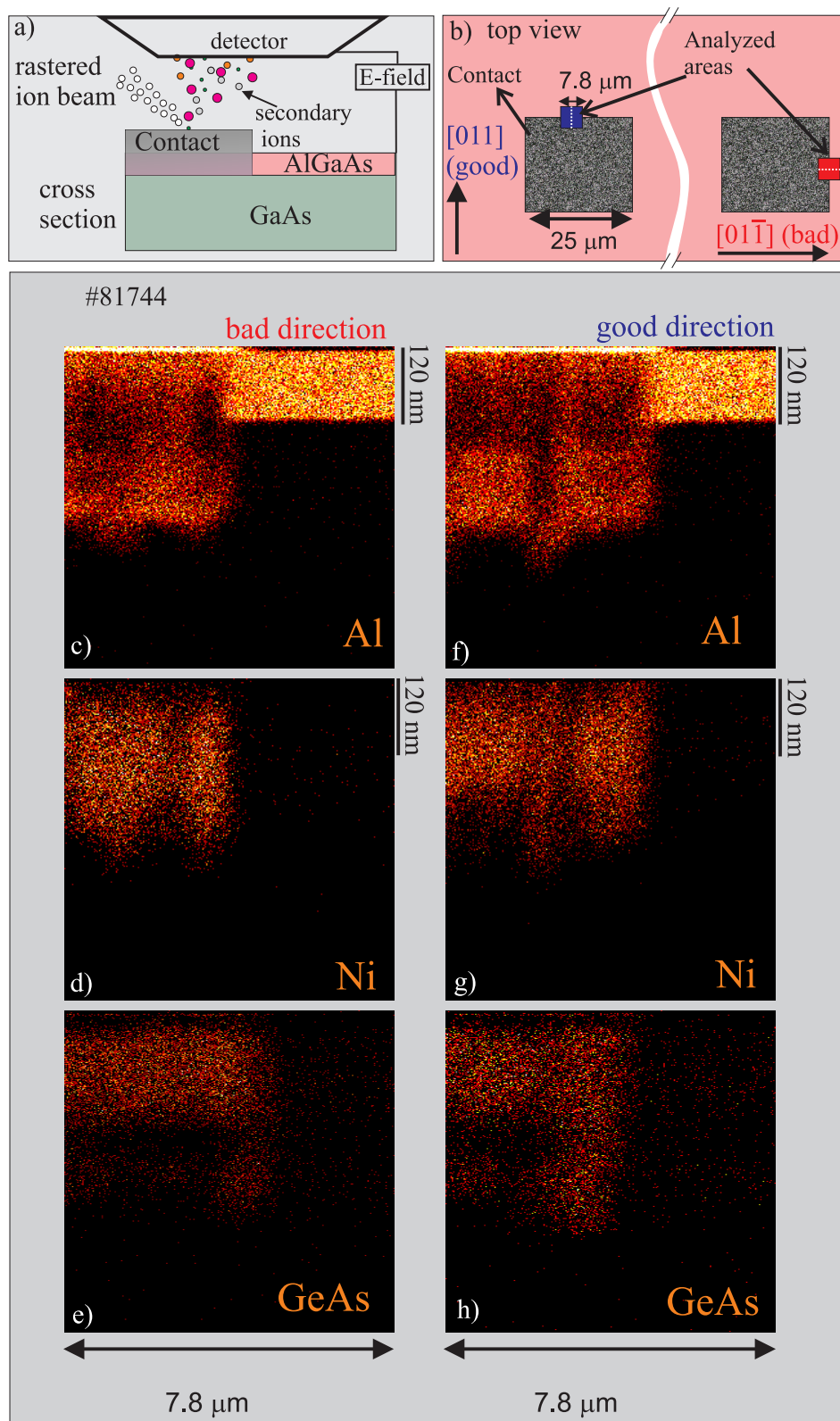


Figure 4.14: Caption on the previous page

sectional intensity images for Al, GeAs, and Ni along the lines shown in Fig. 4.14 (b) are shown. These are cross-sectional snapshots along the dotted white line at the good contacting interface (in the blue rectangle). In the images black means no material found and white means high amount of the material is found. The lateral resolution is around 300 nm and vertical resolution is around 2.5 nm. The sputtering direction is parallel to the border line of metal/2DES. While interpreting the results one has to be careful; the height of the contact is not reflected in the images. There is a height difference between contact and heterostructure surface as shown in Fig. 4.14 (a). However on the measurements one collects data as if it is at the same height. This leads to the offset that appears in the images between contacted and not contacted region. In Fig. 4.14 (f)-(h) depth profile for Al, GeAs, and Ni are shown for the bad contacting direction. These are images along the white dotted line in the red rectangle shown in Fig. 4.14 (b).

In the images Al, Ni and GeAs look similar in both direction. GeAs is detected to monitor the intensity of Ge since Ge does not give a good signal. The offset due to the height of the contact makes things complicated to interpret the results. The sputtering rate is different in the contact region and the heterostructure side. The software has no option for the height compensation. Furthermore the sputtering rate might even differ for the Au rich and Ni rich grains in the contact side. During the sputtering, elements are partly mixed. Lateral resolution is not small enough. All these things make it difficult to resolve small differences. The origin of the discussed orientation problem remains unsolved. Possible mechanism can be stress related piezoelectricity at the interface or diffusion of a dopant atom which can be different on the different crystal orientations. However, TOF-SIMS experiments do not exhibit any anisotropy at the metal/heterostructure interface in the good and bad direction.

Nevertheless, the most surprising outcome of this experiments is that Al is found at the top of the contact. This is visible in Fig. 4.14 (c) and (f) as a white line at the top. Similar results are obtained for the TOF-SIMS investigation of contacts on the wafer #81763 and are shown in Appendix E. The thickness of this Al rich region is between 5 nm to 10 nm. That means an aluminum oxide thin film might exist at the top of the contacts. However one cannot say if this is a continuous thin film or if it is a porous grainy (in nano scale below the lateral resolution of TOF-SIMS) thin film. Usually this is not a big problem: the contact area is generally bonded by pressing gold wire into the contact thereby destroying such an interface. In the case of small ohmic contacts an overlapping metal stripe is deposited on the contacts by evaporation to make electrical connection between the wide bond pads and the alloyed contacts. In this case the existence of the oxide layer might hinder the electrical contact between the ohmic contacts and overlaying metal stripe. However in our small ohmic contact samples we generally

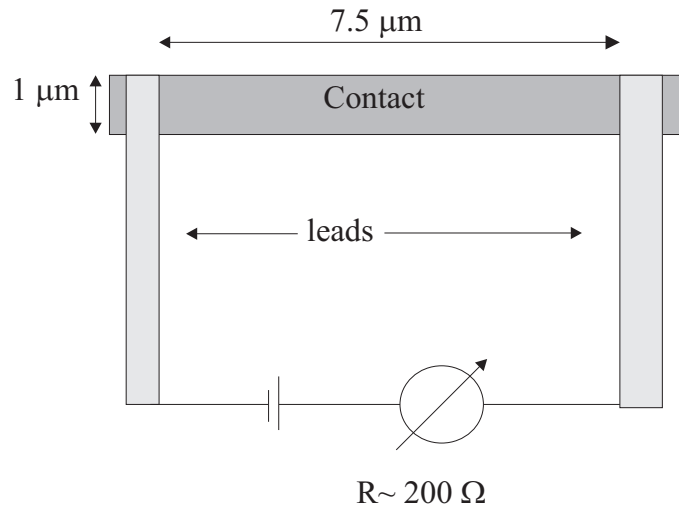


Figure 4.15: A test experiment for the aluminum oxide at the surface of ohmic contacts. An ohmic contact is contacted by two Cr/Au leads at the opposite corners. No evidence of an insulating layer between leads and ohmic contacts was found. The measured resistance is reasonably low.

do not see a clue of such a problem. In one of the samples a direct test of such an interface problem was also tried: a 7.5 micron long ohmic contact was connected to two bond connections at the opposite corners of the contact (that is the bond connections do not touch each other but both lie on the same contact) as shown in Fig. 4.15. The measured resistance was 200 Ω at room temperature and 90 Ω at 4 K. These values are still higher for a typical metal stripe. However, the resistivity of Au/Ge/Ni metal after alloying is known to be high [72]. This reasonably low resistance between these two bond connections indicates that there is no insulating thin film on the top of the contact. None of the chemicals which are used in the process after alloying is known to remove an aluminum oxide layer. The presence of Al at the top of the alloyed ohmic contacts has also been reported by Kamada *et al.* [61].

4.3.3 STEM studies

We have prepared samples for transmission electron microscopy (TEM) and scanning transmission electron microscopy (STEM). The samples are prepared from the wafer #8963 which have a 2DES 120 nm below the surface. The TEM lamellas were prepared in a FIB. Here we will present results for lamellas from good contacting directions and for lamellas from bad contacting directions. The samples are prepared by depositing platinum in a region on the contact/2DES border as shown in the inset of Fig. 4.16 (a). Then two trenches are etched through. The area underneath platinum is cut and analyzed by TEM and STEM. An STEM image of one lamella is shown in Fig. 4.16 (a). The AlGaAs/GaAs interface is clearly visible. The dark and bright appearing grainy structure is similar to previously shown SEM images. The EDX analysis shows that the white appearing grains are Ni_2GeAs , as reported in the literature. The dark appearing region are Au(Ga,As) regions and seem to be mainly Au_4Ga which has also been reported in literature [65, 67, 74]. The EDX analysis at different points are summarized in Fig. 4.16 (b). On the GaAs side the percentage of Ga is higher than that of As. The excess Ga is probably due to the sample preparation since Ga is used as ion source in the FIB to etch the sample. In the $\text{Al}_\delta\text{Ga}_{1-\delta}\text{As}$ region the values are in agreement with the expected value for $\delta = 0.33$. The grainy structure is similar to the one shown in Fig. 4.1 (with opposite contrast). The $\text{Al}_\delta\text{Ga}_{1-\delta}\text{As}$ layer underneath the contact region is mainly consumed during the alloying process. However, there are still some remnants of it which are visible as some white regions under the contact. In the TOF-SIMS experiments we have found Al at the top of the contacts. This is confirmed with the EDX analysis. The EDX analysis at the top of the contact shows 18% of Al, 22% of Ga, 1% of As and 59% of Au. Similar values are found on the other lamellas. O is also present at the top. However, O peak is at very low energies and quantification of O is not reliable. Therefore we did not include it in the quantification process³. The presence of Al and O is very clear, implying the existence of aluminum oxide at the top of the contacts. However, this might be a very porous layer since we do not see a clear evidence for such an insulating layer at the top of contacts from the electrical characterization of the contacts. EDX point analysis at different positions of the contact and heterostructure side for several contacts are presented in Fig. F.1, F.2, and F.1 in Appendix F.

In Fig. 4.17 (a) and (b) cross-sectional STEM images of two lamellas are shown. The lamellas are from the good contacting direction. In Fig. 4.17 (c) and (d) schematic sketches of the two lamellas are depicted. The dark regions are Au-rich and bright regions are Ni-rich and Ge-rich. The Au and Ni/Ge-rich regions

³If we include O in the quantification process it gives 40% of the O and 10% of Al. But the error in this quantification process is very large.

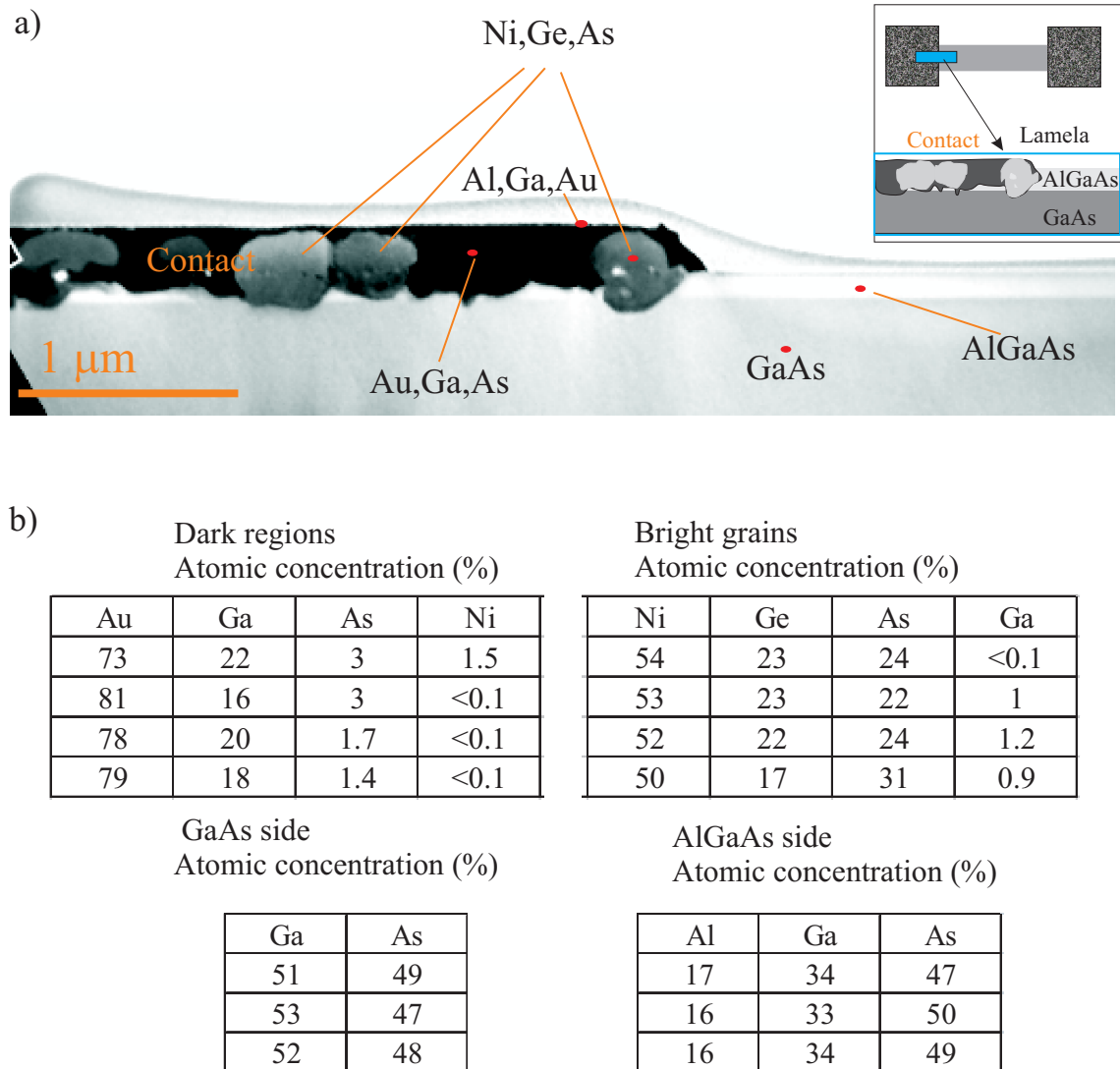


Figure 4.16: (a) A cross-sectional STEM image of an alloyed ohmic contact. The heterostructure is the same as the one used for cross-sectional SEM images (Fig. 4.11) and (Fig. 4.12). The position of the lamella at the ohmic contact/2DES and cross-sectional scheme of lamella are shown in the inset. The AlGaAs/GaAs interface is clearly visible. The bright appearing grains are Ni-rich and Ge-rich rich and are mainly Ni₂GeAs, as also identified in the literature. The dark regions are Au-rich Au(Ga,As) and are mainly Au₄Ga. (b) The EDX analysis at the dark grains, light grains, GaAs layer and AlGaAs layer in different specimens (lamellas). The points where the EDX analyses are performed in this spacemen are indicated by red points. At the top of the contact Al is found which confirms the TOF-SIMS experiments. Typical concentration values of elements at the top are 18% of Al, 22% of Ga, 1% of As and 59% of Au.

are also indicated in Fig. 4.17 (c) and (d). The AlGaAs region is ending earlier than metal contact region. This is visible from the change of contrast. For both lamellas this is similar. This is better visible if one takes Al maps of the lamellas via energy-filtering TEM (EFTEM). In EFTEM, images are formed using only electrons that have suffered a specific energy loss. Therefore it is possible to make elemental maps. In Fig. 4.17 (e) and (f) Al maps of the lamellas are shown. The Al maps confirms that AlGaAs does not have a direct contact to the Au-rich metal regions. There is a region of 50 nm to 100 nm which does not contain Al or very few Al. In Fig. 4.17 (f) a tiny layer of $\text{Al}_\delta\text{Ga}_{1-\delta}\text{As}$ layer underneath the contact is visible which is schematically depicted in figure Fig. 4.17 (d).

STEM images of two lamellas from the bad contacting direction are shown in Fig. 4.18 (a) and (b). As before, the AlGaAs/GaAs interface is very clear. The contacts and heterostructure is schematically sketched in Fig. 4.18 (b) and (d). The dark grains in the contact metal are Au-rich and bright regions are Ni/Ge-rich. In Fig. 4.18 (e) and (f) the Al maps for the same lamellas are shown. As before, there is an approximately 50 nm to 150 nm thick region without Al. This is, however, exactly the case for both orientation.

The electronic properties of this mid region, which has no Al, must be crucial for the contact mechanism. To see the crystal structure of this mid region we made high resolution transmission electron microscopy (HRTEM) images. In Fig. 4.19 (a) the Al map of the investigated contact is shown. This lamella is from the good contacting direction. In Fig. 4.19 (b) the sketch of the contact is shown. Three HRTEM images are shown in Fig. 4.19 (c), (d) and (e). The position of the images are indicated in Fig. 4.19 (a) and (b). The image on Fig. 4.19 (c) is from the AlGaAs region. The atomic crystal structure is very clearly visible. The image on Fig. 4.19 (d) and (e) is from the region that contains no Al. The crystal structure of this region is identical to the GaAs/ $\text{Al}_\delta\text{Ga}_{1-\delta}\text{As}$ region shown in Fig. 4.19 (c). Al diffuses out but the crystal structure is preserved. The similar behavior is also observed in the bad contacting direction.

In Fig. 4.20 the results for a lamella from the bad contacting directions is presented. Fig. 4.20 (a) shows the Al map at the contact/heterostructure interface, Fig. 4.20 (b) shows the schematic representation of the contact and heterostructure and Fig. 4.20 (c), (d) and (e) show HRTEM images. The positions where the images are taken from are indicated in Fig. 4.20 (b). The results are similar to what have been found in good contacting direction. The crystal structure of the region without Al is the same to that of AlGaAs⁴.

As we have seen there is a region which seems to be free of Al between the Au-

⁴It is important to say that at the contact/2DES interface there are not only Au regions but also Ni/Ge-rich regions. We did not have lamellas with Ni/Ge-rich regions at the interface during above mentioned experiments. Therefore, we have explicitly focused on preparing lamellas with Ni/Ge-rich grains at the interface. We will investigate these lamellas in the next section.

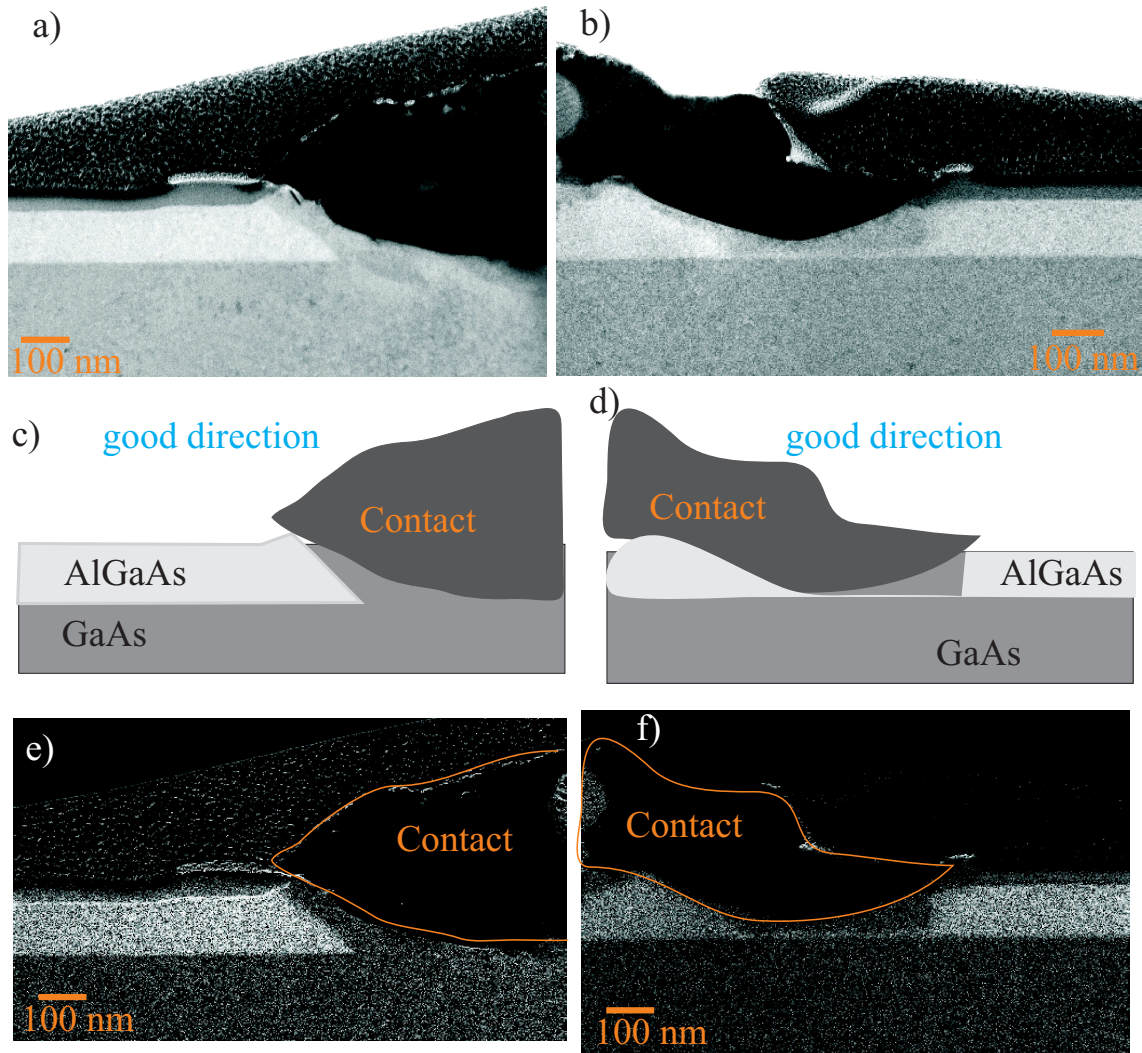


Figure 4.17: (a), (b) Cross-sectional STEM images of alloyed contacts in good contacting direction. (c), (d) Schematic representation of the contacts shown in (a) and (b), respectively. (d), (e) Al map of the contacts (a) and (b), respectively. AlGaAs region is clearly visible and ends about 50 to 100 nm in front of the metal contact. Al seems to have migrated away from the AlGaAs layer.

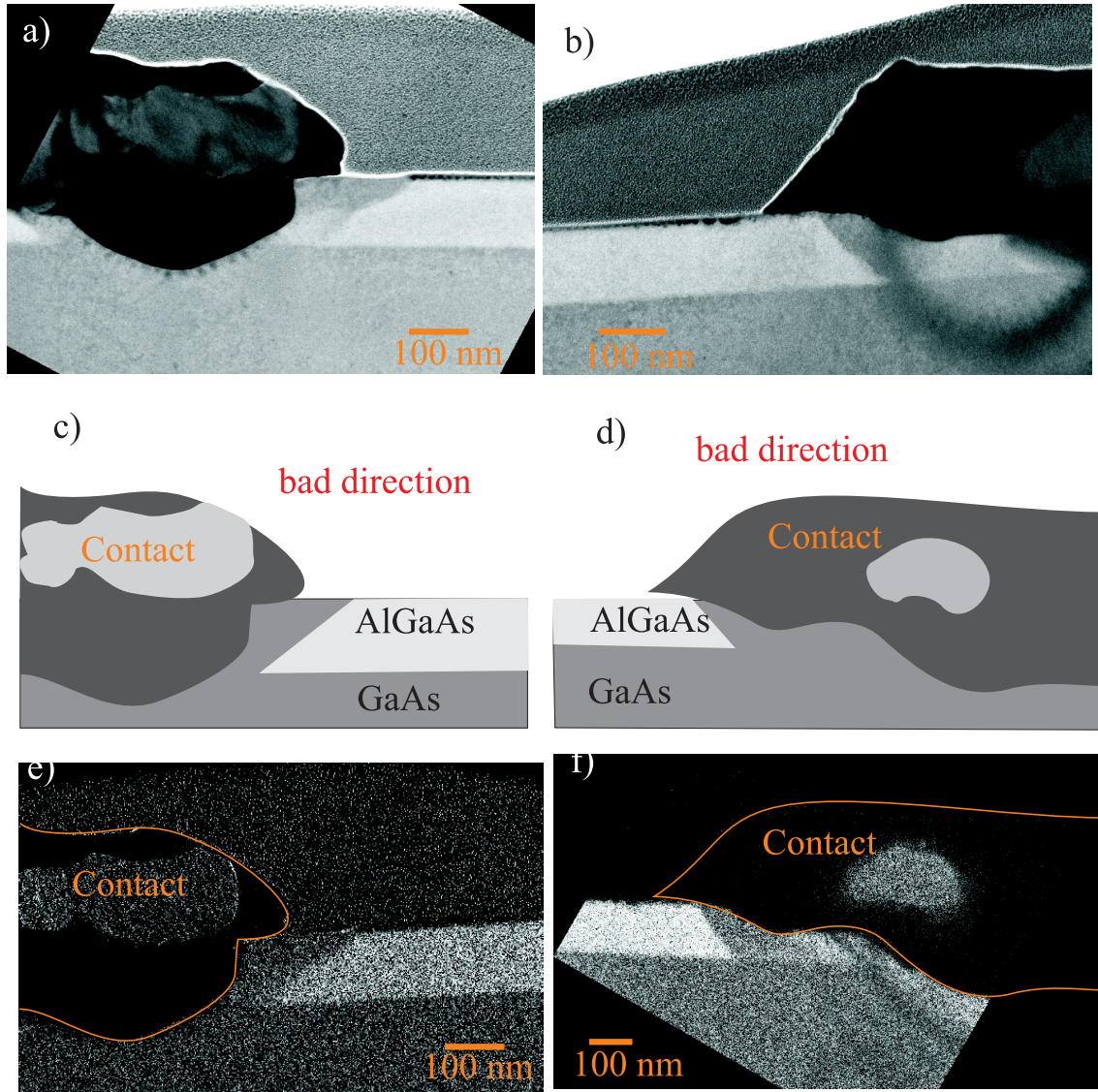


Figure 4.18: (a), (b) Cross-sectional STEM images of alloyed contacts in bad contacting direction. (c), (d) Schematic representation of the contacts shown in (a) and (b), respectively. (e), (f) Al map of the contacts obtained. AlGaAs region is clearly visible and ends about 50 to 100 nm before the metal contact. Al seems to have migrated away from the AlGaAs layer which was also the case in good contacting direction.

rich contact and AlGaAs. Al seem to diffuses out from this region. However, we cannot say if all the Al diffuses out or is it a partial out-diffusion. What replaces Al in this region is also an important question. To get more detailed information we have done EDX investigations as will be discussed in the next section.

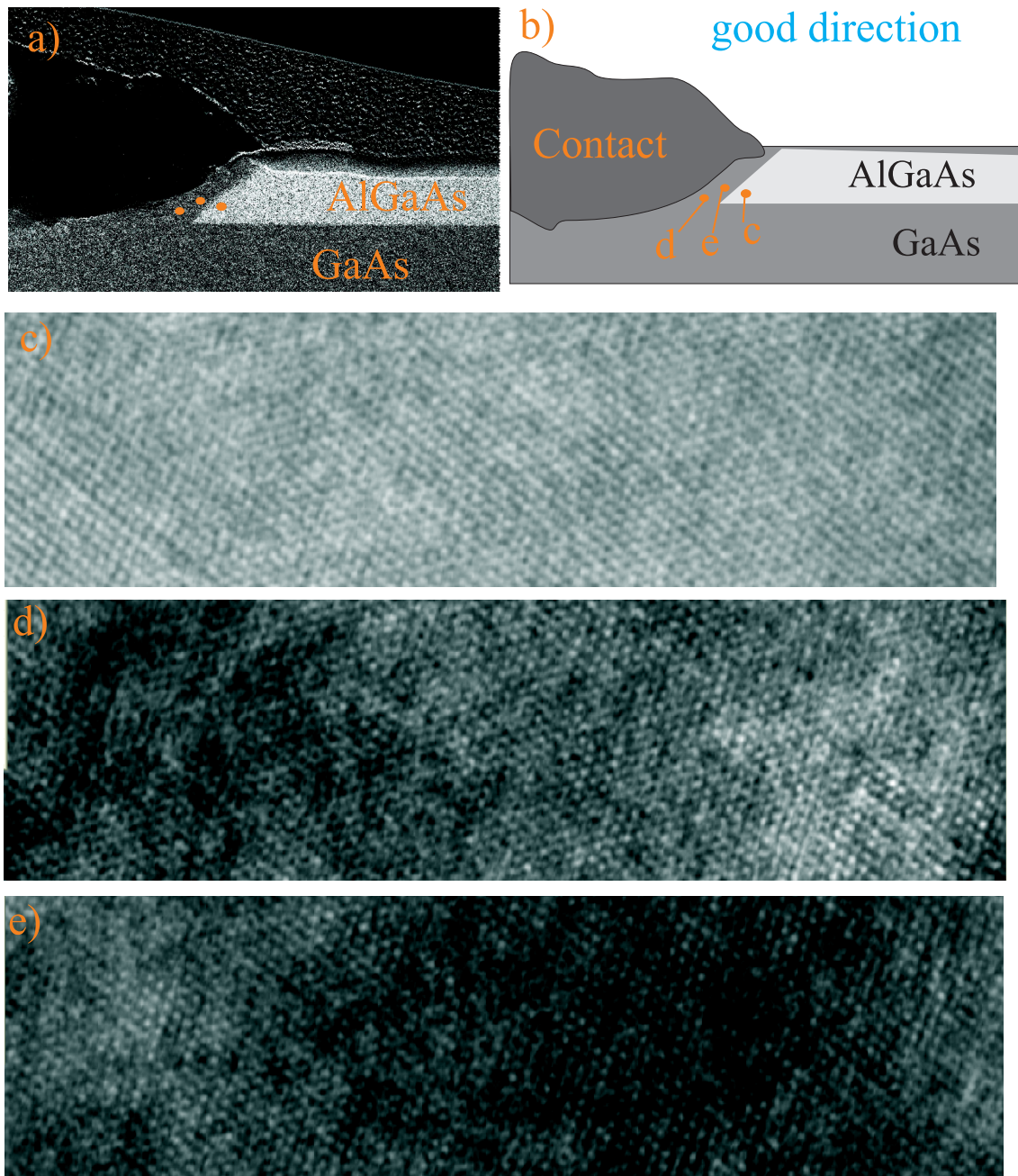


Figure 4.19: Cross-sectional HRTEM images from a contact in good contacting direction. (a) Al map of the contact. (b) Schematic representation of the contact. (c), (d) and (e) Cross-sectional HRTEM images from the positions indicated in (a) and (b). The crystal structure of the Al-free region in front of the contact is the same as that of AlGaAs.

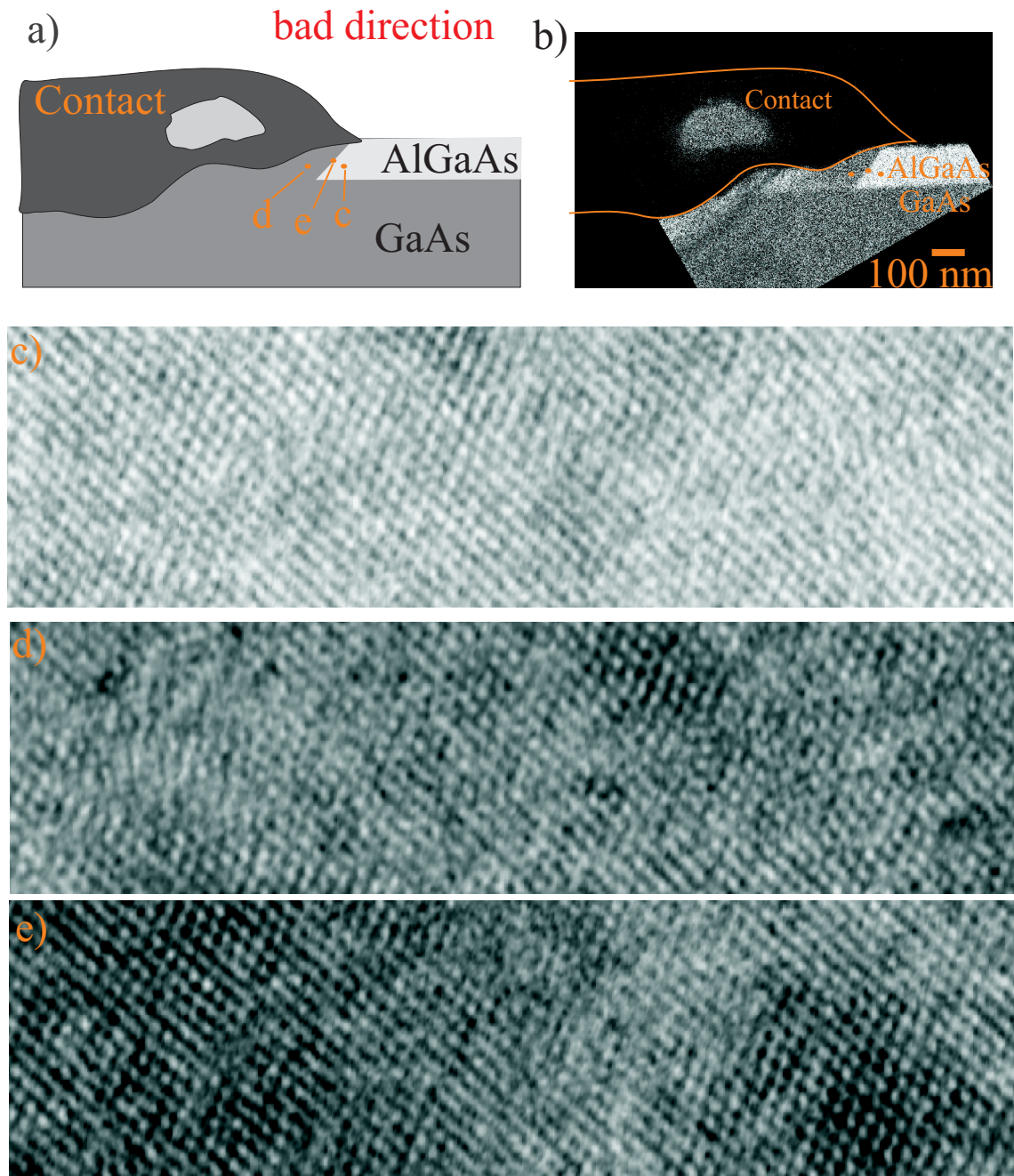


Figure 4.20: Cross-sectional HRTEM images from a contact in bad contacting direction. (a) Al map of the contact. (b) Schematic representation of the contact. (c), (d) and (e) Cross-sectional HRTEM images from the positions indicated in (a) and (b). The crystal structure of the Al-free region in front of the contact is the same as that of AlGaAs.

4.3.4 EDX studies

As we have seen from the STEM studies, the contact/ 2DES interface looks quite similar in both directions. Now a very important question is what replaces Al in this mid region, since Al seems to diffuse out. We also want to investigate diffusion of atoms which might act as dopant. The diffusion of Ge into the GaAs region making a heavily doped n^+ -GaAs region between the contact metal and n -GaAs is most widely cited mechanism for the formation of contact to n -type GaAs [60,72]. In order to answer this questions we performed EDX spectroscopy investigations. A couple of contacts are investigated. A series of points along a line are analyzed, thereby a line profile for the atomic concentration of elements versus analysis point is produced.

The results are presented in Fig. 4.21 (a)-(c) for good contacting direction. In Fig. 4.21 (a) the STEM image of the investigated contact is shown. The HRTEM images of this contact were shown in Fig. 4.19. In Fig. 4.21 (b) the contact and heterostructure is schematically depicted. The position of the line scan is shown in the figure. In the line scans the duration for each point measurement is shorter than for the point measurements shown in Fig. 4.16 . Therefore some point measurements with longer duration were also performed in order to obtain a more accurate information. The position of the point measurement is indicated as a dot in the figure. Fig. 4.21 (c) shows the atomic concentration (at %) of Al, Ga, As, Au, Ge and Ni along the line scan. The high-resolution STEM image and Al map of this contact were shown in Fig. 4.17 (a) and (e). On the $\text{Al}_\delta\text{Ga}_{1-\delta}\text{As}$ side, away from the contact, the average atomic percentage of Al, Ga, As are around usual values for $\text{Al}_\delta\text{Ga}_{1-\delta}\text{As}$ which were given in Fig. 4.16 (b). The position of the metal contact manifests itself via a sharp rise in the Au concentration. Just before reaching the metal contact, approximately 50 nm before, the atomic percentage of the Al decreases and the atomic percentage of the Ga increases. In this mid region, the atomic percentage of Ga and As is roughly equal and this is the case till the Au-rich metal contact region is reached. To get a more accurate quantitative result we performed a local (3 nm by 4 nm rectangle) measurement in this region. The position of the area is indicated in Fig. 4.21 (b) by an orange dot. We found 46% of Ga, 47% of As, 4% of Au and 0,6% of Ni. No Al was found within the detection limit of the measurement. For the point measurement the detection limit is about 0.2%. In the line scans the error bar is larger, between 1% and 4%. Similar results for another lamella (in good contacting direction) are presented in Fig. F.4 in Appendix F.

In Fig. 4.21 (d)-(f) similar investigations for a contact in the bad contacting direction are presented. The high magnification STEM image and Al map of this contact were shown in Fig. 4.18 (b) and (f). The HRTEM images were shown in Fig. 4.20. In Fig. 4.21 (d) the STEM image of the contact is shown. The position

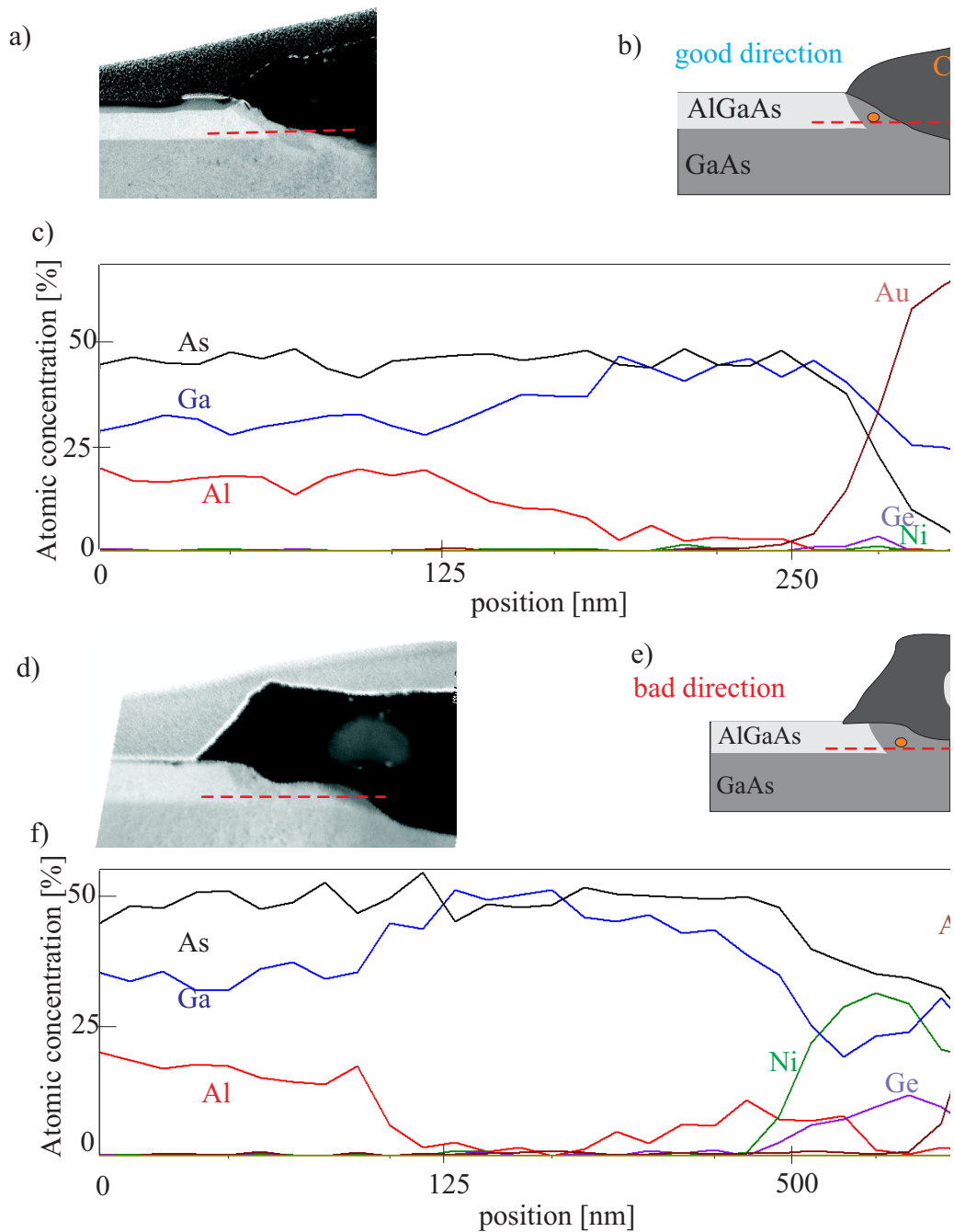


Figure 4.21: (a) STEM image of a contact in good contacting direction. This is the same contact as shown in Fig. 4.17. The position of the line scan is indicated by the dashed red line (b) Sketch of the left STEM image. The position of the line scan is indicated by dashed red line. (c) EDX analysis along the line shown in (a) and (b). The atomic percentages of Al, Ga, As, Ni, Ge and Au versus distance along the line are plotted. (d)-(f) The same analysis for a contact in bad contacting direction.

of the line scan is indicated. In Fig. 4.21 (e) the contact is schematically depicted. The position of the line scan and point measurements are shown. Again, far from the contact, Al, Ga, and As have usual values for the $\text{Al}_\delta\text{Ga}_{1-\delta}\text{As}$ layer. In the contact region a Ni-rich and Ge-rich region is observed in front of the Au-rich region. However, the thickness of the lamellas is typically around 100 nm. The transition between Au rich and Ni/Ge-rich grains are quite sharp. So in a 100 nm thick lamella one might have Au-rich region in one side and Ni/Ge regions on the other side. That is why we see Ni and Ge before the apparent contact region. There must be a NiGe-rich grain on the other side of the contact which might not be visible in the STEM image. Before reaching the Au-rich contact region, Al concentration is lower and at the same position Ga concentration is higher. The point analysis in this mid region shows 1% Al, 51%Ga, 46%As and 2%Au. Au was also found in the good direction. However, here there is no Ni present whereas 0.6% Ni is found on the good contacting direction. Similar results for another lamella (in bad contacting direction) are presented in Fig. F.5 in Appendix F.

Up to here we have investigated lamellas with mainly Au-rich grains at the contact/2DES interface. However, there are also NiGe-rich grains at the interface. We have prepared lamellas for which the contact region at the interface is NiGe-rich. In Fig. 4.22 (a) the STEM image of such a lamella is shown. In Fig. 4.22 (b) the contact and heterostructure is schematically depicted. The position of the the line scan and the point measurements are indicated. In Fig. 4.22 (c) atomic concentrations versus analysis point are shown. Away from the contact, the usual values for Al, Ga and As are measured. The position of the contact is visible from the rise in the percentage of Ni and Ge. Important to note, there is no region free of Al in the $\text{Al}_\delta\text{Ga}_{1-\delta}\text{As}$ layer. The finding, that there is no region free of Al in front of NiGe-rich contact, is confirmed in another lamella and the results are presented in Fig. F.3 in Appendix F. The atomic concentration of Al, Ga and As gradually decrease as the NiGe-rich contact is reached. This is totally contrary to what we observed when we have Au-rich contact at the interface. The EDX analysis at a point in $\text{Al}_\delta\text{Ga}_{1-\delta}\text{As}$ layer close to the NiGe rich contact shows 16% Al, 34% Ga, 47% As, 0.3% Au, 0.7% Ge and 1.3% Ni.

In Fig. 4.23 the results for a lamella in bad contacting direction is shown. In Fig. 4.23 (a) a STEM image of the specimen is shown. From the contrast we can see that there is a NiGe rich grain at the interface. There is a Au-rich region at the top of this grain. In Fig. 4.23 (b) another STEM image of the same specimen is shown. Here the contrast is optimized to see the difference between the $\text{Al}_\delta\text{Ga}_{1-\delta}\text{As}$ and GaAs regions. It is possible to see a region free of Al (or less Al) in front of the contact. In Fig. 4.23 (c) and (d) line scan profiles along the white and orange indicated lines in Fig. 4.23 (a) are shown. Just in front of the NiGe-rich contact, there is a region in which Al concentration is lower and Ga

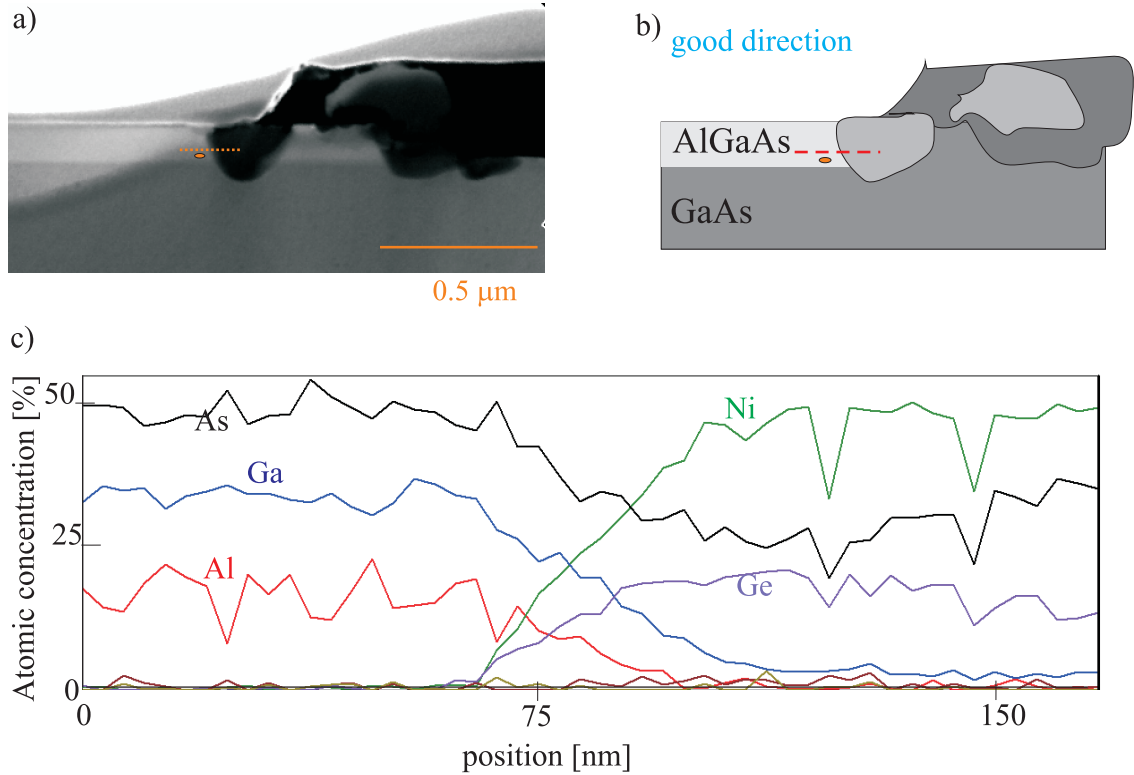


Figure 4.22: (a) STEM image of a contact in good contacting direction. The metal grain at the metal/Al_δGa_{1-δ}As interface is a NiGe rich grain. (b) schematic representation of the contact and heterostructure. The position of the line scan and point analysis is shown. (c) EDX analysis along the the line shown in (a) and (b). Atomic percentage of Al, Ga, As, Ni, Ge and Au versus position along the line is plotted.

concentration is higher and becomes comparable to that of As. This behavior is similar to what we have observed when we have Au-rich grains at the interface. We have confirmed these findings in another lamella and the results are presented in Fig. F.6 in Appendix F.

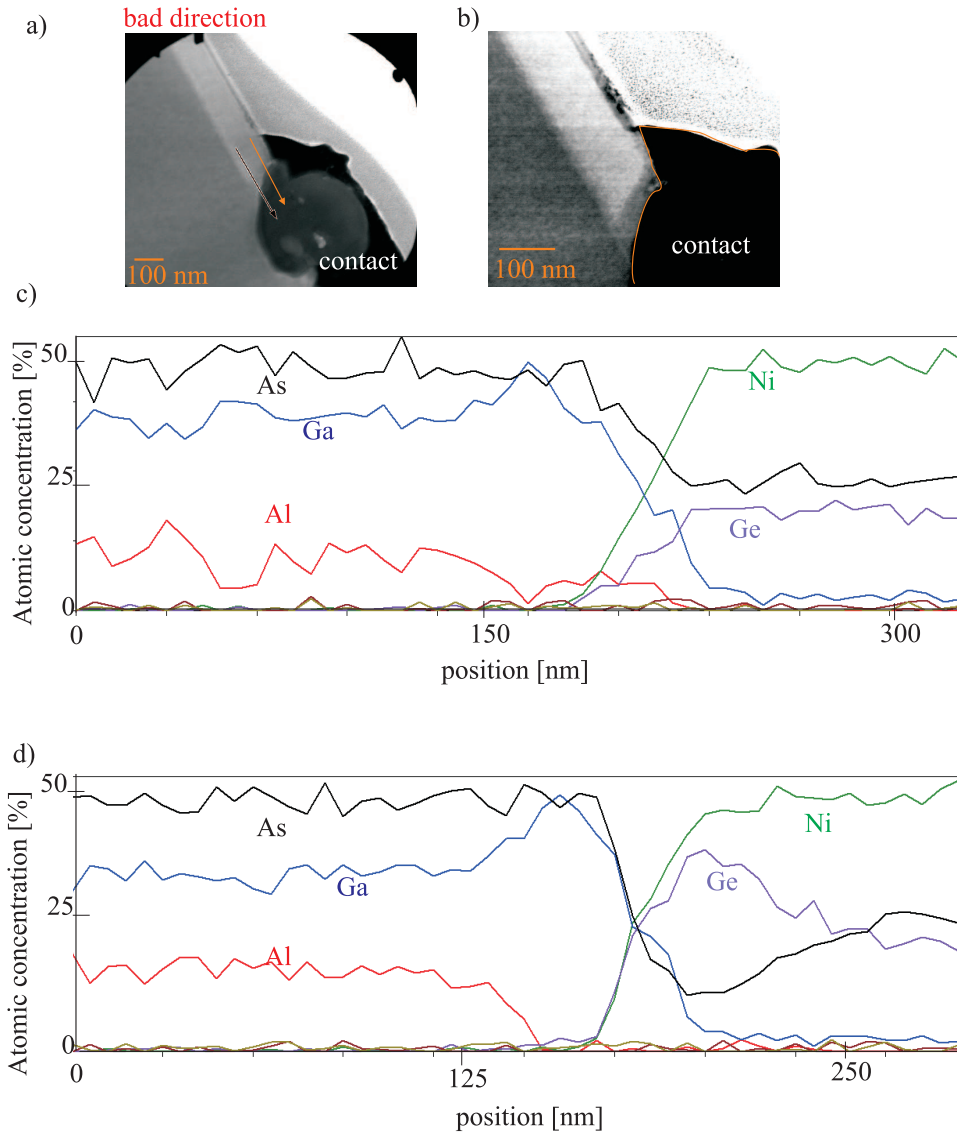


Figure 4.23: STEM image of a contact in bad contacting direction. The metal grain at the metal/ $\text{Al}_\delta\text{Ga}_{1-\delta}\text{As}$ interface is a NiGe-rich grain. The position of the line scan is shown. (b) Another STEM image for the same contact. The contrast is optimized to highlight the difference between GaAs and $\text{Al}_\delta\text{Ga}_{1-\delta}\text{As}$ layers. (c) EDX analysis along the black line shown in (a). Atomic percentage of Al, Ga, As, Ni, Ge and Au versus position along the line is plotted. (d) EDX analysis along the orange line shown in (a)

4.3.5 Discussion of the result of the structural investigations

From scanning electron microscope images it is very clear that we have NiGe-rich and Au-rich regions at the contact/heterostructure interface. The amount and distribution of the NiGe-rich grains is similar in good contacting and bad contacting directions. Cross-sectional scanning electron microscope investigations also do not exhibit any difference for both directions. We have etched several contacts by FIB and monitored while etching. The amount of the Au-rich and NiGe-rich grains at the interface is roughly the same. That is the case in both good contacting and in bad contacting directions. This result is consistent with the (top view) scanning electron microscope images. We also could not see any difference between good contacting and bad contacting direction in the TOF-SIMS investigations. However we find an Al-rich region at the top of the contacts. This is also confirmed by the EDX investigations. Al is present with Au and Ga. O is also present with Al, implying an aluminum oxide region. However, this must be a porous layer since there is no clue of an insulating layer found in the electrical measurements.

STEM and EDX studies show that alloyed Au/Ge/Ni contacts consist of mainly two phases. NiGe-rich grains surrounded with Au-rich Au(Ga,As) phase. NiGe-rich grain are mainly Ni₂GeAs and Au-rich phase are mainly Au₄Ga. These findings are consistent with those reported in literature [65,67,74]. The Al_δGa_{1-δ}As underneath the contact region is mainly consumed during the alloying process. Therefore one cannot speak of the existence of a 2DES under the contact. The results of the electrical characterization of the contact resistance also support this statement. The contact resistance scales with the border length between the contact and the 2DES and does not depend on the area under the contact.

At the contact/2DES interface there is either a Au-rich region or a NiGe rich region. When there is a Au-rich grain at the interface, Al in the Al_δGa_{1-δ}As layer diffuses out and Ga replaces Al in this region. HRTEM images show that the crystal structure of this mid region remains intact. Au is known to enhance the out-diffusion of Ga in contacts to *n*⁺-GaAs [67]. Here it seems that Au is acting as a catalyst to enhance out-diffusion of Al from Al_δGa_{1-δ}As and replace it by Ga. EDX analysis show that the amount of Ga is less than the normal amount of Ga (up to 4%) found in the GaAs layer. 1% to 4% of Au can be found in this region. About 0.5% of Ni is also found for some contacts, but Ni is not always present. Au and Ni are *p*-type dopants in GaAs. The thickness of this mid region is between 50 nm to 150 nm. Since no clue of *n*-type doping is found it is reasonable to assume that current injection cannot take place over this region. This is similar in good contacting and bad contacting directions.

When there is a NiGe-rich grain at the contact/2DES interface in good con-

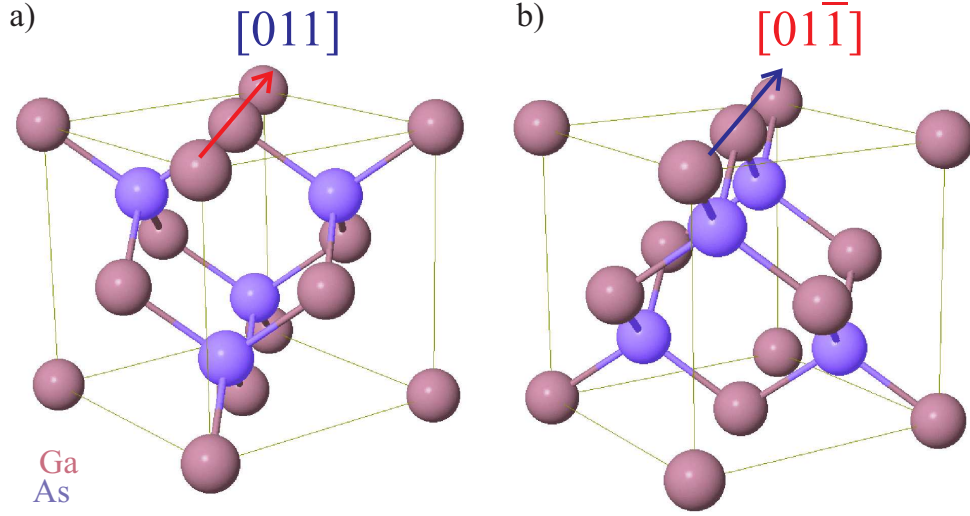


Figure 4.24: Unit cell of the GaAs crystal. The bonds are also indicated. The crystal structure is identical for the good contacting and bad contacting directions. However, the direction of the bonds is different. (a) View in the good contacting direction (b) View in the bad contacting direction. Drawings from <http://emaps.mrl.uiuc.edu/>

tacting direction, the $\text{Al}_\delta\text{Ga}_{1-\delta}\text{As}$ layer is not disturbed till the metal contact interface. That is, there is no out-diffusion of Al in front of the NiGe-rich contact region. 0.3% of the Au, 0.7% Ge and 1.3% of Ni was found in the $\text{Al}_\delta\text{Ga}_{1-\delta}\text{As}$ layer near to the NiGe-rich contact for one of the investigated specimens. However, in another specimen, which also has a NiGe-rich grain at the interface, no Au, Ge and Ni was found within the detection limit of the measurement. We have observed this in good contacting direction. We also investigated a lamella from bad contacting direction which has NiGe rich grain at the contact/2DES interface. In this case we find a similar behavior to what we have observed for Au-rich interfaces. That is, Al diffuses out and Ga replaces it for a certain region in front of the NiGe-rich grains for the contacts in bad contacting direction.

The crystal structure of GaAs is identical in both (good contacting and bad contacting) directions. However, the direction of the bonds are different. The unit cell of the GaAs crystal is depicted in Fig. 4.24. In good contacting ([011]) direction the bonds are directed upward from Ga atoms to As atoms, whereas in the bad contacting ([01 $\bar{1}$]) direction they are directed downward. This anisotropy might cause anisotropic diffusion or out-diffusion of certain type of atoms. Whether it plays a role for the out-diffusion of Al from the $\text{Al}_\delta\text{Ga}_{1-\delta}\text{As}$ layer and for diffusion of Ga into this layer for replacing the Al sites is, however, not easy to say.

4.4 A model for the current injection between alloyed contacts and 2DES

In the light of the findings from the electrical and structural investigations we suggest a model for the current injection mechanism from the alloyed contacts into the 2DES. The model will be based on the results of the electrical and structural investigation on the good contacting direction. We have two different phases at the metal/2DES interface: Au-rich and NiGe-rich regions. These different phases affect a neighboring Al_δGa_{1-δ}As layer in a different way depending on the crystal direction. In front of the Au-rich grains, the GaAs/Al_δGa_{1-δ}As is not extending up to the metal contact as shown in Fig. 4.25 (a). The 2DES is depleted at these regions. This behavior is similar in good contacting and bad contacting directions. In the NiGe-regions the situation is different. The GaAs/Al_δGa_{1-δ}As layer exists to the NiGe-rich contact, as depicted in Fig. 4.25 (b). Since the GaAs/Al_δGa_{1-δ}As heterostructure is reaching NiGe-rich grains without being disturbed, it is reasonable to assume that the 2DES exists to the NiGe-rich interface as depicted in Fig. 4.25 (b). In 4.25 (c) the alloyed contact/2DES interface is depicted. This can be thought of as a snapshot of the elemental map exactly at the depth of 2DES (GaAs/Al_δGa_{1-δ}As interface). The landscape of the 2DES at the contact region is depicted in Fig. 4.25 (d). In front of the Au-rich regions, 2DES is separated from the contact with a depleted region of 50 nm to 150 nm. However, in front of the NiGe-rich grains, the 2DES exist up to the metal interface.

One might think formation of a Schottky-barrier at the contact/GaAs interface. Such a tunneling barrier is depicted in Fig. 4.25 (e). The very weak temperature dependence of the contact resistance support the idea of a tunneling barrier. However, this tunnel barrier must be very high and thin due to lack of temperature dependence and low contact resistance. We have seen that there exist incompressible stripes in front of ohmic contacts revealed by the Hall potential profile experiments on the quantum Hall samples as discussed in Chapter 2. Implication of these results is that there is a variation on the electron concentration in front of the ohmic contacts. The above discussed contact model can also account for these findings. The 2DES is depleted in the Au-rich regions and electron concentration increases towards the bulk and reaches the bulk value far from the contact. Since the 2DES is depleted at the neighboring Au-rich regions the electron density in front of the NiGe-rich regions is also expected to be partially depleted. Therefore, the electron density is expected to be lower than the bulk value. However, it is difficult to model the exact shape and length scale of this depletion.

The distribution of the NiGe grains at the contact and heterostructure interface is similar in both direction. However, the NiGe-rich regions affect the neighboring Al_δGa_{1-δ}As regions differently for the good contacting and bad contacting

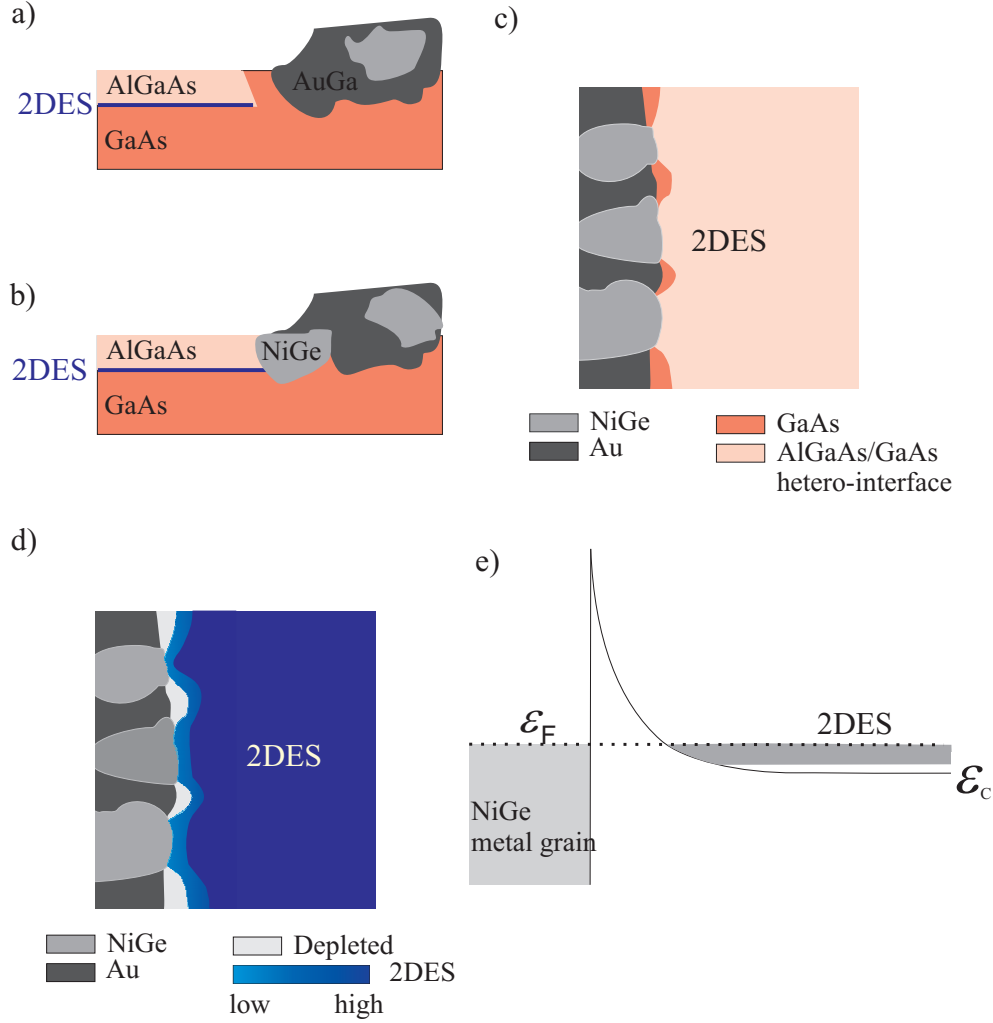


Figure 4.25: (a) The model of the alloyed metal and GaAs/ $\text{Al}_\delta\text{Ga}_{1-\delta}\text{As}$ heterostructures. At the interface two different phases exist. Au-rich phase and NiGe-rich phase. (a) In front of the Au-rich phase, Al diffuses out from the $\text{Al}_\delta\text{Ga}_{1-\delta}\text{As}$ layer and Ga replaces the Al. The width of this Al-free region is between 50 nm to 150 nm. (b) In front of the NiGe-rich grains, GaAs/ $\text{Al}_\delta\text{Ga}_{1-\delta}\text{As}$ exist up to the contact interface. (c) The interface of contacts and GaAs/ $\text{Al}_\delta\text{Ga}_{1-\delta}\text{As}$ at the position of the 2DES. (d) The landscape of 2DES at the contact/heterostructure interface. (e) The Schottky barrier at the NiGe-rich contact and GaAs/ $\text{Al}_\delta\text{Ga}_{1-\delta}\text{As}$ interface. Current injection takes place via tunneling of electrons.

directions. The investigated lamella in the bad contacting direction which had a NiGe-rich grain at the contact/2DES interface showed that in front of the NiGe-rich grain Al in $\text{Al}_\delta\text{Ga}_{1-\delta}\text{As}$ diffuses out, as was the case for Au-rich grains. This

resolves the origin of the observed anisotropy on the contact resistance. In bad contacting direction out-diffusion of Al from neighboring Al_δGa_{1-δ}As layer happens in front of the Au-rich and NiGe rich phases. That is, in bad contacting direction 2DES separated from the metal contact with a depleted region of 50 nm to 100 nm. Therefore, there is no electrical connection between the metal contact and 2DES. This is reasonable as the most of the contacts fails to work which is revealed by electrical characterization of the TLM structures. Rarely, only one or just a few NiGe-rich grains might have a direct contact to the 2DES. This must be the case since some of the contacts in bad contacting direction work but have very high contact resistance values. However, the anisotropic behavior is less pronounced for the shallow lying 2DES. The reason for this needs to be investigated.

Confirmation of the above proposed contact model might be possible with the scanning probe experiments. If a deeper lying heterostructure is used for the experiments the density profile of the 2DES will be quite different in good contacting and bad contacting direction. In the quantum Hall conditions, the positions and the width of the incompressible stripes will depend on the density profile. It should be possible to detect the modulation of the position and the width of the incompressible stripes in front of the contacts. In good contacting direction the modulation in the position of the incompressible stripes can be difficult to detect, since the depleted and not depleted regions change very frequently (about 100 nm to 500 nm). One might detect a smooth position and average width for the incompressible stripes in front of the contacts in good contacting direction. However, in bad contacting direction there will be only a few grains at the interface without depletion and one might be able to detect the modulation on the position and the width of the incompressible stripe in front of the contacts.

4.5 Summary

In this chapter a contact recipe is investigated and discussed in details. Transmission line method measurements were performed to characterize the contact resistance between the alloyed contact and 2DES. The structural investigation of the alloyed contact are performed using SEM, TOF-SIMS, TEM, STEM and EDX.

From the electrical characterizations the following results have been found:

- The value and reproducibility of contact resistance depends on the underlying crystal direction. In [011] (*good* contacting) direction, no contact failure happens (100% yield), the contact resistance values are reproducible and low resistive. In [01 $\bar{1}$] (*bad* contacting) direction the contact resistance values are not reproducible and most of the contacts do not conduct at all.

- Several heterostructures were investigated. The values of the contact resistance in good contacting direction for different heterostructures were found to be between 3.2Ω and 8.5Ω for a $100 \mu\text{m}$ of border length.
- The difference between the good contacting and bad contacting direction becomes less pronounced for shallow lying 2DESs. For the heterostructures which have 2DES 120 nm and 86 nm underneath the surface, contacts mostly do not work in bad contacting direction. For the heterostructures which have 2DES 50 nm below the surface, the percentage of the working contacts is comparable in both directions (no contact failure). However, the contact resistance is still not reproducible and has a large spread. For the heterostructures that have a 2DES depth of 40 nm, no contact failure happens and the contact resistance becomes comparable in both directions.
- In good contacting direction, the contact resistance generally scales with the border length between the contact and heterostructure.
- In good contacting direction contacts work down to $1 \mu\text{m}$ mesa width. The contact resistance values on $1 \mu\text{m}$ length scale are still quite reproducible. In bad contacting direction, for the deeper lying 2DES the contacts mostly do not work. However, for the shallow lying heterostructure contacts work down to $1 \mu\text{m}$ mesa width. For the heterostructures which have a 2DES 40 nm below the surface the contact resistance values are comparable in both directions down to $1 \mu\text{m}$.
- The dependence of the contact resistance on temperature is very weak. The increase in the contact resistance from 1.5 K to 25 mK is about 0.7Ω for a border length of $100 \mu\text{m}$. This very weak temperature dependence implies a current injection mechanism via a tunneling barrier.
- The effect of the contact quality for the QHE measurement were also investigated. QHE measurements on a deeper lying heterostructure shows that when the contacts which are defined in bad contacting direction used for the QHE measurements, the accuracy of plateau is lost. This is in agreement with the measurement of F. Dahlem [29].

From the structural investigations:

- The alloyed Au/Ge/Ni ohmic contacts have mainly two phases. NiGe-rich (mainly Ni_2GeAs) grains are surrounded by Au-rich (mainly Au_4Ga) regions.
- The $\text{Al}_\delta\text{Ga}_{1-\delta}\text{As}$ layer underneath the contact region is mainly consumed during the alloying process. There are some remnants of this layer but one

can not speak about the presence of a 2DES underneath the contact region. This is consistent with the electrical characterization measurements, since the contact resistance scales with the border length between the contact and heterostructure.

- A thin layer of Al-rich region is present at the top of the contacts. This was confirmed by the TOF-SIMS and EDX analyses independently. However, this must be a porous layer, since we did not detect any insulating layer on top of the contact from the electrical characterization of the contacts.
- The amount of Au-rich and NiGe-rich grains at the contact and 2DES interface is roughly the same. This is similar in both directions.
- At the contact/Al_δGa_{1-δ}As interface two different behavior is observed. When there is a Au-rich region, Al in the Al_δGa_{1-δ}As layer diffuses out and Ga replaces it. There is a region of GaAs between the Au rich contact and Al_δGa_{1-δ}As. A few percent of Au (up to 4%) is found in this region. Au is a p-type dopant in GaAs. The width of this region is between 50 nm to 150 nm. 2DES is depleted in this region. When the contact region at the interface is NiGe-rich, Al_δGa_{1-δ}As continuously exists up to the NiGe-rich contact region. Therefore, the 2DES exists up to the metal region.
- Based on these findings a model for the current injection mechanism between the alloyed Au/Ge/Ni contact and 2DES is proposed. A Schottky-barrier is assumed to form at the interface between the NiGe-rich contact and the Al_δGa_{1-δ}As layer. Current injection takes place via tunneling of electrons through this tunneling barrier.
- The origin of the observed anisotropy on the contact resistance between good contacting and bad contacting direction is also clarified. Contrary to good contacting direction, Al seems to diffuse out from the Al_δGa_{1-δ}As layer in front of the NiGe-rich regions in bad contacting direction. This seems to be the reason for the observed difference in contact resistance between good contacting and bad contacting direction. However, the reason for why this anisotropy is not present for the shallow lying heterostructures needs to be investigated.

Chapter 5

Alloyed contacts to 2DES on submicron scale

One of the main motivation of this work was to make small Corbino devices as discussed in Chapter 3. To achieve this goal we need to make small contacts. We manage to make small contacts to 2DES down to a contact diameter of $0.2 \mu\text{m}$. The preparation and the properties of *submicron* scale ohmic contacts will be the topic of this chapter.

In section 5.1 the description of the samples will be given. Then the measured contact resistance at liquid He temperature and room temperature for the circular and square contacts will be given in section 5.2. In section 5.3 we will have a look at the properties of these contacts at very low temperatures and finite magnetic fields. We have also investigated structural properties of small contacts. The cross-sectional SEM images of two submicron scale contacts will be shown in section 5.4.

5.1 The sample

To investigate small ohmic contacts to 2DES we have prepared samples with circular and rectangular shaped ohmic contacts, diameter/length ranging from $0.2 \mu\text{m}$ to $5 \mu\text{m}$ (in some samples $10 \mu\text{m}$). The contact recipe is the same as described in Chapter 4.1.1 but the contact areas were prepared by electron beam lithography (EBL). The preparation details can be found in Appendix G.

Here we will give some explanations about the sample which will be helpful to understand the data presented in this chapter. The sketch of the sample is shown in Fig. 5.4 (a). There are four identical devices (sometimes more than four) on the same sample. To make it clear, four identical devices are defined on the same piece of the heterostructure, what we call sample, and each of these four device

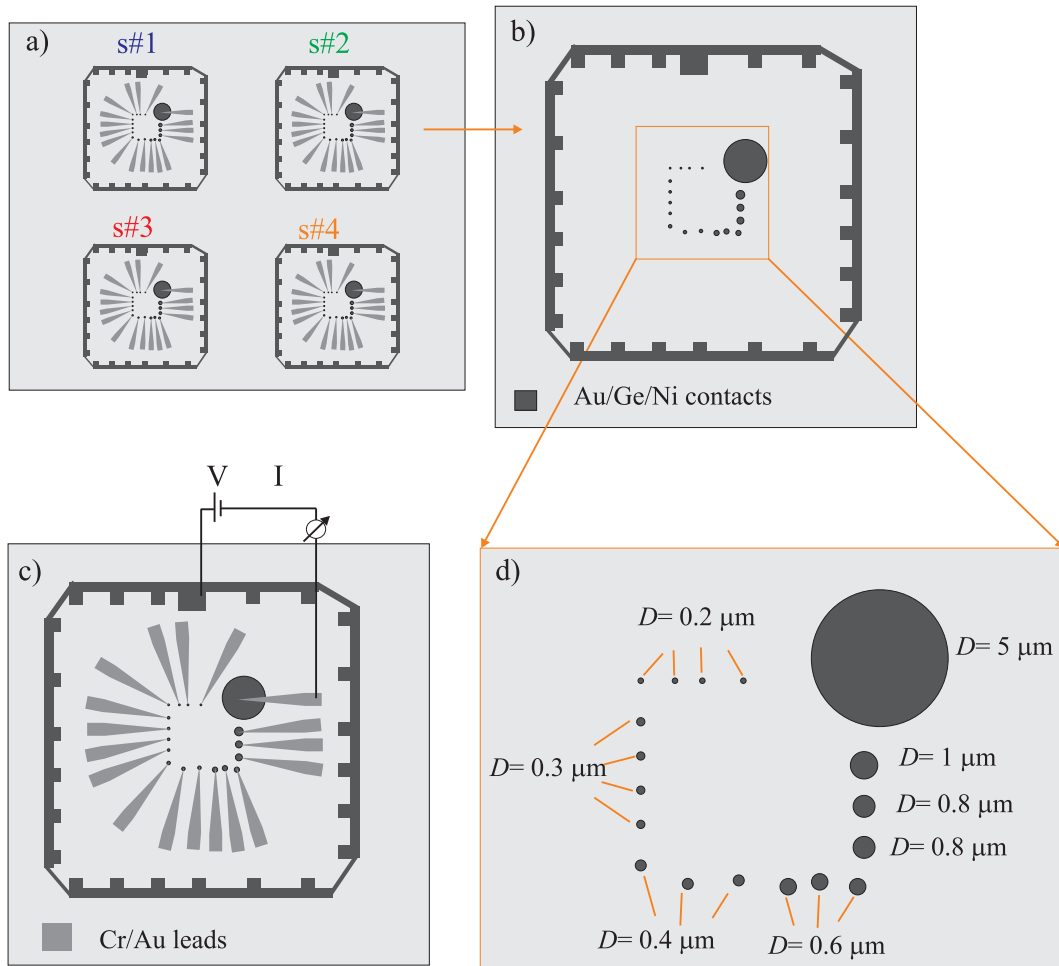


Figure 5.1: (a) The sketch of the sample. There are four identical structures. Ohmic contacts are defined in the first lithography step, then alloyed. The outer circulating stripe is an ohmic contact. Small contacts are in the mid field of structure as shown in (b). (c) Cr/Au leads for the bond wires are deposited in the second lithography step. (d) The mid field of structure from (b). The diameter of the contacts are given.

will be named as structure. We will use s#1 for the 1st structure on the sample and s#2 for the 2nd structure and so forth. The sample is named after the wafer

which is used together with a number to distinguish samples from the same wafer. However, it is important to keep in mind that all of these structure on the same sample (piece of heterostructure) undergo in parallel the same process, that is, cleaning of the sample, evaporation of the metal layers and alloying.

A sketch of one of the structures is shown in Fig. 5.1 (b). To determine contact resistance more accurately, structures are prepared in a quasi Corbino configuration; that is, there is a outer circulating ohmic contact, and small ohmic contacts are placed in the mid region of the sample. The mid field of the device is shown in Fig. 5.1 (c). This particular configuration ensures an isotropic electric field around the inner contact. This reduces the error in the contact resistance determination. The outer ohmic contacts is made meander-like to have good contacting direction available in all sides, to ensure a good contact to 2DES. To make electrical connection to the ohmic contacts, Cr/Au bond pads have been defined on the top of the contacts, connecting them to wide regions for bond wires as shown in Fig. 5.1 (d). Two-point measurements are performed by taking one of the inner contacts (drain lead) and measuring it with respect to the outer contact (source lead) as depicted in Fig. 5.1 (c). A scanning electron microscope (SEM) image of such a structure is shown in Fig. 5.2 (a). The scanning electron microscope image is taken after transport measurements, therefore, bonding wires are also present. An SEM image of the inner field of the structure, where the small contact are present, is shown in Fig. 5.2 (b). There are some additional small contacts which were not connected to any of bond pads. These are meant for SEM images. An SEM image of one of the small contact is shown in the inset of the Fig. 5.2 (b).

Since we want to extract the contact resistance it is necessary to know the contribution of the 2DES to the measured resistance. To get an approximate value for the resistance of 2DES one can approximate the structure in Fig. 5.1 (b) to a Corbino device and calculate the resistance. We will assume a Corbino device with the inner radius r_i and the outer radius r_o . In polar coordinates the current density is

$$j_r = \sigma_{rr} E_r \quad , \quad (5.1)$$

where $\sigma_{rr} = \sigma_{xx}$ is the radial (longitudinal) conductivity. For a homogenous current distribution and a total current I_r

$$j_r = \frac{I_r}{2\pi r} \quad . \quad (5.2)$$

The radial electric field at the radius r is

$$E_r = \frac{1}{2\pi\sigma_{rr}} \frac{I_r}{r} \quad (5.3)$$

and the voltage difference V_{DS} between the contact is

$$V_{DS} = \int_{r_i}^{r_o} E_r dr = \frac{\ln(r_o/r_i)}{2\pi} \frac{I_r}{\sigma_{rr}} \quad . \quad (5.4)$$

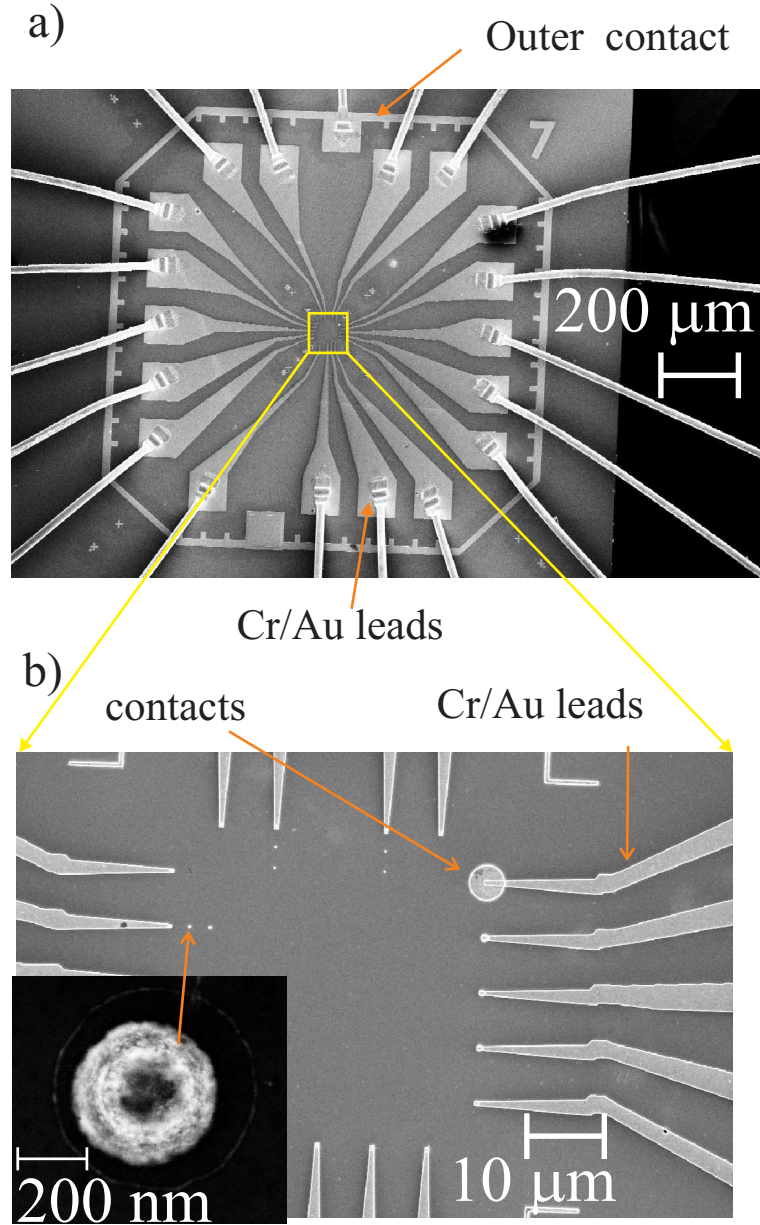


Figure 5.2: (a) The SEM image of one of the structures. (b) SEM image of the inner field of the structure. In the inset, small contacts are visible in the middle of the structure which are not connected to any of the leads. The scale bars is indicated for each of SEM images.

Finally we can find the resistance following Ohm law,

$$R = \frac{V_{DS}}{I} = \frac{\ln(r_o/r_i)}{2\pi} \rho_{rr} \quad . \quad (5.5)$$

Here we used $\sigma_{rr} = 1/\rho_{rr}$ where $\rho_{rr} = \rho_{xx}$ is the radial (longitudinal) sheet resistivity. The formula (5.5) will be used to calculate the resistance of the 2DES whenever it is necessary.

5.2 Alloyed contacts to 2DES on submicron scale at liquid He and room temperature

In Fig. 5.3 (a) current-voltage characteristics for a few contacts are shown. All contacts have an ohmic behavior. The measured two-point resistance versus diameter of the contacts for the circular contacts is shown in Fig. 5.3 (b). The wiring resistance of the measurement apparatus is subtracted. The measured value of the resistance is the sum of the contact resistance due to outer contact, the inner contact and the resistance of 2DES. The value of the contact resistance extracted from TLM measurements for this heterostructure is $r_c = 0.3 \Omega \cdot \text{mm}$. The perimeter of the outer contact is larger than 1 mm. Therefore, contact resistance of the outer contact is less than 1 Ω and is negligible. The value of the sheet resistivity extracted from the TLM measurements for this heterostructure is $\rho_s = 25 \Omega/\square$ and can be used in (5.5) to estimate the contribution of the resistance from the 2DES. The contribution of the 2DES is 20 Ω and 33 Ω for the smaller contacts ($D = 0.2 \mu\text{m}$) and for the largest contact ($D = 5 \mu\text{m}$), respectively. These values are significantly smaller than the measured values. Therefore, the largest contribution in measured resistance in Fig. 5.3 (b) is due to the contact resistance of the inner contact.

The contact resistance of 2 k Ω for the smallest contacts of diameter of 0.2 μm is obtained. Taylor et al. [63] reported small contact of diameter of 0.5 μm with a contact resistance of 5 k Ω . With our contact recipe smaller contacts with lower contact resistance are realized. A few of the small contacts have a contact resistance larger than 10 k Ω . However, most of submicron contacts have a contact resistance below 10 k Ω . In Fig. 5.3 (c) the normalized contact resistance to the unity length 1 μm is shown. In order to obtain more accurate results the above calculated values of resistance of 2DES is subtracted. Normalization is done by multiplying contact resistance by perimetry of the contact,

$$r_c = R_c \cdot (\pi D) \quad , \quad (5.6)$$

for circular contacts and

$$r_c = R_c \cdot (4L) \quad , \quad (5.7)$$

for square contacts, where $D(L)$ is the diameter (length of one border) of the contact. As clearly visible, for the most of contacts the normalized contact resistance lies between 0.5 k $\Omega\mu\text{m}$ and 10 k $\Omega\mu\text{m}$. The normalized contact resistance

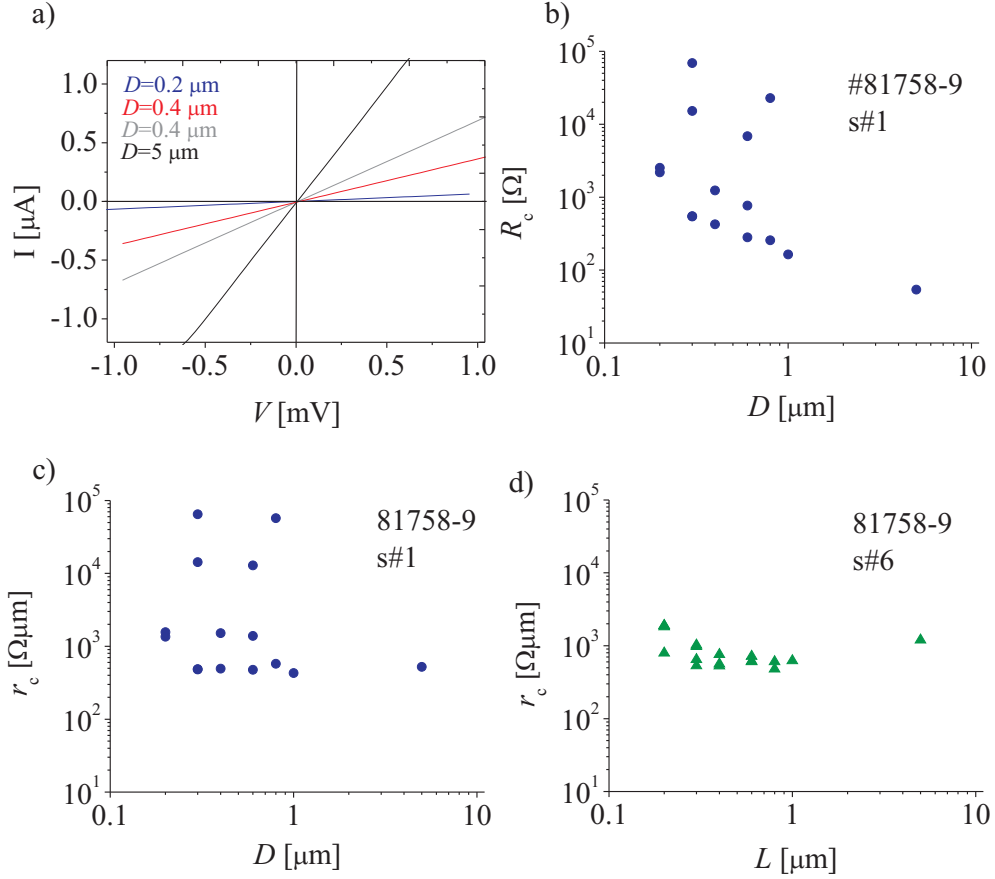


Figure 5.3: (a) The current-voltage data for some of the contacts. The I-V data are taken between any of the small contacts and the outer large contacts as depicted in Fig. 5.1(c). (b) The measured contact resistances derived from the two-point I-V measurement after subtracting wiring resistances. The outer contact is common contact for all the two point measurements. The contact resistance of the outer contact is negligible. Contribution of two-dimensional electron system resistance is about 20Ω for the largest contact and 33Ω for the smallest contacts. (c) Normalized contact resistance to unity length $1 \mu\text{m}$. Normalization was done after subtracting the 2DES resistance. Normalization was done by multiplying contact resistance by the perimeter of the contact according (5.6) and (5.7). (d) Normalized contact resistance to unity length $1 \mu\text{m}$ for square contacts. The resistance of 2DES is subtracted. All measurements are performed at liquid Helium temperature.

is about $0.5 \text{ k}\Omega\mu\text{m}$ for the larger contacts. This value is slightly larger than the contact resistance ($0.3 \text{ k}\Omega\mu\text{m}$) measured on the TLM samples for this wafer. However, if one take the anisotropy of the contact resistance into account this is not a large deviation. For the small contacts a normalized contact resistance as low as $0.5 \text{ k}\Omega\mu\text{m}$ is also obtained. This implies a very good contact quality. In Fig. 5.3 (d) the normalized contact resistance for the square shaped contacts is shown. L is the length of one border of the contact. For the square contacts the normalized contact resistance is mostly about $0.6 \text{ k}\Omega\mu\text{m}$. The largest contact with the edge length of $5 \mu\text{m}$ has a higher contact resistance. This higher contact resistance for larger contacts is surprising. However, as we will see later the spread of the contact resistance for the larger contacts can be really large. The spread in the contact resistance for square contacts is smaller compared to the circular contacts. However, as we will see later that is mostly the case but not always.

In Fig. 5.4 (a) measured resistance as a function of the diameter of contacts is plotted for three structures on the same sample (sample #81758-9). As we already described the concept of the sample and structures in the previous section, here it will be just mentioned that the same sample (indicated with the number of heterostructure in the figures) means that all structures (s#1,s#2,...,s#6) have seen the same process steps (cleaning, evaporation, alloying ...) during the preparation. Here we neglect the contact resistance due to the outer contact. Since the resistance of 2DES is smaller than the measured values we simply neglect it and call the measured resistance as contact resistance. As clearly visible, the spread in the contact resistance is large for small contacts. The spread in the measured contact resistance values for the large contacts ($D = 5 \mu\text{m}$) is also relatively large. This is also the case for the square shaped contacts as shown in Fig. 5.4 (b). The square contacts and circular contacts are from the same sample. The spread for the square contacts seem to be smaller. In Fig. 5.4 (c) contact resistance versus diameter of the contacts is shown for the wafer # 81628. For these wafer the spread in the contact resistance for the large contacts is also observed. Such a large spread in the contact resistance for larger contacts is unexpected. For the TLM structures characterized for this wafer the contact resistance was quite reproducible in this scale in good contacting and in bad contacting directions as discussed in Chapter 4. Therefore, the origin of the large spread even for large contacts is not quite clear.

In Fig. 5.5 the statistical data for the yield of contacts as a function of the diameter D (the length of one border L) for the circular contacts (for the square contacts) is shown. Dark gray represents the number of the contacts in the sample. Light gray represents the number of working contacts. When we say a contact is not working that means a current was not measurable through the contact on the detection range of the measurements apparatus. That is the contact resistance is

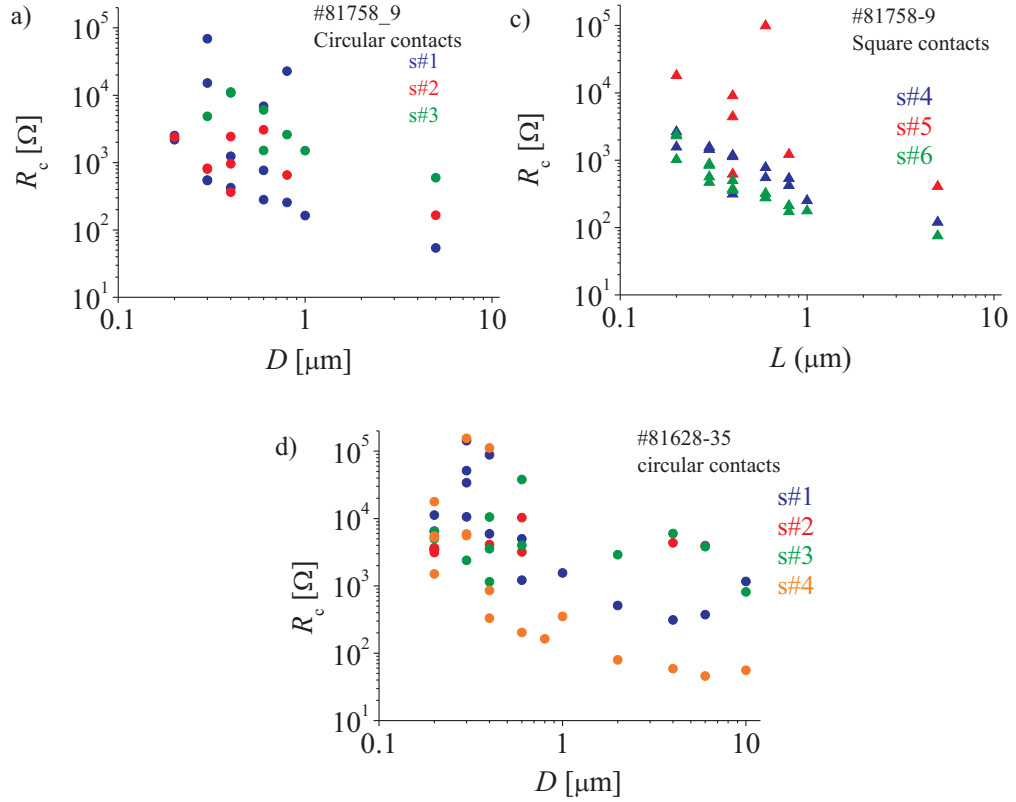


Figure 5.4: a) The measured contact resistances for (a) circular contacts (s#1,s#2,s#3) and (b) square contacts (s#4,s#5,s#6). The sample is from the wafer #81758. Circular (s#1, s#2, s#3) and square contacts (s#4, s#5, s#6) were on the same sample. (c) The same measurements on another sample from wafer #81628. s#1, s#2, s#3, s#4 are all in the same sample. Contacts are circular shaped. Measurements are performed at 4 K.

larger than 10 MΩ. In Fig. 5.5 (a) and (b) the statistics for the heterostructure #81758 (depth of 2DES is 50 nm) are shown. The percentage of the working contacts is quite high. For the circular contacts, 3 out of 12 contact working for the smallest contact diameter of 0.2 μm (25%). For the square contacts 8 contacts out of 12 were working (75%). If we compare circular and square contacts the percentage of the working contacts seems to be higher for the square contacts. In Fig. 5.5 (c) the statistics for the heterostructure #81628 (depth of 2DES is 40 nm) is shown. For this wafer the percentage of working contacts is about 85% (14 out of 16) for the smallest contact diameter of 0.2 μm. The percentage of the working contacts in the small scale is higher for the smaller 2DES depth. Overall

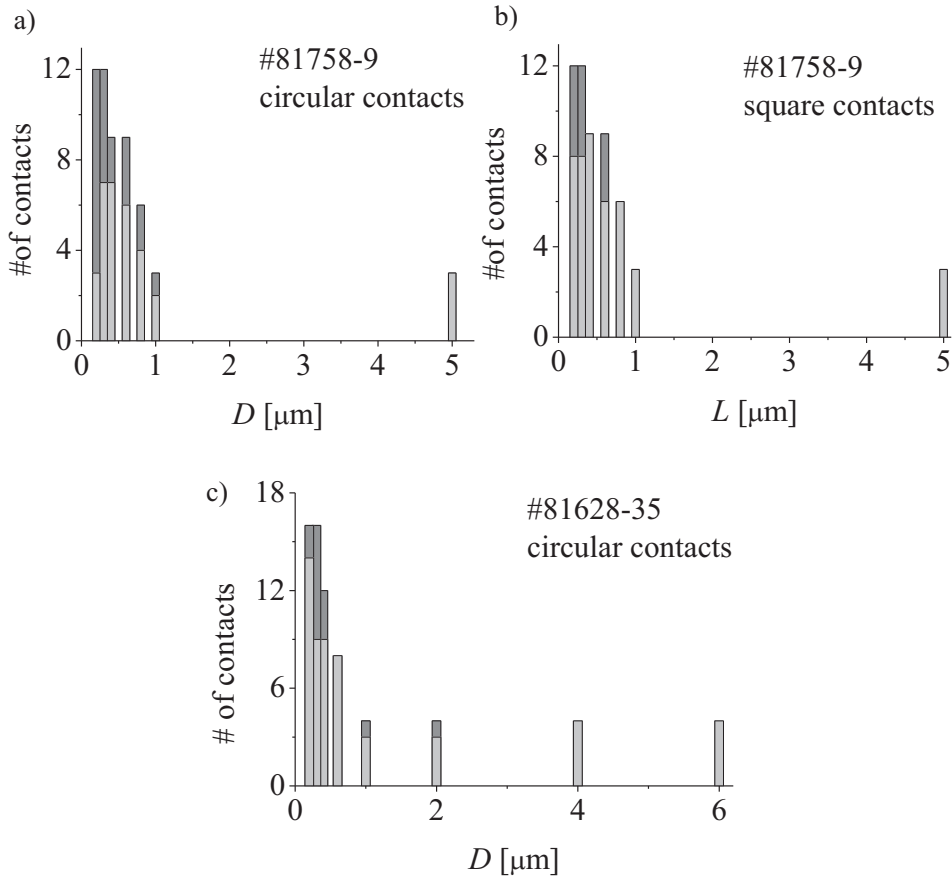


Figure 5.5: (a) The yield of working contacts as a function of diameter/length. Dark gray shows number of contacts on the sample. Light gray represents number of the working contacts. (a) Circular contacts on the wafer #81758. (b) Square contacts on the wafer #81758 (c) Circular contacts on the wafer #81628.

the percentage of the working contacts is quite high for contacts in submicron scale for both heterostructure. Some of the contacts which have diameter larger than $1 \mu\text{m}$ also did not work. The failure of large contacts is surprising. We did not observe any contact failure on the TLM structures for these wafers down to $1 \mu\text{m}$ as discussed Chapter 4. One reason for this can be that in the TLM structures the contact dimension was always large ($100 \mu\text{m} \times 100 \mu\text{m}$) even for small mesa width. However, here for small contacts the contact area is small therefore amount of the alloyed material is less and that might play a role.

Another interesting outcome of our experiments is that the effect of thermal cycling the sample on the contact resistance and on the yield of working contacts. The measured contact resistance at room temperature before and after cooling the

sample to liquid He temperatures is shown in Fig.5.6 (a). Here the contribution of 2DES at room temperature in the measured resistance is around 0.7 k Ω for the largest contact ($D = 10 \mu\text{m}$) and around 1.4 k Ω for the smallest contacts ($D = 0.2 \mu\text{m}$). These values are calculated from (5.5) using the sheet resistivity value of $\rho_s = 1.1 \text{ k}\Omega/\square$ extracted from room temperature measurements. All the contacts have a contact resistance around 250 k Ω for the first room temperature measurement. When the sample is cooled in liquid He a few of the contacts are working as shown in Fig.5.6 (b) (red points). After taking sample to room temperatures we have measured the resistance values again. The contact resistances are in the range of a few k Ω for the most of the contacts as shown in Fig.5.6 (a)(blue points). If we subtract the 2DES resistance then for the largest contact, the contact resistance is between 1k Ω to 10k Ω . For the small contacts, the contact resistance is ranging from 1 k Ω to a few ten k Ω s. For some of the contacts contact resistance do not decrease and stay around 250 k Ω as before. If the sample is cooled in the liquid He once again, almost all the contacts, which were low resistive (less than 100 k Ω) at room, works at the low temperature. Therefore, the percentage of the working contacts is higher in the second cooling. The contact resistance values of the contacts which were already working in the first cooling generally are lower in the second cooling. For instance the largest contact with diameter of 10 μm has a contact resistance larger than 3 k Ω in the first cooling and about 0.8 k Ω in the second cooling. The interesting outcome of these experiments implies that strain can be a mechanism hindering formation of contact at the contact/2DES interface. The thermal expansion coefficient of Au, Ni, Ge, GaAs, and $\text{Al}_\delta\text{Ga}_{1-\delta}\text{As}$ are 14, 5.7, 13, 6.4 and $6.1 \times (10^{-6}\text{K}^{-1})^1$, respectively. These values are for high temperatures but nevertheless give an idea. The values of thermal expansion coefficient for Au and Ni are large compared to GaAs and $\text{Al}_\delta\text{Ga}_{1-\delta}\text{As}$. This difference in the volumetric expansion might result in the rearrangement of the strain at the interface. During the cooling-down and warming-up process the induced strain at the interface might relax. This might reduce the strain induced depletion and a ohmic contact might form at the interface.

5.3 Submicron scale ohmic contacts at very low temperatures and strong magnetic fields

In this section we will have a look on the behavior and quality of the small contacts at very low temperatures (in miliKelvin range) and in high magnetic fields. Measurements presented in this section are performed in a $^3\text{He}/^4\text{He}$ dilution re-

¹The values of thermal expansion coefficient for GaAs, and $\text{Al}_\delta\text{Ga}_{1-\delta}\text{As}$ are taken from Adachi et al. [75], for the metals the values are taken from wikipedia

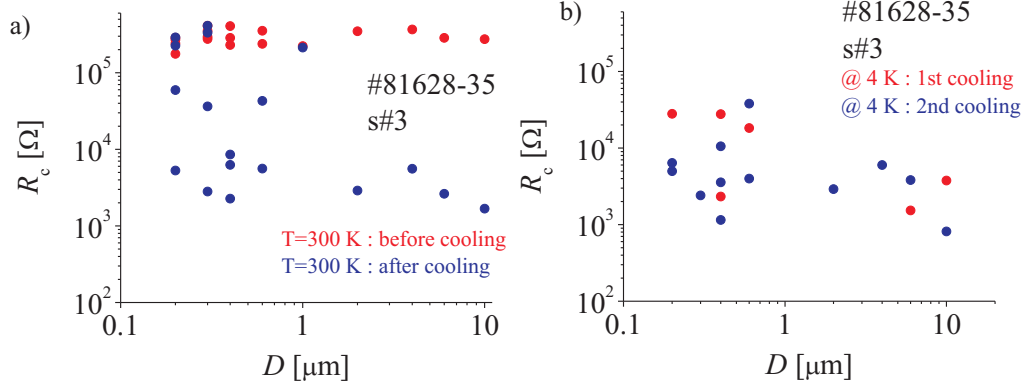


Figure 5.6: (a) Measured resistance values at room temperatures for circular contacts. The contribution of resistance of 2DES is around $0.7 \text{ k}\Omega$ for the largest contact and around $1.4 \text{ k}\Omega$ for the smallest contacts. The resistance is measured before (red points) and after (blue) cooling the structure to liquid He temperature. Before cooling the structure to liquid He, contacts resistance is about $250 \text{ k}\Omega$ for all the contacts. After cooling structure to liquid He and warming it up to room temperature, most of the contacts have lower contact resistance (blue points). (b) The resistance values measured at liquid He for the consequent cooling. In the first cooling a few contacts work. In the second cooling most of the contacts work.

frigerator at 30 mK. The sample is a quasi-Corbino sample similar to one which is shown in Fig. 5.1. The two terminal measurements done by applying voltage between one of the inner contact and the outer circular contact. The measured differential conductance as a function of bias voltage is shown in Fig. 5.7(a) for some of the contacts.

The measured differential conductance value generally stay constant. There is a very slight nonlinearity around zero bias for some of the contacts ($D = 0.4 \mu\text{m}$). The measured conductance does not scale with the diameter of the contacts. However, as we have already seen the contact resistance for large contacts can be higher than that of small contacts (see Fig. 5.4). In Fig. 5.7 (b) conductance as a function of magnetic field is shown for some of the contacts. Here the dc bias is zero; only a small ac excitation (about $2 \mu\text{V}$) is applied to the inner contact. Expected Shubnikov-de Haas oscillations are visible. The period of the Shubnikov-de Haas oscillations are the same for all measured contacts. This implies that a homogenous 2DES exist around the contacts. At zero magnetic fields the contact resistance dominates. As the magnetic field is increased the resistance of 2DES increases and dominates the measured conductance. Conductance for the higher magnetic fields is shown in Fig. 5.7 (c). The conductance for the magnetic field values larger than 4 T is shown in the inset of figure Fig. 5.7 (c). After $B = 5 \text{ T}$

no conductance is measurable for contact with $D = 0.3 \mu\text{m}$. Two contacts with $D = 0.4 \mu\text{m}$ were measured at high magnetic fields. The one which has larger conductance (lower contact resistance) at zero magnetic field has a finite conductance at higher magnetic fields ($B > 5T$). No conductance is measurable for the contact which has a smaller conductance (higher contact resistance) at zero magnetic field. We will refer this experiments in the next chapter to compare them with the

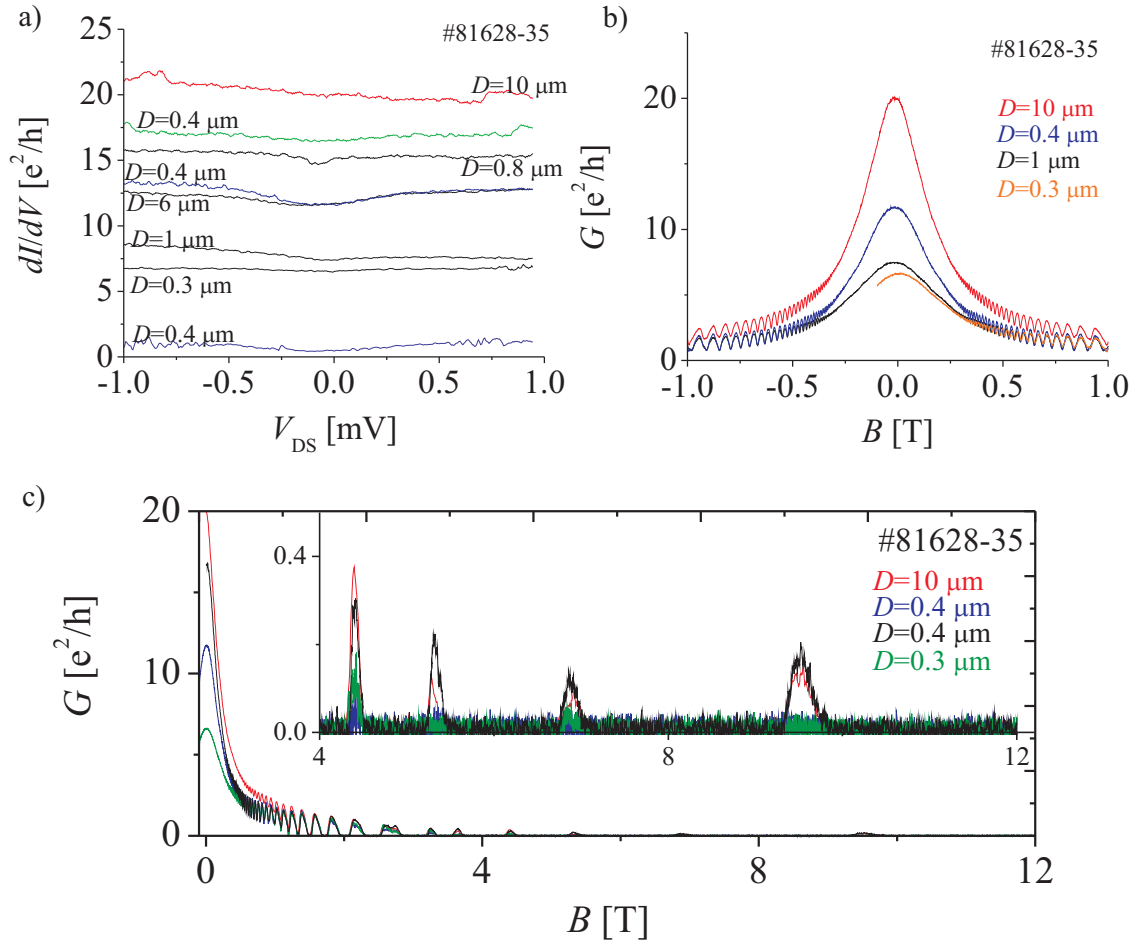


Figure 5.7: (a) Differential conductance versus bias voltage at $T = 30\text{mK}$ and zero magnetic field. Sample is a quasi-Corbino sample and similar to one which is shown in Fig. 5.1 (a) and (b). The two terminal measurements are performed by taking the outer contact as reference contact. (b) Conductance measured as a function of perpendicular magnetic field for some of the contacts. An ac excitation of $2\mu\text{V}$ is applied. No dc bias is applied. (c) Conductance measured for a wide range of magnetic field for some of the contacts. Conductance for the higher magnetic field side is shown in the inset.

submicron scale Corbino devices. From the $1/B$ periodicity of the Shubnikov-de Haas oscillation one can extract the density of electrons in the 2DES,

$$n_s = \frac{e}{h} \frac{g_s}{\Delta(1/B)} \quad (5.8)$$

Electron density is $n_s = 5.5 \cdot 10^{15} \text{ m}^{-2}$ and Fermi energy is $\varepsilon_F = 19.5 \text{ meV}$. Magnetic field at which filling factor is one is, $B_{\nu=1} = 22.4 \text{ T}$.

5.4 SEM study of submicron scale ohmic contacts

In Fig. 5.8 cross sectional SEM images of two submicron contacts are shown. The white encapsulated regions are alloyed ohmic contacts. The back going metallic stripe is a Cr/Au lead connecting the contact to the bonding pad for wiring to measurements setup (see Fig. 5.1). The sketch of the contact, Cr/Au lead and etched area is shown in the inset of figure. The transparent blue area is etched away in a FIB. Then the cross sectional SEM images are taken.

The orange lines indicate the position of the 2DES in the heterostructure. The sample has been characterized at liquid He temperatures before SEM images are taken. The SEM image which is shown in Fig. 5.8 (a) belongs to contact which does not have an electrical contact to the 2DES. The SEM image which is shown in Fig. 5.8 (b) belongs to a contact which has an electrical contact to the 2DES with a contact resistance value of about 6 k Ω . However, both SEM images seem quite similar. Both contacts penetrate deep into heterostructure that goes deeper than the depth of the 2DES. From the contrast of SEM image it seems that we mainly have Au rich region at the contact/2DES interface. However, it can be that there is a NiGe rich grain at the back side or at etched front side. We did not have

Caption for the Fig. 5.8: Cross sectional SEM images of two small contacts are shown. Alloyed ohmic contacts are encapsulated with white circles. The back going metal is a Cr/Au lead connecting the contact to a bond pad for wiring (see Fig. 5.1). The ohmic contact and Cr/Au metals are depicted in the inset. The transparent blue indicated area is etched away in a FIB and cross-sectional SEM images are taken afterwards. Heterostructure is #81628 and measured contact resistance values for this heterostructure are shown in Fig. 5.4 (c). (a) Cross sectional SEM image of a contact which was not working at low temperatures. 2DES depth is 40 nm. The orange lines show the position of the 2DES at the heterostructure. (b) Cross sectional SEM image of a contact which was working at low temperatures. As clearly visible, in both cases the alloyed contacts penetrate deep into the 2DES. However only one of the contact has electrical connection to the the 2DES.

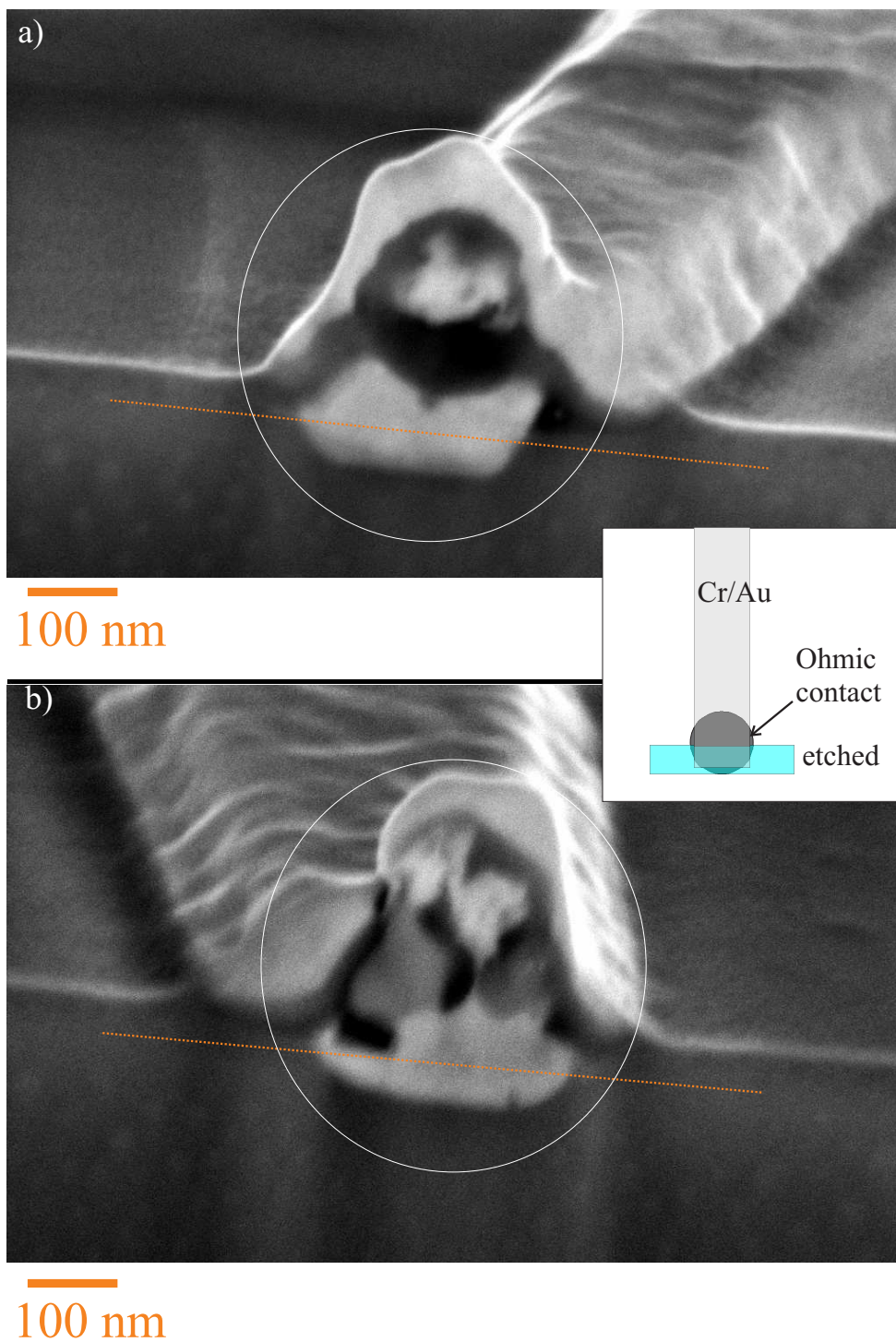


Figure 5.8: (Caption is in the previous page)

a chance to investigate these small contacts with transmission electron microscope. Therefore we do not know how the $\text{Al}_\delta\text{Ga}_{1-\delta}\text{As}$ layer look like around the contact. However, this SEM images show that just penetration of contact material into the heterostructure is not sufficient for formation of ohmic contacts. Additional SEM images for small contacts are presented in Appendix H.

5.5 Summary

In this chapter electrical and structural properties of submicron scale alloyed ohmic contacts have been discussed.

- Alloyed contacts to 2DES as small as $0.2 \mu\text{m}$ have been realized. Contacts are prepared in circular and square shape. Contacts work down to a diameter (edge length) of $D = 0.2 \mu\text{m}$ ($L = 0.2 \mu\text{m}$).
- Contacts have a linear I - V characteristic, i.e. show an Ohmic behavior.
- Contact resistance for the smallest contact of $D = 0.2 \mu\text{m}$ ($L = 0.2 \mu\text{m}$) ranges between $1 \text{ k}\Omega$ to $100 \text{ k}\Omega$ at 4 K .
- Normalized contact resistance to unity length $1 \mu\text{m}$ for submicron contacts can be as low as $0.5 \text{ k}\Omega\mu\text{m}$.
- For the smallest circular contacts ($D = 0.2 \mu\text{m}$), the yield was 25% for the heterostructure with depth of 2DES 50 nm . For the heterostructure with depth of 2DES 40 nm , the yield was about 85% for the smallest contacts. The average yield for the working contacts is more than 50% for submicron scale ohmic contacts, for both heterostructures.
- The cooling of samples to liquid He temperatures has a drastic effect on the contact resistance. Before cooling samples to liquid He temperatures for the first time, contact resistance is around $250 \text{ k}\Omega$. At the first cooling a few of contacts work. Then after warming up sample to room temperature, most contact which had $250 \text{ k}\Omega$ of contact resistance before cooling, now have a low contact resistance ranging from $1 \text{ k}\Omega$ to a few $10 \text{ k}\Omega$. Cooling sample for the second time to liquid He, all the contacts which have contact resistance less than $100 \text{ k}\Omega$ work at low temperature. The contacts which were working in the first cooling have generally lower contact resistances in the second cooling. We attribute this this effect to relaxation of strain at the contact heterostructure interface.
- The conductance measurement at very low temperatures (30 mK) exhibits a very slight nonlinearity for some of the small contacts.

- The conductance measurements at high magnetic fields shows that the contacts are not isolated from the 2DES. Generally a finite conductance is measurable up to 12 T.
- Cross-sectional SEM images of two submicron contacts are shown, one for a working contact and one for a not working contact. In both cases, the contact material penetrates deep into the heterostructure, deeper than the 2DES depth. This shows that penetration of contact material into heterostructure to depth of the 2DES is not sufficient for the formation of ohmic contact between alloyed metal and 2DES.

Chapter 6

Observation of a zero bias anomaly and positive magneto conductance increase at small magnetic fields on submicron Corbino devices

On the previous chapter we have seen that we are able to contact 2DES down to a contact diameter of $0.2 \mu\text{m}$. We have prepared several Corbino devices with inner contact diameter as small as $0.2 \mu\text{m}$ and outer contact diameter ranging from $0.5 \mu\text{m}$ to $1.5 \mu\text{m}$. As we characterized our devices at low temperatures at zero magnetic field we have observed a huge conductance dip at zero bias. The dip disappears with the increasing temperature. As we will see in this Chapter, the presence of a small magnetic field suppresses the zero bias dip partly.

In the first part, in section 6.1, we will introduce the device geometry and fabrication process. In section 6.2.1 we will shortly introduce the available theoretical work for magneto-conductance in ballistic Corbino devices. Then the bias dependent differential conductance measurements at low temperatures which exhibits an anomalous zero bias dip will be presented in section 6.2.2. The temperature dependence of the zero bias dip will be presented in the same section.

A small magnetic field result in a positive magneto-conductance increase as will be shown in section 6.2.3. Temperature dependence of the positive-magneto conductance will be presented in the same section. The possible scenarios for the observed phenomena will be discussed in section 6.3. The differential conductance versus bias voltage shows an asymmetric behavior for some of the devices as will be presented in section 6.4. We have measured the electrochemical potential be-

tween the leads of the Corbino as the magnetic field is swept. We have found an unusual dip at zero magnetic field. This unusual behavior observed only at very low temperatures. The experimental findings will be presented in section 6.5.

6.1 The device and measurement setup

The devices were prepared on GaAs/Al_δGa_{1-δ}As heterostructures. We have used two different wafers for preparing Corbino devices-wafer #81628 and #81758-which have the 2DES 40 nm and 50 nm below the surface, respectively. In TLM measurements on both wafers, contacts were working down to 1 μm mesa stripe width in good contacting and bad contacting direction as discussed in section 4.2.2. As discussed in Chapter 5, we are able to contact these heterostructures down to a contact diameter of 0.2 μm. Therefore we choose these heterostructures to prepare the devices.

A Corbino device is schematically shown in the Fig. 6.1 (a). There is an inner ohmic contact, an outer ohmic contact and 2DES in between. The ohmic contact recipe is discussed in Chapter 4. Ohmic contacts are defined by electron beam lithography. Inner and outer contacts are not defined in the same lithography steps. The reason is that when the outer contact is exposed, due to the proximity effect the inner part is already exposed quite a lot, i.e. for exposing the inner contact even a very small dose result in an overexposure of the whole area of the device. Therefore, we defined the ohmic contacts in two EBL steps. The inner contacts and alignment marks are exposed in the first EBL lithograph step. The contact materials are evaporated and a lift-off process is applied. Then the outer contacts are exposed. For the alignment the alignment marks which are defined together with the inner contacts are used. After developing the EBL resist, again the contact materials are evaporated and a lift-off process is applied. Before each evaporation process, a cleaning process with Semico Clean 23 and HCl is applied as described in section 4.1.1. Then contacts are alloyed. The next step is to define leads for the inner and outer contacts. Connecting the inner contact is somehow challenging. We have used a method that has been developed in Weizmann Institute of Science in Israel to make a suspended thin layer of metal [76,77]. In this method three layer of EBL resist is deposited on the sample. Each layer have a different sensitivity to electron beam. The two bottom layers are less sensitive, that is they need higher doses to be developed. For the foost of the bridge, a higher dose is used such that all three layers are developed in the development process. For the suspended part of the bridge, a lower dose is used to expose the resist. In the development step the top two layers are developed but the bottom layer remains. Then, a metal (usually Cr/Au or Au/Pd) is evaporated. After lift-off process we have a bridge-like metal connection. Therefore, we can make an electrical connection to

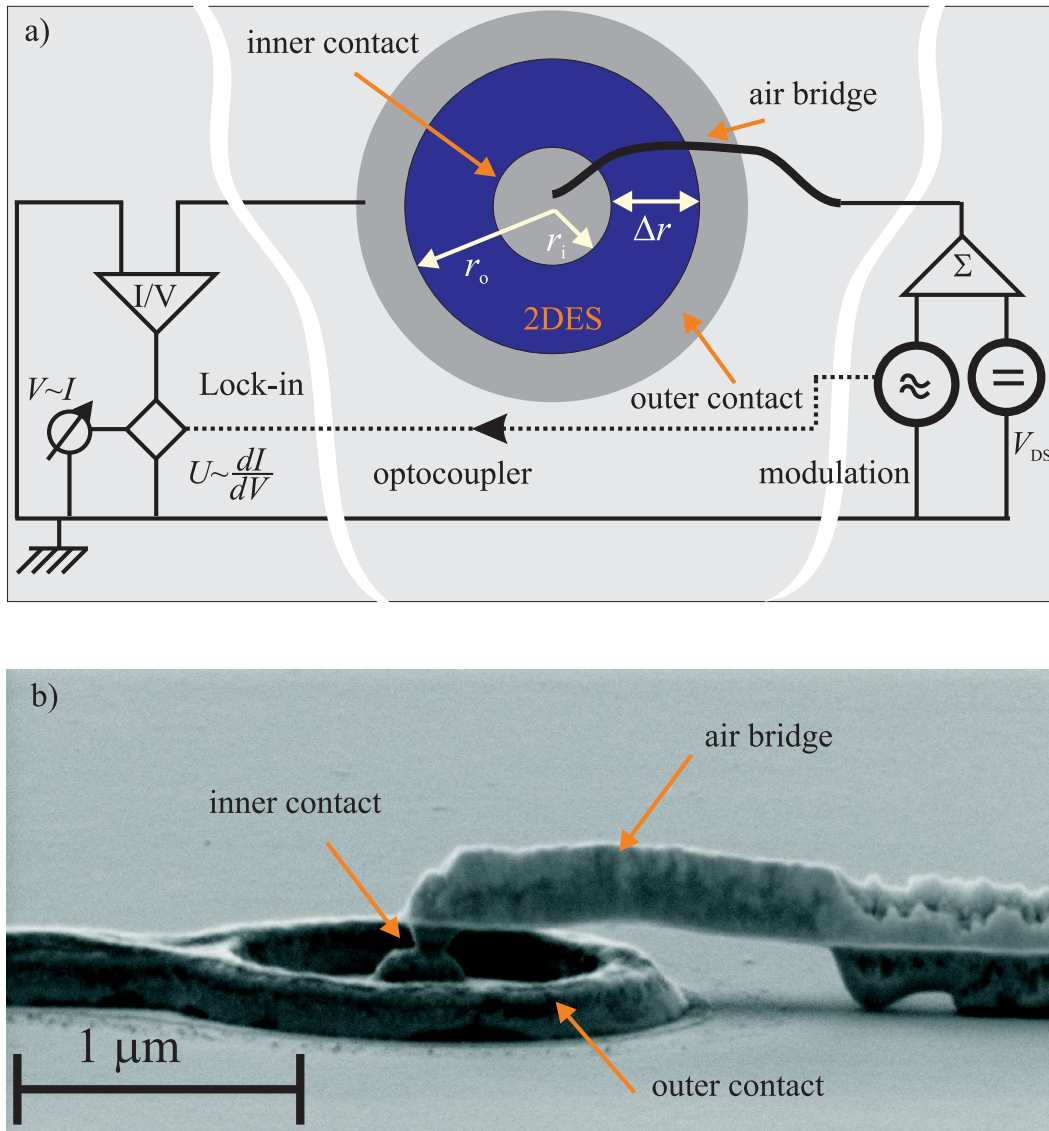


Figure 6.1: (a) Scheme of a Corbino device. The electrical measurement setup is also depicted. (b) An SEM image of a Corbino device from the side.

the inner contact without a shortage to the outer contact. An SEM image of one of the devices is shown in Fig. 6.1 (b). The inner and outer contacts are alloyed Au/Ge/Ni contacts. The bridge is Cr/Au metal. The outer contact and the bridge is connected to the large bonding pads for wiring. The detailed preparation recipe can be found in Appendix I.

Transport experiments are performed in a $^3\text{He}/^4\text{He}$ dilution refrigerator. Elec-

trical characterizations are done by applying a dc voltage to the inner contact (source) as shown in Fig. 6.1 (a). The outer contact (drain) is kept fixed at the reference potential. An ac voltage of $2 \mu\text{V}_{\text{pp}}$ at 19 Hz is superimposed to the dc voltage. The current is measured with a home built current-voltage-converter [78]. The output voltage of the current-voltage-converter composed of dc and ac components. The ac component is monitored by a lock-in amplifier. The dc component of the voltage (proportional to dc current) is also recorded. By calibrations the output voltage is converted to a current.

It is useful to give some statistics about the yield of the devices. As mentioned early we have used two wafers: wafer #81628 and wafer #81758. We have prepared 36 Corbino devices from each wafer. The device dimensions ranged between $0.1 \mu\text{m}$ and $0.5 \mu\text{m}$ for the radius of the inner contact and between $0.6 \mu\text{m}$ and $1.5 \mu\text{m}$ for the outer contact radius. For both wafers, almost 100% of the outer contacts worked when measured with respect to a reference contact on the sample¹. That means the outer side of the contacts have contact to the 2DES. However, it does not mean that the inner side has an electrical connection to the 2DES. Because these are different interfaces. Therefore, as long as the inner ohmic contacts do not work we cannot judge whether the outer ohmic contact has a contact to 2DES in the inner side. For wafer #81628, in 9 out of 36 devices the inner contact worked and 5 of them are characterized in detail. For wafer #81758, in 8 out of 36 devices the inner contact worked and only one of them is characterized in detail. These values of yield are lower than the value of the yield obtained for the small ohmic contacts presented in Chapter 5 for the same heterostructures. However, this becomes less drastic if we think that here two contacts should work at the same time which already decrease the percentage of the working devices.

The heterostructures used to prepare Corbino devices and their relevant parameters are listed in Table 6.1. The given value of mobility is measured on these devices at 4 K. The density n_s , the value of magnetic field $B_{\nu=1}$ at $\nu = 1$, the Fermi energy ε_F and mean free path l_e are, for the devices s#1, s#2, s#4 and s#6 derived from the magneto-conductance measurements at high magnetic field as will be shown in the next chapter. Density in the Corbino devices is generally less than bulk value. For instance, for the device s#4 density is 42% of the bulk value. For the Corbino devices s#3 and s#5 the values could not be obtained from the magneto-conductance measurements on the device, therefore we give the bulk values which are calculated from Shubnikov-de Haas oscillations measured between the outer contact of the Corbino device and the reference contact on the sample. These values of ε_F and l_e are expected to be slightly different in the Corbino device since due to the partial depletion in front of alloyed metal contact [27,28] the

¹The outer contact of the Corbino is surrounded by 2DES since there is no etching process used. The reference contact is a $15 \mu\text{m} \times 15 \mu\text{m}$ ohmic contact prepared in the same sample.

Sample	Wafer	D_{2DES}	n_s	μ	$B_{\nu=1}$	ε_F	l_e	r_i	r_o	Δr
#	#	[nm]	[cm ⁻²]	[cm ² /Vs]	[T]	[meV]	[μ m]	[μ m]	[μ m]	[μ m]
1	81628	40	3.14×10^{11}	5.7×10^5	13	10.9	5.13	0.1	0.6	0.5
2	81628	40	3.6×10^{11}	5.7×10^5	15	12.6	5.51	0.15	0.85	0.7
3	81628	40	5.7×10^{11}	5.7×10^5	23.8	19.7	7.10	0.25	0.7	0.45
4	81628	40	2.4×10^{11}	5.7×10^5	10	8.34	4.5	0.25	0.7	0.45
5	81628	40	5.8×10^{11}	5.7×10^5	23.8	19.17	7.10	0.25	0.7	0.45
6	81758	50	3.06×10^{11}	8.1×10^5	12.7	10.65	7.2	0.15	0.8	0.65

Table 6.1: The list of Corbino devices and their relevant parameters. D is the depth of the GaAs/Al $_{\delta}$ Ga $_{1-\delta}$ As heterojunction. μ is measured bulk mobility at 4 K. The given value of the n_s is determined from the magneto-conductance measurements on the devices at high magnetic field for devices s#1, s#2, s#4 and s#6. For devices s#3 and s#5 the value of the density could not be determined on the device therefore the bulk values are used. $B_{\nu=1}$ is the value of the magnetic field for filling factor $\nu = 1$ calculated from density. ε_F is the Fermi energy. l_e is the mean free path. r_i is the radius of the inner contact, r_o is the inner radius of the outer contact and $\Delta r = r_o - r_i$ is the width of the Corbino disk.

electron density in the Corbino disk is expected to be less than bulk value which is confirmed on the Corbino devices s#1, s#2, s#4 and s#6.

6.2 Submicron scale Corbino devices at low temperatures and small magnetic field

We have proposed the submicron scale Corbino devices as a new type of single-electron charging device. To test this proposal we have to go to high magnetic fields at low temperatures which will be the topic of next chapter. Here, the properties of these small Corbino devices at low temperatures and zero magnetic field, and in the second step under a small perpendicular magnetic field will be investigated. As already shown in Table 6.1 the mean free path is larger than the device dimension. No scattering events are expected to take place as the electrons are emitted from one contact and absorbed by the other contact-transport is ballistic. Before presenting the experiments we would like to introduce available theoretical works for the ballistic transport on submicron scale Corbino devices.

6.2.1 Theoretical predictions due to the ballistic motion of single electrons

The first theoretical study of ballistic transport in a small Corbino device (in nano scale) was done by Kirczenow *et al.* [79]. The same problem was later on considered by Satofumi *et al.* [80, 81] including effect of impurity scattering on the ballistic transport. In the work of Kirczenow *et al.* a Corbino device with non-interacting electrons with ideal metallic ohmic contacts is considered. The ideality of contacts means electrons flows freely into and out of the contacts and any electron that enters a contact is absorbed by it. Conductance was calculated in classical and quantum limit. The result of the calculation is shown in Fig. 6.2. The inner and outer radii of the Corbino device are $r_i = 0.1 \mu\text{m}$ and $r_o = 0.2 \mu\text{m}$, respectively. The Fermi energy is 2 meV. The solid line is the result of the quantum calculation, the dashed line is the conductance for the classical trajectories and the dotted line is the conductance for the semi-classical approximation. At zero magnetic field, conductance is quantized at *odd* multiples of $2e^2/h$. Electrons flow from one contact to the other through the conduction channel of the azimuthal modes l formed in the Corbino device. l takes integer values. Contacts are threaded as if it were a two-dimensional system with an l -dependent effective potential energy term $(l^2 - 1/4)/r_x^2$ where $r_x = \{r_i, r_o\}$. At zero magnetic field for each conduction channel there is a contribution from two modes, $-|l|$ and $+|l|$. Therefore, the total conductance of each conduction channel is $2e^2/h$. For $|l| \geq 1$ modes the total semiclassical conductance at zero magnetic field is

$$G_{\text{SC}} = (2l^* + 1)2e^2/h \quad , \quad (6.1)$$

where l^* is the largest integer smaller than $(2\varepsilon_{\text{F}}m^*r_i^2/\hbar^2 + 1/4)^{1/2}$ [79, 81]. The understanding of the results presented in Fig. 6.2 is much easier from classical point of view. As long as the cyclotron radius l_{cycl} is larger than the average of the inner and outer radii of the Corbino disk, $l_{\text{cycl}} \geq (r_i + r_o)/2$, all the electrons emitted from the inner contact reaches the outer contact (all possible trajectories between curve A and C in the figure), the conductance is constant. As magnetic field is increased further, some of the electrons can not reach the outer contact and are reabsorbed by the inner contact. The conductance begins to decrease. In this regime the classical conductance G_{C} is given by

$$G_{\text{C}} = \frac{G_0}{\pi} \cos^{-1} \left(\frac{r_o^2 - 2r_o l_{\text{cycl}} - r_i^2}{2r_i l_{\text{cycl}}} \right) \quad , \quad (6.2)$$

where G_0 is the conductance for the zero magnetic field [79, 81]. As the cyclotron radius becomes less than half of the width of the corbino disk $l_{\text{cycl}} \leq (r_o - r_i)/2$ none of the electrons, emitted from the inner contact, can reach the outer contact and conductance becomes zero (curve B in Fig. 6.2).

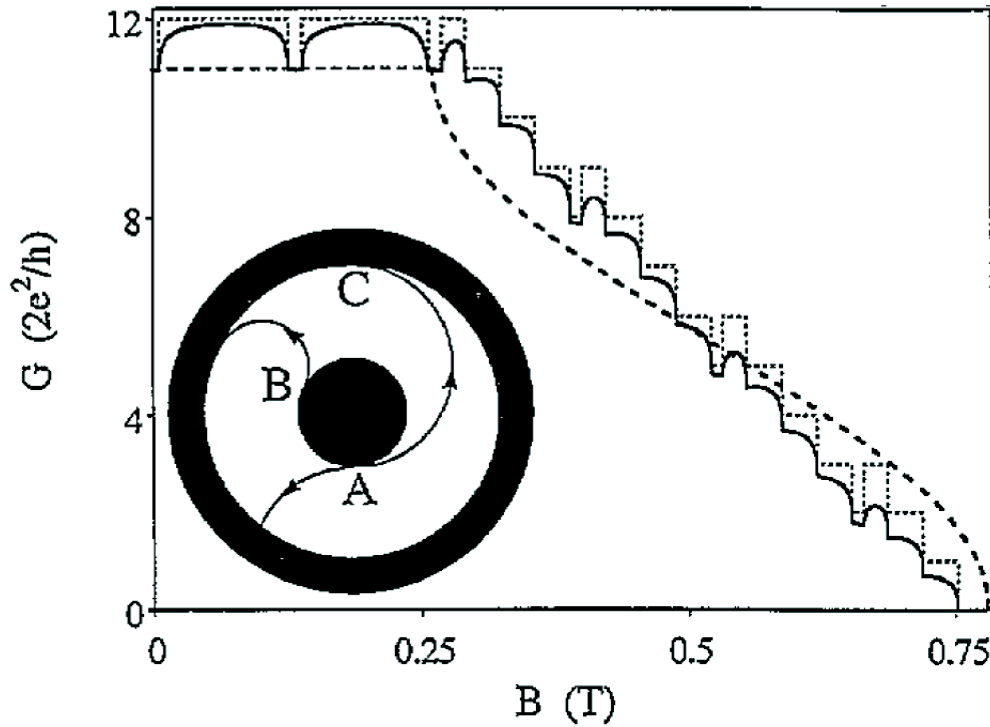


Figure 6.2: Conductance G versus magnetic field B . $r_i = 0.1 \mu\text{m}$, $r_o = 0.2 \mu\text{m}$ and $\varepsilon_F = 2 \text{ meV}$. The solid line is the quantum conductance, the dashed line is the conductance for the classical trajectories, the dotted line is the conductance in the semi-classical approximation. Inset: scheme of a Corbino device showing limiting classical electron trajectories. From Kirczenow *et al.* [79].

The result of semi-classical calculation follows the result of the classical calculations. The difference are due to switching on and off modes as the magnetic field is changed. The result of the quantum mechanical calculations follow the semi-classical results. The rounded edges are due to the finite transmission between different modes which is ignored in the semiclassical approximation. Souma *et al.* [80,81] investigated the effect of δ -impurities on the ballistic transport through Corbino disks. The effect of δ -impurities is that conductance peaks appear at certain regions of high magnetic field where otherwise ballistic conductance is zero.

6.2.2 Transport experiments at low temperatures and observation of a zero bias anomaly

In this section we will present experiments on submicron scale Corbino devices at zero magnetic field and low temperatures. The measured current voltage characteristic for Corbino device s#3 is shown in Fig. 6.3 (a) for 1.5 K and 50 mK. The green curve corresponds to measurements at 1.5 K and shows a linear ohmic behavior as expected. However, the current voltage characteristic measured at 50 mK shows a nonlinear behavior around zero bias. This is more clear to see in differential conductance measurements as shown in Fig. 6.3 (b). At 1.5 K the measured conductance is constant with applied bias as expected. The value of the conductance is about $9 e^2/h$. The value of the conductance for this device expected from the theory of Kirczenow *et al.* is about $122 e^2/h$. The exact value of the density and Fermi energy could not be determined on this device, therefore, the value of $\varepsilon_F = 8.3$ meV is used which is extracted from measurement on a similar device (measured on s#4 which has a conductance about $10 e^2/h$ at 1.5 K) on the same sample. The striking difference between the theory and the experiment put the applicability of the theory in doubt. The source of the deviation between the theory and experiment is the definition of the contact since in the theory ideal contacts are assumed.

Now we turn our attention again to the experiments presented in Fig. 6.3. At 50 mK, contrary to 1.5 K, the conductance has a huge dip at zero bias. Moreover, there are two kinks at both sides of the dip located at ± 0.25 meV where the measured low temperature conductance is higher than the high temperature conductance and large bias conductance. At larger bias voltages the low temperature conductance is equal to the high temperature conductance. The origin of the kinks can be explained as follow: at large bias voltages the effect is no longer present and the current should be the same as the current measured at high temperature if we assume that contact resistance is the same at high temperate and low temperature. However, at 50 mK at large bias voltages the dc current is slightly lower than the high temperature current for the same voltages. This is probably due to the increase on the contact resistance at low temperature. 3% of increase on the contact resistance can result in such a difference on the dc current.

The temperature dependence of the zero bias dip is shown in Fig. 6.4 (a). At 50 mK, the dip is well developed. As the temperature increases the depth of the dip decreases and the width becomes wider, the kinks becomes less pronounced. At 480 mK the depth of the dip is significantly less and the kinks completely disappear. At 1.5 K there is no dip visible. We will denote the high temperature conductance as $G^H = G(T = 1.5 \text{ K})$. The temperature dependence of the depth $\Delta G = G(T) - G^H$ and the full width at half maximum (FWHM) of the zero bias dip is shown in Fig. 6.4 (b). The values of ΔG and the FWHM are obtained by a

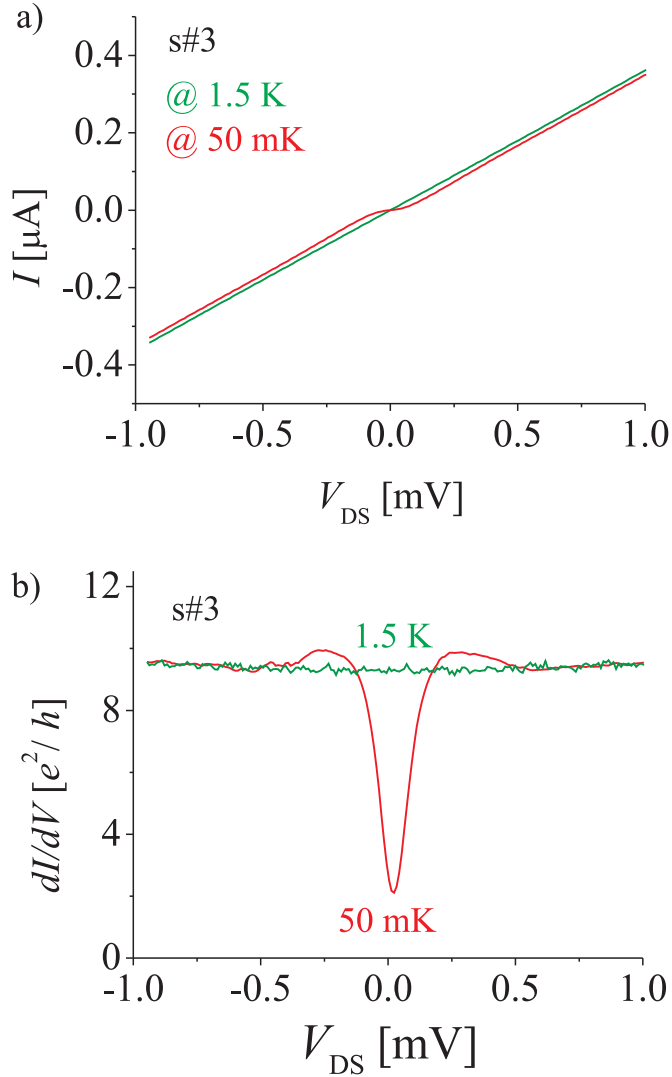


Figure 6.3: (a) Current-voltage data taken at 1.5 K (green curve) and 50 mK (red curve) for sample s#3. Differential conductance data for the same measurements shown in (a).

Lorentzian fit to data and two examples of the fit curves are given in Fig. J.1 in Appendix J.1. The width of the dip at 50 mK is 0.140 meV. This approximately corresponds to thermal energy $k_{\text{B}}T$ at 1.5 K (0.129 meV), the temperature at which the dip disappears completely. The value of ΔG and FWHM tend to saturate at around 50 mK. The origin of such an anomalous behavior possibly arises due to interference effect since phase coherence length becomes larger and interference of electrons becomes visible at this low temperatures. We will discuss the possible scenarios for the observed effect in section 6.3.

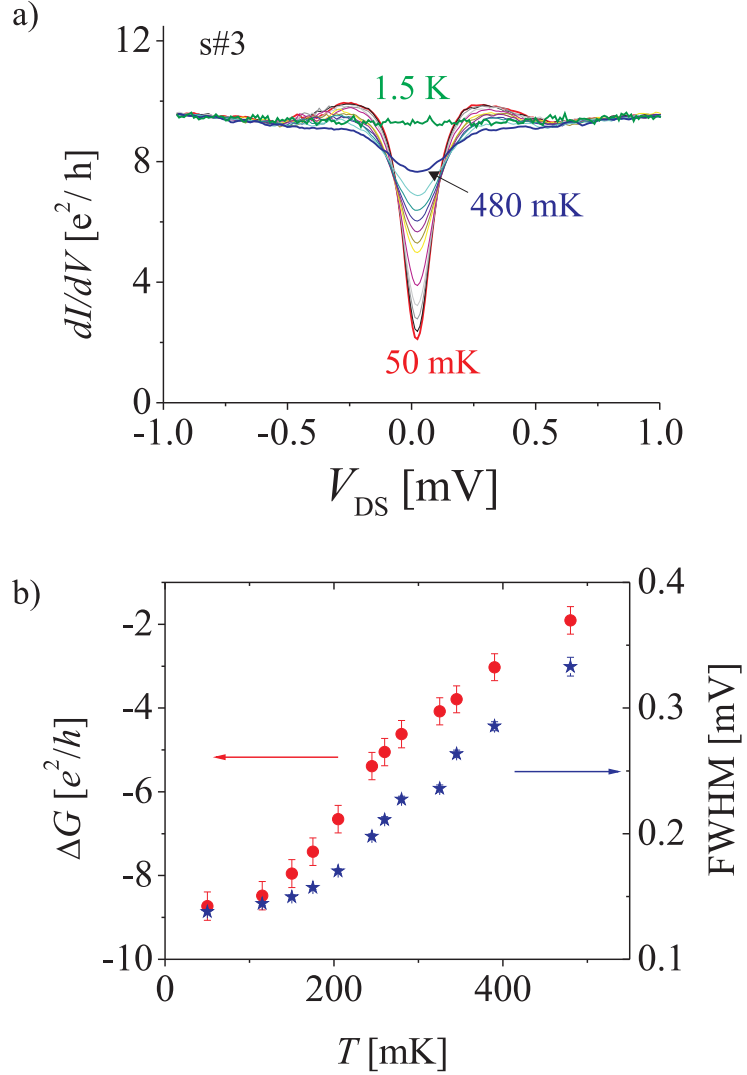


Figure 6.4: (a) Temperature dependence of the zero bias dip. (b) Depth $\Delta G = G(T) - G^H$ and FWHM of the zero bias dip as a function of the temperature. The values of ΔG and FWHM are obtained by a Lorentzian fit to the data.

The zero bias dip is observed for all the devices that have been measured. The differential conductance measured on the different devices is shown in Fig. 6.5. The value of the zero bias conductance varies between $0.9 e^2/h$ and $4.5 e^2/h$ for the devices. The value of large bias conductance where the effect is not present changes between $2 e^2/h$ and $12 e^2/h$. The deviation in the large bias (high temperature) conductance is expectable since the deviation in the contact resistance are expectable as we have shown in Chapter 5. The kinks at both sides of the dip are

present for some of the devices but not for all of them. For device s#2 the kinks have dips on both sides. The reason for these dips is not clear. For the device s#6 a similar behavior very slightly is present. For the devices s#1 and s#5 there is a slight asymmetry between the positive and negative bias side. We will have a closer look on this asymmetry in section 6.4.

For the comparison between the geometrical size of the Corbino devices and ΔG and FWHM of the dips, we present the data for all of the measured devices in Table 6.2. r_i is the radius of the inner contact, r_o is the inner radius of the outer contact and $\Delta r = r_o - r_i$ is the width of the Corbino disk. The FWHM is obtained by a Lorentzian fit to data. Conductance $G(V_{DS} = 0)$ at 50 mK and high temperature conductance G^H are also given in the table. For the Corbino devices s#1, s#2 and s#6 a reminiscent of the zero bias dip is slightly present at 1.5 K. The low and high temperature measurements for these devices are shown in Fig. J.2 in Appendix J. Therefore, to define the value of high temperature G^H for these devices we instead use the large bias conductance. So we take the value of the conductance at $G^H = G(V_{DS} = 0.5 \text{ mV})$ as high temperature conductance. We do not give the depth obtained from the Lorentzian fit but rather $\Delta G = G^L - G^H$ where $G^L = G(V_{DS} = 0, T = 50 \text{ mK})$. Therefore, we can eliminate the error due to the kinks at both sides of the dip where the conductance is higher than the high temperature conductance. The FWHM varies between 0.10 mV and 0.15 mV and seems not to depend on any geometrical parameters of the Corbino devices. Sample s#3, s#4 and s#5 have the same dimensions. The value of the FWHM (140 μeV for s#3 and 153 μeV for s#4) and depth of the dips (7.2 e^2/h and 7.4 e^2/h) are similar. However, s#5 has lower values for FWHM (102 μeV) and depth (4.1 e^2/h). The high temperature conductance of s#5 (5.9 e^2/h) is lower than those of s#3 and s#4 (9.2 e^2/h and 10.3 e^2/h respectively).

To see correlation better, we investigate the data given in Table 6.2 more closely. The ΔG and FWHM values of the zero bias dips as a function of the geometrical width of the Corbino devices is presented in Fig. 6.6 (a). The reason for large error bar for the Corbino device with $\Delta r = 0.5 \mu\text{m}$ (s#1) is that during the measurements of this device a small permanent magnetic field was present in the system (30 mT). The depth and the FWHM of the dip depend on the magnetic field as we will see in section 6.2.3. We have corrected the depth for this offset using magnetic field sweep measurements as will be shown in section 6.2.3. The ΔG given in Table 6.2 is the corrected value. For the FWHM we estimated an error in the determination of the FWHM and this error is used in the plots as the error bar. The error that might happen in the determination of FWHM is about 10% (that is it can be 10% less but not more). For the Corbino devices s#4 and s#5 there was a magnetic field of 12 mT during measurements. However, the amount of error due to this magnetic field in the FWHM is negligibly small. We

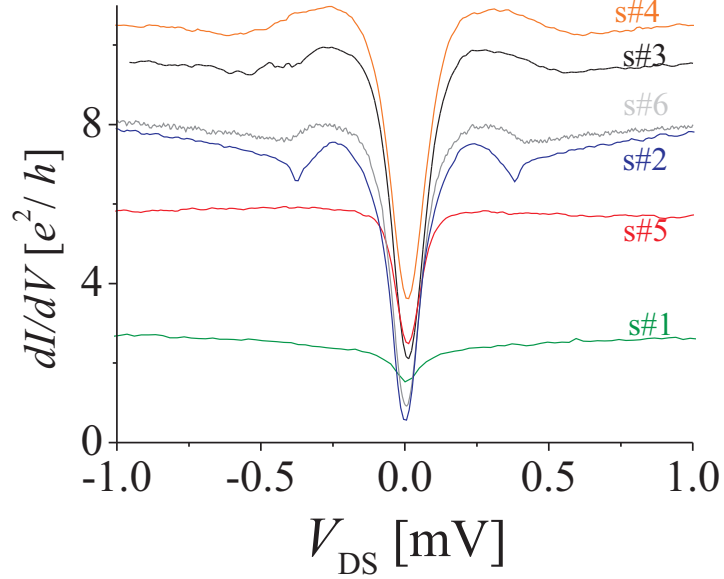


Figure 6.5: Differential conductance versus applied voltage for several Corbino devices. The geometrical size and heterostructure parameters of the devices are given in Table 6.1.

Sample #	r_{in} [μm]	r_{out} [μm]	Δr [μm]	FWHM [mV]	G^{H} [e^2/h]	G^{L} [e^2/h]	ΔG [e^2/h]
1	0.1	0.6	0.5	0.116	2.50	1.2	-1.3
2	0.15	0.85	0.7	0.128	7.30	0.5	-6.8
3	0.25	0.7	0.45	0.140	9.20	2	-7.2
4	0.25	0.7	0.45	0.154	10.30	2.9	-7.4
5	0.25	0.7	0.45	0.102	5.90	1.8	-4.1
6	0.15	0.8	0.65	0.127	7.60	1	-6.6

Table 6.2: The list of Corbino devices and their relevant parameters. r_{i} is the radius of the inner contact, r_{o} is the inner radius of the outer contact and $\Delta r = r_{\text{o}} - r_{\text{i}}$ is the width of the Corbino disk. The FWHM is obtained by a Lorentzian fit to data. Conductance G^{L} at 50 mK and high temperature conductance G^{H} are also given in the table. The depth is difference between the high temperature conductance and low temperature ($T=50$ mK and zero bias) conductance, $\Delta G = G^{\text{L}} - G^{\text{H}}$.

checked this in the Corbino device s#3 which we have characterized at $B = 0$ T and $B = 12$ mT as shown in Fig. J.3 in Appendix J. From Fig. 6.6 (a) a clear correlation between the width of the Corbino and depth and FWHM of the zero bias dip is absent. For larger width the FWHM is more or less constant and is about 125 mV. For the smaller device which have the same size the FWHM varies between 0.10 mV and 0.15 mV. A correlation between ΔG and Δr is also absent. ΔG for small and large devices can be similar and also ΔG for the devices that have the same size can be quite different. We should keep in mind that the size of the devices is much smaller than the mean free path (about $7 \mu\text{m}$) and the range of Δr is limited. We have prepared devices with the outer contact radius as large as $1.5 \mu\text{m}$ but unfortunately none of these large devices worked.

The depth and width of the zero bias dip versus high temperature conductance of the Corbino devices is plotted in Fig. 6.6 (b). As the high temperature conductance becomes higher the dip is deeper. ΔG decreases monotonically (that is the dip is becomes deeper) as the high temperature conductance becomes larger. A linear fit to data give a slope of -0.85 . This implies that 85% of the conduction electrons contributes to the dip feature. We will define this value as the visibility of the observed phenomenon. The FWHM values seem to have a tendency to go to larger values as the G^{H} becomes large. As we already mentioned above the error bar in data with lowest G^{H} is large. For this data point the FWHM is probably overestimated. So the actual FWHM is expected to be about 10% less. This can make the above statement that the FWHM increases with increasing G^{H} even stronger.

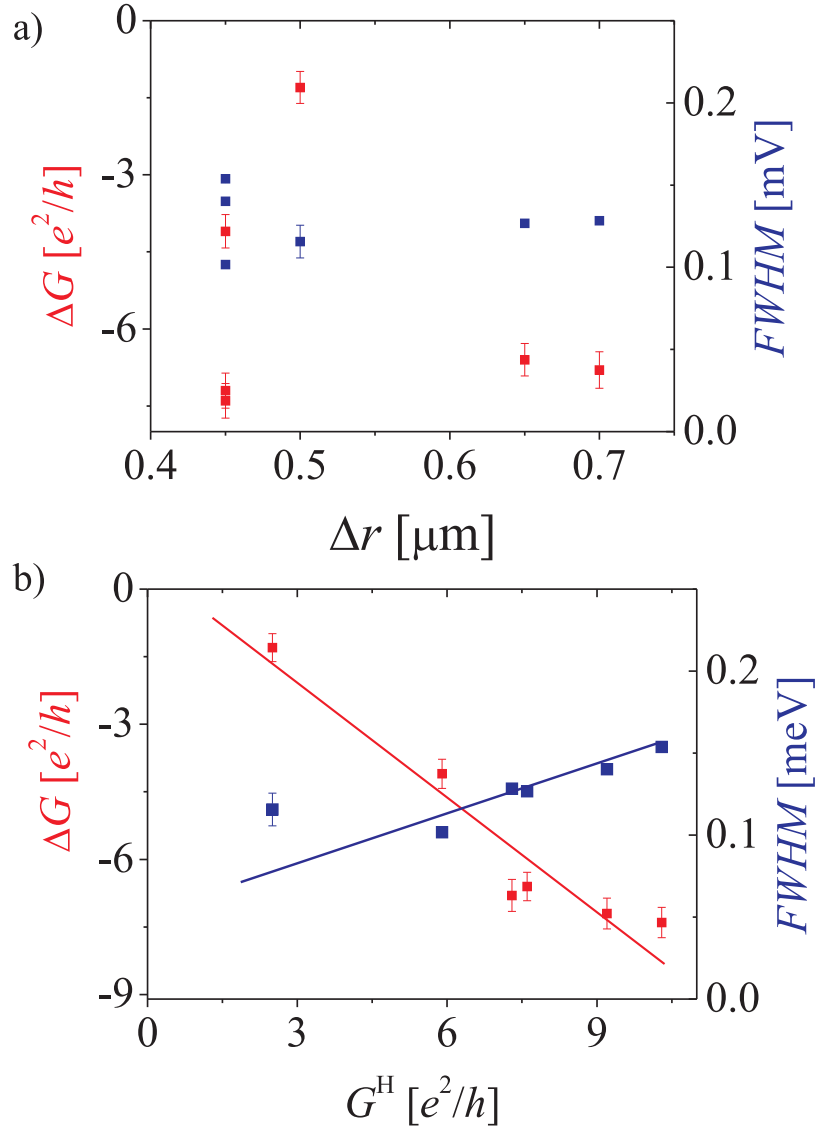


Figure 6.6: (a) The depth and FWHM values of the zero bias dip as a function of the width ($\Delta r = r_o - r_i$) of the Corbino devices. (b) $\Delta G = G^L - G^H$ and FWHM of the zero bias dip as a function of the high temperature conductance of the Corbino devices.

6.2.3 Zero bias anomaly at finite magnetic field: observation of a positive magneto conductance

What happens to the zero bias dip if we apply a perpendicular magnetic field? The conductance versus magnetic field for $s \neq 3$ is shown in Fig. 6.7. In this measurements no dc bias is applied, only a small ac voltage is applied to the inner contact. As clearly visible, the conductance of the Corbino device increases with applying the magnetic field and saturates at already around 0.2 T. There are two trends in the increasing conductance as magnetic field increases. First there is a steep increase in the conductance till 20 mT with a positive curvature. Then around 20 mT there is a small plateau with a width of 4 mT. After this plateau the increase in the conductance happens with a negative curvature and saturates at about 200 mT. The value of cyclotron radius at 20 mT for this sample is about $4 \mu\text{m}$ and is much larger than the device dimensions. The value of the magnetic length l_B is about $0.18 \mu\text{m}$ (at 20 mT). The radius of the inner contact r_i is $0.25 \mu\text{m}$, the radius of the outer contact r_o is $0.7 \mu\text{m}$ and the width Δr is $0.45 \mu\text{m}$. All of these values are already larger than l_B . Therefore, the appearance of a plateau like feature and the change in the curvature of the magneto-conductance does not seem to be directly correlated to the magnetic length or cyclotron radius. At 0.2 T, where the positive magneto-conductance saturates, $l_{\text{cycl}} = 0.4 \mu\text{m}$ which is just comparable to the width Δr of the Corbino device. However, as we will see later on this section for the most of devices the conductance saturates at already 0.1 T. At this magnetic field $l_{\text{cycl}} \geq 0.8 \mu\text{m}$ and larger than the width of the Corbino devices. The observed behavior does not resembles the result of theoretical calculations presented in section 6.2. Where can such a positive magneto-conductance rise? A positive magneto-conductance has been observed and investigated in quantum structures as a result of the weak localization [82–84]. We will discuss possible scenarios for the origin of the observed magneto-conductance in section 6.4.

The value of the saturation conductance is about $7.5 e^2/h$ and lower than the value of the high temperature (or high bias voltage) conductance $G^H = 9.2 e^2/h$ for the same sample at $B=0$ (see Fig. 6.3). To see this more clear we will plot differential conductance versus bias voltage and magnetic field in Fig. 6.8. In this measurement the differential conductance is measured by sweeping the bias voltage for different magnetic field values. That is we set the value of magnetic field, say, to -0.1 T, sweep the source-drain bias and measure the differential conductance. Then the magnetic field is increased by a certain amount, say to -0.09 T, source-drain bias is swept and the differential conductance is measured again, and so on. In Fig. 6.8 (a) color coded mesh plot of differential conductance versus bias voltage and magnetic field is shown. In Fig. 6.8 (b), a color plot of differential conductance versus bias voltage and magnetic field is shown for the same measurements as in Fig. 6.8 (a). The zero bias dip and kinks at the negative and positive side are

clearly visible. The dip is symmetric for bias voltage and magnetic field reversal. As magnetic field increases, the zero bias dip is suppressed. The suppression is not complete but rather partly. The suppression due to magnetic field saturates already around 0.1 T. However, the zero bias deep still persist at these magnetic field and also for the larger magnetic fields. The kink at the both side of the zero bias dip are not present at these magnetic fields. It seems that there are indeed two different effects which are superimposed to each other at the zero bias and zero magnetic field. One is suppressed by magnetic field. However, the other one is either not effected by magnetic field or partly effected. Later we will make this point more clear by comparing temperature dependent measurements.

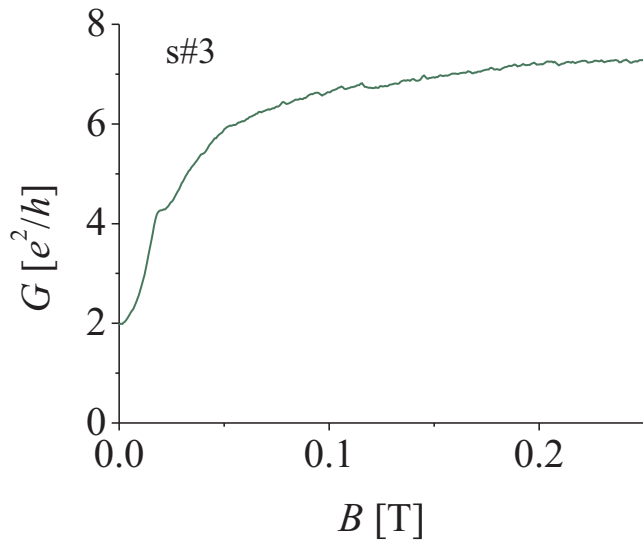


Figure 6.7: Conductance of a Corbino device (s#3) measured as a function of perpendicular magnetic field. No dc bias is applied. Only a small ac voltage applied to inner contact.

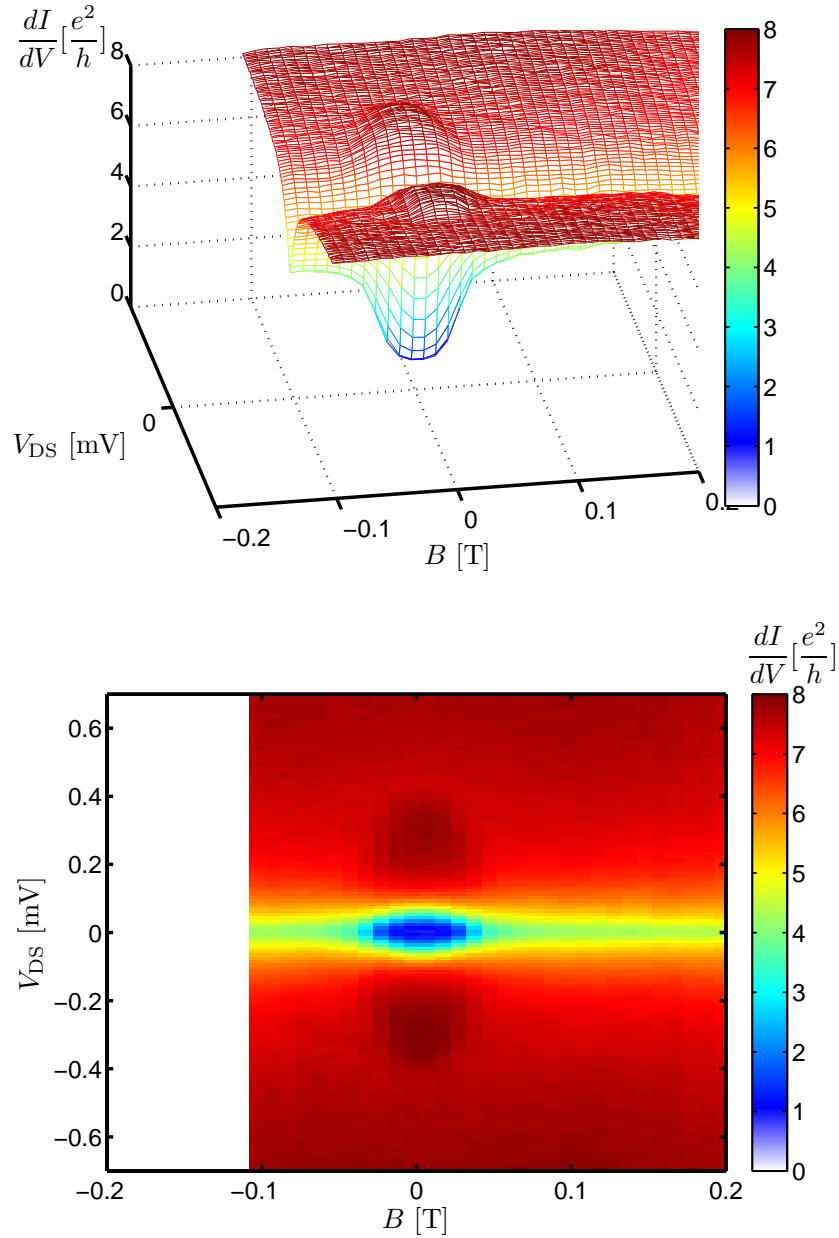


Figure 6.8: (a) Differential conductance versus bias voltage and magnetic field for s#6. (b) Color plot of the same measurements.

The positive magneto conductance increase is observed for all the devices. We will use the term *magneto conductance dip* for this observed phenomena to distinguish it from the zero bias dip which is discussed in section 6.2.2. The results are presented in Fig. 6.9 (a). The width of the valleys are not the same for all the samples. The conductance saturates for all the devices at about 0.2 mT. For some of the devices (s#1, s#5 and s#6) conductance already saturates at 0.1 T. The plateau like feature around 20 mT which is present for s#3 is also present for s#4, but is not present for the other devices. To make a better comparison between the curves we plot $\Delta G^B = G(B = 0 \text{ T}) - G(B = 0.2 \text{ T})$ versus magnetic field. The results are presented in Fig. 6.9 (b). Then we subtract the depth of the conductance dips and FWHM of the dips from this plot. For the FWHM we take the width of the dips and multiply by two. For the definition of the FWHM we take the position of the dip where it changes the curvature as full maximum and then took the value of the width at the half maximum. That is for s#3 (or s#4) the curvature changes at 20 mT. However, for sample s#6 the curvature changes at about 45 mT.

The result of these measurements are summarized in Table 6.3 with the geometrical parameters of the devices. The parameters of the zero bias dip obtained from bias dependent measurements are also presented in the table. The devices s#3, s#4 and s#5 have the same lithographic dimensions. The FWHM is nearly the same for s#3 and s#4 (about 25 mT) but is less than that of s#5 (32 mT). The FWHM of zero bias dip for s#3 and s#4 (0.140 meV and 0.150 meV) are similar and larger than that of s#5 (0.102 meV).

Now we will have a look at the correlation between saturated conductance at finite field and depth and height of the dips. We define $\Delta G^B = G(B = 0 \text{ T}) - G(B = 0.2 \text{ T})$. In Fig. 6.10 (a) ΔG^B versus $G(B = 0.2 \text{ T})$ is shown. As the value of finite field saturated conductance becomes larger the dip is deeper. A best fit to data give a slope of 0.75. This value is less than the value of the slope (0.85) which is found from the depth of the zero bias dip versus high temperature (large bias) conductance. This is reasonable since the saturated conductance at finite magnetic field is less than the high temperature conductance. For the larger saturated conductance the FWHM is smaller. However, the FWHM can be quite different even though the devices have approximately the same saturated conductance.

In Fig. 6.10 (a) ΔG^B and FWHM versus geometrical width Δr of the Corbino devices are shown. There is not a direct correlation between ΔG^B and Δr . ΔG^B can be quite different even for the devices which have the same geometrical size. For the larger devices the FWHM is larger. The error in FWHM for the device with $\Delta r = 0.5 \mu\text{m}$ is large since the magneto-conductance dip is not very much pronounced.

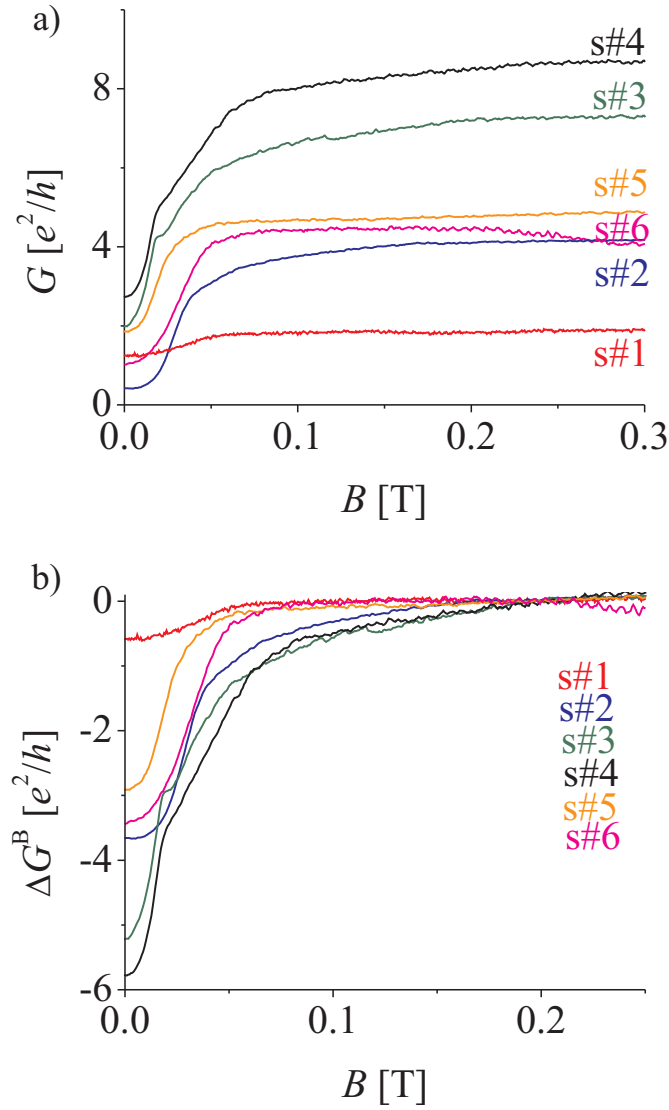


Figure 6.9: (a) Conductance versus magnetic field for different Corbino devices. (b) ΔG^B versus magnetic field for the same measurements presented in (a).

Sample	r_i [μm]	r_o [μm]	Δr [μm]	FWHM [B]	G ($B=0.2\text{T}$) [e^2/h]	ΔG^B [e^2/h]	\mathcal{E}_F [meV]	l_{cycl} 50 mT [μm]	FWHM [mV]	ΔG [e^2/h]
s#1	0.1	0.6	0.5	50	1.82	-0.58	10.9	1.84	0.116	-1.30
s#2	0.15	0.85	0.7	52	4.11	-3.66	12.6	1.98	0.128	-6.80
s#3	0.25	0.7	0.45	25	7.25	-5.22	19.7	2.49	0.140	-7.20
s#4	0.25	0.7	0.45	26	8.52	-5.79	8.34	1.60	0.154	-7.40
s#5	0.25	0.7	0.45	32	4.75	-2.91	19.7	2.49	0.102	-4.10
s#6	0.15	0.8	0.65	58	4.44	-3.43	10.6	1.80	0.127	-6.60

Table 6.3: The parameters of the FWHM of magneto conductance dip and zero bias dip for the Corbino devices. r_i is the radius of the inner contact, r_o is the inner radius of the outer contact and $\Delta r = r_o - r_i$ is the width of the Corbino device. The FWHM given in fifth column is that of the magneto-conductance dip. $G(B = 0.2 \text{ T})$ is the value of the conductance at 0.2 T. $\Delta G^B = G(B = 0 \text{ T}) - G(0.2 \text{ T})$ is the depth of magneto-conductance dip. The value of Fermi energy \mathcal{E}_F and l_{cycl} are extracted from the density measured on the devices for s#1, s#2, s#4 and s#6. For s#3 and s#5 the value of density on the device could not be measured, therefore, the bulk values extracted from the bulk measurements in the same sample are given. However, we expect the density and Fermi energy on these devices to be close to the one measured on the device s#4 which has similar size. The value of l_{cycl} is for 50 mT. In last two columns the FWHM and the depth of the zero bias dip obtained for the samples are given.

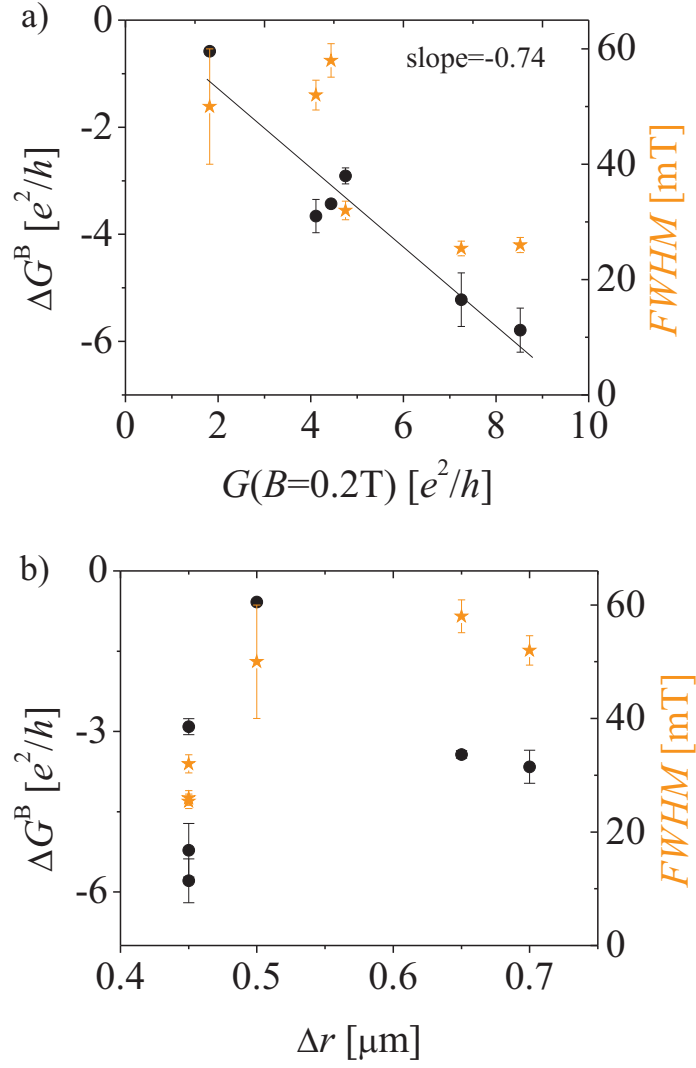


Figure 6.10: (a) The FWHM and depth ($\Delta G^B = G(0 \text{ T}) - G(0.2 \text{ T})$) of the magneto-conductance dip versus $G(0.2 \text{ T})$. (b) The FWHM and depth ($\Delta G^B = G(0 \text{ T}) - G(0.2 \text{ T})$) of the magneto-conductance dip versus the geometrical width of the Corbino device Δr .

6.2.4 Temperature dependence of magneto-conductance dip

In Fig. 6.11 the temperature dependence of the magneto-conductance dip together with the temperature dependence of zero bias dip is presented. In Fig. 6.11 (a) measured conductance versus magnetic field at different temperature for s#3 is shown. As the temperature increases the magneto-conductance dip becomes less pronounced and finally disappears at about 0.5 K. Similar measurements are performed for s#4 and s#5 and are presented in Fig. J.4 (a) in Appendix J. The value of the conductance at large magnetic field values, where the magneto-conductance dip is not present any more, also increases. This is due to the temperature dependence of zero bias anomaly: as presented in Fig. 6.8 zero bias anomaly persist in finite magnetic fields. As the temperature increases the minimum of the dip increases, therefore, we see also a conductance increase with temperature at large magnetic field values. To compensate for this and to make a better comparison, ΔG^B versus B is shown Fig. 6.11 (b). The decrease on the depth of the magneto-conductance dip is more clear on this plot. However, now the curve for 50 mK and 113 mK looks almost the same. In Fig. 6.11 (c) ΔG^B versus temperature for three devices (s#3 s#4 s#5) is shown. The depth of the magneto-conductance dip decreases as the temperature increases for all three devices. For the device s#3 ΔG^B seems to saturate below 100 mK, which is also clear from Fig. 6.11 (b). Such a saturation seem to be present for the device s#4 but less clear. For comparison the temperature dependence of the zero bias dip measured on device s#3 is shown in Fig. 6.11 (d). Saturation of the depth of zero bias dip below 100 mK is also visible on this plot. The magneto-conductance dip disappears at about 500 mK whereas the zero bias dip still persists at these temperature range and disappears at about 1.5 K.

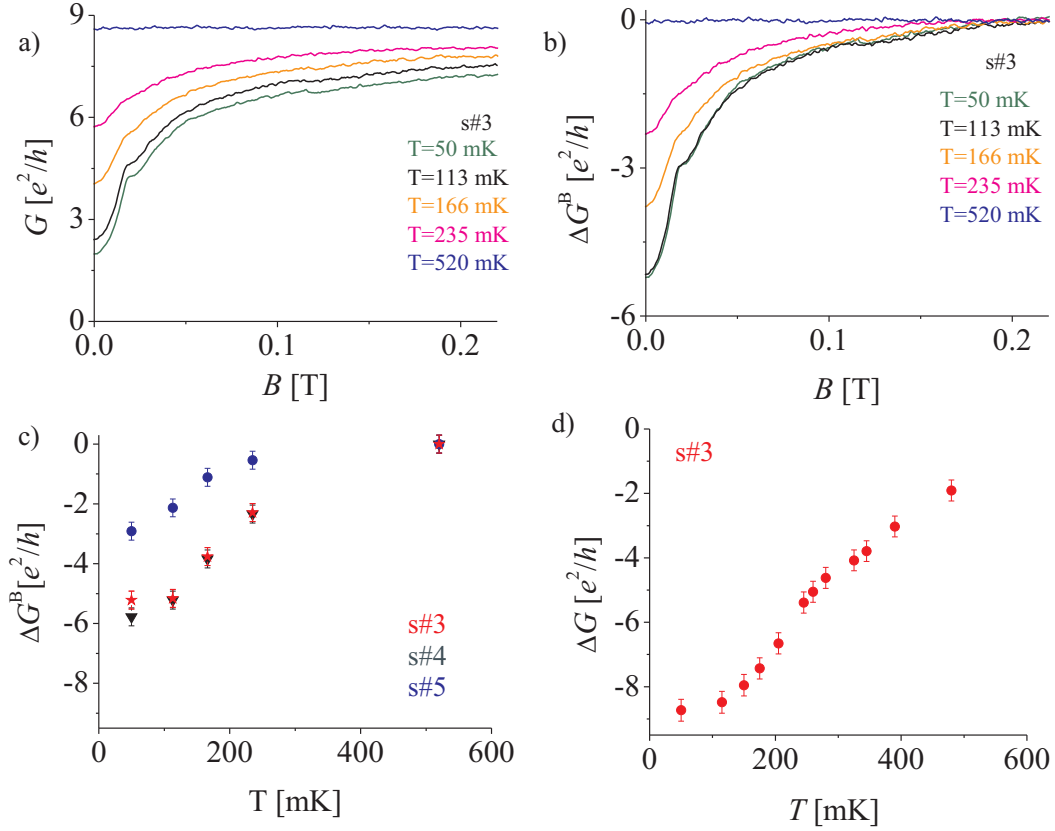


Figure 6.11: (a) Temperature dependence of magneto-conductance dip. (b) $\Delta G(B)$ versus magnetic field for the same data presented in (a). (c) Temperature dependence of ΔG^B at zero magnetic field for Corbino devices s#3, s#4 and s#5. (d) Temperature dependence of ΔG for the zero bias dip.

6.3 Discussion of zero bias anomaly and interference effects as a possible source of the phenomenon

In this section we will discuss possible scenarios for the observed anomalous zero bias dip and magneto-conductance dip. In section 5.3 we have presented similar conductance measurements at low temperatures for larger Corbino device with small inner contacts. The inner contacts were comparable in size to one in submicron scale Corbino devices. The outer contact radius, however, was very large a few hundred micron, much larger than the mean free path. Such a zero bias anomaly has not been observed for these contacts. There was a slight nonlinearity for one of the contact which can be due to the nearby sitting contacts $2.5 \mu\text{m}$ and $7.5 \mu\text{m}$ away. This shows that the observed phenomenon is not due to only smallness of the inner contact but rather smallness of the Corbino device itself.

We first concentrate on the origin of the positive magneto-conductance increase. As we have seen the effect disappears with increasing temperature and is suppressed with the presence of a small magnetic field. These are signature of an interference process which is known as the weak localization [85–88]. The intuitive understanding of the phenomenon is clear in the Feynman path integral description as shown in Fig. 6.12. The probability $P(r_1, r_2, t)$ for an electron to move from r_1 to r_2 in the time interval t is the squared sum of the probability amplitudes A_i for the corresponding propagations in the time interval t :

$$P(r_1, r_2, t) = \left| \sum_i A_i \right|^2 = \sum_i |A_i|^2 + \sum_{i \neq j} A_i A_j^* \quad , \quad (6.3)$$

where A_j^* is the complex conjugate of A_j . The sum is over all possible paths. When the starting and ending points are different as shown in Fig. 6.12 (a) the phase of the paths are uncorrelated. Therefore the second term in (6.3) which is responsible for the interference averages to zero. However, when the starting and end point are the same point as shown in Fig. 6.12 (b), the phase of the time reversal trajectories A_i^+ and A_i^- are identical and leads to constructive interference. That is, the probability of the coherent back scattering is $|A_i^+ A_i^-| = 4|A_i|^2$. This enhanced coherent back scattering reduces the conductance at low temperatures when the phase coherence length is large enough. The presence of the magnetic field breaks the time reversal symmetry, thereby decreasing the constructive interference and therefore lead to a positive magneto-conductance. In the following we will try to fit our data to two different approximation of weak localization: weak localization in one dimensional quantum wires and weak localization in ballistic cavities.

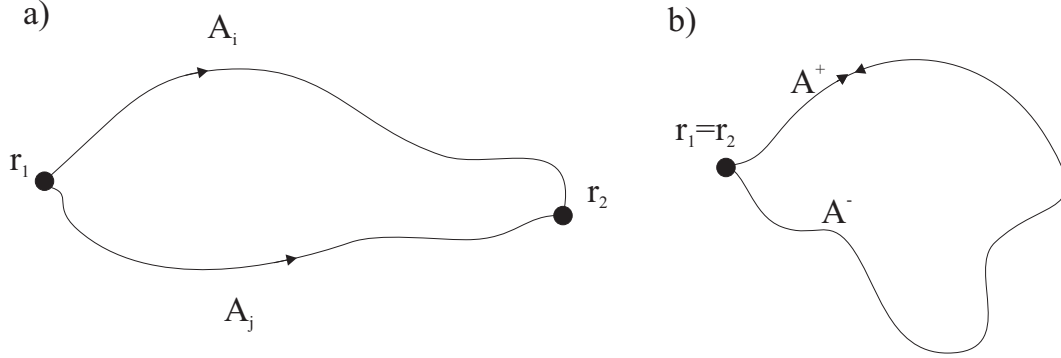


Figure 6.12: Mechanism of the coherent back scattering (a) When the starting and ending points are different, the probability amplitudes of the trajectories have uncorrelated phases for different trajectories. (b) When the starting and ending points are identical the time reversal paths have identical phases which lead to enhanced coherent back scattering of electrons.

6.3.1 1-D weak localization as a possible source of the interference in submicron Corbino devices ?

The theory of the weak localization has been adapted to include effect of boundary scattering in ballistic mesoscopic devices where the mean free path is larger than the device width [84,88,89]. Experiments on the submicron width GaAs/Al_δGa_{1-δ}As heterostructures fits the theory very well [89,90]. The correction $\Delta G(B)$ to the conductance due to weak localization and boundary scattering is

$$\Delta G(B) = -\frac{e^2}{\pi\hbar} \frac{\sqrt{D}}{L} \left[\left(\frac{1}{\tau_\phi} + \frac{1}{\tau_B} \right)^{-\frac{1}{2}} - \left(\frac{1}{\tau_\phi} + \frac{1}{\tau_e} + \frac{1}{\tau_B} \right)^{-\frac{1}{2}} \right], \quad (6.4)$$

and

$$\tau_B = \frac{l_B^4}{K_1 w^3 v_F} + \frac{l_B^2 \tau_e}{K_2 w^2}. \quad (6.5)$$

Here τ_e is the elastic scattering time, τ_ϕ is the phase coherence time, $l_B = \sqrt{\hbar/eB}$ is the magnetic length, D is the diffusion constant and K_1 and K_2 are constants which depend on the nature of the boundary scattering. For diffuse boundary scattering $K_1 = 1/4\pi$ and $K_2 = 1/3$. For specular boundary scattering $K_1 = 0.11$ and $K_2 = 0.23$. For the specular boundary scattering $D = v_F l_e / 2$ and for the diffuse scattering $D = (v_F w / \pi) \ln(l_e / w)$ in the limit $w \ll l_e$.

In principle this theory might apply to submicron scale Corbino devices as well. Reflection or scattering of electrons at the ohmic metal contact and 2DES interface is expectable. Moreover, it is natural to expect that the ohmic contact

is not formed everywhere at the boundary of the contact and 2DES as shown in Fig. 6.13 (a). Therefore, the place where the ohmic contact is not formed will act as confining boundaries. The mean free path is larger than the width of the device. The above theory applies where the length L of the sample is larger than $l_e = v_F\tau_e$ and $l_\phi = v_F\tau_\phi$. This condition is not satisfied in our Corbino devices if the bulk value of $l_e \geq 4 \mu\text{m}$ is taken into account. However, it worths to see at what extend it fits to data.

To fit theory to data is not an easy task since there are too many parameters. For the fit we fix the width of the device to some approximate values and let τ_ϕ and τ_e , L and D be the free fit parameters. The data, fitted curve and the fit parameters are shown in Fig. 6.13 (c). Fit of (6.4) and (6.5) to data gives a good qualitative agreement. However, the obtained value of the τ_e and τ_ϕ are too small implying l_e around 3 nm and l_ϕ around 300 nm. The length obtained from the fit is about $L = 0.45 \mu\text{m}$. If we fix L to larger values, 1 μm for instance, the fit is poor. The above fit was for the specular boundary scattering. For the value of the K_1 and K_2 for the diffuse boundary scattering not a good fit is possible. The result of the fit for the diffuse boundary scattering is shown in Fig. J.5 in Appendix J. As we already mentioned above, the length of the device is small and that probably violates the applicability of the theory in this situation. Therefore, we turn our attention to the weak localization in the ballistic cavities.

6.3.2 Weak localization in ballistic cavities as a possible source of the interference in submicron Corbino devices ?

A zero field peak in the resistance of the ballistic cavities is observed and attributed to the coherent back scattering associated with interference of time-reversed paths [82, 91, 92]. The line shape of the magneto-conductance predicted to be Lorentzian for classically chaotic cavities and linear for the classically regular cavities [83, 92]. The correction to the resistance due to the weak localization is

$$\delta R = \frac{R}{1 + (2B/\alpha_{cl}\Phi_0)^2} \quad , \quad (6.6)$$

where α_{cl} is the inverse of the area enclosed by a typical classical trajectory, Φ_0 is the magnetic flux quantum and $\alpha_{cl}\Phi_0$ gives the FWHM of the magneto resistance peak. For the chaotic cavities the resulting line shape is Lorentzian and for regular cavities the resulting line shape is linear [91, 92] as confirmed experimentally. We show experiment of Chang *et al.* in Fig. 6.14. Chaotic cavity means a small perturbation in the initial conditions of trajectory creates exponentially large unpredictable deviations in the final conditions. For the regular cavities, however, a

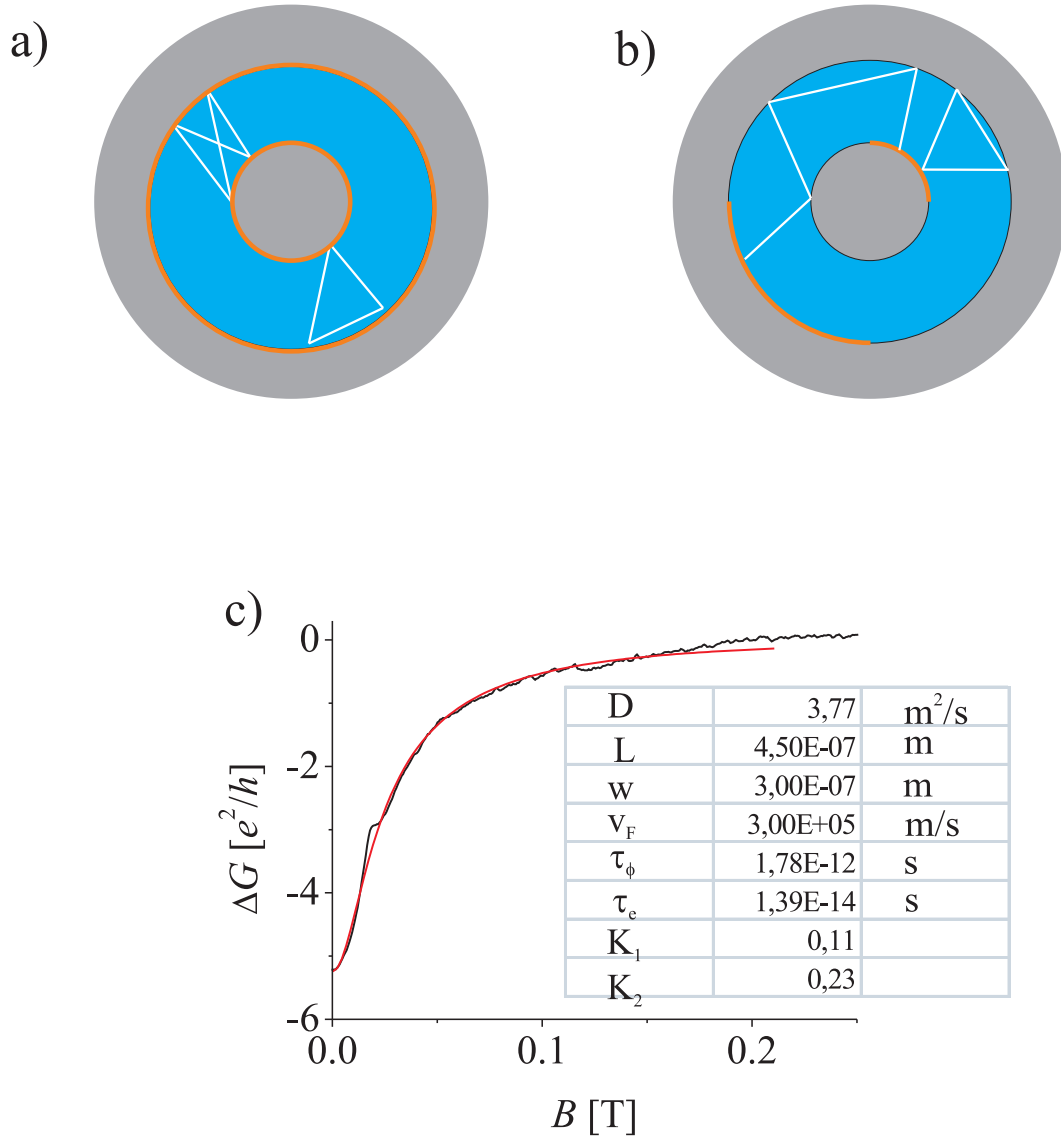


Figure 6.13: (a) A Corbino device with ohmic contacts. Orange represents the formation of the ohmic contacts between the 2DES and metal contact. Contacts are not perfect but partly reflecting. A few example of classical trajectories are shown. (b) Ohmic contact is not formed all around boundary but only in a limited region. The boundary where the ohmic contact formation is absent act as confining walls. (c)

small perturbation in the initial conditions result in a change in the same order. The fit of (6.6) to data of $s\#3$ and $s\#4$ are shown in Fig. 6.15 (a) and (b). Note that before we always plotted the conductance, however, here resistance versus

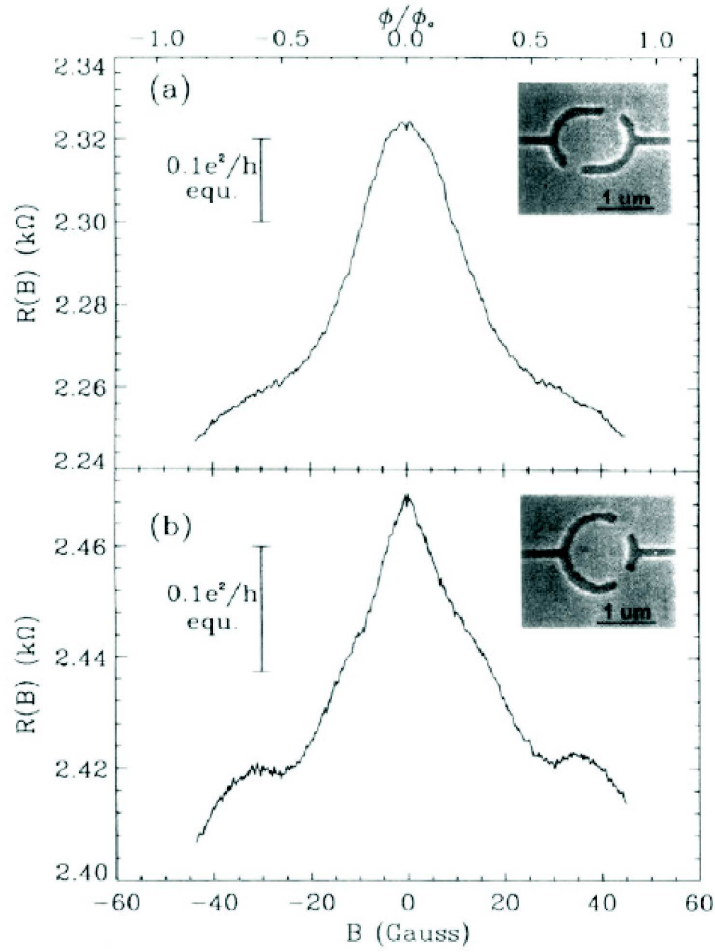


Figure 6.14: The magneto-resistance for (a) for a stadium cavity and for a circle cavity, at $T = 50$ mK. The measurements are performed for 48 cavities in 6 rows in parallel and 8 cavities in each row in series. The plotted magneto-resistance is normalized to a single cavity. The vertical bar shows the equivalent change in the conductance. From Chang *et al.* [92].

magnetic field is plotted, in order to fit relation (6.6) to the data. Therefore, we have now a magneto-resistance peak instead of a magneto-conductance dip. The fit for the rest of the devices is shown in Fig. J.6 in Appendix J. The parameters obtained from best fit of (6.6) to the data are presented in Table 6.4. The area enclosed by a typical classical trajectory is $A_{cl} = 1/\alpha_{cl}$ and r is the radius of a circle enclosing the area A_{cl} .

The extracted area is shown in Fig. 6.16 (a) for $s\#3$ compared to the actual

6.3. Discussion of zero bias anomaly and interference effects as a possible source of the phenomenon

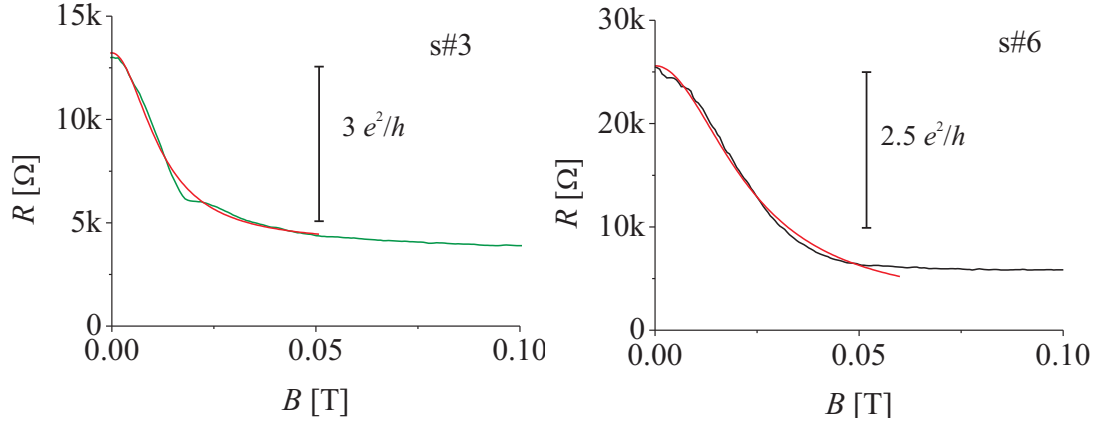


Figure 6.15: Fit of (6.6) to data (a) for Corbino device s#3 and (b) for s#6.

dimension of the device. The extracted area is equivalent to the area of the orange circle. The radius of the circle is $0.24 \mu\text{m}$ is slightly small but comparable to the radius of inner contact. This radius r_{cl} is also comparable to the width Δr of the Corbino devices. This is also the case for other two devices (s#4 and s#5) which have the same size. For Corbino devices s#1, s#2 and s#3, r_{cl} is larger than the inner contact radius, which imply that classical electron trajectory might encircle the inner contact. The extracted area for s#6 is shown in Fig. 6.16 (b) compared to the actual dimension of the device. For this device the radius r_{cl} of the circle

Sample	r_i [μm]	r_o [μm]	Δr [μm]	$\alpha\Phi_0$ [mT]	α_{cl} [μm^{-2}]	A_{cl} [μm^2]	r_{cl} [μm]
s#1	0.10	0.60	0.50	64	15.4	0.065	0.14
s#2	0.15	0.85	0.70	41	9.9	0.101	0.18
s#3	0.25	0.70	0.45	24	5.7	0.175	0.24
s#4	0.25	0.70	0.45	28	6.8	0.147	0.22
s#5	0.25	0.70	0.45	32	7.8	0.129	0.20
s#6	0.15	0.80	0.65	46	11.1	0.090	0.17

Table 6.4: The parameters of the FWHM of magneto conductance dip for the Corbino devices. r_i is the radius of the inner contact, r_o is the inner radius of the outer contact and $\Delta r = r_o - r_i$ is the width of the Corbino device. The FWHM is that of the magneto-conductance dip. A_{cl} is the area extracted from the FWHM and r_{cl} is the radius of the circle that encloses the area A_{cl} .

encircling the extracted area is slightly larger than the radius of the inner contact. However, r_{cl} is smaller than the width of Corbino device Δr . We do not expect that the ohmic contact is formed every where in the interface of contact/2DES. As schematically depicted in Fig. 6.16 (c) the ohmic contact might form only at some limited regions. Then the regions where the ohmic contact is not formed simply behave as confining walls. The 2DES at these regions is fully depleted. It is possible that some stable classical trajectories might form in this contribution as depicted in Fig. 6.16 (c) and thereby leading to constructive interference between time reversal paths.

The amplitude of the conductance dip is in the range of $0.3 e^2/h$ for the experiments on the ballistic cavities [91, 92] as shown in Fig. 6.14. However, the amplitude of the dip in submicron Corbino devices can be as large as $6 e^2/h$. Such a large contribution due to weak localization has not been measured on quantum dots. If magneto resistance peak is due to weak localization, the reason for such a large enhancement of the interference compared to the ballistic cavities is not clear. Nevertheless, all the experimental findings suggest that the observed phenomenon is an interference effect. However, such a large visibility is surprising. We have observed Aharonov-Bohm effect in some of the devices. For instance in Corbino device s#6 there are B periodic oscillation very clearly visible in the magnetic field range of $0.15 \text{ mT} < B < 0.25 \text{ mT}$. Fast Fourier Transform (FFT) gives main period at 6 mT and another one at 50 mT which corresponds to an area enclosed by a circle with $r_{AB} = 0.48 \mu\text{m}$ and $r_{AB} = 0.16 \mu\text{m}$. The FFT results are shown in Fig. J.7 in Appendix J. The inner radius of this device is $r_i = 0.15 \mu\text{m}$ and the outer radius is $r_o = 0.8 \mu\text{m}$. The $r_{AB} = 0.16 \mu\text{m}$ extracted from FFT is similar to $r_{cl} = 0.17 \mu\text{m}$ obtained from magneto-resistance peak. The obtained value of $r_{AB} = 0.48 \mu\text{m}$ is almost at the middle of the device and implies that electron can travel along the Corbino device phase coherently. However, the oscillation amplitude is about $0.25 e^2/h$ and is very small compared to amplitude of magneto-conductance dip. Aharonov-Bohm oscillations are not present for all the devices. For some of the devices Aharonov-Bohm oscillations are present at high magnetic fields as we will see in Chapter 7. Observation of Aharonov-Bohm oscillations suggest that electrons can travel around the closed loops on the Corbino device phase coherently.

Taylor *et al.* reported experiments on small Corbino devices [73]. The radius of the inner contact is $7.5 \mu\text{m}$, the inner radius of the outer contact is $25 \mu\text{m}$ and their outer radius of the outer contact is $40 \mu\text{m}$ for their device². The mean free path is $4 \mu\text{m}$. They observed a magneto-resistance peak which they related to

²Taylor *et al.* [73] reported on the preparation of Corbino devices in submicron scale. However, in their device the inner and outer contact seem to be shorted. Therefore, no useful experiment could be done in the device.

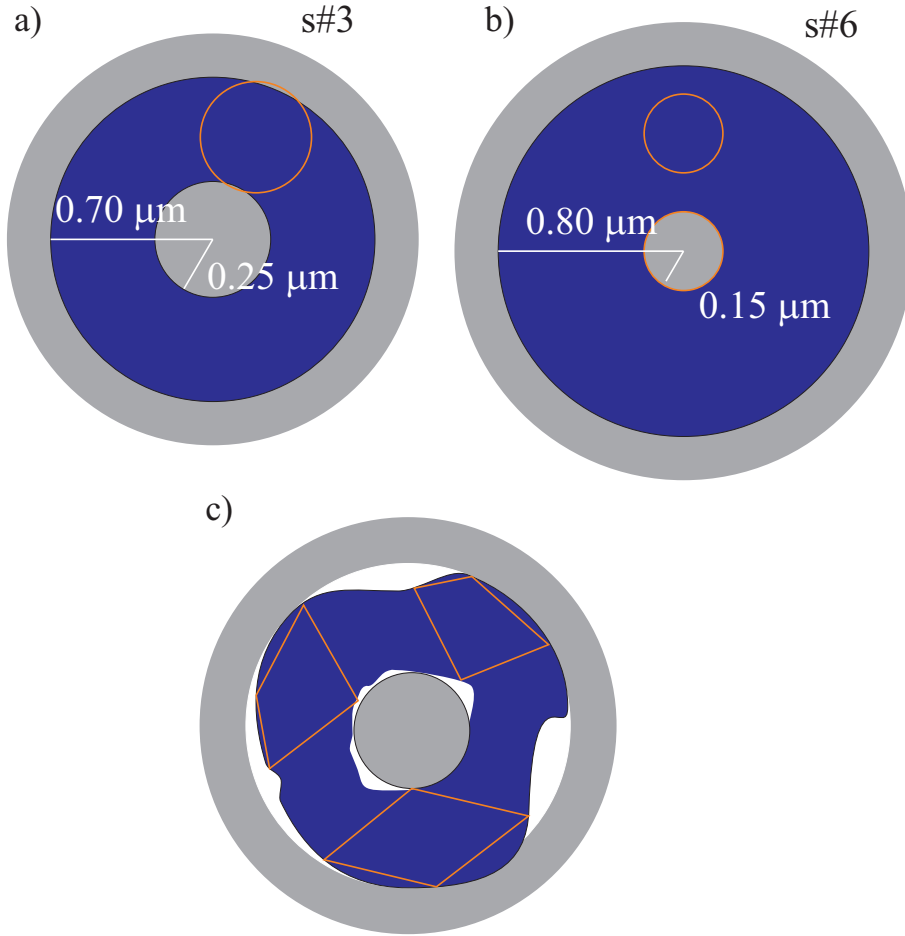


Figure 6.16: (a) The schematic representation of Corbino device s#3. The orange circle encloses the area A_{cl} extracted from FWHM following the theory of weak localization in ballistic cavities. (b) The schematic representation of Corbino device s#6. The orange circle encloses the area A_{cl} extracted from FWHM following the theory of weak localization in ballistic cavities. (c) The ohmic contact does not form everywhere at the border of contact/2DES interface. In the white areas the 2DES is depleted. Orange polygons represents some possible stable trajectories in the constriction.

the weak localization of electrons in the contact region due to the scattering from ohmic spikes. However, in their contact there are spikes which penetrate deep into the heterostructures and this spikes are responsible for the contact formation between the alloyed metal and 2DES. They assume to have a modified 2DES under the contact area. However, this is not the case in our contacts as we already discussed in Chapter 4. Moreover, the width of the contacts in our Corbino devices is small ($0.2 \mu\text{m}$) and does not allow presence of spikes which are reported to have

a diameter of $0.3 \mu\text{m}$ or larger. Therefore, we exclude the role of the ohmic spikes for observed magneto-resistance peak in our device.

The origin of the zero bias anomaly is even less clear. The bias dependent anomaly persist at finite magnetic fields where the magneto conductance is already saturated. The saturation temperature for these two effects are different. This might imply that phase coherence length has a different dependency on temperature for these two effects. The kink at the $\pm 0.25 \text{ mV}$ are unusual. The value of the differential conductance at these bias voltage is larger than the high temperature conductance and large bias conductance. For some of the devices the measured differential conductance is not symmetric on the positive and negative bias side as we will discuss in the next chapter.

6.4 Asymmetric zero bias anomaly

For the Corbino device s#1 there is a slight asymmetry around zero bias voltage, V_{DS} . For this device we have repeated the measurements for two cool-down process. The measured conductance for the first cool-down and for the second cool-down are shown in Fig. 6.17 (a). The asymmetry on the measured differential conductance is clearly visible. In the second cool-down the high temperature (and large bias) differential conductance is higher. In Chapter 5 we have seen that the contact resistance might change for subsequent cool-downs. Therefore increase of conductance (decrease of the contact resistance) for the second cool-down is not surprising. The depth of the dip is also larger in the second cool-down. The FWHM for the second cool-down is also larger and is around 0.15 meV . At 1.5 K the reminiscent of the zero bias dip is still present (The data are shown in Fig. J.3 in Appendix J).

We have exchanged the source and drain terminal to see whether the asymmetry also changes. The results are shown in Fig. 6.6 (b). The dark curve is usual measurement, that is voltage is applied to inner contact (drain) and outer contact (source) is kept at the reference potential. The red curve is for the exchanged setup, that is, the inner contact is kept fixed at the reference potential and the voltage is applied to outer contact. With exchange of the role of the terminals the asymmetry is also reversed. The same asymmetry is also present in the dc current. The dc current is shown in Fig. 6.17 (c).

Now we will discuss possible origin of this asymmetric behavior. The tunnel barriers at the inner contact and outer contact can be asymmetric. This is expectable since the contact resistance on this scale has large deviations. If this is the reason for observed asymmetry, one might expect such an asymmetry for most of the devices since the contact resistances of the inner and outer contact are most probably different. However, we do not see asymmetry for most of the

devices. In Chapter 4 we have seen that contact resistance does not depend on the temperature or has a very weak dependence which imply an infinitely high tunnel barrier between 2DES and the contact. That is, we expect that the strength of the tunnel barrier is not effected by temperature or bias voltage (in the range of 4 K). However, it can happen that for one of the contacts the tunneling barrier is not very high and the strength of the barrier is bias dependent. Such an asymmetric case is depicted in Fig. 6.17 (d) for an 2DES island coupled to leads via tunneling barriers. The right barrier (outer contact) is assumed to be infinitely high and

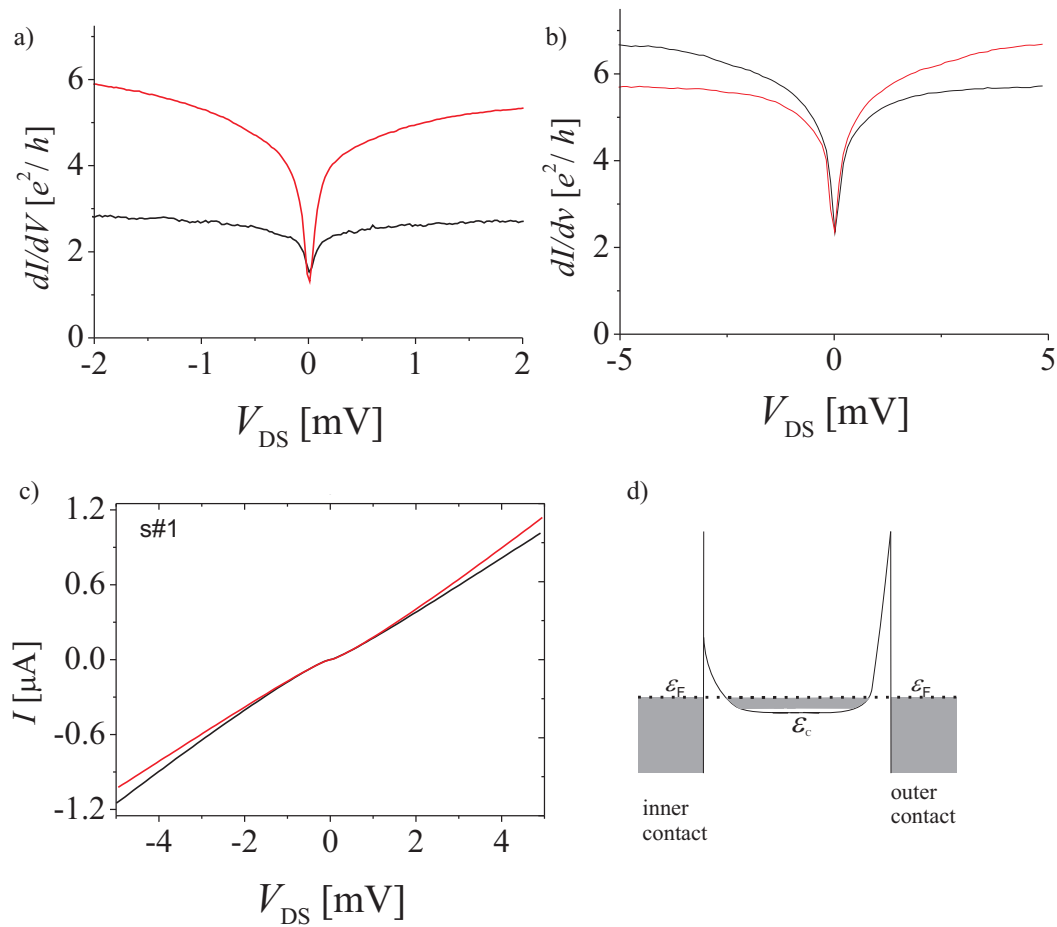


Figure 6.17: (a) Differential conductance measured for two consequent cooling. Black is for first cooling and red is for second cooling. In both cases there is an asymmetry. (b) Differential conductance measured in second cooling for voltage applied to inner (black) and outer (red) contact. (c) The dc current for measurements presented in (a). (d) Model of asymmetric tunnel barriers at the inner and outer contact.

have a bias independent barrier transparency whereas the left one (inner contact) is assumed to have bias dependent barrier transparency. In that case the conductance can depend on which side the voltage drop occurs leading to an asymmetric conductance.

6.5 Induced difference in the electrochemical potential difference between the contact of the Corbino device with sweeping magnetic field

In a Corbino device, as magnetic field is swept there can be a voltage difference between the inner and outer contact due to induced eddy currents in the 2DES [93]. We have performed experiments to observe eddy currents. In one of the Corbino devices (s#6) we have measured the voltage difference between inner and outer contact of the Corbino device as the magnetic field is swept. The outer contact is grounded and the voltage between the inner contact and outer contact is measured by a home-made differential amplifier as magnetic field is swept. The measured voltage is proportional to the electrochemical potential difference between the inner and outer contacts of the Corbino. The result are presented in Fig. 6.18. The red curve is taken at 1.5 K. The green curve is taken at 50 mK for a positive sweep rate and the black curve for a negative sweep rate. As clearly visible, there is a dip at zero magnetic field. As the sweep direction of magnetic field is reversed the same dip is observed (black curve). The FWHM of this dip is 50 mT. This is consistent with the value of the FWHM of the magneto-conductance dip. However, the observed effect can not be explained by eddy currents since the eddy currents should not be effected by the temperature, on this temperature range. Even if it does, there is no reason why it should be sensitive to temperature only around zero magnetic field. Second, as the sweep direction is reversed the electrochemical potential does not change the sign which is expected in the case of eddy currents. The observed effect seems to be correlated to the interference effect which is responsible for the positive magneto-conductance increase since the FWHM is the same. Setup allows for the current flow and the voltage drop over the Corbino device is reflected in this measurement.

6.6 Summary

In this section, we have presented experiments on submicron scale Corbino devices at low temperatures. This is the first successful realization of Corbino devices on this scale. Experiments are performed under small magnetic fields and at zero

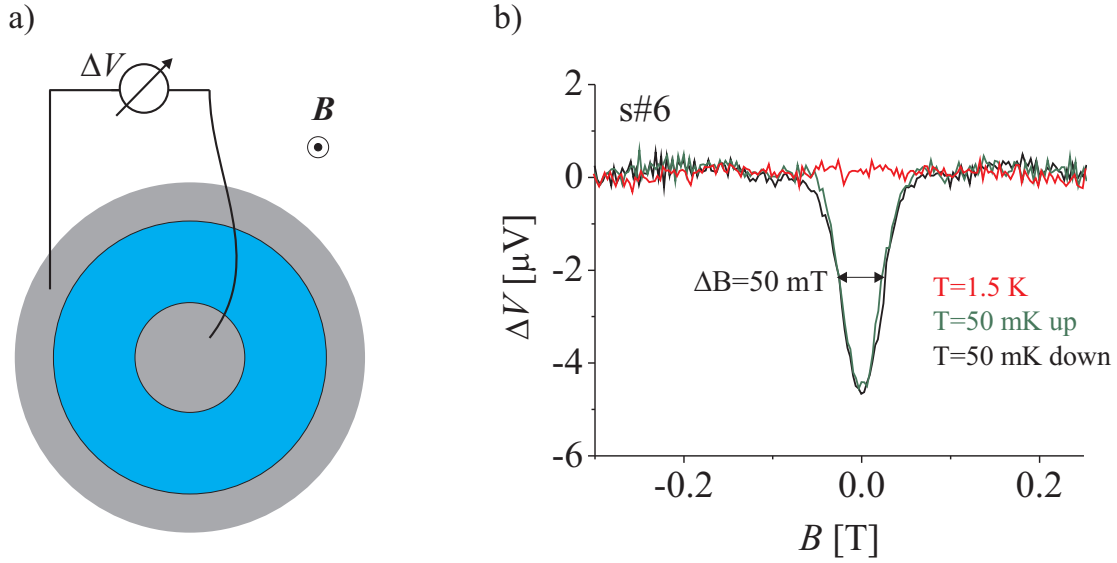


Figure 6.18: (a) Voltage difference between inner and outer contact of the Corbino is measured as the magnetic field is swept. (b) Measured voltage difference at 1.5 K (red) and 50 mK (green) for positive sweep rate of 0.3 T/min. The black curve is for negative sweep rate of -0.3 T/min at 50 mK.

magnetic field.

- We have prepared several Corbino devices in submicron scale. The yield of working devices is about 25%. For the dimension of measured devices the radius of the inner contact is between $0.1 \mu\text{m}$ and $0.25 \mu\text{m}$. The inner radius of the outer contact is between $0.4 \mu\text{m}$ and $0.85 \mu\text{m}$. Overall, 6 devices are characterized.
- At zero magnetic field, at 50 mK we have observed a zero bias anomaly—a large dip— in differential conductance. There is a huge dip in the differential conductance versus bias voltage curve, centered at zero bias. The amplitude of the zero bias dip decreases with increasing temperature. At 1.5 K the dip completely disappears in three devices and in three devices are slightly present.
- The depth and width of the zero bias dip tends to saturate below 100 mK.
- The FWHM obtained from a Lorentzian function fit to the data varies between 0.10 mV and 0.15 mV. The amplitude $\Delta G = G^L - G^H$ of the zero bias dip varies between $1e^2/h$ to $7.5e^2/h$, where G^L is the low temperature conductance at zero bias and G^H is the high temperature conductance. ΔG

scales linearly with G^H with a proportionality constant of -0.85 . This suggest that 85% of the conduction electrons take part in the interference. The FWHM of the dips has a tendency to increase as the G^H increases.

- When a perpendicular magnetic field is applied, we have observed a positive magneto-conductance dip. That is the conductance increases and saturates at already 0.2 T. The observed magneto conductance dip is symmetric for the magnetic field reversal. The saturated magnetic field value $G(B = 0.2 \text{ T})$ is smaller than the high temperature value of conductance G^H . Although, the positive magneto conductance dip saturates at 0.2 T, the zero bias anomaly is partly present. This suggest that two effect might be of different origin.
- The depth of the magneto-conductance dip linearly scales with the finite field saturated conductance $G(B = 0.2 \text{ T})$ with a slope of -0.75 . The FWHM of the magneto-conductance dip is smaller for larger $G(B = 0.2 \text{ T})$. The FWHM is larger for the larger devices (for larger width of the Corbino devices)
- As the temperature increases the magneto-conductance dip is less pronounced and completely disappears at about 500 mK. Therefore, temperature scales for magneto-conductance dip and zero bias dip are different, since the zero bias dip persist at temperatures higher than 500 mK.
- We have considered weak localization as a possible source of observed phenomena. The fit of theory of Beenakker *et al.* for weak localization in 1-D wires to magneto-conductance dip gives a good qualitative agreement. However, the phase coherence length and mean free path obtained from the fit is unreasonably small.
- As a second scenario we considered theory of weak localization in ballistic cavities following Baranger *et al.* The fit of theory to magneto-resistance peak gives an area enclosed by the typical classical trajectories responsible for the interference. The radius r_{cl} of the circle enclosing the area obtained from the fit ranges between $0.15 \mu\text{m}$ to $0.24 \mu\text{m}$. The obtained radius is comparable or slightly smaller than the radius of the inner contact for three of the devices and slightly larger than the radius of the inner contact for three of the devices, i.e. trajectories enclosing inner contact in the 2DES are possible.
- The electrochemical potential difference between the contacts of the Corbino has an unusual dip centered at zero magnetic field. The FWHM of this dip is similar to the value of the FWHM of the magneto-conductance dip.

Chapter 7

Experiments on submicron GaAs/Al_δGa_{1-δ}As Corbino devices at high magnetic fields: observation of single-electron charging

We have discussed in Chapter 2 that there exist compressible and incompressible stripes in the depletion region of a 2DES. Compressible stripes have metallic and incompressible stripes insulating properties. We also have seen that scanning probe experiments on the Hall potential profile of QHE samples show that incompressible stripes exist also along boundaries to the alloyed ohmic contacts. Based on this findings we have proposed in Chapter 3.3 the submicron scale Corbino devices as a new type of single-electron charging device. In this Chapter we will investigate transport properties of submicron scale Corbino devices under high magnetic field.

7.1 Submicron scale Corbino devices under strong magnetic fields

The details of the device and measurement setup are described in Chapter 6. Measurements are performed at 30 mK. The conductance versus magnetic field measured on Corbino device s#1 is shown in Fig. 7.1 as red line. The blue line is measured between the outer contact of the Corbino device and a reference contact in the sample in order to determine the bulk properties of the 2DES, like the electron concentration. Bulk filling factor values are indicated with blue color

extracted from the Shubnikov-de Haas oscillations visible in the blue curve. It is not easy to extract the exact value for the density in the Corbino device since the Shubnikov-de Haas oscillations are not clear. The reason for the absence of clear Shubnikov-de Haas probably is the inhomogeneous density profile around the contact due to partial or full depletion. However, comparing the bulk measurement and Corbino measurement one can see that the density in the Corbino is almost half of the bulk value. The first way to see this is the absence of a peak between 6 T and 8 T. If the density are nearly the same one would expect a peak between bulk $\nu = 3$ and $\nu = 4$, which is not the case. However, if we assume that the plateau between 5 T and 8 T is the $\nu = 2$ plateau then the other conductance minima are found to be consistent with the filling factor values. The filling factor values for the Corbino device are shown in red color. As clearly visible the minima in the conductance are consistent with $\nu = 4$ and $\nu = 6$. We confirmed the given filling factor values by an independent measurement: we have tuned the density by tuning the voltage applied to the back side of the sample (back gate voltage). As the density is changed by Δn_s , the position of a feature in the conductance located at $\nu = x$ shifts by the amount $\Delta B = \Delta n_s/x$. To eliminate n_s one can compare two features, i.e. located at $\nu = \nu_1$ and $\nu = \nu_2$. Then

$$\frac{\Delta B_1}{\Delta B_2} = \frac{\nu_2}{\nu_1} \quad , \quad (7.1)$$

where ΔB_1 is the shift in the position of peak at $\nu = \nu_1$ and ΔB_2 is the shift in the position of peak at $\nu = \nu_2$. By comparing the shift of two peaks, located at the $B = 6.8$ T and $B = 14.02$ T, we obtained $\nu_2/\nu_1 = 2.08$ in a good agreement with the value of $B_{\nu=2} = 6.5$ T which is the mid point of the conductance plateau between $5 \text{ T} < B < 8 \text{ T}$. Thus, we have confirmed the validity of the values of filling factor given in red in Fig. 7.1 for the Corbino device. Therefore, the sheet density in the annulus is $n_s = 3.14 \times 10^{11} \text{ cm}^{-2}$, which is half of the bulk value. The possible error on the position of the filling factor is indicated by the green bars on the figure. We estimate the number of electrons in the annulus as $N_e = 3.45 \times 10^3$ taking the area of the Corbino device as $A_C = \pi(r_o - r_i)^2$ where $r_o = 0.6 \mu\text{m}$ and $r_i = 0.1 \mu\text{m}$. However, we expect N_e to be smaller since the area of the annulus is expected to be smaller due to partial or full depletion at some regions at the contact/2DES interface.

Now we want to show that from the magneto-transport data we can state that we have a Corbino topology, that is, the 2DES in the annulus is not completely depleted in any region. The fact that the conductance is zero for $\nu = 2$ and $\nu = 1$ means that we indeed have an unterminated Corbino geometry. In Fig. 7.2 two scenarios for the electron density distribution in the Corbino device under high magnetic field are shown. When the 2DES in the annulus is not depleted completely, as depicted in Fig. 7.2 (a), compressible stripes encircle along the

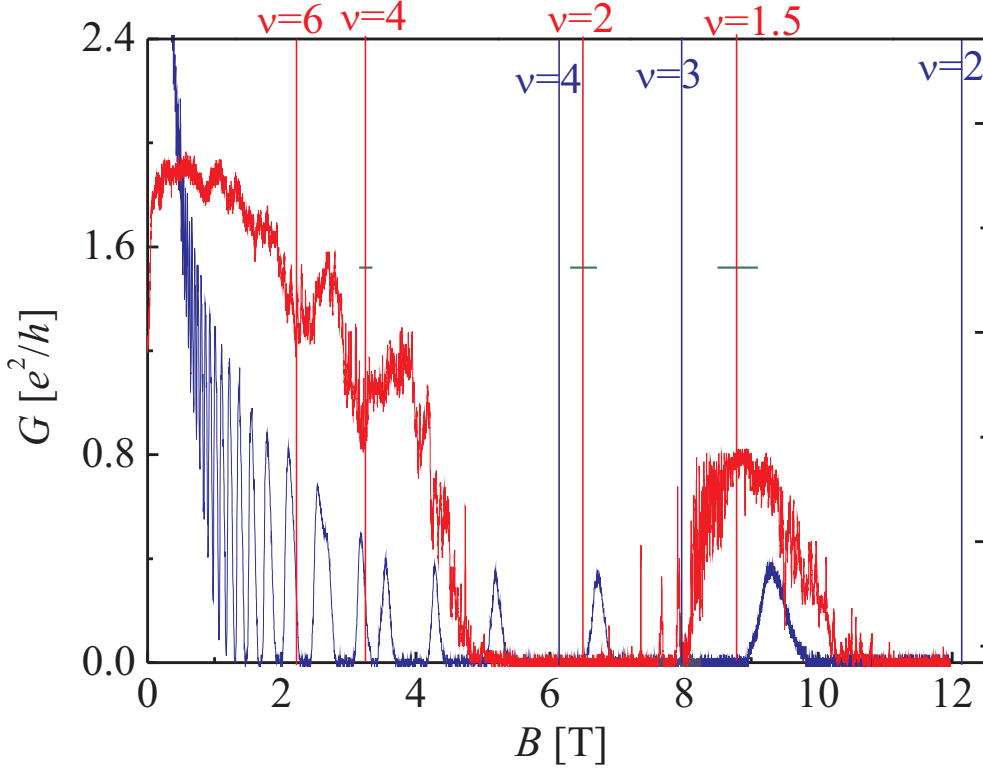


Figure 7.1: Magneto-conductance measured on the Corbino device *s*#1 (red curve). Blue curve is measured between the outer contact of Corbino and a reference contact on the sample. The red indicated filling factor values are for the Corbino device extracted from the red curve and the blue indicated filling factor values are bulk values extracted from the Shubnikov-de Haas oscillations of the bulk (blue) measurement.

contact but the inner incompressible stripe and outer one are not connected. The conductance becomes zero when the incompressible stripes are wide enough to insulate the inner compressible region from the contacts. Since the conductance goes zero for $\nu = 2$ and $\nu = 1$ we are convinced that we have a Corbino topology for the 2DES in the device. However, this is not the case for all the devices that we have measured. Now assume that we have a Corbino device as shown in Fig. 7.2 (b) in which the 2DES is depleted completely in some regions. In this geometry the inner and outer contact are always connected by a compressible stripe, and conductance does not become zero for any magnetic field. For Corbino devices *s*#3 and *s*#5 conductance does not become zero even at high magnetic fields. Magneto-conductance for these devices are shown in Fig. K.1 in Appendix K.

Now we will have a close look on the fine details of the conductance curve of

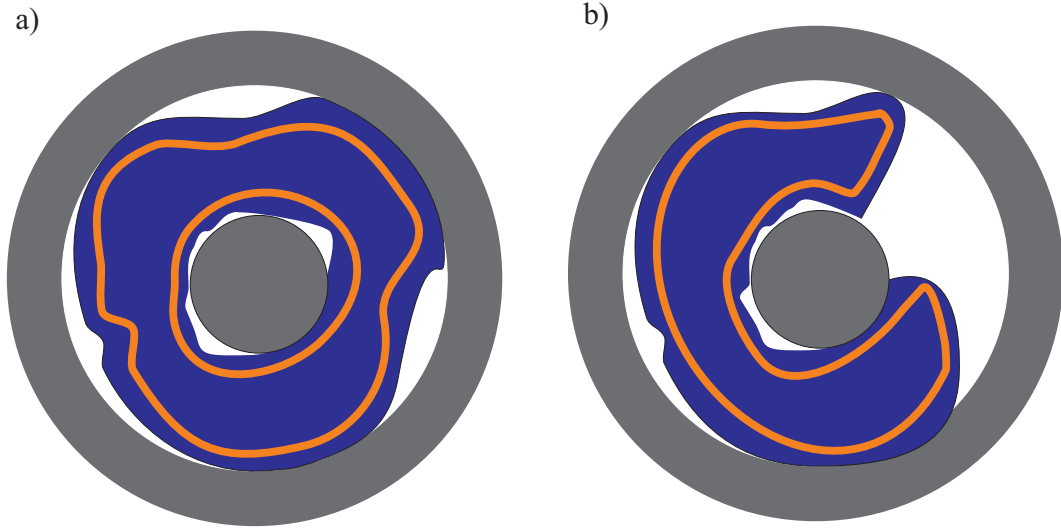


Figure 7.2: (a) Schematic representation of a Corbino device under strong magnetic field. White represent depleted regions, orange represents incompressible regions and blue represents compressible regions. (b) Schematic representation of a Corbino device with a complete depletion between the contact at some regions. In this situation, under strong magnetic field, compressible regions always connect inner and outer contact.

the Corbino device which has already been shown in Fig. 7.1. In Fig. 7.3 (a) the conductance versus magnetic field between 0 T and 2.5 T is shown. The dip around zero magnetic field was discussed in Chapter 6. In Fig. 7.3 (b) the conductance versus magnetic field is shown for the magnetic field range $2.5 \text{ T} < B < 5 \text{ T}$. In this range there are reproducible conductance oscillations. The field range for consequent peaks is mainly around 60 mT for $2.0 \text{ T} < B < 2.5 \text{ T}$ and changes between 30 mT to 40 mT for the magnetic field range $3.0 \text{ T} < B < 3.4 \text{ T}$. There are conductance peaks in the magnetic field range $7 \text{ T} < B < 8 \text{ T}$ as shown in Fig. 7.3 (c) and (d). Beyond 8 T the conductance increases and there are some oscillations between 8 T and 10 T. The oscillation between magnetic field range $8 \text{ T} < B < 9 \text{ T}$ are B periodic. The FFT analysis of the data between magnetic field range $8 < B < 9$ is shown in Fig. 7.4. The blue curve in Fig. 7.4 (a) is the measured data. To get rid of smooth background, we fit a polynomial to the data. This gives us a measure for the smooth background and then the smooth background (the fitted polynomial) is subtracted from the data. The red curve in Fig. 7.4 (a) shows the data after subtraction of smooth background. In Fig. 7.4 (b) the FFT of the data is shown. The FFT gives three main peaks for $\Delta B_{AB} = 14 \text{ mT}$, $\Delta B_{AB} = 18 \text{ mT}$ and $\Delta B_{AB} = 38 \text{ mT}$. Aharonov-Bohm type oscillations are expectable since we have a ring geometry. The period of the magnetic field is

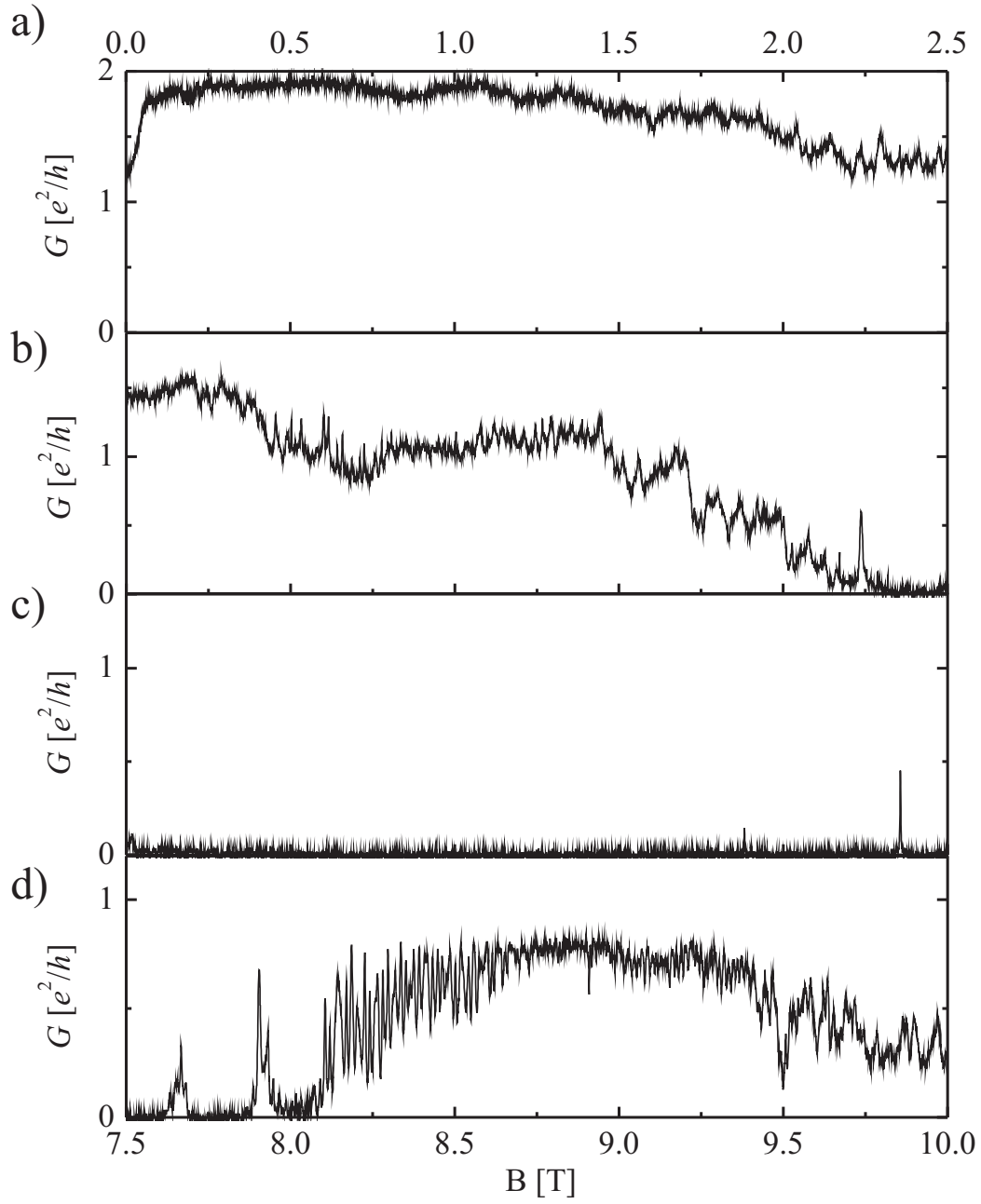


Figure 7.3: Conductance versus magnetic field measured in Corbino device s#1. (a) For magnetic field range $0 \text{ T} < B < 2.5 \text{ T}$, (b) $2.5 \text{ T} < B < 5 \text{ T}$, (c) $5 \text{ T} < B < 7.5 \text{ T}$ and (d) $7.5 \text{ T} < B < 10 \text{ T}$.

related to the area A_{AB} enclosed by the interfering trajectories,

$$A_{AB} = \frac{\Phi_0}{\Delta B_{AB}} . \quad (7.2)$$

The radii of the circle enclosing the areas corresponding to $\Delta B_{AB} = 14$ mT, $\Delta B_{AB} =$

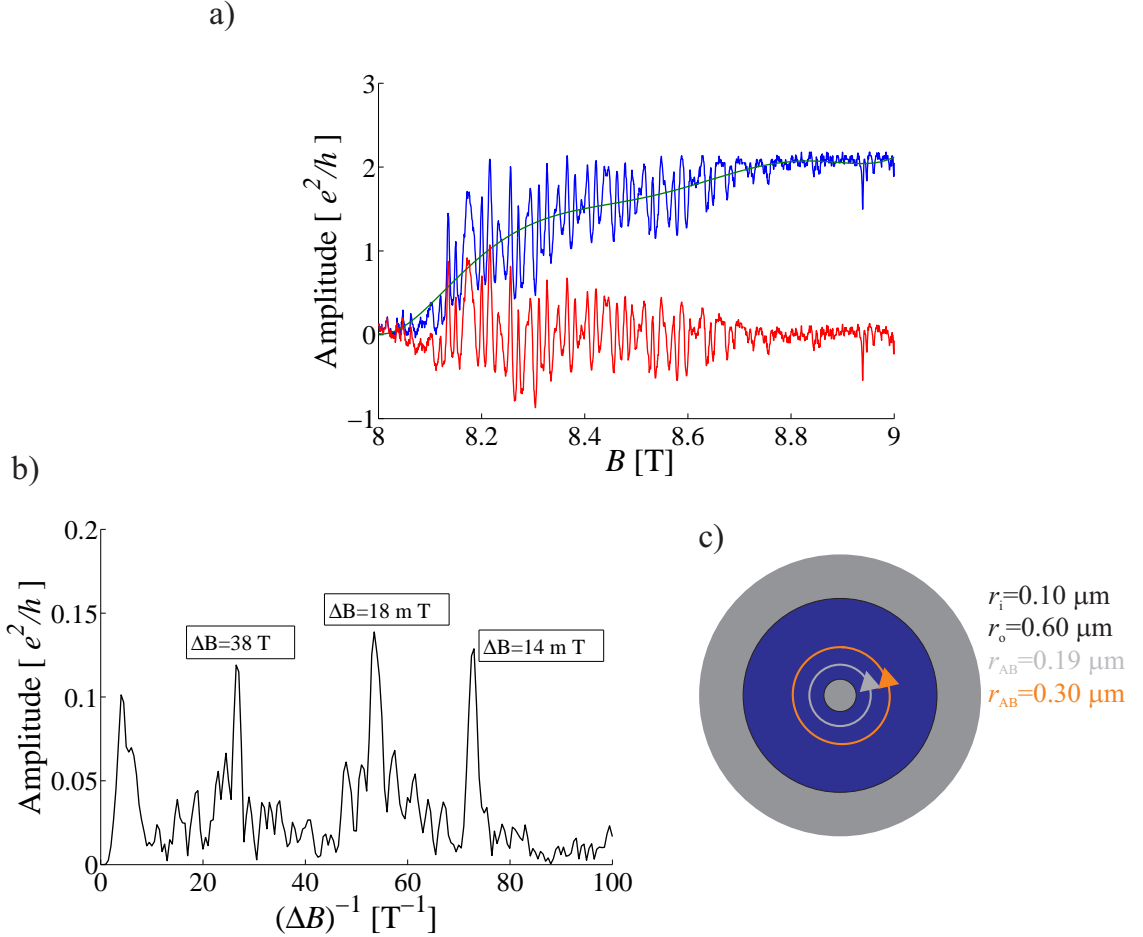


Figure 7.4: (a) Periodic magneto-conductance oscillations. The blue line gives the measured data. The green line is a polynomial best fit to data. The red curve represent the data after subtraction of smooth back ground (green line). (b) FFT of red curve in (a). Magnetic field period for each peak is indicated. The peak at low frequency is probably due to the reminiscent of background since the polynomial fit does not get rid of the background completely. (c) Schematic representation of the Corbino device. The gray and orange circles enclose the Aharonov-Bohm area extracted from periodicity $\Delta B_{AB} = 38$ mT and $\Delta B_{AB} = 14$ mT. The radius r_i of the inner contact and inner radius r_o of the outer contact are indicated.

18 mT and $\Delta B_{AB} = 38$ mT are $r_{AB} = 0.30 \mu\text{m}$, $r_{AB} = 0.27 \mu\text{m}$ and $r_{AB} = 0.19 \mu\text{m}$, respectively. All these values are larger than the inner contact radius which is $r_i = 0.10 \mu\text{m}$. The peak for $\Delta B_{AB} = 18$ mT is probably the second harmonic of the $\Delta B_{AB} = 38$ mT peak. That is, this peak is the $\Phi_0/2$ *Altshuler-Aronov-Spivak* (AAS) [58] effect which corresponds the same area for the $r_{AB} = 0.19 \mu\text{m}$. The extracted values of radius for the interfering trajectories encloses the inner contact as shown in Fig. 7.4 (c), i.e. interference can take place around the inner contact.

7.2 Observation of single-electron charging in Corbino devices

As we have seen there are some conductance peaks in the $\nu = 2$ plateau. In this section we will investigate the nature of these peaks. The measurement method is already described in section 6.2.3. Here the source-drain bias is swept for a fixed magnetic field and magnetic field is changed in a step-like manner. The differential conductance measured as a function of source-drain bias voltage and magnetic field is shown in Fig. 7.5. The diamond-like features which are signature of the Coulomb blockade effect are clearly visible. It is important to note that the horizontal axis is the magnetic field not the gate voltage. The energy level of the system shift linearly with magnetic field. That is, the magnetic field plays the role of the gate voltage on quantum dot systems. Starting from lower magnetic field values we will give center position and filling factor values for the diamonds. The first diamond is centered at 7.19 T ($\nu = 1.80$). This diamond is, however, not visible at the lower half. The second diamond is centered at 7.5 T which corresponds to filling factor value of $\nu = 1.73$. The third one is located at 7.8 T which corresponds to filling factor value $\nu = 1.66$. The fourth one is located at 8.05 T which corresponds to filling factor value $\nu = 1.61$. This one is less pronounced.

Let us look at some of the general features on this plot. The diamond-like features are observed between $\nu = 1.5$ and $\nu = 1.8$. The differential conductance is zero for zero bias voltage and also for small bias voltages in the plateau region. We will call this region of zero conductance as zero conductance valley. However, a finite differential conductance is measured beyond $V_{DS} \approx 0.22$ mV on the positive bias side and beyond $V_{DS} \approx -0.45$ mV on the negative bias side. The value of the differential conductance in this regime is constant of voltage and is $0.5 e^2/h$ which is more clearly visible in Fig. 7.5 (b). The measurement of a finite differential conductance with applied bias is probably due to breakdown of the QHE. We will discuss the origin of this behavior in section 7.6 comparing data for different samples and different filling factor values.

Now we want to have a close look on the diamond structures. In Fig. 7.6 (a)

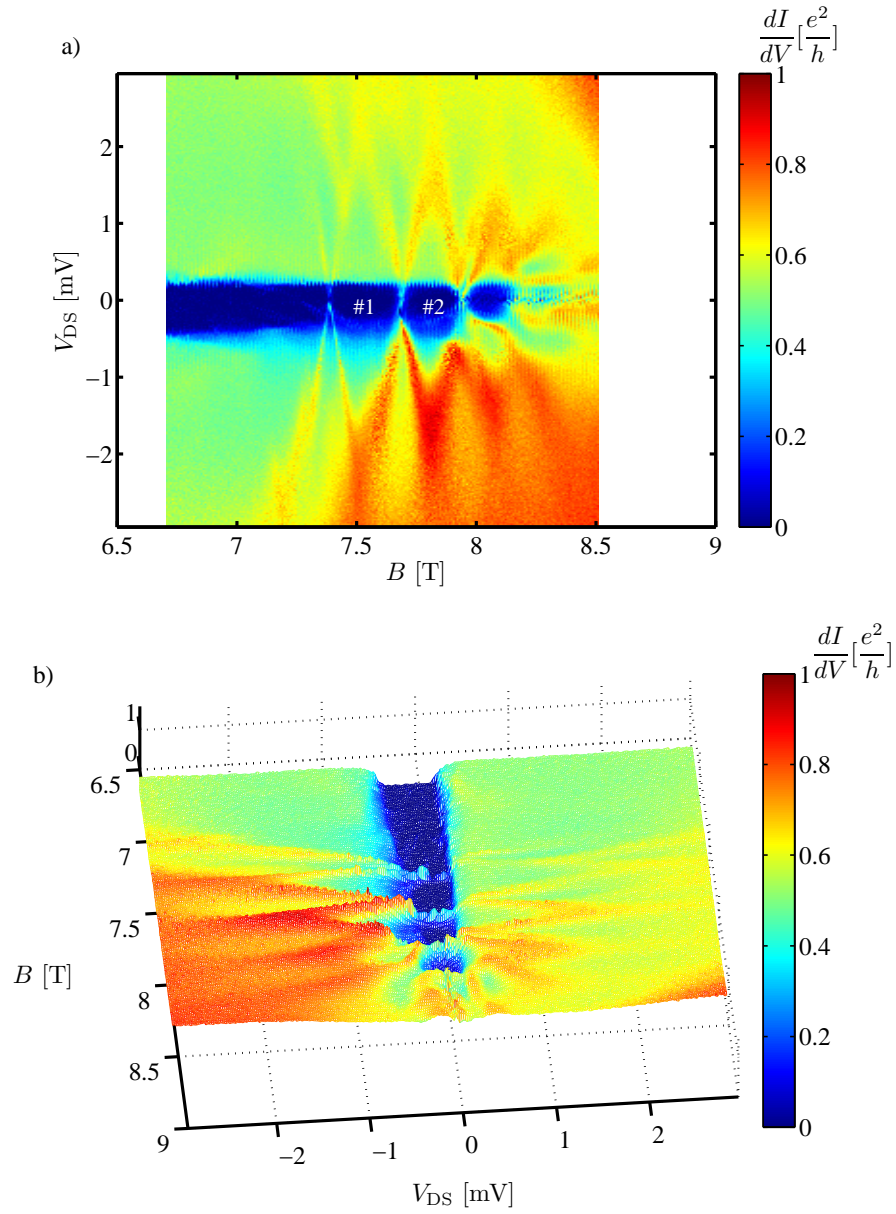


Figure 7.5: (a) Differential conductance versus bias voltage and magnetic field for s#6. (b) Pseudo 3D plot of the same measurement.

the same measurement of Fig. 7.5 is shown. The charging energy $E_c = e^2/2C_\Sigma = e\Delta V_{DS}/2 \approx 1$ meV, where ΔV_{DS} is the width of the diamonds in bias voltage axes. One can extract the size of the island from the charging energy via the total capacitance. For a flat disk, the self capacitance is $C = 8\epsilon\epsilon_0 r_0$ where r_0 is the radius of the disk [40]. Then one obtains the value $r_0 = 85$ nm for $E_c = 1$ meV. This value of $r_0 = 85$ nm is very small compared to the size of the Corbino device. For a ring with radius r and width of ring Δr one can approximate the ring as a long wire which has a self capacitance of $C = 2\pi\epsilon\epsilon_0 L(\ln(L/\Delta r))$ where $L = 2\pi r$. $E_c = 1$ meV and $\Delta r = 10$ nm gives $r = 64$ nm which is also small compared to the size of the Corbino.

The width of diamond # 1 is $\Delta B = 0.29$ T and the width of diamond # 2 is $\Delta B = 0.27$ T. The energy levels of the structure shifts linearly with magnetic field. Important to note, the magnetic field acts like a gate voltage. For instance, a magnetic field change $\Delta B = 0.29$ T shifts the energy level of the island by $\Delta E = e\Delta V_{DS} = 2.37$ meV. The change in the Landau level energy for the magnetic field change is described by

$$E_n = \hbar\omega_c(n + \frac{1}{2}) \quad . \quad (7.3)$$

Since the filling factor is in the range $1 < \nu < 2$, i.e. $n = 0$, we obtain $\Delta E_n = 0.26$ meV for $\Delta B = 0.29$ T. Therefore, the linear shift in the energy levels cannot be simply due to the energy shift in the Landau level. We have defined a dimensionless parameter

$$\alpha = \frac{e\Delta V_{DS}}{\Delta(\hbar\omega_c)} \quad . \quad (7.4)$$

Here ΔV_{DS} is the width of the diamond in the source-drain bias voltage axis and $\Delta(\hbar\omega_c) = e\Delta B/m^*$ is the change on the cyclotron energy due to the magnetic field interval ΔB . Indeed, α gives the slope of the lines at the border of diamonds. The values of α are indicated along each border. The α values can be different on both sides of the diamonds. As the role of the terminals of the Corbino exchanged (that is the voltage is applied to outer contact and the inner contact is fixed) the diamonds are simply mirrored as shown in Fig. 7.6 (b).

What is the origin of this behavior? As we have seen a simple charging energy does not fit the device dimension and the energy scale. If we consider the diamond #2 and #3 the periodicity in magnetic field is about $\Delta B = 0.29$ T. Let us assume we have a ring as shown in Fig. 7.7 (a). As we have seen in Chapter 3.4 crossing between the energy levels of a quantum ring is periodic with the addition of a flux quantum to the area of the ring. However, $\Delta B = 0.29$ T corresponds to the addition of a flux quantum to the area of a ring that have a radius about 60 nm. Interestingly, this value is consistent with the size of the ring extracted from the charging energy assuming a ring with a width of $\Delta r = 10$ nm. This value is

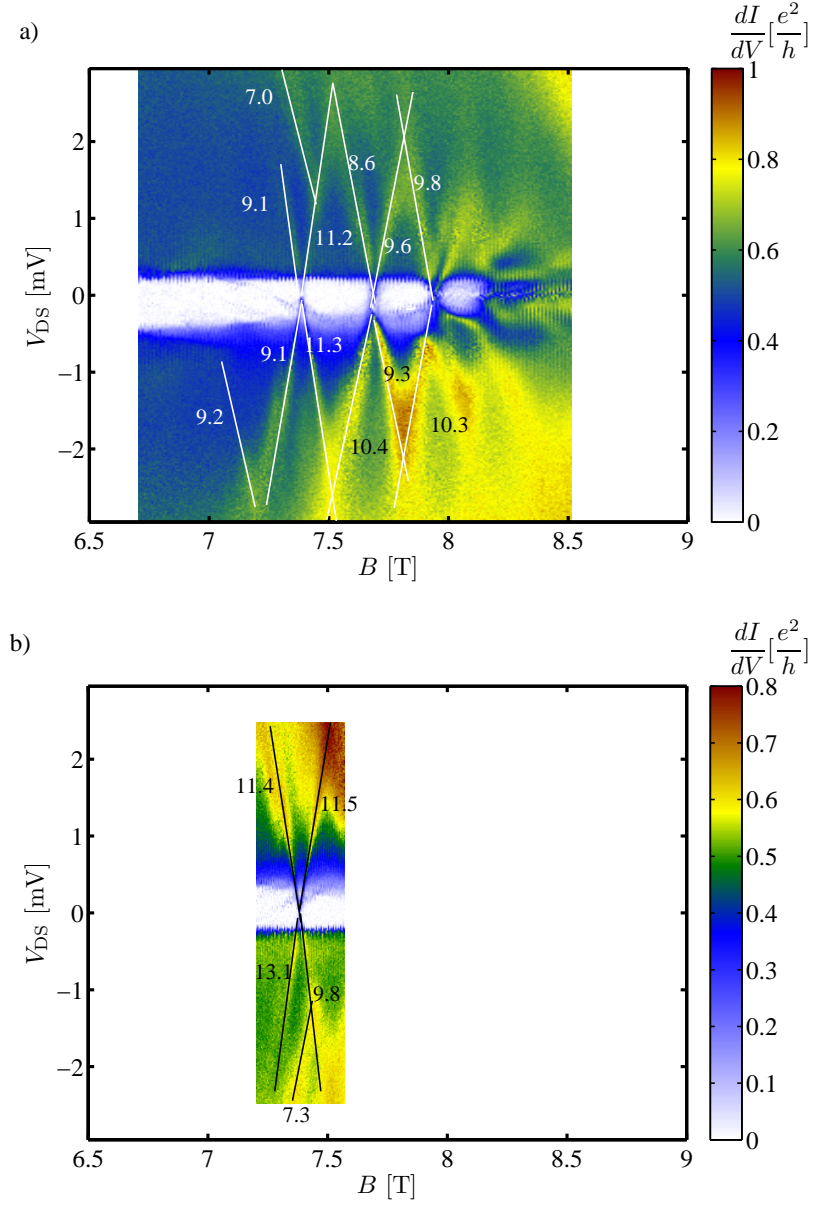


Figure 7.6: (a) Differential conductance versus bias voltage and magnetic field for s#6. (b) The role of the terminals are exchanged. That is the bias voltage is applied to the outer contact and the inner contact is kept at the reference potential. α indicates the slope of the lines according relation (7.4).

very small compared to the size of the device. The fact that the periodicity for the diamond features is $\Delta B = 0.29$ T means that the periodicity is not due to

the addition of the flux quantum to an area enclosing the inner contact. On the other hand, the radius of the circle enclosing the area extracted from B periodic oscillations is larger than the inner contact radius. Therefore, we cannot explain the data in terms of energy levels of the quantum rings since the periodicity does not fit.

Now let us assume that we have the geometry shown in Fig. 7.7 (b). There is an incompressible stripe in the middle of the Corbino device. However, there can be a small compressible puddle in the incompressible region. Then the single-electron tunneling is possible through this compressible island. As we already calculated before from the value of charging energy the radius of such an island can be around 85 nm. This picture can also explain the existence of the resonant lines of the diamond in the zero conductance valleys: even if the transport through the Corbino device is blocked due to the incompressible ring, there will be a finite conductance whenever the energy level of the island is resonant. Now one might ask why the energy level of the island shifts linearly with magnetic field. One possibility is that a quantum dot is formed in a region that have a local filling factor $2 < \nu < 4$. If that would be the case then the energy level of the quantum dot oscillate in a zigzag fashion with magnetic field as we have seen in Chapter 3.2.1. The periodicity in magnetic field can be approximated to $\Delta B \approx (\omega_0/\omega_c)^2 B$ where $\hbar\omega_0$ is the strength of the confining potential. For $\Delta B = 0.29$ T and $B = 7.5$ T one obtains $\hbar\omega_0 = 2.6$ meV. Then the $\Delta E = \hbar(\omega_0^2/\omega_c) \approx 0.5$ meV. This is smaller than $\Delta E = e\Delta V_{DS} = 2.37$ meV. However, this is valid for the $2 < \nu < 4$. Another possibility is that as the magnetic field is increased the incompressible region shrinks and the island becomes smaller. However, in that case the charging energy should become larger which is not the case in the experiment. The size of the diamonds becomes smaller with increasing magnetic field. But this might also be due to the fact that the island is more strongly coupled to the leads, since generally for the quantum dot systems as coupling become stronger the total island capacitance get smaller [40]. The weakest point of the above argument having a compressible island is that why only one island. There is no reason why not having more than one. Cycling the device to room temperature and cooling it again one probably get another density profile. With cycling the device to room temperature and cooling it again the charge configuration in the donor layer might be different. Therefore, if this is just by coincidence it should not be reproducible. However, we reproduce this results after cycling the device to the room temperature as we will see in the next section.

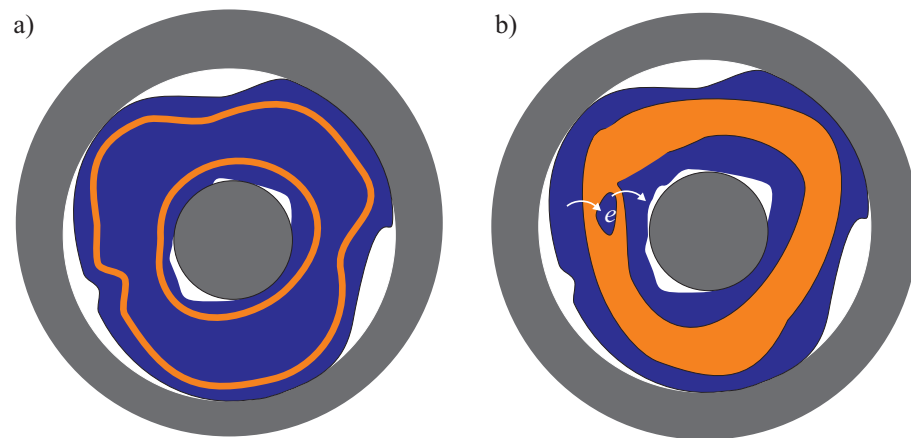


Figure 7.7: (a) Scheme of a Corbino device under high magnetic field. Incompressible stripes (orange) encloses the main compressible stripe (blue). The inner compressible stripe can be thought of being a quantum ring. (b). There is a wide incompressible stripe in the middle of the device and a small compressible island in the incompressible region. The island is a quantum dot coupled to the inner and outer compressible regions via insulating incompressible region.

7.3 Reproducing the experimental results after cycling the device to room temperature.

We have cycled the Corbino device *s#1* to room temperature and cooled it to low temperatures again. Conductance versus magnetic field measured at 30 mK is shown in Fig. 7.8 (a). The density seems to be roughly the same as previous cooling. However, the features around 8 T is slightly modified compared to the first cooling which was shown in Fig. 7.1. In the first cooling there was a sharp peak at this magnetic field, however, now it is broad. In Fig. 7.8 (b) periodic magneto conductance oscillations between 7 T and 10 T for three different temperatures are shown. The oscillations are very sensitive to temperature and at 240 mK already absent. The FFT analyzes between 7.8 T and 8.2 T gives the periods $\Delta B = 38$ mT, $\Delta B = 25$ mT and $\Delta B = 14$ mT. The extracted Aharonov-Bohm radii are $r_{AB} = 0.18 \mu\text{m}$, $r_{AB} = 0.22 \mu\text{m}$ and $r_{AB} = 0.30 \mu\text{m}$, respectively. Between 8.4 T and 9.2 T, FFT analyzes give the period $\Delta B = 40$ mT, $\Delta B = 32$ mT and $\Delta B = 14$ mT. The FFT results are shown in Fig. K.2 and Fig. K.3 in Appendix K. The temperature dependence of the amplitude of FFT peak ($8.4 \text{ T} < B < 9.2 \text{ T}$) is shown in Fig. 7.8 (c). As clearly visible, the oscillations disappear already at 160 mK.

The differential conductance measured as a function of source-drain bias voltage and magnetic field is shown in Fig. 7.9. The diamond-like features are clearly visible. Diamonds are smaller compared to the first cooling. The fact that we reproduce the main results of the previous cooling shows that the obtained results are not by a coincidence. The diamonds look a bit modified. However, they are present about the same filling factor range. The zero conductance valley at zero bias voltage and the asymmetry of the valley is also reproduced.

We have repeated the above measurement which is shown in Fig. 7.9 with a better resolution in a limited range and the result is shown in Fig. 7.10 (b). Here we see the periodic oscillations at finite bias voltage. This oscillations persist at finite bias voltages as large as $V_{DS} = -0.5$ mV. Two line cuts are shown in Fig. 7.10. The magnetic field periodicity is $\Delta B_{AB} = 15$ mT. If they are h/e Aharonov-Bohm oscillations then the radius of the circle enclosing the area implied by the period is $r_{AB} = 0.30 \mu\text{m}$. These can also be $h/2e$ AAS oscillations [58]. In this case, the radius of the circle enclosing the area implied by the period is $r_{AB} = 0.21 \mu\text{m}$. Where and how can such an interference take place? Electrons entering into Corbino device from one contact can travel on a inner compressible ring and interfere before leaving to the other contact. Another possibility is that electrons on a incompressible stripe shrinks to keep the enclosed flux constant as the magnetic field is increased. This might change the width of the incompressible stripe thereby modifying the conductance. The interference is visible in the plateau region whenever

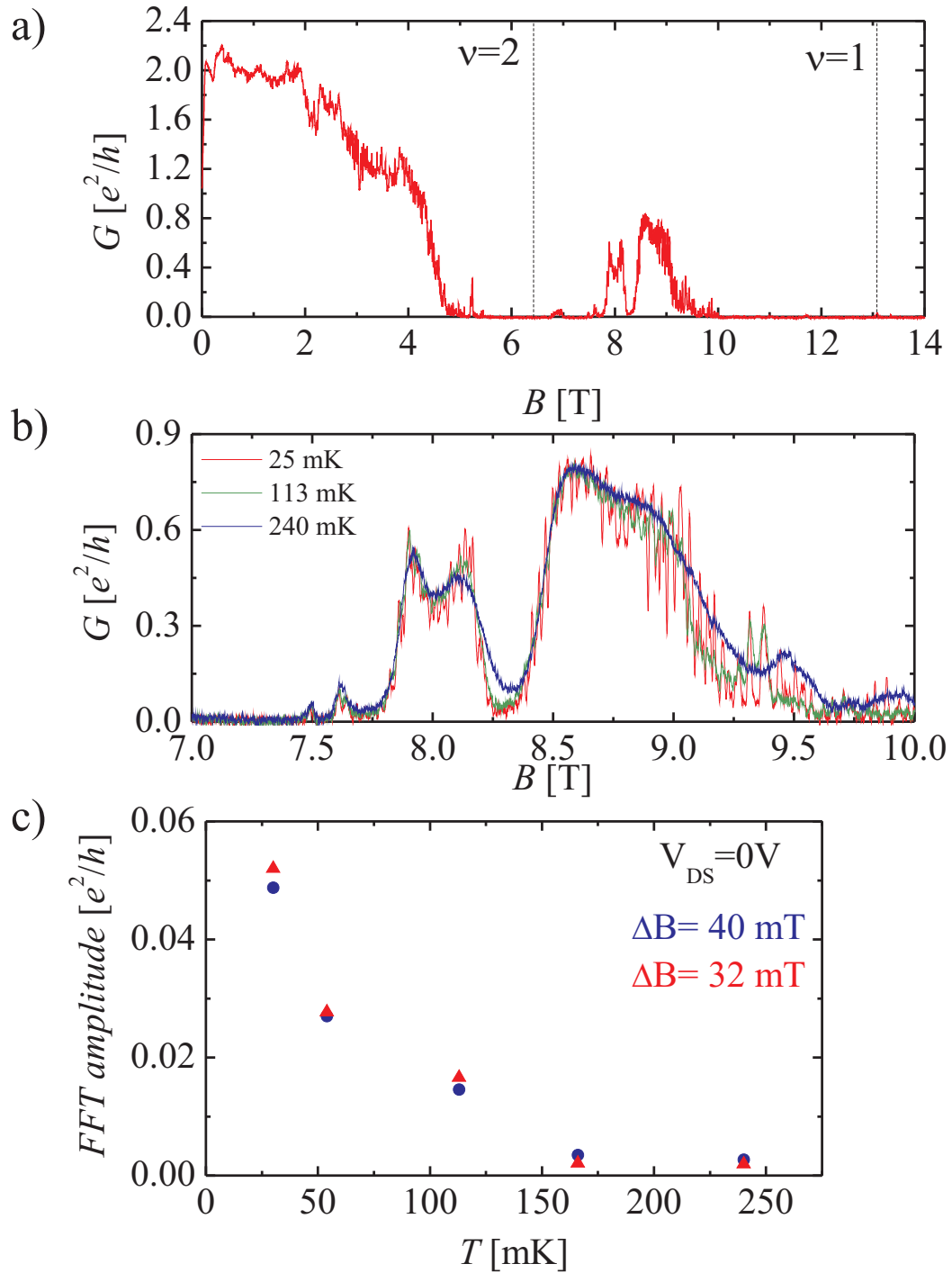


Figure 7.8: (a) Magneto-conductance measured on the Corbino device s#1 on the second cooling of the device. (b) B periodic oscillations between $8.4 \text{ T} < B < 9.2 \text{ T}$ at three different temperatures. (c) FFT amplitude versus temperature for the $B = 32 \text{ mT}$ and $B = 40 \text{ mT}$ oscillations.

7.3. Reproducing the experimental results after cycling the device to room temperature.

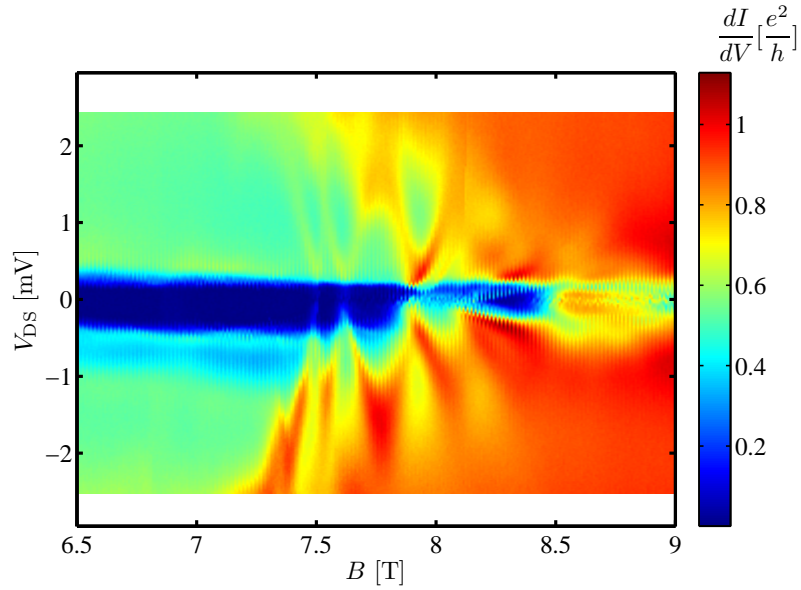


Figure 7.9: Differential conductance versus bias voltage and magnetic field for s#2 in second cooling down of the sample.

a finite conductance is measurable. In this case one cannot speak about a well defined incompressible stripe around the contacts. It is visible also out of the zero conductance valley where the QHE breaks down. It is visible also at half integer filling factor values. Concluding about how and where interference take place is not easy.

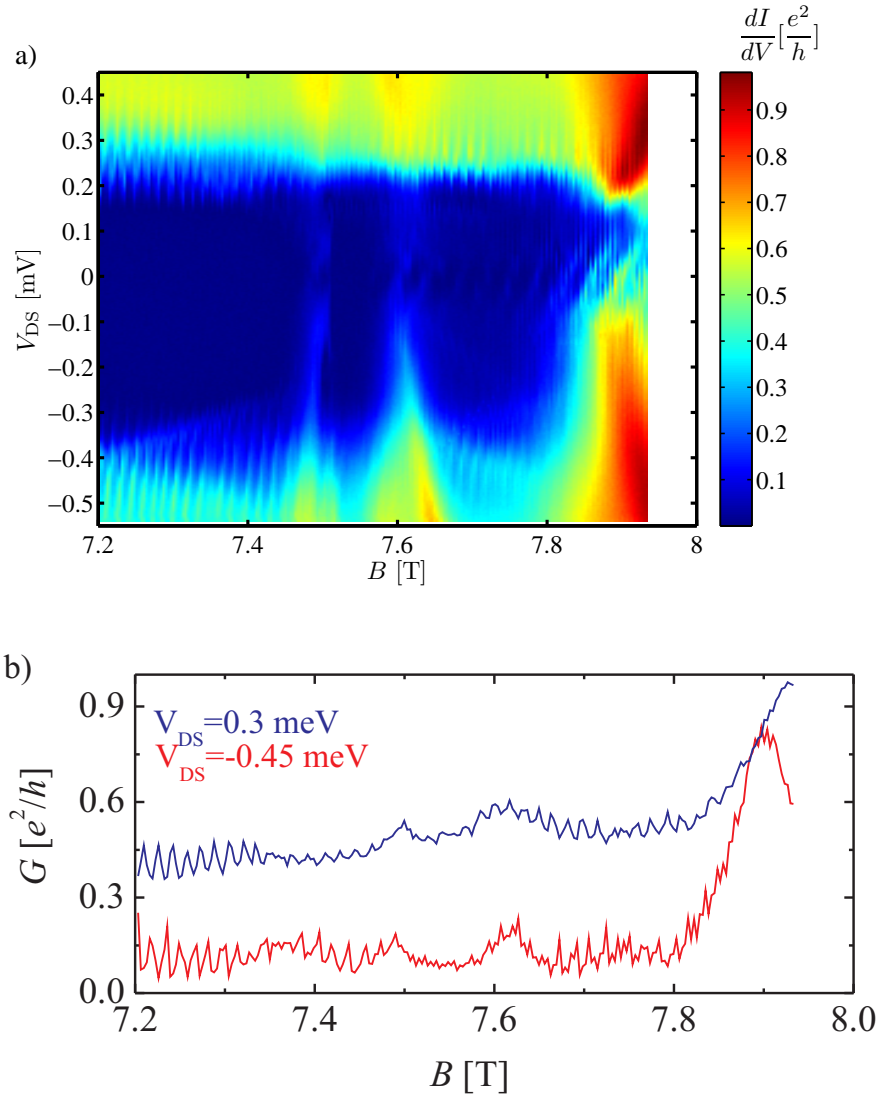


Figure 7.10: (a) Differential conductance versus bias voltage and magnetic field for $s\#1$ with a finer resolution. Magnetic field periodic oscillations are visible where conductance is not zero. We extract $\Delta B_{AB} = 15$ mT. (b) Two line cuts from the measurements shown in (a).

7.4 Third cool down of the Corbino device s#1 and effect of back gate

In the previous cooling the sample had a voltage shock by accident. The density decreased after the voltage shock, conductance was not zero anymore in the $\nu = 2$ region and diamond features disappeared. Conductance versus magnetic field before and after voltage shock is shown in Fig. K.4 in Appendix K. The sample was warmed to room temperature and cooled to low temperatures again. Conductance versus magnetic field is shown in Fig. 7.11. Density is determined to be $n_s = 2.89 \times 10^{11} \text{ cm}^{-2}$ and is slightly smaller compared to the value of density ($n_s = 3.14 \times 10^{11} \text{ cm}^{-2}$) for the previous cooling. The conductance goes to zero in the $\nu = 2$ and $\nu = 1$ plateau. Now there are some peaks also appearing on the high magnetic field side of the $\nu = 1$ plateau. The conductance versus bias voltage and magnetic field around the peaks in the $\nu = 2$ plateau is shown in Fig. 7.12 (a). The diamond features are reproduced. However, they are not as sharp as before. In Fig. 7.12 (b) measured conductance versus bias voltage and magnetic field is shown for $\nu = 1$ plateau. Here the linear shift of the peak position with magnetic field is visible in the valley. However, the peaks are not visible out of the valley. One reason can be that the configuration that lead to the observed single-electron charging is destroyed after the breakdown. Note that the asymmetry for

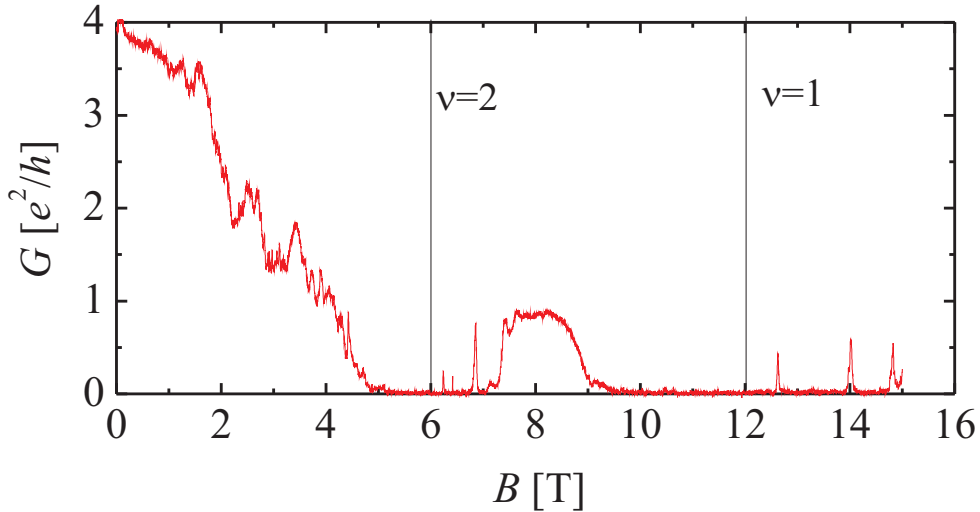


Figure 7.11: Magneto-conductance of the corbino device s#1 measured on the third cooling of the sample.

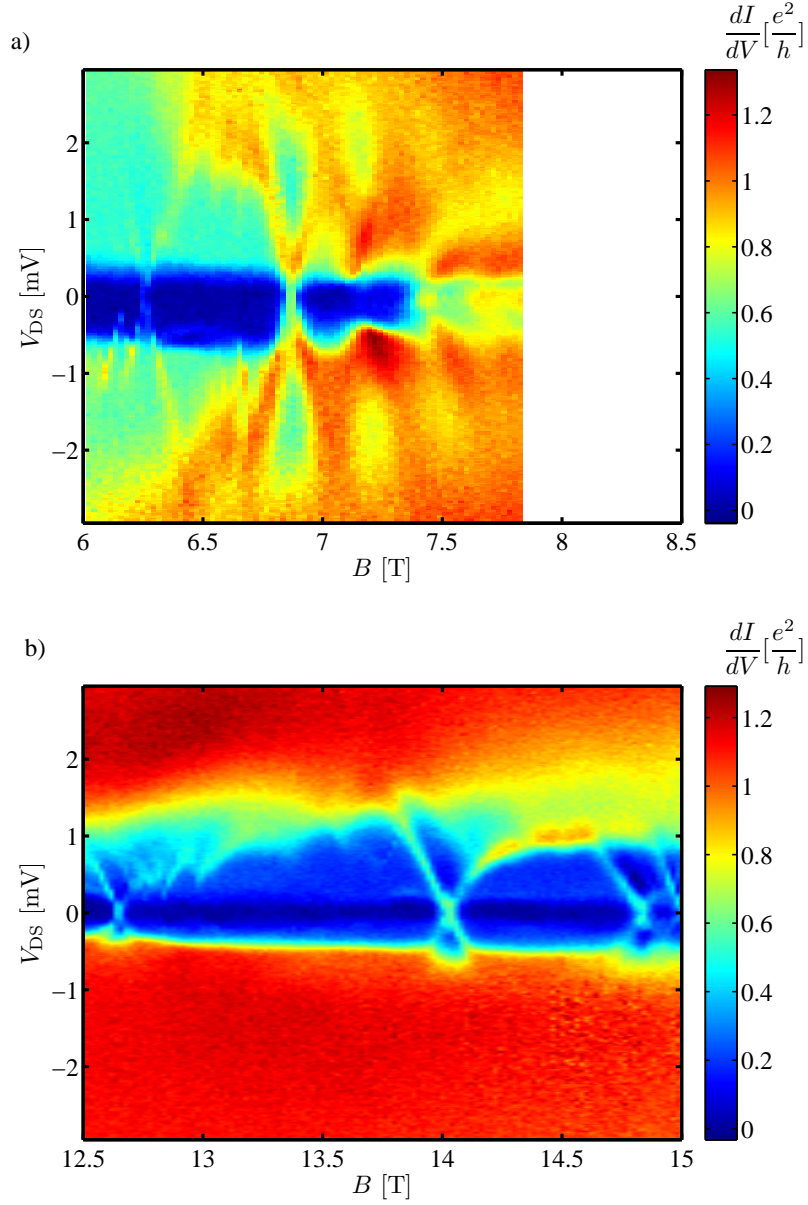


Figure 7.12: (a) Differential conductance versus bias voltage and magnetic field for s#1 measured at $\nu = 2$ plateau on the third cooling of the sample. (b) Similar measurement on the $\nu = 1$ plateau.

the breakdown is just opposite of the $\nu = 2$ plateau.

We have investigated the effect of back gate on this cool down. We used the metal on the chip carrier as back gate which was roughly 0.5 mm far from the 2DES.

Therefore, the back gate has not a drastic effect. The measured conductance for $V_{BG}=0$ V and for $V_{BG}=-90$ V is shown in Fig. 7.13 (a). For $V_{BG}=-90$ V the peaks are shifted to lower magnetic field values. From the shift of the peak position indicated as ΔB_1 and ΔB_2 in Fig. 7.13 (a) we extract $\Delta B_1/\Delta B_2 = 2.08$. This is just the ratio of the filling factor values since the peaks are located in $\nu = 2$ and $\nu = 1$ plateau. However, the shift in the position of the broad conductance peak corresponding to $\nu = 1.5$ is hardly visible. The upper side of this peak (at 9 T) also does not shift very clearly. Therefore, density seems not to be effected very much. In Fig. 7.13 (b) the magneto conductance for four different back gate voltages are shown. As before the position of the Coulomb blockade oscillation (CBO) peaks shift to lower values for applied negative back gate voltages. The height of the peak between 6 T and 6.5 T becomes larger for negative back gate voltages (smaller density). In Fig. 7.14 (a) and (b) conductance versus back gate voltage and magnetic field is shown for the CBO peaks in $\nu = 2$ plateau and $\nu = 1$ plateau. The position of the peak shifts to lower magnetic field values with negative back gate voltages. That is along the resonance lines the shift due to magnetic field is compensated by the back gate and the energy level of the island stays in resonant. The ratio of the slope of the CBO peaks marked as #1 and #2 in Fig. 7.14 (a) and 7.14 (b) is

$$\frac{slope_{\#2}}{slope_{\#1}} = 2.37 \quad . \quad (7.5)$$

At zero back gate voltage the CBO peak #1 is at $B_{\#1} = 6.836$ T and corresponds to $\nu_{\#1} = 1.75$. The CBO peak #2 is at $B_{\#2} = 14.010$ T and corresponds to $\nu_{\#2} = 0.85$. The ratio of the filling factor for two peaks

$$\frac{\nu_{\#1}}{\nu_{\#2}} = 2.05 \quad . \quad (7.6)$$

This is similar to the ratio obtained from the slope of the peaks. The effect of back gate seems to be related to the filling factor values on the device.

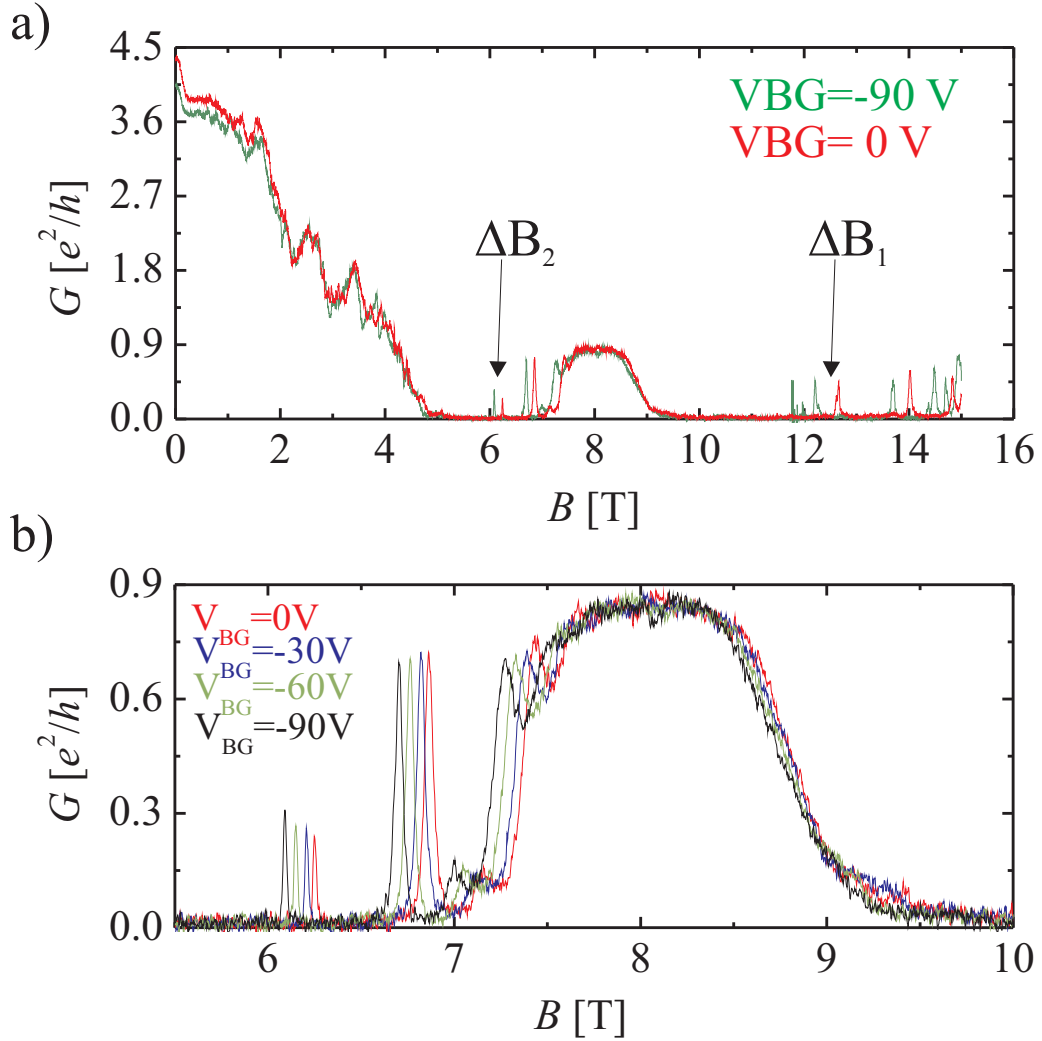


Figure 7.13: (a) Magneto-conductance measured on the Corbino device s#1 in the third cool down of the device for zero $V_{BG} = 0$ V and $V_{BG} = -90$ V. (b) Magneto-conductance measured on the Corbino device s#1 in the third cool down of the device for $V_{BG} = 0$ V, $V_{BG} = -30$ V, $V_{BG} = -60$ V and $V_{BG} = -90$ V.

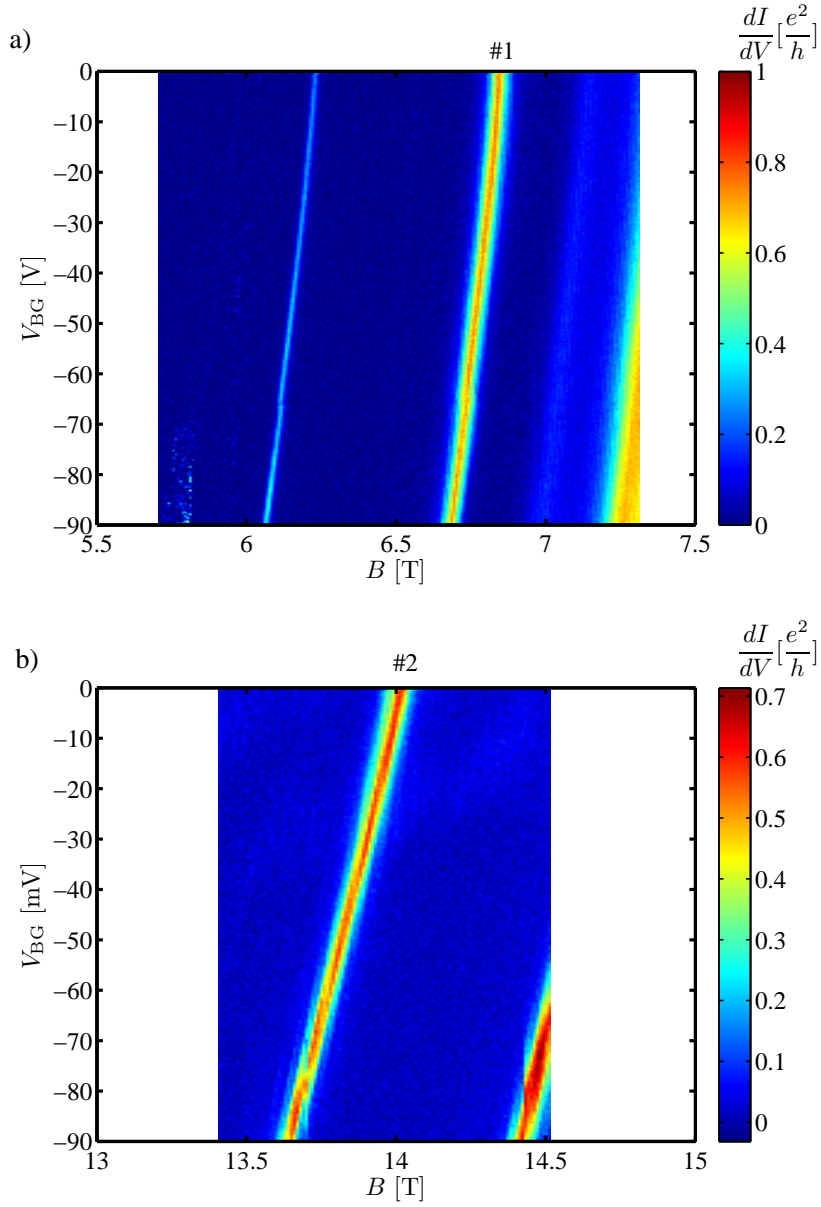


Figure 7.14: (a) Conductance versus back gate voltage as a function of magnetic field measured around the $\nu = 2$ plateau on s#1 in the third cooling. (b) The same measurements around the CBO peaks in $\nu = 1$ plateau.

7.5 Comparison of single-electron charging effect on different Corbino devices

We have measured other samples to reproduce the observation of single-electron charging. Conductance versus magnetic field for Corbino device s#2 is shown in Fig. 7.15 (a). Wafer is 81628 and has a 2DES 40 nm below the surface. It is not easy to determine the filling factor values since conductance does not go to zero. We assume that the minima at 7.5 T is the $\nu = 2$ minima. However, one has to keep in mind that error in this estimation can be large since the conductance does not go to zero and it is difficult to estimate exact position of the integer filling factor values. Density extracted from this value is $n_s = 3.6 \times 10^{11} \text{ cm}^{-2}$ which is 62% of the bulk value. Conductance peaks are clearly visible in the $\nu = 2$ plateau. There are also peaks visible between 10 T and 11.5 T with a period of $\Delta B_{AB} = 50 \text{ mT}$. The radius of the circle enclosing the area implied by the periodicity is $r_{AB} = 0.16 \text{ } \mu\text{m}$. This is slightly larger than the inner contact radius. The conductance versus bias-voltage and magnetic field is shown in Fig. 7.15 (b). The diamonds are clearly visible. $E_c = eV_{DS}/2 = 0.55 \text{ meV}$ for the most clear diamond whose center is at about 7.65 T. This value of charging energy is just half of the value found for the previous device. The width in magnetic field $\Delta B = 0.30 \text{ T}$ which is roughly the same value ($\Delta B = 0.29$) found for Corbino device s#1. A model for a possible configuration is shown in Fig. 7.15 (c). There is an island in the incompressible region coupled to the inner and outer compressible regions. This configuration is similar what is shown for s#1. However, here at some region of the device the incompressible stripe is not wide enough to block the transport. The fact that the diamond features are reproduced on the different devices shows that it is not an artefact or a coincidence. This is a reproducible effect. We performed similar measurements on the higher magnetic field side. The features are not very clear. The measured data is shown in Fig. K.5 (a) in Appendix K. Differential conductance versus magnetic field for a wider range of magnetic field is shown in Fig. K.5 (b) in Appendix K.

Magneto-conductance data of Corbino device s#4 are shown in Fig. 7.16 (a). Wafer is 81628 and has a 2DES 40 nm below the surface. The density extracted from the magneto transport measurement is $n_s = 2.4 \times 10^{11} \text{ cm}^{-2}$ which is 42% of bulk value. This value of the density is extracted assuming that plateau at 10 T is $\nu = 1$ plateau. However, this is not for sure, it can also be $\nu = 2$ plateau. We assume that it is $\nu = 1$ plateau since this is more reasonable if we consider the value of the density obtained on the other devices (s#1 and s#2) from the same wafer. Conductance goes to zero at $\nu = 1$ plateau. There are some conductance oscillations on the higher magnetic field side of the $\nu = 1$ plateau as shown in Fig. 7.16 (b). Differential conductance versus bias voltage and magnetic field is

7.5. Comparison of single-electron charging effect on different Corbino devices

shown in Fig. 7.17 (a). There are several diamonds extending into each other. The resonant line of the diamonds extend into the zero conductance valley. The width of diamonds are 40 mT to 60 mT at lower magnetic field side and is mainly 30 mT at the higher magnetic field side. Charging energy is around $E_c = 0.5$ meV between 11.5 T and 12 T and is about $E_c = 0.25$ meV at around 12.5 T.

A model for a possible configuration is shown in Fig. 7.17 (b). There can be a few compressible islands separated from the outer compressible regions by

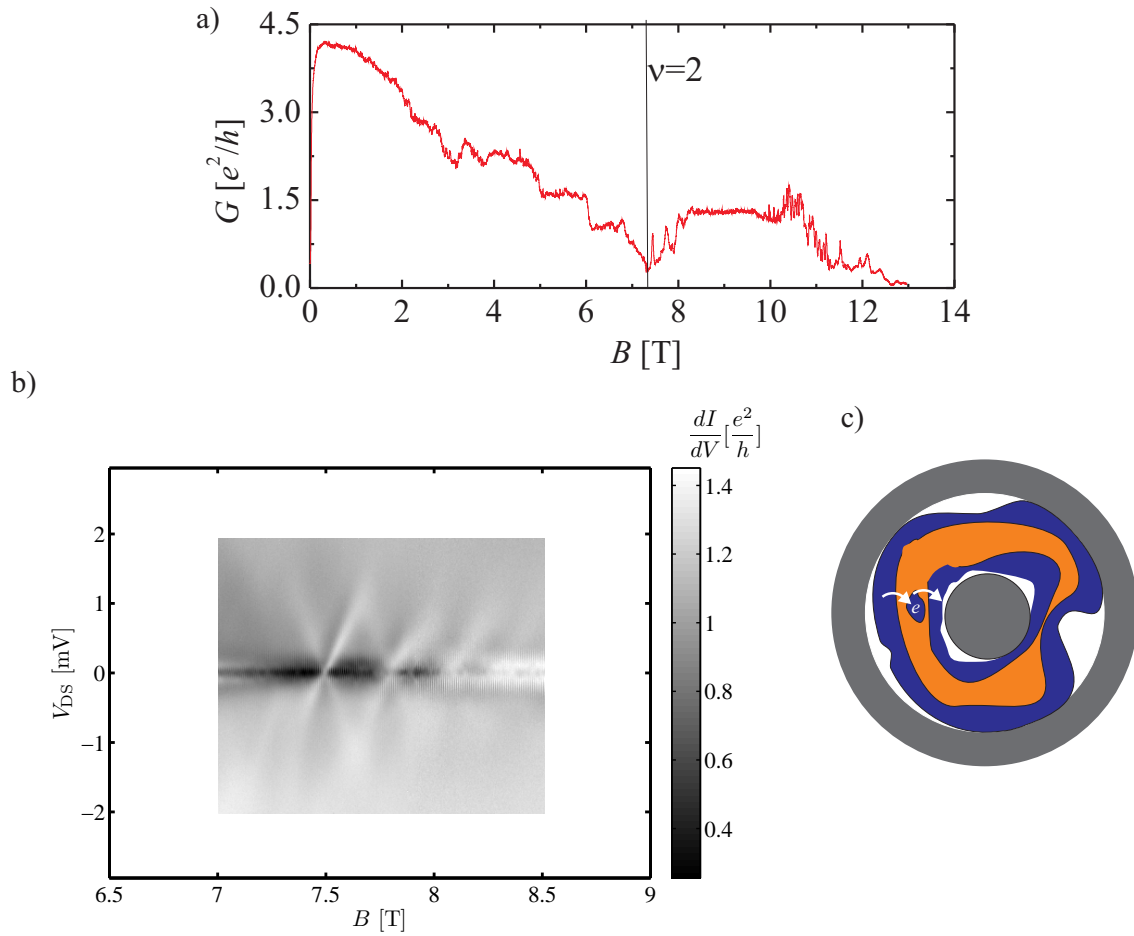


Figure 7.15: (a) Magneto conductance measured on Corbino device s#2. (b) Differential conductance versus bias voltage and magnetic field for s#2 measured around the peaks of $\nu = 2$ plateau. (c) A model based on the compressible and incompressible stripes for the measured features on the device. Blue represents compressible regions and orange incompressible regions.

incompressible stripes. Then in the measurements one see several diamonds extending into each other. From the charging energy one find the radius of the island $r = 0.17 \mu\text{m}$ for charging energy of $E_c = 0.5 \text{ meV}$ and $r = 0.34 \mu\text{m}$ for charging energy of $E_c = 0.25 \text{ meV}$.

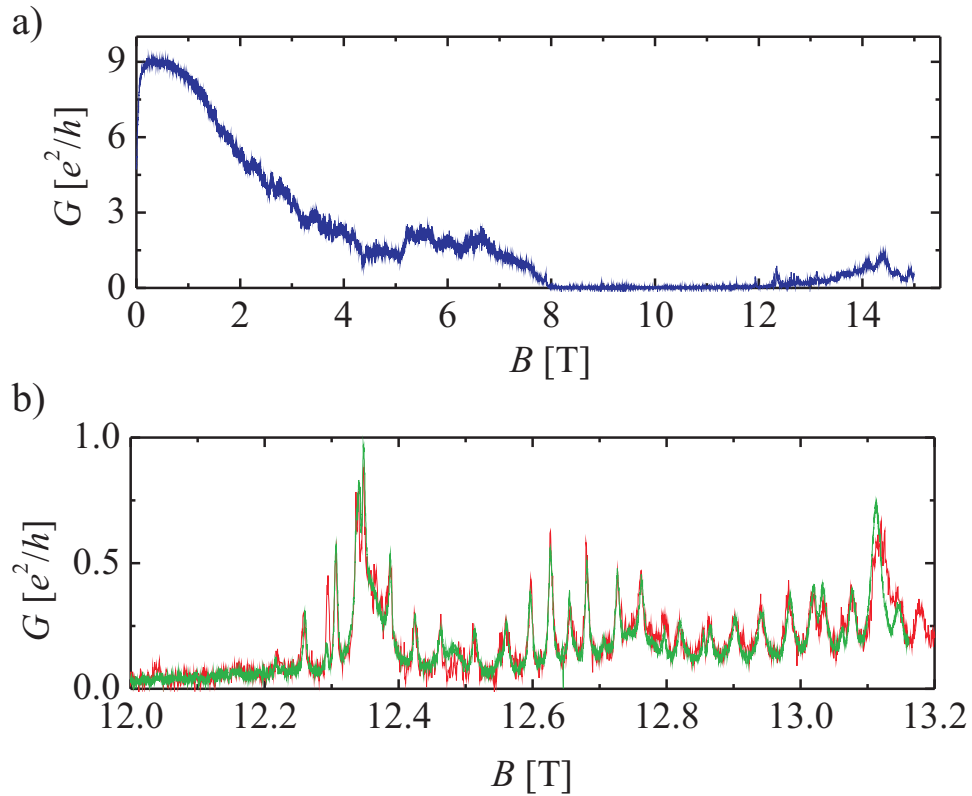


Figure 7.16: (a) Magneto-conductance measured on s#4. (b) Magneto-conductance between $12 \text{ T} < B < 13.2 \text{ T}$ for two magnetic field sweeps.

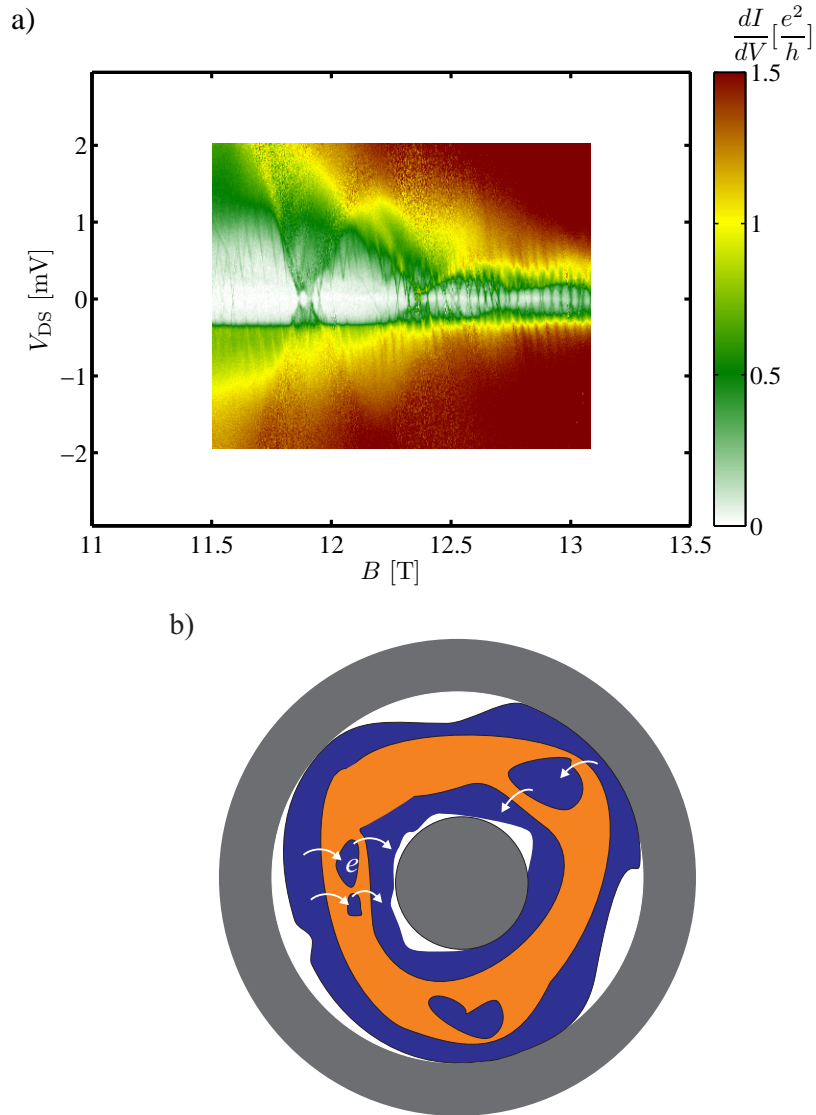


Figure 7.17: (a) Differential conductance measured as a function of magnetic field on the s#4 at the $\nu = 1$ plateau. (b) A model based on the compressible and incompressible stripes for the device. Blue represents compressible regions and orange incompressible regions.

Magneto-conductance data of the Corbino device s#6 are shown in Fig. 7.18 (a). The wafer is 81758 and has the 2DES 50 nm below the surface. Density in the Corbino device extracted from the magneto transport measurement is $n_s = 3.7 \times 10^{11} \text{ cm}^{-2}$ which is 20% less than bulk value. Conductance goes to zero at $\nu = 1$ and $\nu = 2$ plateau. Minima at $\nu = 3$ and $\nu = 4$ are also clear. In Fig. 7.18 (b) magneto conductance between 3 T and 8 T is shown. There are no sharp peaks visible at $\nu = 2$ plateau as was the case for device s#1. There are some peaks and dips between $\nu = 2$ and $\nu = 3$. Conductance is close to zero but is finite at $\nu = 3$ and some peaks are visible. At the $\nu = 4$ plateau conductance is higher compared to the $\nu = 3$ plateau and there are two dips.

Differential conductance versus bias voltage as a function of magnetic field is shown in Fig. 7.19 (a) for $-0.2 \text{ T} < B < 6.5 \text{ T}$ and $6.5 \text{ T} < B < 15 \text{ T}$ (b). The dip

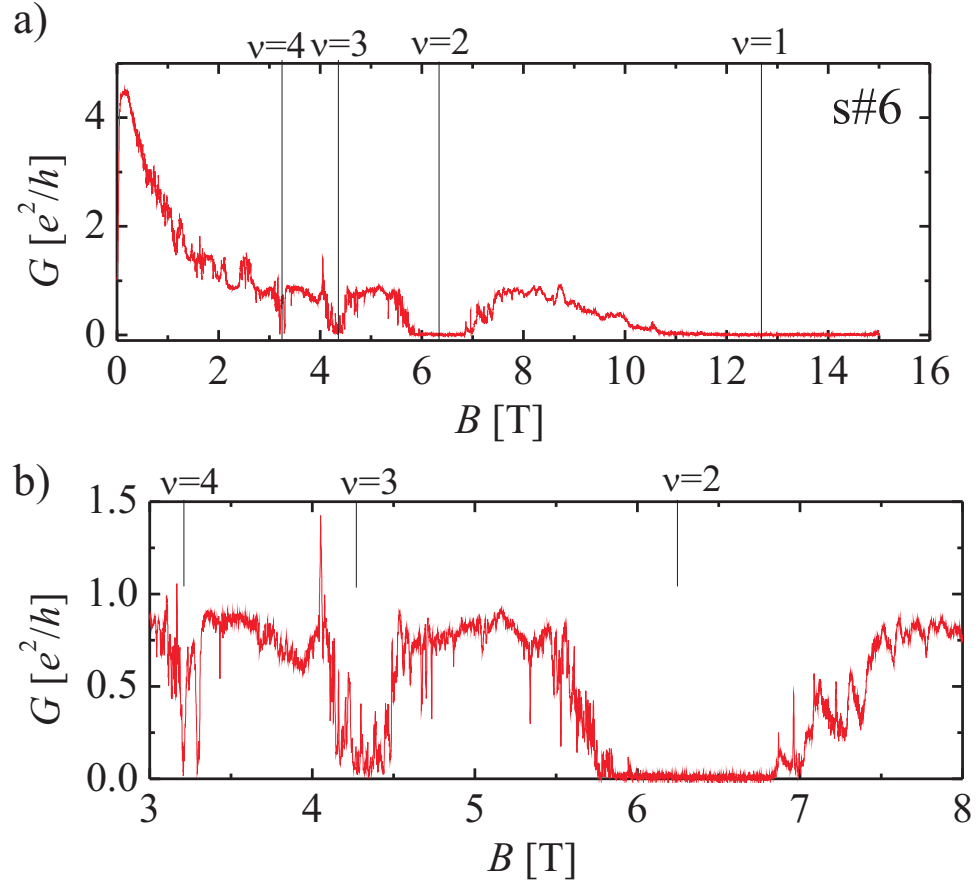


Figure 7.18: (a) Magneto-conductance measured on Corbino device s#6. (b) The same measurement shown for magnetic field range of $3 \text{ T} < B < 8 \text{ T}$.

and kinks around zero bias and zero magnetic field has already been discussed in Chapter 6. At the $\nu = 2$ and $\nu = 1$ plateau, regions of zero differential conductance are visible. The region of zero differential conductance valley is symmetric which was not the case for the devices s#1, s#2 and s#4. At the edges of the zero conductance valley there are differential conductance peaks. It is not easy to analyze the data and to derive a charging energy. However, we will give some examples. At the $\nu = 1$ region, $E_c = 0.25$ meV with the width of 60 mT. This value of charging energy implies $r = 0.34$ μm if we assume a flat disk of radius r . The resonant conductance peak does not extend into the zero conductance valley. However, this was the case for the device s#1, s#2 and s#4. The region of $\nu = 3$ and $\nu = 4$ are more complicated to analyze. The plots for this regions is shown in Fig. K.6 in Appendix K. The peaks at the edges of the zero conductance valley are quite sensitive to temperature as shown in Fig. K.7 in Appendix K. At 160 mK the peaks are not present.

As we have seen we have reproduced observed single-electron charging effect on three devices. On Corbino device s#1 and s#2 the effect is observed almost at same magnetic and filling factor range with only one island being present. On Corbino device s#4 similar effect is observed at higher magnetic field range with several island being present. In all these devices, the magnetic field acts like a gate electrode and shifts the energy level of the islands linearly. On Corbino device s#6 there are conductance peaks which seem like Coulomb blockade oscillations but they exist at the edge of the zero conductance valley and are not easy to analyze.

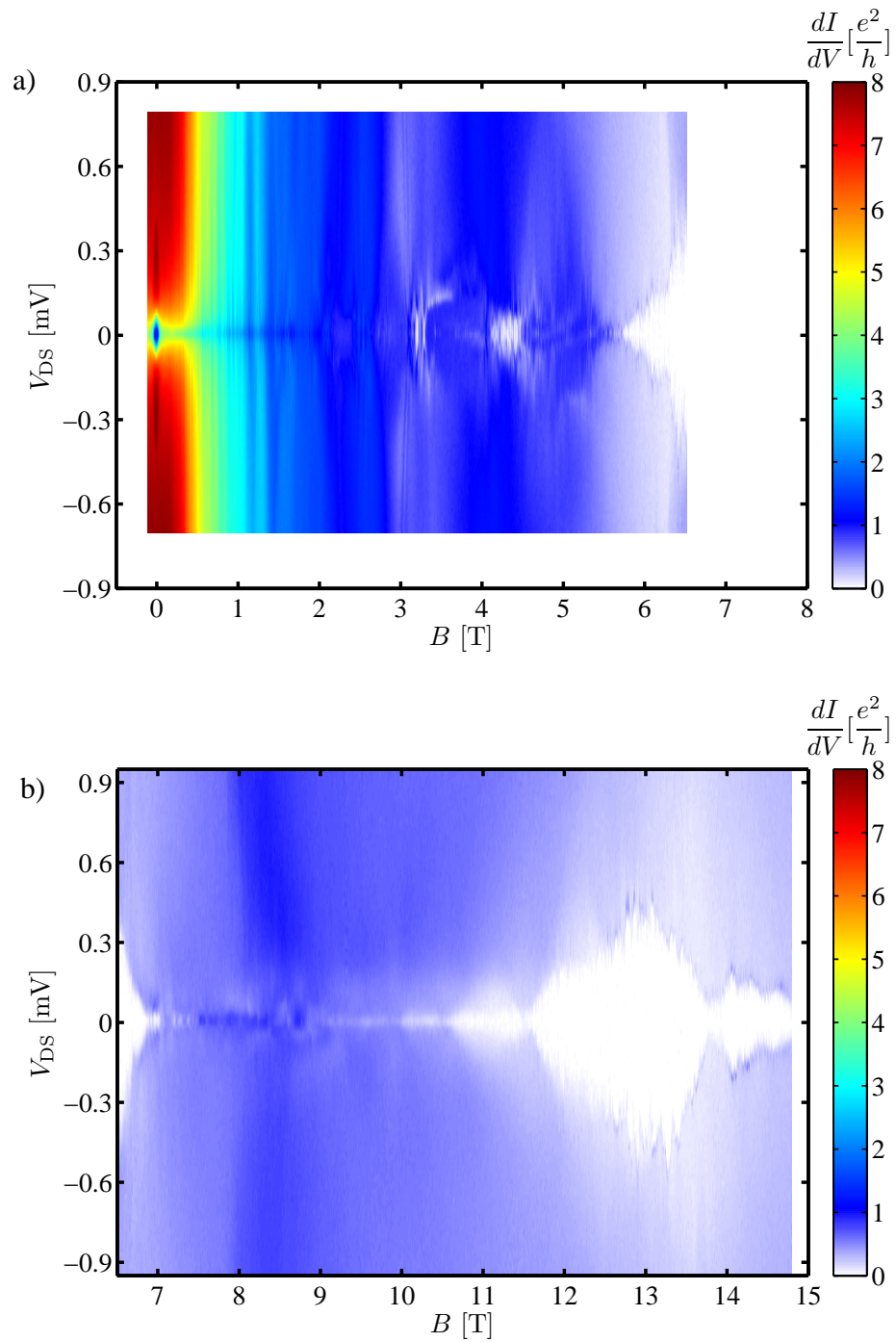


Figure 7.19: Differential conductance versus bias voltage measured as a function of magnetic field on the Corbino device s#6.

7.6 Discussion of the asymmetry of the breakdown of QHE

As we have seen, in plateau regimes the differential conductance is zero around zero bias voltage. After a certain bias voltage value, differential conductance becomes finite. The value of bias voltage at which the differential conductance becomes finite is generally not symmetric on the positive and negative bias side. For the Corbino device s#1, at $\nu = 2$ plateau as shown in Fig. 7.5 (b), a finite differential conductance is measured beyond $V_{\text{DS}}^{\text{Critical}} \geq 0.22$ mV on the positive bias side, and $V_{\text{DS}}^{\text{Critical}} \leq -0.45$ mV on the negative bias side. The value of the differential conductance in this regime is constant of voltage and is about $0.5 e^2/h$.

The measurements of a finite conductance with applied bias is probably due to breakdown of the QHE [7, 94]. For a Corbino device the radial component of electric field at radial position r according to relations (5.3) and (5.4),

$$E_r(r) = \frac{V_{\text{DS}}}{r \ln(r_o/r_i)} \quad . \quad (7.7)$$

The value of electric field around the inner contact for this device ($r = r_i = 0.1 \mu\text{m}$ and $r_o = 0.6 \mu\text{m}$) for the applied bias voltage of $V_{\text{DS}}^{\text{Critical}} = 0.22$ mV is $E = 1.2$ kV/m. This value is comparable to the critical Hall field $E^{\text{Critical}} = 3$ kV/m for Hall bar samples at 7 T [7]. Due to the radial inhomogeneity of the 2DES, the bias voltage value for the breakdown is expected to be smaller when the voltage drop occurs at the outer incompressible stripe according to the relation (7.7).

The asymmetry of the breakdown of QHE is reproduced after cycling the sample to room temperature and cooling it again. In the second cooling of the sample a finite differential conductance is measured after $V_{\text{DS}}^{\text{Critical}} \approx 0.21$ mV on the positive side and $V_{\text{DS}}^{\text{Critical}} \approx -0.38$ mV on negative bias side, for $\nu = 2$ plateau. The measured differential conductance versus bias voltage and magnetic field is shown in Fig. 7.20 (a). The value of the differential conductance is about $0.5 e^2/h$ as was the case for the first cooling. In the $\nu = 1$ plateau, in contrast, the value of differential conductance is between $1.0 e^2/h$ and $1.2 e^2/h$. The asymmetry for the break down of the QHE under finite bias is just opposite to $\nu = 2$ plateau in the $\nu = 1$ plateau as visible in Fig. 7.20 (a).

A Corbino device under high magnetic field is depicted in Fig. 7.21 (a). In Fig. 7.21 (b) and Fig. 7.21 (c) the energy level scheme along the radial direction for positive and negative bias voltage are shown. If we assume that incompressible stripes are tunneling barriers with a bias voltage independent width then the breakdown voltage should be symmetric for the positive and negative bias side. However, if we assume that the density profile in front of the contacts depends on the applied bias voltage then the incompressible stripes will be modified with

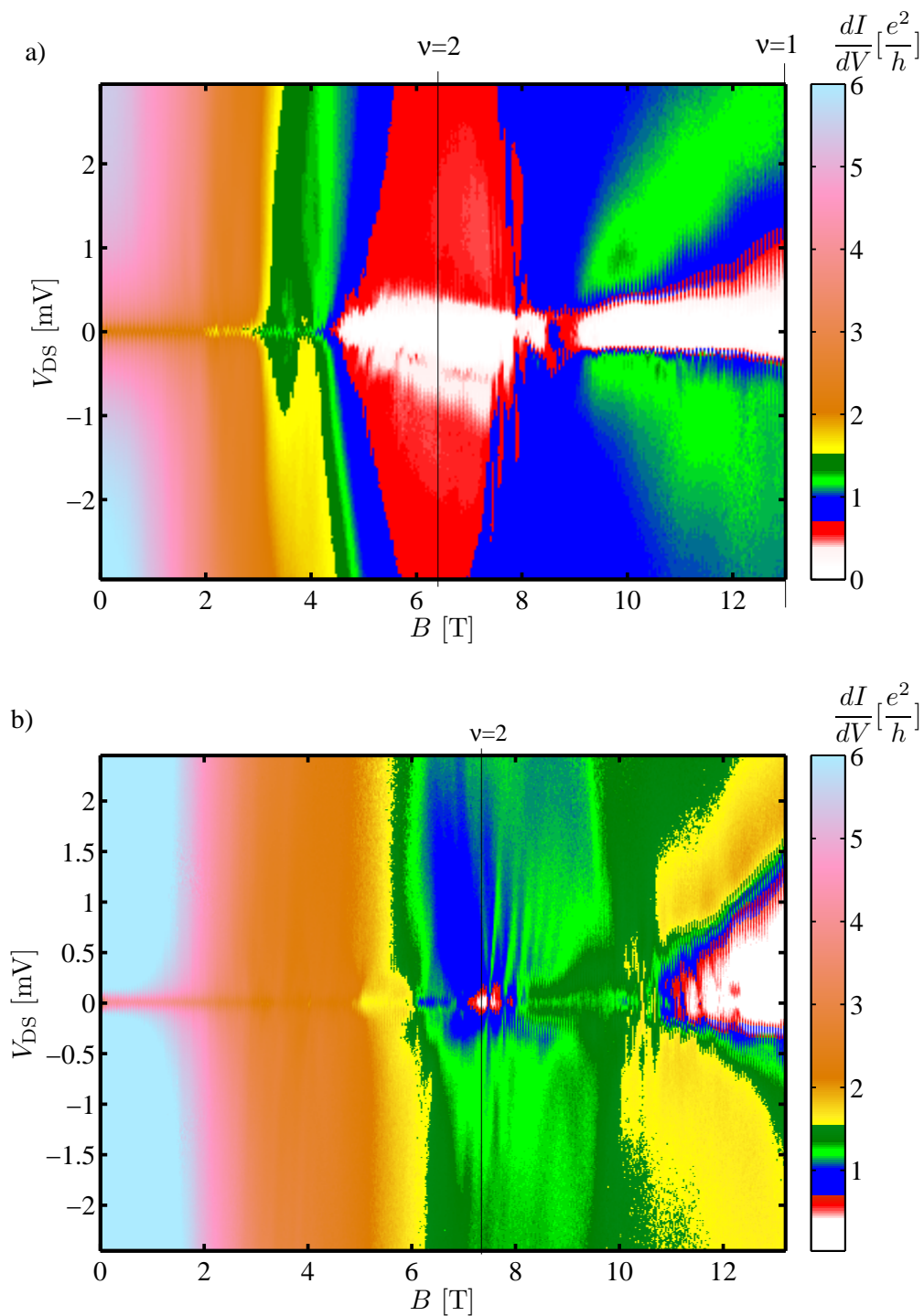


Figure 7.20: Differential conductance in color versus bias voltage measured as a function of magnetic field on the Corbino devices s#1 (a) and s#2 (b).

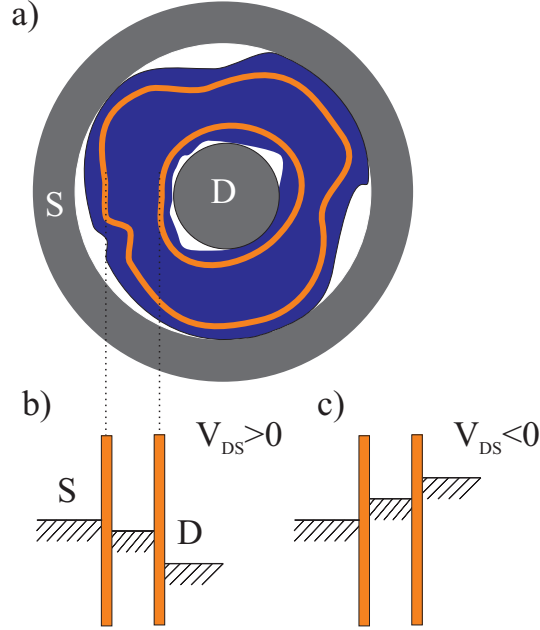


Figure 7.21: (a) A Corbino device under strong magnetic field. Compressible (blue) and incompressible (orange) stripes are shown. Energy level scheme for the positive bias voltage (b) and for negative bias voltage (c).

the applied bias voltage. For instance, assuming that density profile is smoother (wider incompressible stripes) for the positive bias voltage and sharper (thinner incompressible stripes) for the negative bias voltage in front of the inner ohmic contact will resolve the origin of the asymmetry. However, the fact that the asymmetry is just opposite for the $\nu = 2$ and $\nu = 1$ plateau can not be explained with this argument.

The asymmetric behavior is reproduced also on the other samples. For the Corbino device s#2 the conductance does not go to zero at $\nu = 2$ plateau as shown in Fig. 7.15 (b) and there is no asymmetry visible. However, at $\nu = 1$ plateau, conductance goes zero as shown in Fig. 7.20 (b). The asymmetry for the $\nu = 1$ valley observed in s#1 is reproduced on this device. The value of V_{DS}^{Critical} at $\nu = 1$ plateau increases with magnetic field on both side of the bias voltage. However, the increase on the negative side is small as compared to positive side. At 13 T the value of the bias voltage for the breakdown is about $V_{DS}^{\text{Critical}} = 1$ mV for both devices. 13 T corresponds to $\nu = 1$ for the Corbino device s#1. The fact that the value of V_{DS}^{Critical} is smaller on the lower magnetic field side of the plateau is consistent with theory of CSG since the width of the incompressible stripes are thinner on the lower side and becomes wider as mid of the plateau is reached.

From these measurements we can not judge whether the increase stops at the integer value of filling factor or not since data is not available beyond $\nu = 1$. However, on third cooling down of this device density was smaller and data is available on the upper side of the $\nu = 1$ ($B_{\nu=1} = 12$ T) plateau. The measurement is already presented in Fig. 7.12 (b). This measurement shows that the value of V_{DS}^{Critical} increases on the upper side of the $\nu = 1$ plateau for positive and negative bias voltages. On the upper magnetic field side of the plateau bulk of the sample is expected to be mainly incompressible. However, as the magnetic field is increased, on the high magnetic field side of the plateau, it is expected that the incompressible regions become less and breakdown should take place for smaller bias voltage values. This is not the case on the experiment. The reason for this controversy is not clear.

The asymmetric behavior of the breakdown is also reproduced on the Corbino device s#4. For this device conductance also does not go to zero at $\nu = 2$. At $\nu = 1$ plateau, conductance is zero. The data was already presented in Fig. 7.17. The data are available only for the higher side of the $\nu = 1$ plateau. The transition to zero conductance to the finite conductance is at $V_{DS}^{\text{Critical}} = -0.35$ mV and transition is sharp. On the positive bias side transition takes place smoothly. Moreover, transition is at $V_{DS}^{\text{Critical}} = 1$ mV at 11.5 T and shifts to lower bias voltage values at the higher side of the plateau. The value of the conductance is about $0.5 e^2/h$ at the transition region and increases to $1.5 e^2/h$ at larger bias voltage values.

For the Corbino device s#6 there is no asymmetry visible. Conductance goes zero for $\nu = 2$ and $\nu = 1$ plateau. The results are presented in Fig. 7.19 for this device. For $\nu = 2$ plateau the value of V_{DS}^{Critical} start to increase from the lower magnetic field side of the plateau. The increase stops at the integer value of filling factor, and it decreases on the upper side of the plateau. The maximum value of $V_{DS}^{\text{Critical}} \approx 0.4$ mV for both $\nu = 2$ and $\nu = 1$ plateau. The behavior on the $\nu = 1$ plateau is mainly similar to that of $\nu = 2$. However, here there are regions at the lower side and higher side of the plateau where V_{DS}^{Critical} has zigzag behavior. This is probably due to the inhomogeneity in the density profile on the device that local filling factor is different. That is as the magnetic field is changed the profile of the compressible and incompressible regions is modified and at some positions on the sample incompressible stripes becomes thinner or wider thereby effecting the value of V_{DS}^{Critical} .

7.7 Summary

In this chapter we have investigated submicron scale Corbino devices under strong magnetic field. We summarize the findings as follow:

- The conductance of a macroscopic Corbino device is zero under high magnetic field around integer filling factor values. However, the conductance for the small Corbino devices under strong magnetic field does not always go to zero due to partial or full depletion in the devices. We have characterized 6 devices. For two devices it goes to zero for only $\nu = 1$ plateau. For two devices it goes zero at $\nu = 2$ and $\nu = 1$ plateau. For two devices it does not go zero at all.
- The fact that conductance goes to zero shows that we have a Corbino topology, that is the 2DES is not completely depleted in any region. However, this is not always the case since conductance does not go to zero for all the devices.
- Periodic oscillations in the conductance are observed for certain magnetic field ranges. Assuming that these periodic oscillations are Aharonov-Bohm type oscillations, the radius of interference loop extracted from the periodicity is generally slightly larger than the radius of the inner contact. This suggests that the interference loop can enclose the inner contact.
- We have observed signatures of single-electron charging in the $\nu = 2$ plateau and $\nu = 1$ for some of the devices. We suggested compressible islands surrounded by incompressible stripes as the origin of the observed phenomena. The energy levels of the islands shift linearly with magnetic field. That is magnetic field plays the role of a gate voltage on the quantum dot systems. The origin of this behavior is, however, not completely clear.
- For the devices with vanishing conductance at the $\nu = 2$ and $\nu = 1$, a finite conductance is observed with finite bias. We suggested breakdown of QHE as the possible explanation. The value of the electrical field around the inner contact for the value of bias voltage V_{DS}^{Critical} (the value of voltage at which breakdown takes place) is in the same order as the critical Hall field found for the macroscopic samples. The breakdown bias voltage can be different on the positive and negative bias side. For the devices where this asymmetry is present the asymmetry is just opposite in the $\nu = 2$ and $\nu = 1$ plateau. On one of the devices no asymmetry is present. On this device the value of V_{DS}^{Critical} increases from the lower magnetic field side of the plateau and takes the maximum value at the integer value of filling factor and then decreases. This can be explained with the change of width of incompressible stripes as magnetic field is changed.

Chapter 8

Conclusion and outlook

In this work we have proposed and realized submicron scale Corbino devices as a new type of single-electron charging device based on the present understanding of the microscopic picture of the QHE. Existence of compressible and incompressible stripes in front of the ohmic contacts was the main ingredient for the proposed device. Therefore, we have made a detailed study of electrical and structural properties of alloyed Au/Ge/Ni contacts. We have found that there is an anisotropy on the contact resistance for the deeper lying 2DES. That is, there is a good contacting and bad contacting direction. This effect is less pronounced in the shallow lying 2DES. From the structural investigations we have found that the Au/Ge/Ni contacts mainly have two phases and these phases affect the neighboring $\text{Al}_\delta\text{Ga}_{1-\delta}\text{As}$ layer in a different way. In good contacting direction, in front of the Au-rich phases Al diffuse out from the $\text{Al}_\delta\text{Ga}_{1-\delta}\text{As}$ layer for a region of 50 nm to 150 nm and Ga replaces it. Therefore, 2DES is depleted in this region. When the contact region at the interface is NiGe-rich, $\text{Al}_\delta\text{Ga}_{1-\delta}\text{As}$ continuously exists up to the NiGe-rich contact region. Therefore, the 2DES exists up to the metal region. A Schottky-barrier is assumed to form at the interface between the NiGe-rich contact and the $\text{Al}_\delta\text{Ga}_{1-\delta}\text{As}$ layer. In bad contacting direction, Al seems to diffuse out from the $\text{Al}_\delta\text{Ga}_{1-\delta}\text{As}$ layer both in front of the NiGe-rich regions and in front of the Au-rich region. However, this is true for the deeper lying 2DES. For shallow lying 2DES the behavior in bad contacting direction must be similar to good contacting direction since the anisotropy is less pronounced. This point still needs to be investigated.

We could contact 2DES down to a contact diameter of 0.2 μm . Contact resistance for these small contacts is low and is mostly between 1 k Ω and 10 k Ω . Contacts have a linear I-V characteristic, i.e. show an Ohmic behavior. The average yield for the working contacts is more than 50% for submicron scale ohmic contacts.

We have prepared Corbino devices in submicron scale and characterized at low

temperatures. At zero magnetic field, we have observed at a temperature of 50 mK a zero bias anomaly - a large dip - in the differential conductance centered at zero bias. The depth and width of the zero bias dip tends to saturate below 100 mK. The amplitude of the zero bias dip decreases with increasing temperature and at 1.5 K the dip completely disappears in three devices and in three devices is slightly present. If a perpendicular magnetic field is applied, conductance increases and saturates at about 0.2 T. However, the zero bias anomaly is still slightly present at the finite magnetic fields. We have considered weak localization as the origin of the observed phenomena. However, it is not possible to explain the observed phenomena in terms of weak localization in a straightforward way due to its unusual properties, i.e. very high visibility of interference. A theoretical treatment of ballistic Corbino devices with non ideal contacts might be useful to understand observed effects.

Under high magnetic field we have observed magnetic field periodic oscillations which can be Aharonov-Bohm type oscillations implying that electrons travel around closed loops phase coherently. The radius of the loop corresponding to the the area extracted from the periodicity, assuming that they are Aharonov-Bohm oscillations, is mostly slightly larger than the radius of the inner contact implying that interference loop can encircle the inner contact. We have observed signatures of single-electron charging in the $\nu = 2$ and plateau and $\nu = 1$ quantum Hall plateaus for some of the devices. The effect is reproducible for different cycling of sample to room temperature and low temperature. It is reproduced also on different devices which shows that the effect is not due to a coincidence. We suggested compressible islands surrounded by incompressible stripes as the origin of the observed phenomena. The energy level of the islands shift linearly with magnetic field. This, however, was not possible to explain in a straight forward way.

We have prepared structures as shown in Fig. 8.1. In this structures there is a small ohmic contacts surrounded with the split gates which can be used to deplete 2DES underneath. This geometry allow to control and investigate several parameters and properties of observed zero bias anomaly and single-electron charging effect. At zero magnetic field, by depleting 2DES partly or completely at some region around the contact give the possibility to check how sensitive is the zero bias anomaly to the position where electrons are emitted or absorbed. It is possible to perform transport experiments between the S1 and S2 while D is grounded to observe Aharonov-Bohm effect to confirm the fact that electrons travels around the inner contact phase coherently. One can use S1 and D or S2 and D to see the anisotropic properties of the contact.

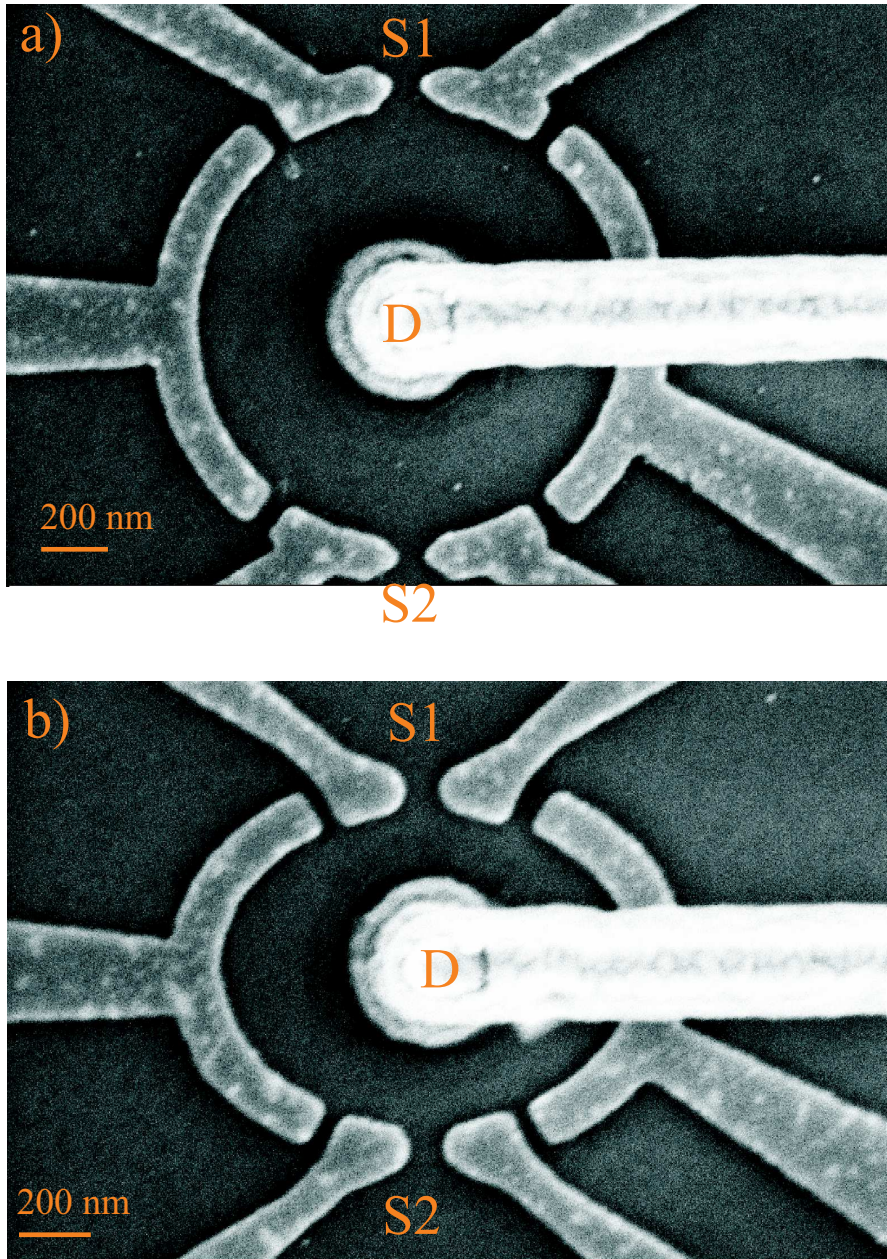


Figure 8.1: A small ohmic contact surrounded by split gates to form a interferometer and a quantum dot system under strong magnetic field.

Chapter 9

Zusammenfassung

Der 1980 [1] in einem zweidimensionalen Elektronensystem (2DES) entdeckte Quanten-Hall-Effekt (QHE) wies unerwartete Charakteristika auf: Im Hall-Widerstand bilden sich für bestimmte Bereiche des magnetischen Feldes Plateaus aus, wobei gleichzeitig der longitudinale Widerstand verschwindet. Der Hall-Widerstand der Plateaus ist dabei in Werten von h/ie^2 (i ganzzahlig) quantisiert. Der Effekt wurde in einem 2DES an der Si-SiO₂-Grenzfläche eines Metalloxid-Halbleiter-Feldeffekttransistors entdeckt. Aufgrund der hervorragenden Elektronenbeweglichkeiten wird der QHE mittlerweile vorwiegend in 2DES auf Basis von modulationsdotierten GaAs/Al_δGa_{1-δ}As-Heterostrukturen untersucht. Diese Strukturen werden mittels Molekularstrahl-Epitaxie gewachsen, wobei sich das 2DES an der GaAs/Al_δGa_{1-δ}As-Grenzfläche ausbildet, die typischerweise 35 nm bis 200 nm unter der Oberfläche der Heterostruktur liegt. Von entscheidender Bedeutung für die QHE-Forschung ist die Kontaktierung des 2DES in derartigen Heterostrukturen. Die Kontakte sollen ohmsches Verhalten zeigen, geringe Widerstände aufweisen und zuverlässig in reproduzierbarer Qualität hergestellt werden können. Zur Kontaktierung von GaAs/Al_δGa_{1-δ}As-Heterostrukturen werden, wie bei n-GaAs, einlegierte Au/Ge/Ni-Kontakte verwendet. Obwohl ein umfassendes Verständnis einlegierter ohmscher Kontakte in 2DES für die mikroskopische Beschreibung des QHE unabdingbar ist, mangelt es in der Literatur an systematischen Studien; die technischen Vorgehensweisen bei der Kontaktierung sind oftmals nur innerhalb der jeweiligen Arbeitsgruppen bekannt.

Verständnis und Beschreibung des Quanten-Hall-Effekts sind auch heute noch Gegenstand der wissenschaftlichen Diskussion. Ein Großteil der experimentellen Resultate konnte erfolgreich mit dem sogenannten Randkanalbild theoretisch erklärt werden. Neuere Messungen zum Verlauf des Hall-Potentialprofils mit Rasterkraftmikroskopie wiesen jedoch die Existenz kompressibler und inkompressibler Streifen in der Verarmungszone an den Rändern einer Quanten-Hall-Probe nach. Dies favorisiert Theorien, die elektrische Abschirmungseffekte berücksichtigen. Wei-

terhin wurden in diesen Experimenten kompressible und inkompressible Streifen auch an der Grenzfläche zwischen ohmschen Kontakten und dem 2DES gefunden. Aufgrund der isolierenden Eigenschaften inkompressibler Streifen werden wir in dieser Arbeit eine Corbino-Geometrie mit sub- μm -Abmessungen als neuartigen Einzel-Elektronen-Transistor einführen.

Im Verlauf dieser Arbeit wurden die elektrischen und strukturellen Eigenschaften einlegierter Au/Ge/Ni-Kontakte zu 2DES in GaAs/Al _{δ} Ga_{1- δ} As-Heterostrukturen ausführlich untersucht und auf Grundlage der experimentellen Erkenntnisse ein mikroskopisches Modell zur Ausbildung ohmscher Kontakte in diesem Materialsystem entwickelt. Der Schwerpunkt lag dabei auf der Anfertigung von Kontakten mit Abmessungen von weniger als einem Mikrometer. Funktionsfähige Kontakte mit Durchmessern von bis zu 0,2 μm konnten hergestellt werden, die wiederum erfolgreich in sub- μm -Corbino-Proben integriert wurden. Deren Charakterisierung bei kryogenen Temperaturen ergab eine sogenannte Zero-Bias-Anomalie in Form eines Einbruchs der differentiellen Leitfähigkeit bei Vorspannung Null. Diese Anomalie kann durch ein schwaches Magnetfeld zumindest teilweise unterdrückt werden. Wir vermuten als Ursache der Zero-Bias-Anomalie einen Interferenzeffekt. In starken Magnetfeldern konnten wir sowohl mit dem Magnetfeld periodische Oszillationen als auch Anzeichen von Einzel-Elektronen-Ladeeffekten beobachten, und schlagen mehrere Modelle auf Basis kompressibler und inkompressibler Streifen zur Erklärung dieser Phänomene vor.

Die vorliegende Arbeit ist wie folgt aufgebaut:

- In Kapitel 1 wird die Motivation für diese Arbeit kurz dargestellt.
- In Kapitel 2 werden die Grundlagen des QHE erläutert. Dazu gehören das Randkanalbild sowie Theorien, die die Existenz alternierender kompressibler und inkompressibler Streifen im Verarmungsbereich von 2DES in hohen Magnetfeldern voraussagen. Die Experimente zu den Hall-Potentialprofilen in Quanten-Hall-Proben mittels Rasterkraftmikroskopie, in denen das Vorhandensein kompressibler und inkompressibler Streifen sowohl in den Verarmungszonen der Probenränder als auch an der Grenzfläche ohmscher Kontakte nachgewiesen wurde, werden ebenfalls hier diskutiert.
- In Kapitel 3 werden die Grundlagen von Einzel-Elektronen-Ladeeffekten, der Coulomb-Blockade sowie der Physik von Quantenpunkten dargelegt. Anschließend werden sub- μm -Corbino-Proben in starken Magnetfeldern bei kryogenen Temperaturen als neue Realisierung eines Einzel-Elektronen-Transistors vorgestellt. Dies basiert auf folgenden Überlegungen: In den Corbino-Proben ist das kompressible Probeninnere bei tiefen Temperaturen und bei bestimmten Bereichen hoher Magnetfelder durch inkompressible Streifen von

den ohmschen Kontakten isoliert. Daher sollten bei einer Größe der Corbino-Probe im sub- μm -Bereich Einzel-Elektronen-Ladeeffekte zu beobachten sein.

- In Kapitel 4 folgt eine detaillierte Untersuchung einlegierter ohmscher Kontakte auf Au/Ge/Ni-Basis. Die elektrische Charakterisierung zeigt, wie bereits bekannt, eine Anisotropie des Kontaktwiderstandes in Bezug auf die Orientierung der Kontaktfläche. Diese Anisotropie ist bei tiefer liegenden 2DES stärker ausgeprägt. Offensichtlich gibt es eine bevorzugte und eine benachteiligte Kontaktierungsrichtung. In der bevorzugten Kontaktierungsrichtung skaliert der Kontaktwiderstand proportional zur Begrenzungslänge zwischen dem ohmschen Kontakt und dem 2DES. Die strukturellen Eigenschaften der einlegierten Kontakte wurden mit SEM, TOF-SIMS, TEM und EDX untersucht. Dabei wurden vorwiegend Au-reiche bzw. NiGe-reiche Phasen identifiziert. Diese unterschiedlichen Phasen wechselwirken mit der benachbarten $\text{Al}_\delta\text{Ga}_{1-\delta}\text{As}$ -Schicht in unterschiedlicher Weise. Vor der Au-reichen Phase wird das Al der $\text{Al}_\delta\text{Ga}_{1-\delta}\text{As}$ -Schicht durch Ga ersetzt, wodurch eine 50 nm bis 150 nm breite Zone entsteht, die frei von Al ist. Vor der Ni-reichen Phase ist das $\text{Al}_\delta\text{Ga}_{1-\delta}\text{As}$ jedoch unverändert. Anhand dieser Erkenntnisse entwickeln wir ein Modell für die Ladungsträger-Injektion zwischen dem einlegierten Metall und dem 2DES in GaAs/ $\text{Al}_\delta\text{Ga}_{1-\delta}\text{As}$ -Heterostrukturen.
- In Kapitel 5 werden die Herstellung und Charakterisierung von Kontakten mit Abmessungen im sub- μm -Bereich diskutiert. Kontakte zu 2DES mit einem kleinstmöglichen Durchmesser von 0,2 μm und spezifischen Kontaktwiderständen zwischen 0,5 $\text{k}\Omega\mu\text{m}$ und 10 $\text{k}\Omega\mu\text{m}$ konnten präpariert werden. Die Erfolgsquote beim Kontaktieren eines 2DES mit einem sub- μm -Kontakt betrug durchschnittlich 50 %. Dabei kann durch zyklisches Abkühlen und Aufwärmen der Probe zwischen Raumtemperatur und 4 Kelvin der Kontaktwiderstand drastisch beeinflusst werden. Ein bei 4 Kelvin nicht leitender Kontakt kann unter Umständen nach Erwärmen bis auf Raumtemperatur beim nächsten Abkühlen auf 4 Kelvin elektrisch leitend sein.
- In Kapitel 6 werden Experimente an sub- μm -Corbino-Proben bei kryogenen Temperaturen und schwachen Magnetfeldern bzw. ohne Feld dargestellt. Bei Temperaturen von 50 mK ohne Magnetfeld wird eine unerwartete Zero-Bias-Anomalie in der elektrischen Leitfähigkeit beobachtet. Die differentielle Leitfähigkeit, aufgetragen gegen die Vorspannung, zeigt einen deutlichen Einbruch. Dieser Effekt ist mit steigender Temperatur immer schwächer ausgeprägt und verschwindet bei Temperaturen um 1,5 K. In einem schwachen Magnetfeld mit senkrechter Orientierung zum 2DES steigt die Leitfähigkeit mit dem Magnetfeld und sättigt bei etwa 0,2 T, wobei immer noch ein gewisser Abfall bei Vorspannung Null vorhanden ist. Mit steigender Temperatur

verringert sich der Abfall, bis er bei ungefähr 0,5 K nicht mehr nachweisbar ist. Aufgrund der verschiedenen Temperaturskalen vermuten wir für diese beiden Effekte unterschiedliche Ursachen, und diskutieren die Messungen im Kontext schwacher Lokalisierung.

- In Kapitel 7 folgen die Experimente in hohen Magnetfeldern. In diesem Regime treten in bestimmten Feldbereichen Oszillationen auf, die sich periodisch mit dem Magnetfeld verhalten. Unter der Annahme Aharonov-Bohm-artiger Oszillationen kann aus der Oszillationsperiode eine Fläche ermittelt werden, deren Radius im Allgemeinen geringfügig größer als der Radius des inneren Kontakts ist. Dies deutet auf Interferenzen am inneren Kontakt hin. An einigen der Proben wurden darüber hinaus Anzeichen von Einzel-Elektronen-Ladeeffekten beobachtet. Weiterhin geht bei diversen Proben die Leitfähigkeit bei Füllfaktoren 2 und 1 gegen Null. Die differentielle Leitfähigkeit nimmt jedoch ab einer gewissen Schwellen-Vorspannung wieder finite Werte an, was auf den Zusammenbruch des Quanten-Hall-Effektes hinweist.
- In Kapitel 8 werden abschließend die Schlussfolgerungen aus dieser Arbeit gezogen, sowie ein Ausblick gegeben.

Die Anhänge enthalten die Details der Probenpräparation und weitere ergänzende Experimente.

Appendices

Appendix A

Clean room process for ohmic contacts by optical lithography

In this section the detailed recipe for the preparation of ohmic contacts will be given. First, the preparation of mesa stripes for the TLM structures will be described. Then the lithography steps for the definition of ohmic contacts on the mesa stripes will be given. The cleaning is a critical step at this process. The thickness ratios of the Au/Ge/Ni layers is important. If the depth of 2DES is larger than 86 nm the thicknesses of the evaporated metals should be scaled up following (A.1). Following the lift-off process, the alloying steps are described. After alloying a Cr/Au top metallization step is performed. This step is necessary to process since the Au bonding wires does not stick to Au/Ge/Ni alloyed metals very well. However, this step can be skipped if you have no problem with bonding or if you use glue bonding.

1. Preparation of the mesa

(a) Cleaning of the heterostructure

- 2 min in acetone in ultrasonic bath
- Consequently dips in three bechers filled with acetone(30 s:15 s:5 s)
- Dip in propanol becher
- Dry with nitrogen

(b) Coating with photoresist S1805

- Put a few drop of the resist on the sample
- Spin coating (30 s 4500 rpm)
- 2 min on hot plate 90 °C

(c) Exposure

- Mount the sample and mask on the mask-aligner
- There are several masks available. The one which is designed during this study for the TLM measurements is Mask R120.
- Exposure 6 s in "ST" mode

(d) Development

- Develop sample in the AZ726MIF developer with shaking constantly 30 s
- Dip sample in DI water for about 30 sec

(e) Etching

- Prepare etching solution: ($\text{H}_2\text{O} : \text{H}_2\text{O}_2 : \text{H}_2\text{SO}_4$ with volume ratios 1000 : 8 : 1 (200 ml : 1.6 ml : 0.2 ml)); etching rate is around 40 nm/min for GaAs and it is better to make a calibration for each heterostructure
- Put sample in the etching solution with a glass holder and keep there for desired etching depth - normally we etch deeper than the heterostructure depth
- Put sample in the DI water and keep there till the DI water bath is clean enough (that it, reaches high resistance values again)
- Take sample from the DI water bath and dry with nitrogen
- Mesa height can be measured by profilometer to check whether desirable etching depth is reached.

2. Lithography for the ohmic contacts on the mesa

(a) Clean the sample as (1a)

(b) Coating with photoresist AZ5214E 1:0

- Put sample in the spin coater
- Put a few drop of photoresist AZ5214E 1:0 on the sample
- Spin for 30 sec at 6000 rpm
- Bake for 4 min at 90 °C on the hot plate

(c) Exposure

- Mount Cr-mask R120 and sample in the mask aligner (MJB3)
- Expose 6 seconds in "ST" mode in mask aligner (7 seconds in new mask aligner (MA6))
- Bake at the hot plate for 1 min at 122 °C for the image reversal process. It makes positive resist behave like negative resist

-
- Expose 70 seconds in "Soft" mode (Flat exposure, no mask is mounted)
- (d) Develop for 30 seconds as in (1d)
3. Evaporation of the Au/Ge/Ni layers
- (a) Prepare evaporation chamber- place Au, Ge, and Ni in the boats and mount the boats in the chamber
- (b) Preparing of the surface
- O₂ plasma cleaning (30 s, pressure 0.3 torr, power 200 W) -place sample under the rostr
 - Dip sample into Semico Clean 23¹ for 2 minutes
 - 5 seconds into DI water
 - 5 seconds into HCl (30 %)
 - 3 seconds into DI water
 - Dry with nitrogen
 - *The last four steps (starting from Semico Clean 23) are done very quickly after each other. After cleaning, the sample should be placed in the evaporation chamber immediately (we do not wait more than 5 minutes.)*
- (c) Place sample immediately in the evaporation chamber and start evacuating
- (d) Evaporation
- For thickness of the metals used in this study see Table A.1. For a depth of 2DES smaller than 86 nm, Au, Ge, and Ni layer thicknesses are 107.2 nm, 52.8 nm and 40 nm, respectively. For a depth of 2DES deeper than 86 nm all the metal thicknesses must be scaled up by a factor s according to following formula [64]

$$s = \frac{D_{2DES} + 30 \text{ nm}}{110 \text{ nm}}, \quad (\text{A.1})$$

where D_{2DES} is the depth of the 2DES in nanometers.

- Pressure is about 5×10^{-6} mbar or lower
- Evaporate Au; rate is about 3 Å/s
- Evaporate Ge; rate is about 2 Å/s
- Evaporate Ni; rate is about 1 Å/s

¹Furuuchi Chemical Corporation, Fine Trading Division, 6-17-17 Minamioi, Shinagawa-ku Tokyo 140-0013, Japan

Depth of 2DES	Au	Ge	Ni
nm	nm	nm	nm
$D_{2DES} = 120$	146.0	72.0	54.0
$D_{2DES} \leq 86$	107.2	52.8	40.0

Table A.1: The thickness of the metal layers evaporated for different depth of 2DES

4. Lift-off

- (a) Put sample into acetone bath and wait till all the resist dissolves
- (b) Take sample out of acetone and immediately splash with acetone (sample should not get dry)
- (c) Put sample into propanol and have a look under the light microscope whether the lift-off has worked successfully (sample is still in propanol becher); if not repeat the process
- (d) Dry with nitrogen

5. Annealing

- (a) Place sample in the annealing oven AZ500
- (b) Start annealing cycle (under N_2/H_2 atmosphere volume ratio 80% / 20%)
 - i. $T = 370$ °C, $t=120$ s, $p=300$ mbar (no gas flow)
 - ii. $T = 340$ °C, $t=50$ s, $p=300$ mbar (no gas flow)
 - iii. $T = 100$ °C, $t=2$ s, $p=300$ mbar (gas flow with constant pressure)

6. Bond pads : The gold wire does not stick alloyed contact very well. So if you are not using a glue bonding method then it is necessary to evaporate an additional Cr/Au layer on top of the contacts

- (a) Follow the steps in (2) to define bond pads area
- (b) Put samples in the evaporation chamber
- (c) Wait till a good pressure (less than $5 \cdot 10^{-6}$ mbar) is reached.
- (d) Evaporate Cr/Au
 - i. Cr 20 nm at a rate of 1.5 \AA/s
 - ii. Au 100 nm at a rate of 3 \AA/s
- (e) Lift-off as in (4)

Appendix B

List of chemicals and equipment

In this section the details of the some of the equipment and chemicals which are used during this work are are listed.

1. Clean room :

- Evaporation chamber Model Univex 450 from Leybold-Heraeus, Hanau
- Alloying oven AZ450 with the software AZ500 (Dr. Eberl, MBE-Components GmbH, Weil der Stadt)
- Electron beam lithography (EBL) e_Line from Raith (Dortmund) with software version 4.0

2. Chemicals :

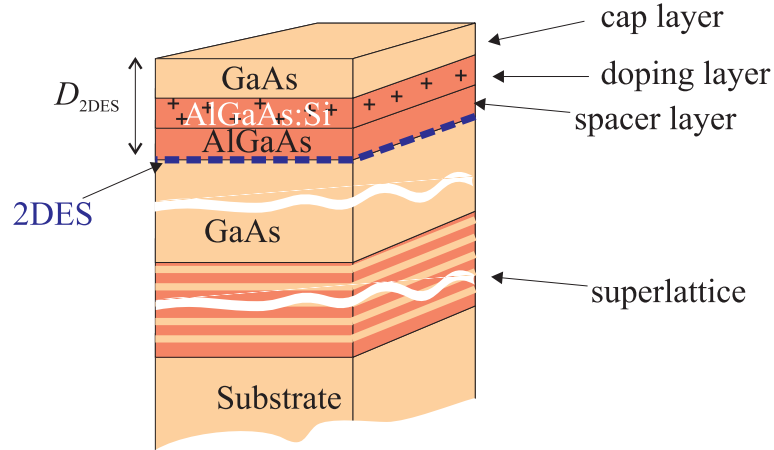
- Positive-photoresist Microposit S1805 from Shipley Europe Ltd. (Convertry, United Kingdom)
- Negative-positive-photoresist AZ5214E from AZ Electronic Materials (Germany) GmbH, Wiesbaden
- Developer AZ726MIF from AZ Electronic Materials (Germany) GmbH, Wiesbaden
- Semico Clean 23, Furuuchi Chemical Corporation, Fine Trading Division, 6-17-17 Minamioi, Shinagawa-ku Tokyo 140-0013, Japan
- PMMA 200K 7% (E-Beam resist AR-P641.07 with molecular weight 200000 u thinned to 7% solid contents using chlorobenzene as solvent) Allresist GmbH (Strausberg, Germany)
- PMMA 950K 5% (E-Beam resist AR-P671.05) Allresist GmbH (Strausberg, Germany)

- PMMA 950K 1.5% (E-Beam resist AR-P671.01) Allresist GmbH (Strausberg, Germany)
- PMMA 950K A5 (E-Beam resist) micro resist technology GmbH (Berlin, Germany)
- MMA MAA EL9 (E-Beam resist) micro resist technology GmbH (Berlin, Germany)
- PMMA 200K A3 (E-Beam resist) micro resist technology GmbH (Berlin, Germany)
- Semico Clean 23 Furuuchi Chemical Corporation, Fine Trading Division, 6-17-17 Minamioi, Shinagawa-ku Tokyo 140-0013, Japan
- Au, purity 99.99 %
- Ge, purity 99.999 %
- Ni, purity 99.97 %
- Cr, purity 99.99 %

Appendix C

Additional TLM experiments on alloyed ohmic contacts

In this section more experimental data on ohmic contacts will be presented. The necessary information is given in the figure captions. The figures and tables are cited in Chapter 4 where it was necessary. In Table C.1 the growth sequences of the heterostructures are given. Room temperature measurements TLM measurements are given in Fig. C.1. TLM measurements at 4 K for all the wafers are given in Fig. C.2, Fig. C.3 and Fig. C.4. TLM measurements for different thickness of the alloyed contacts is presented in Fig. C.5. TLM measurements for alloyed contacts with and without Ni layer are shown in Fig. C.6. The sheet resistivity for the 2DES as a function of mesa width for all the wafers is presented in Fig. C.7. The TLM measurements for the sample which is used for the SEM, STEM and EDX investigations is shown Fig. C.8. The TLM measurements at 1.5 K and 25 mK for a TLM structure is shown in Fig. C.9.



Wafer	GaAs	AlGaAs	AlGaAs:Si	AlGaAs	D_{2DES}	GaAs	Superlattice
	cap		doping	spacer	depth of		
	layer		layer	layer	heterojunction		
#	[nm]	[nm]	[nm]	[nm]	[nm]	[nm]	GaAs/AlGaAs
8963	10	10	60	40	120	1000	50x(10 nm/10 nm)
81744	10	10	60	40	120	1000	50x(10 nm/10 nm)
81763	6	-	50	30	86	1000	50x(10 nm/10 nm)
81758	10	-	20	20	50	500	50x(10 nm/10 nm)
81757	5	-	25	10	40	1000	25x(10 nm/10 nm)
81628	5	-	25	10	40	1000	25x(10 nm/10 nm)

Table C.1: Growth sequence of the wafers used in this work. The thicknesses of layers are given beginning from the top cap GaAs layer. The sketch of a wafer is also shown for clarity.

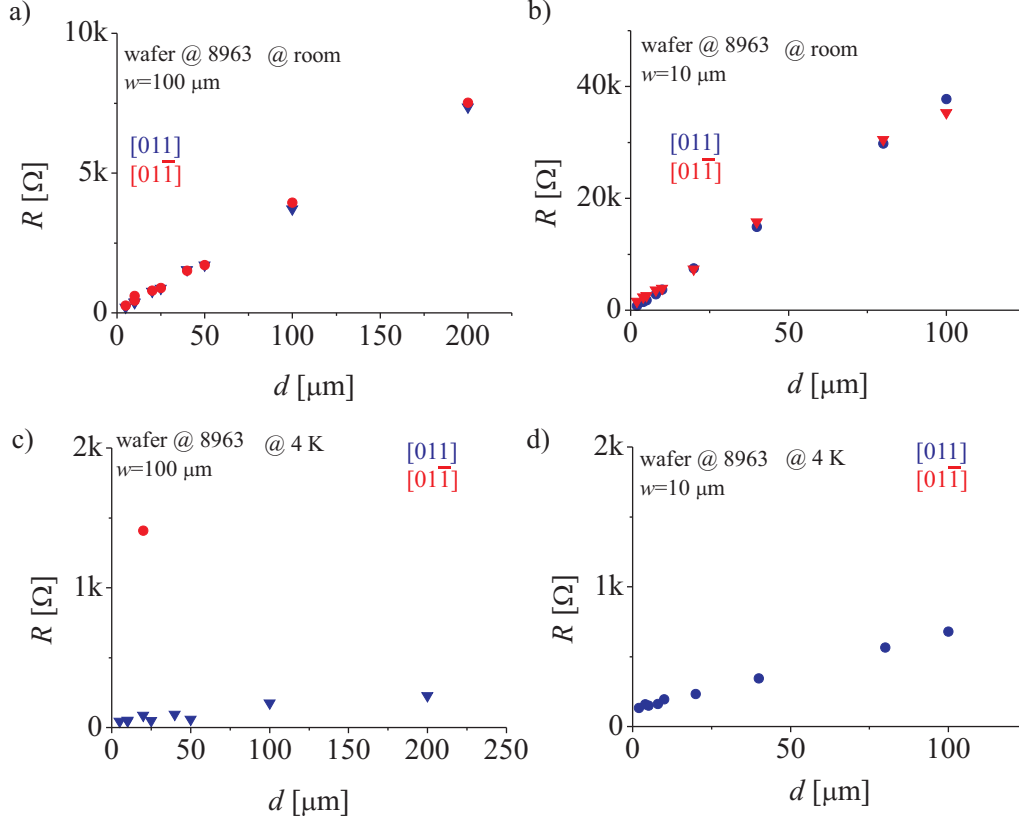


Figure C.1: TLM measurements at room temperature and at 4 K. (a) TLM measurements at room temperature for a sample with mesa stripe width of $w = 100 \mu\text{m}$, (b) for a sample with mesa stripe width of $w = 10 \mu\text{m}$. At room temperature there is no difference between good contacting and bad contacting direction. Contact resistance for the $w = 100 \mu\text{m}$ sample is $R_c = (0 \pm 28) \Omega$ in good contacting direction and $R_c = (54 \pm 56) \Omega$ in bad contacting direction. By length of a line: For $w = 10 \mu\text{m}$ sample $R_c = (-72 \pm 60) \Omega$ in good direction and $R_c = (821 \pm 326) \Omega$ in bad contacting direction. (c) and (d) TLM measurements at 4 K for the same samples. $R_c = (21 \pm 4.5) \Omega$ for $w = 100 \mu\text{m}$ sample and $R_c = (63 \pm 1.6) \Omega$ for $w = 10 \mu\text{m}$ sample. Contacts in bad contacting direction mostly do not work or have very high contact resistances.

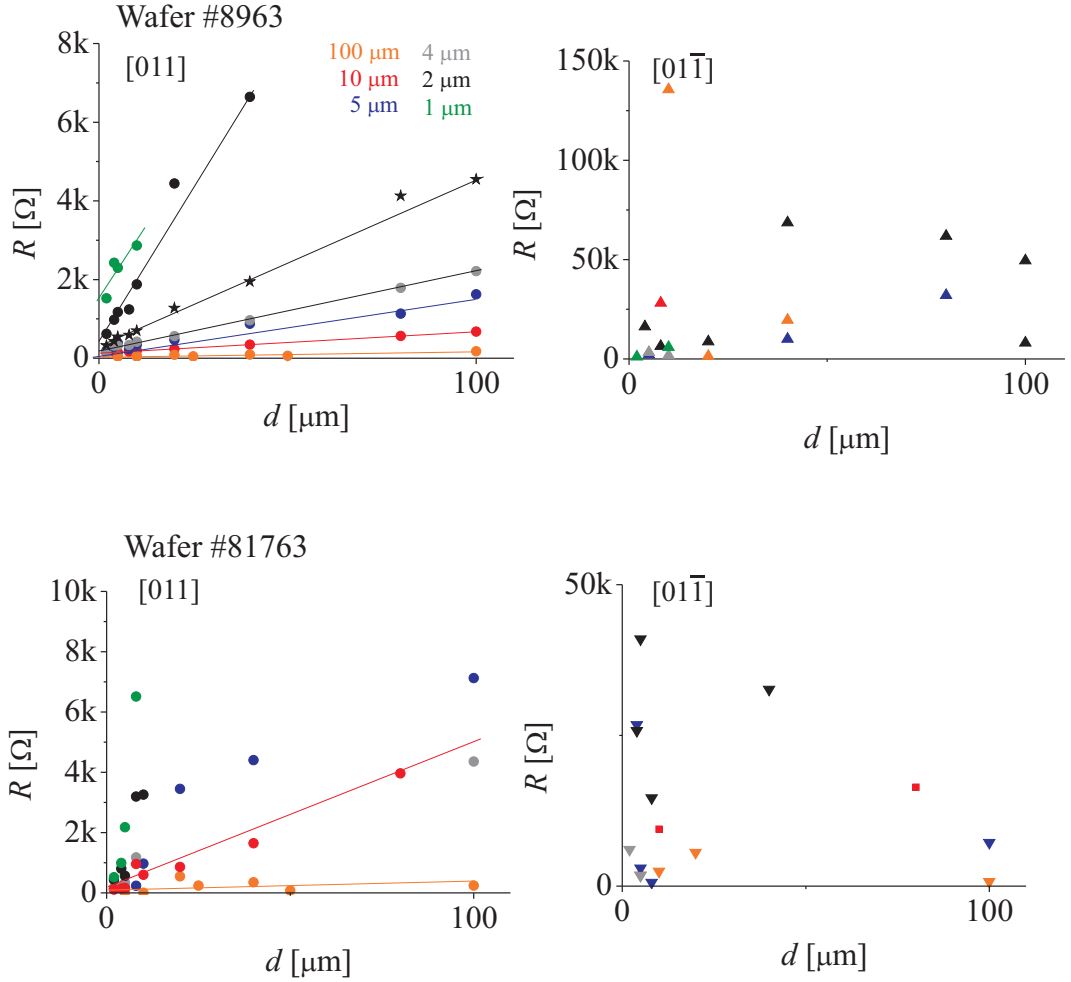


Figure C.2: (a) TLM measurements in good contacting and (b) in bad contacting direction for wafer # 8963. (c) TLM measurements in good contacting and (d) in bad contacting direction for wafer# 81763. The electron density, mobility and depth of 2DES is given in Table 4.1. The width of mesa is indicated with the same color as corresponding data set. Color coding and mesa width is the same for all the figures.

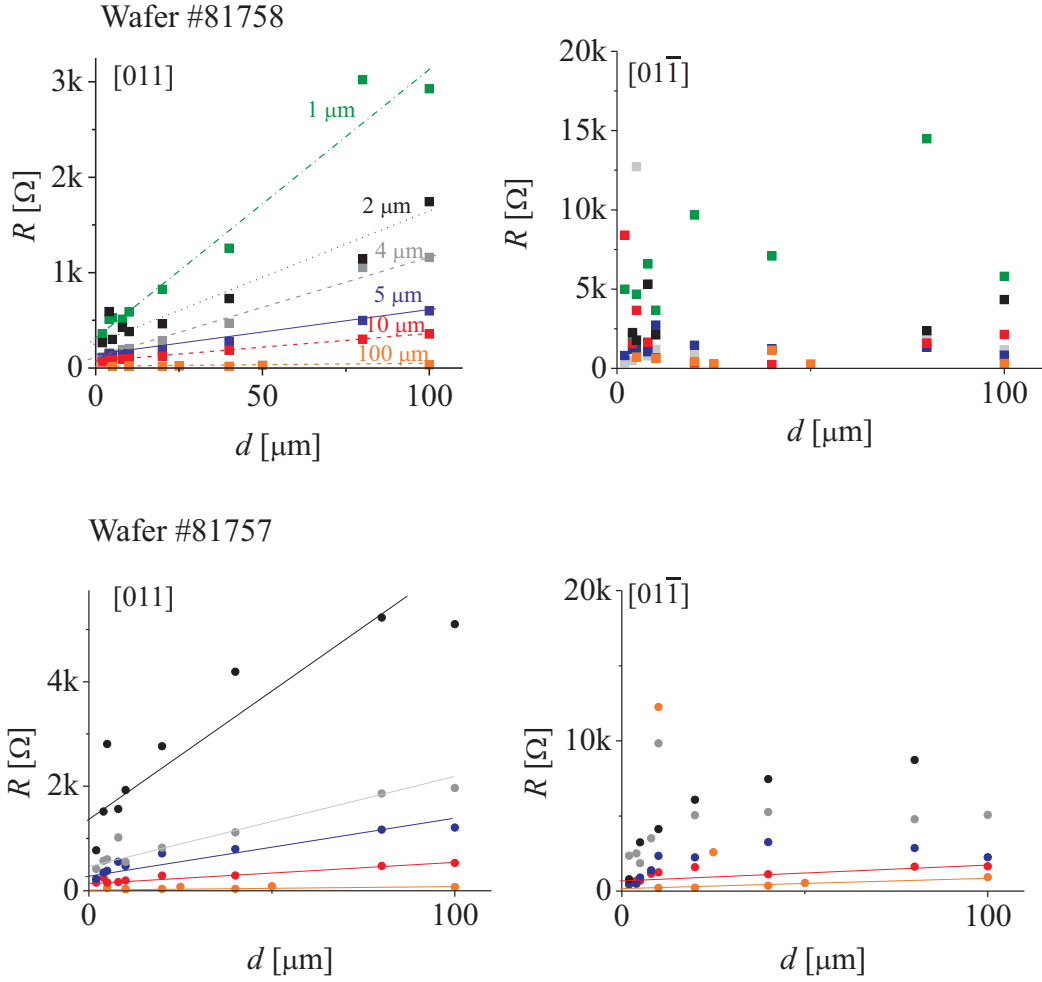


Figure C.3: (a) TLM measurements in good contacting and (b) in bad contacting direction for wafer # 89758. (c) TLM measurements in good contacting and (d) in bad contacting direction for wafer #81757. The electron density, mobility and depth of 2DES is given in Table 4.1. The width of mesa is indicated with the same color as corresponding data set. Color coding and mesa width is the same for all the figures.

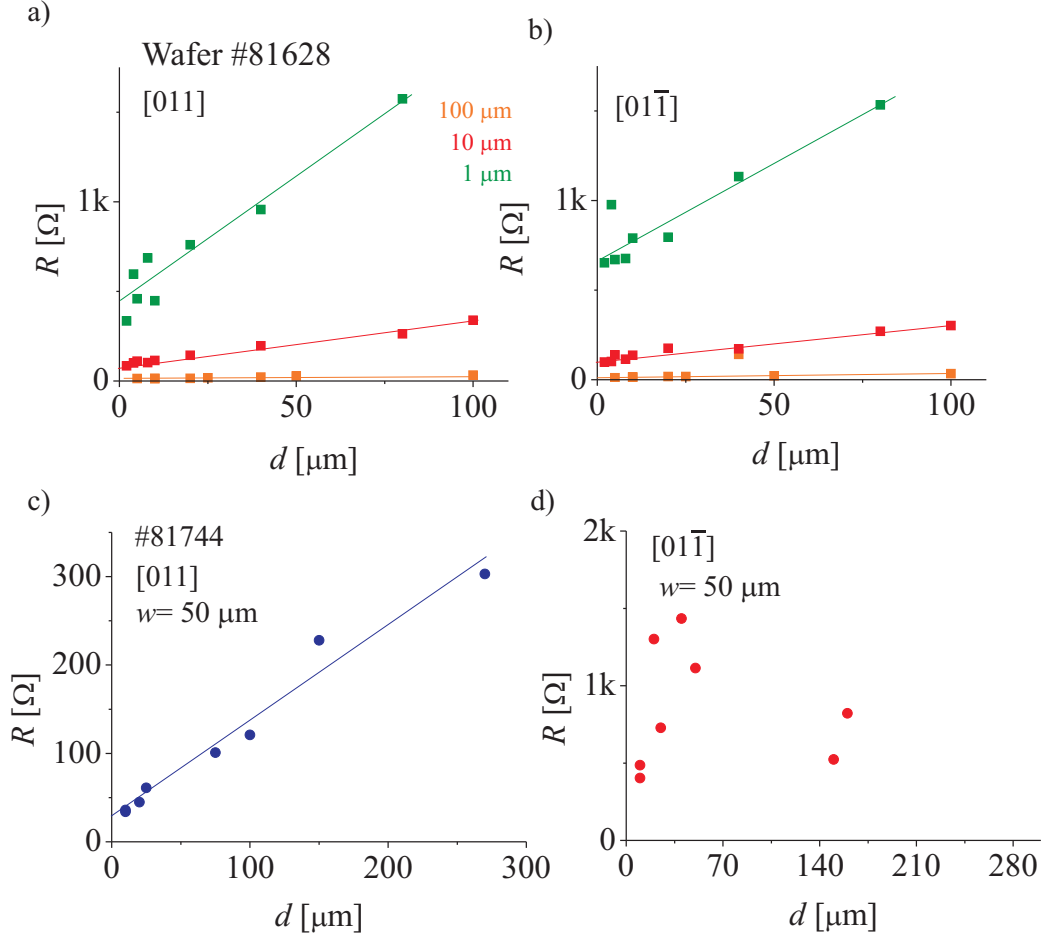


Figure C.4: (a) and (b) TLM measurements in good contacting and bad contacting direction for wafer # 81628. The electron density, mobility and depth of 2DES is given in Table 4.1. The width of mesa is indicated with the same color as corresponding data set. Color coding and mesa width is the same for both figures. (c) TLM measurements in good contacting direction and (d) in bad contacting direction. The mesa stripe width is $w = 50 \mu\text{m}$. The sample is prepared by EBL.

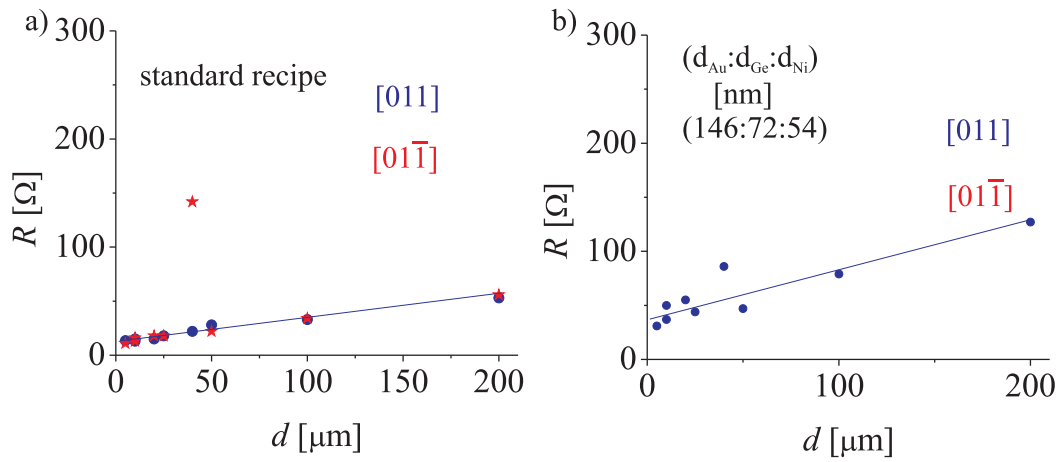


Figure C.5: (a) TLM measurements in good contacting and bad contacting direction for wafer # 81628 for a standard contact recipe (107.2 nm Au, 52.8 nm Ge and 40 nm Ni). (b) The contact material was scaled for 120 nm depth of 2DES (146 nm Au, 72 nm Ge and 54 nm Ni). The width of mesa is 100 μm . For the standard recipe the results are similar in both direction. If the contact metal thicknesses are scaled up contact resistance in good contacting direction is $(18 \pm 3) \Omega$. This value is larger than the value of $(6.5 \pm 0.5) \Omega$ obtained for the standard recipe. In the bad contacting direction contact mostly do not work (a few contact work with a contact resistance larger than 10 k Ω).

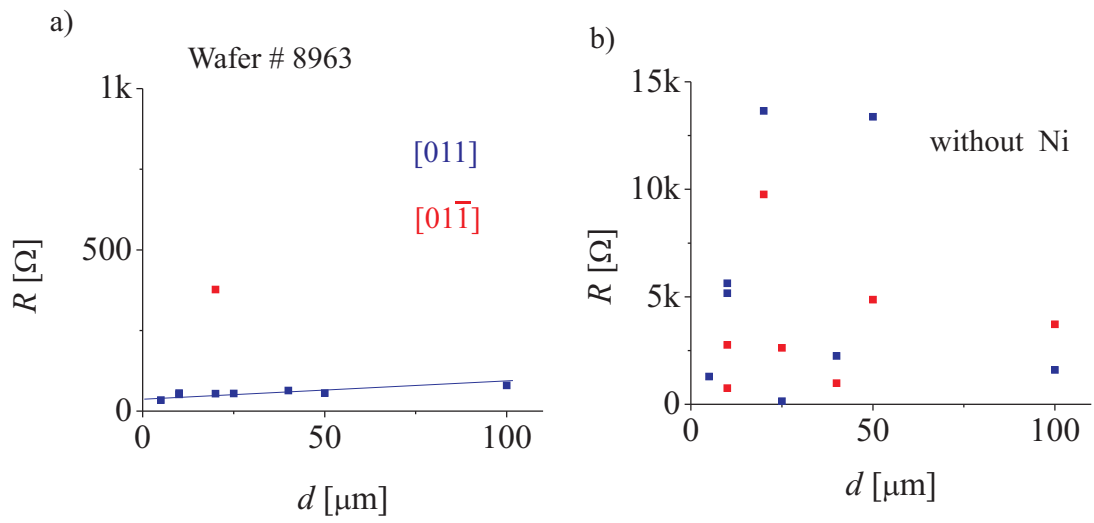


Figure C.6: (a) TLM measurements on the wafer # 8963. Expected behavior depending orientation. The thickness of the Au/Ge/Ni layers are 146.0/71.5/54.5 nanometers as usually used for this wafer. (b) Contacts which are defined without Ni. Only 146.0/71.5 nanometers of Au/Ge are evaporated. Contact resistance is high with a large spread in both direction.

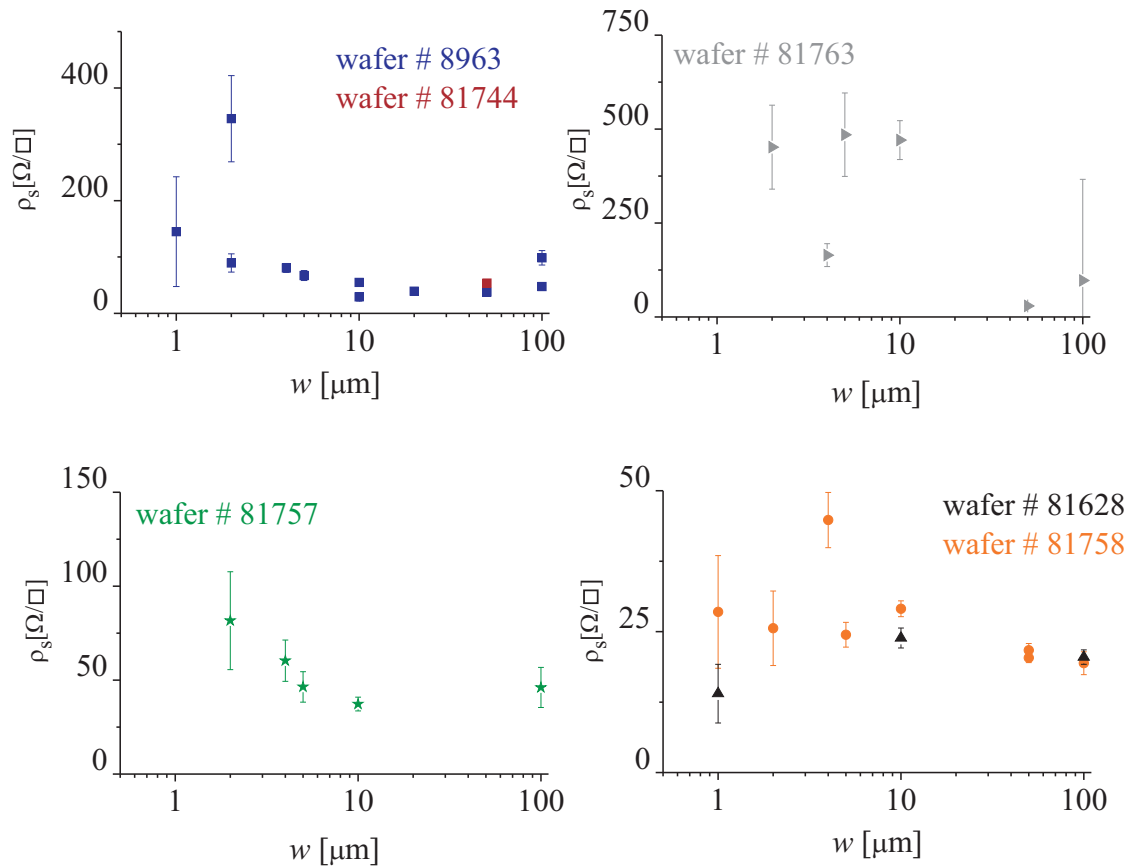


Figure C.7: The sheet resistivity ρ_s , extracted from the TLM measurements, as a function of mesa width w for different heterostructures. The wafers are labeled with numbers (different colors) and corresponding data set are given with the same colors.

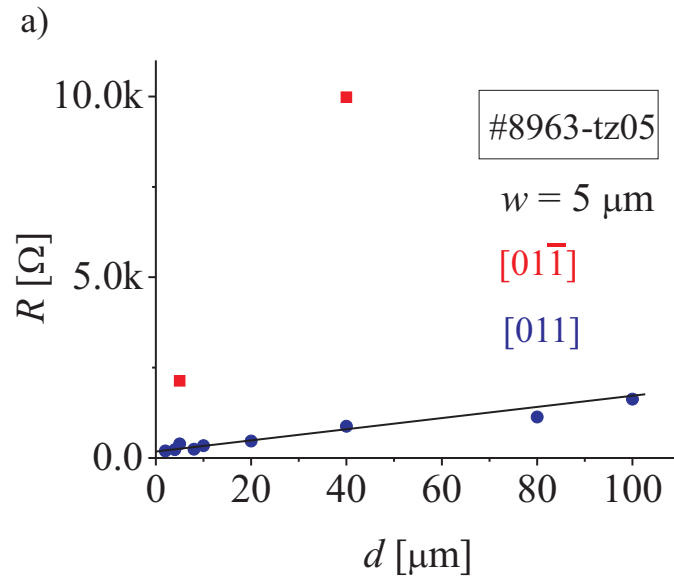


Figure C.8: TLM data for the sample which is used for the SEM, STEM and EDX investigations.

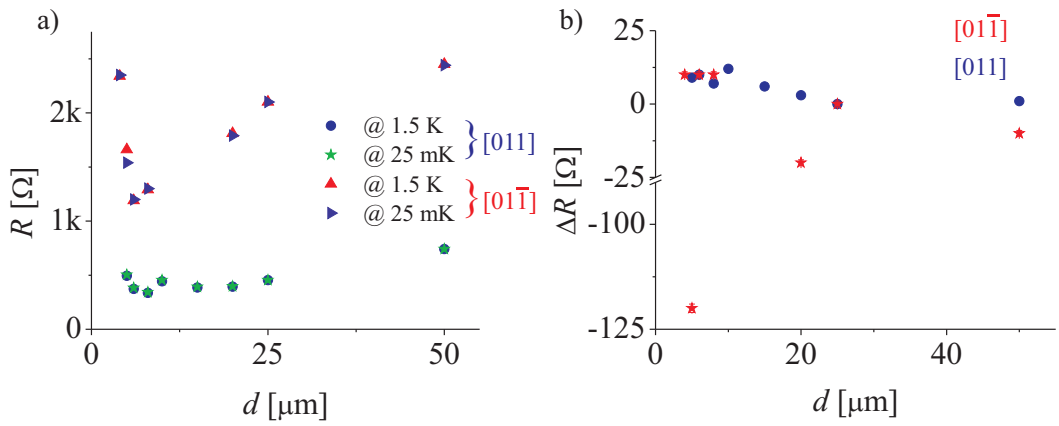


Figure C.9: (a) TLM measurements at 1.5 K and 25 mK on the wafer # 8963. The mesa width is $w = 5 \mu\text{m}$. The dependence of the contact resistance to temperature is very weak. (b) The change in the resistance $\Delta R = R(25 \text{ mK}) - R(1.5 \text{ K})$ for good contacting and bad contacting directions

Appendix D

Additional SEM images of the alloyed contacts

In this section the cross-sectional SEM images of alloyed contacts are shown. In Fig. D.1, Fig. D.2, Fig. D.3, , Fig. D.4 and Fig. D.5 the wafer is #8963.

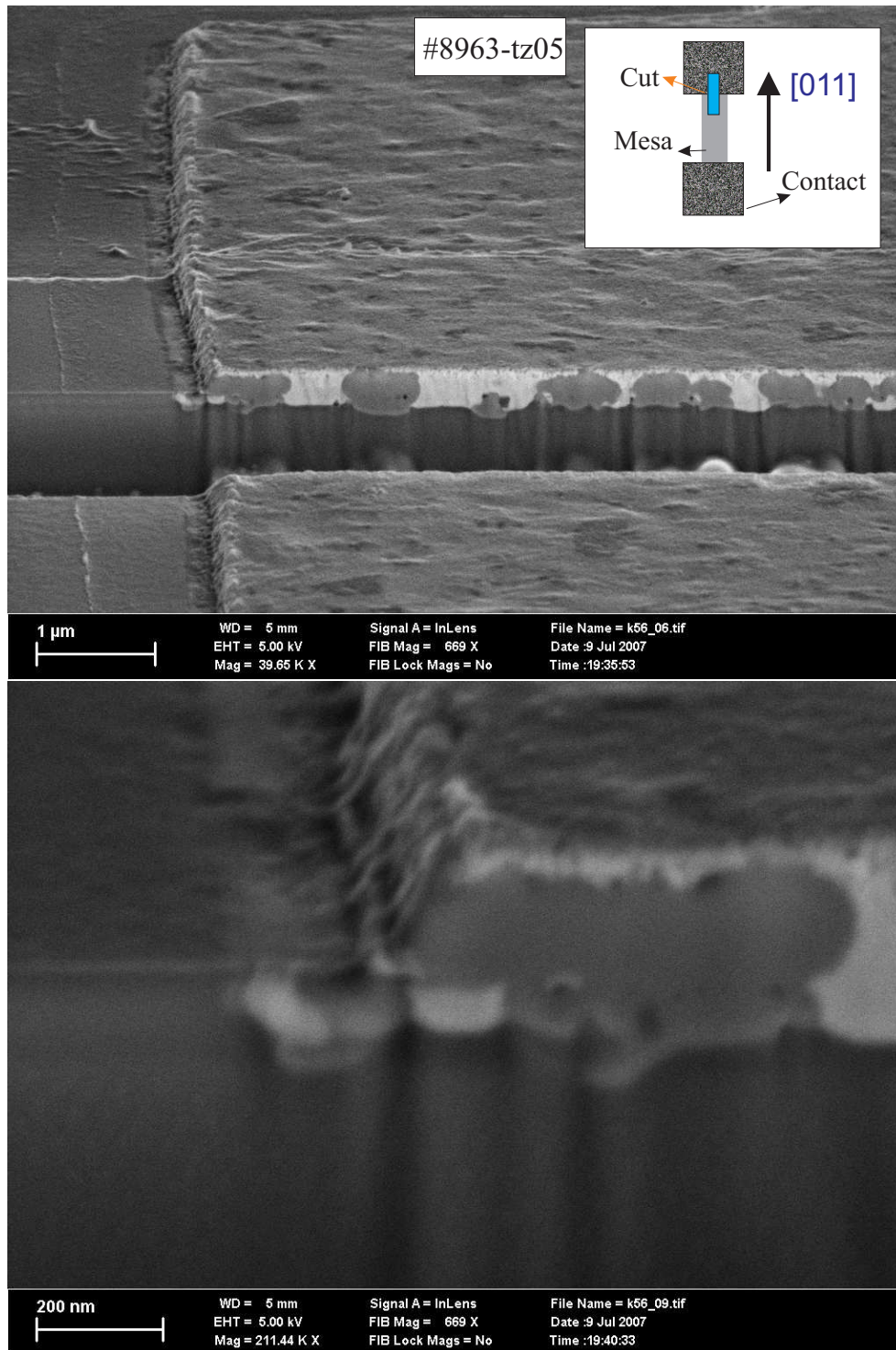


Figure D.1: Cross sectional SEM images of the alloyed contacts in good contacting orientation

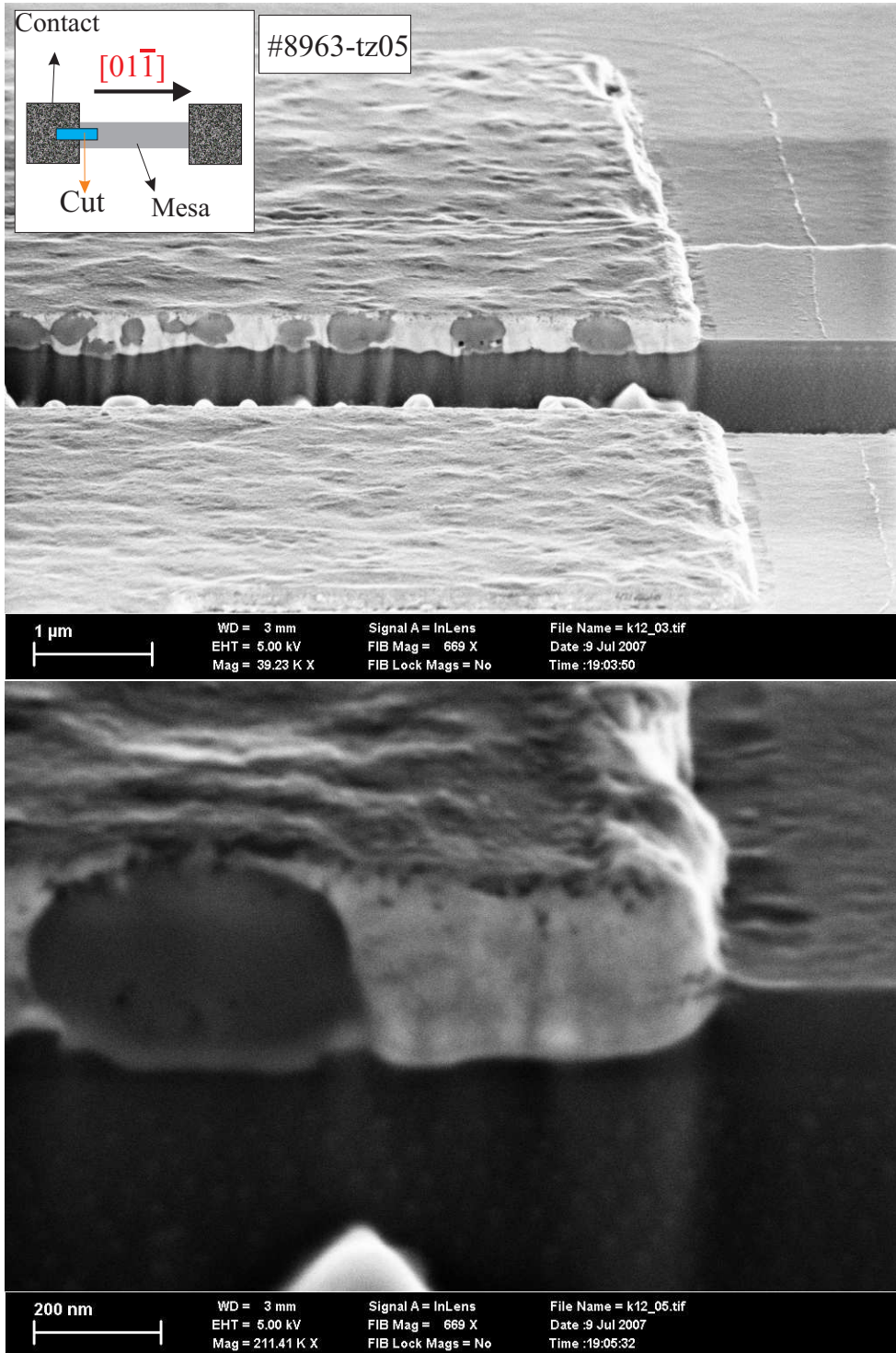


Figure D.2: Cross sectional SEM images of the alloyed contacts in bad contacting orientation

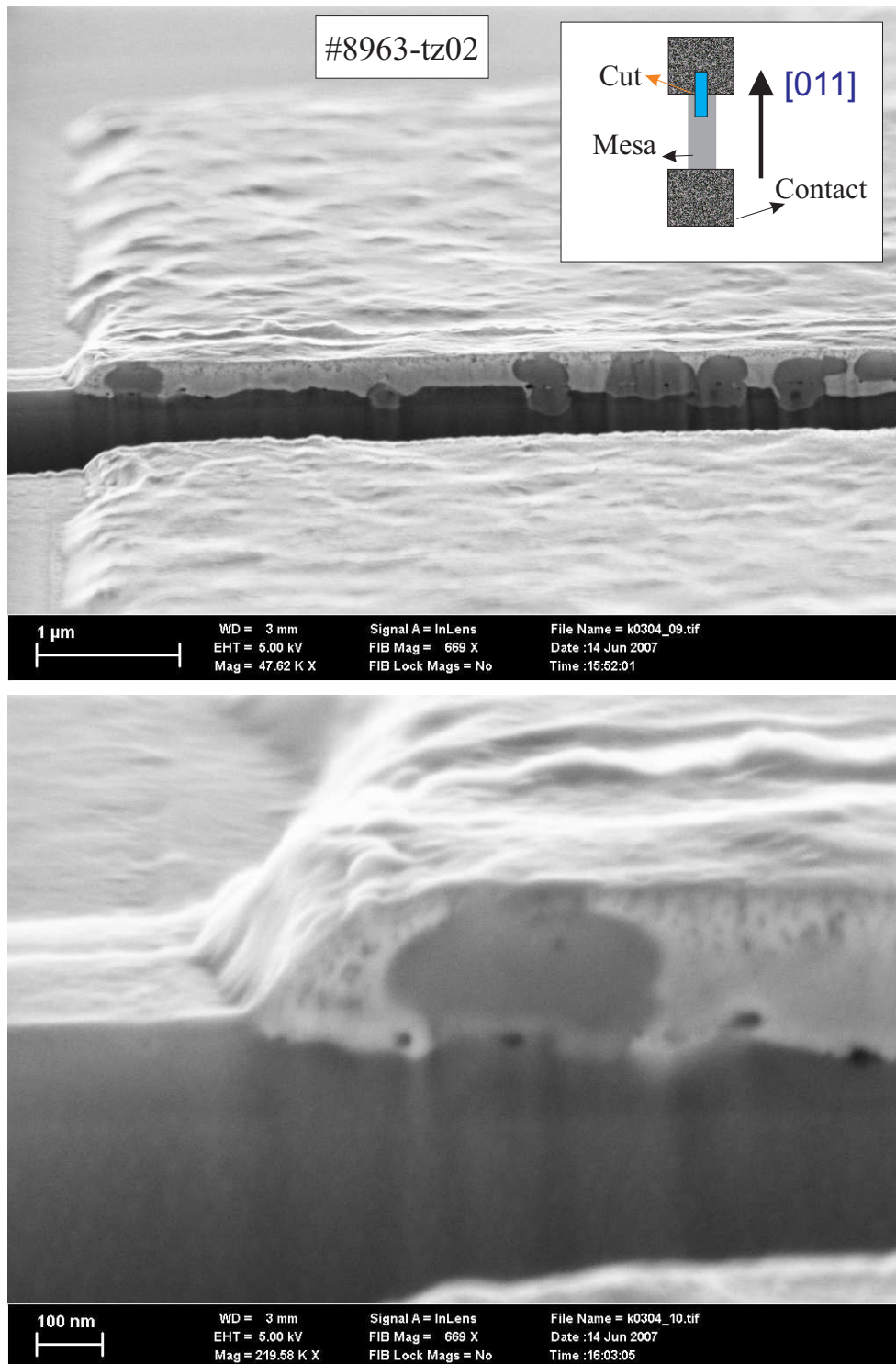


Figure D.3: Cross sectional SEM images of the alloyed contacts in good contacting orientation

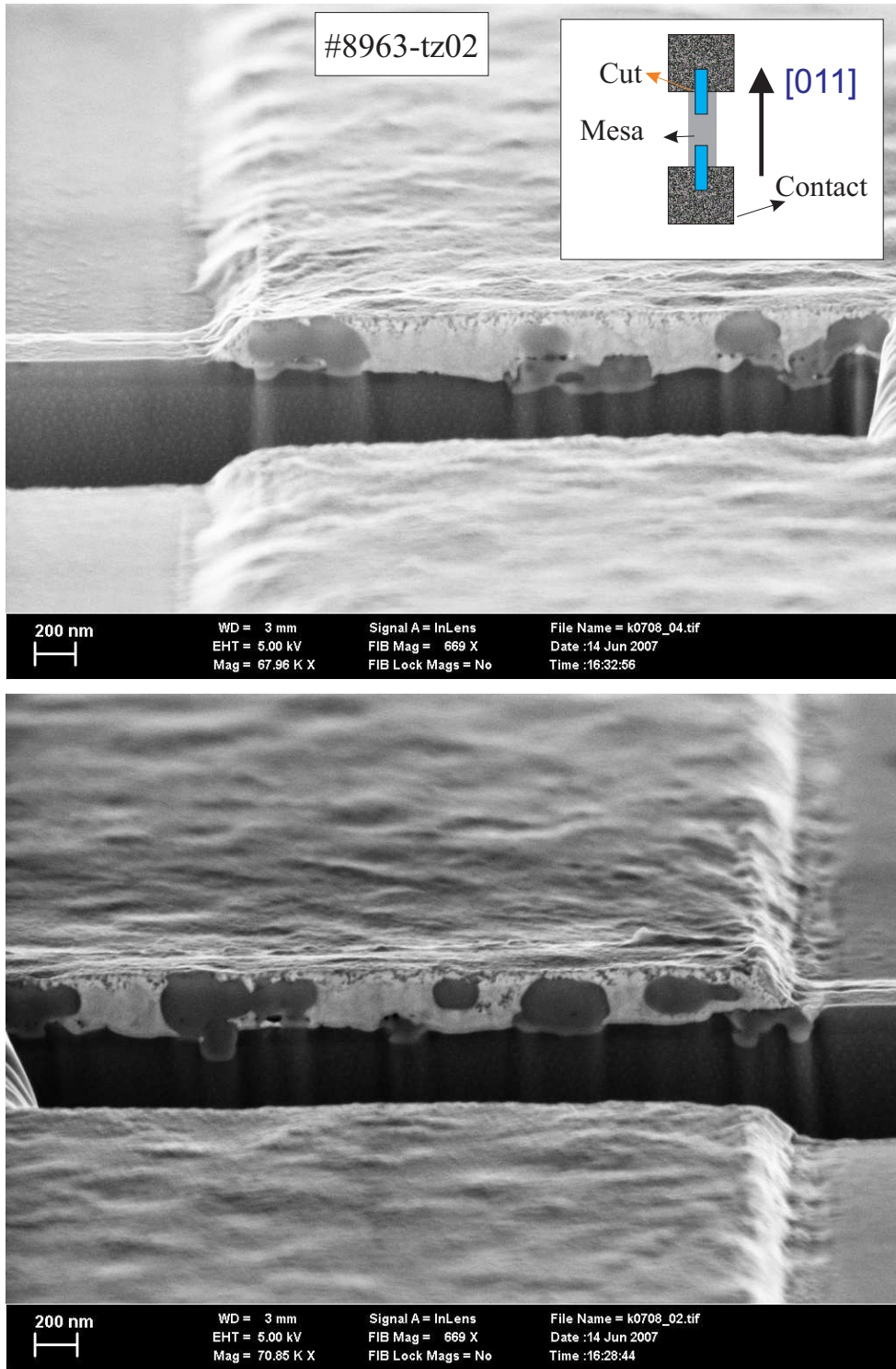


Figure D.4: Cross sectional SEM images of the alloyed contacts in good contacting orientation

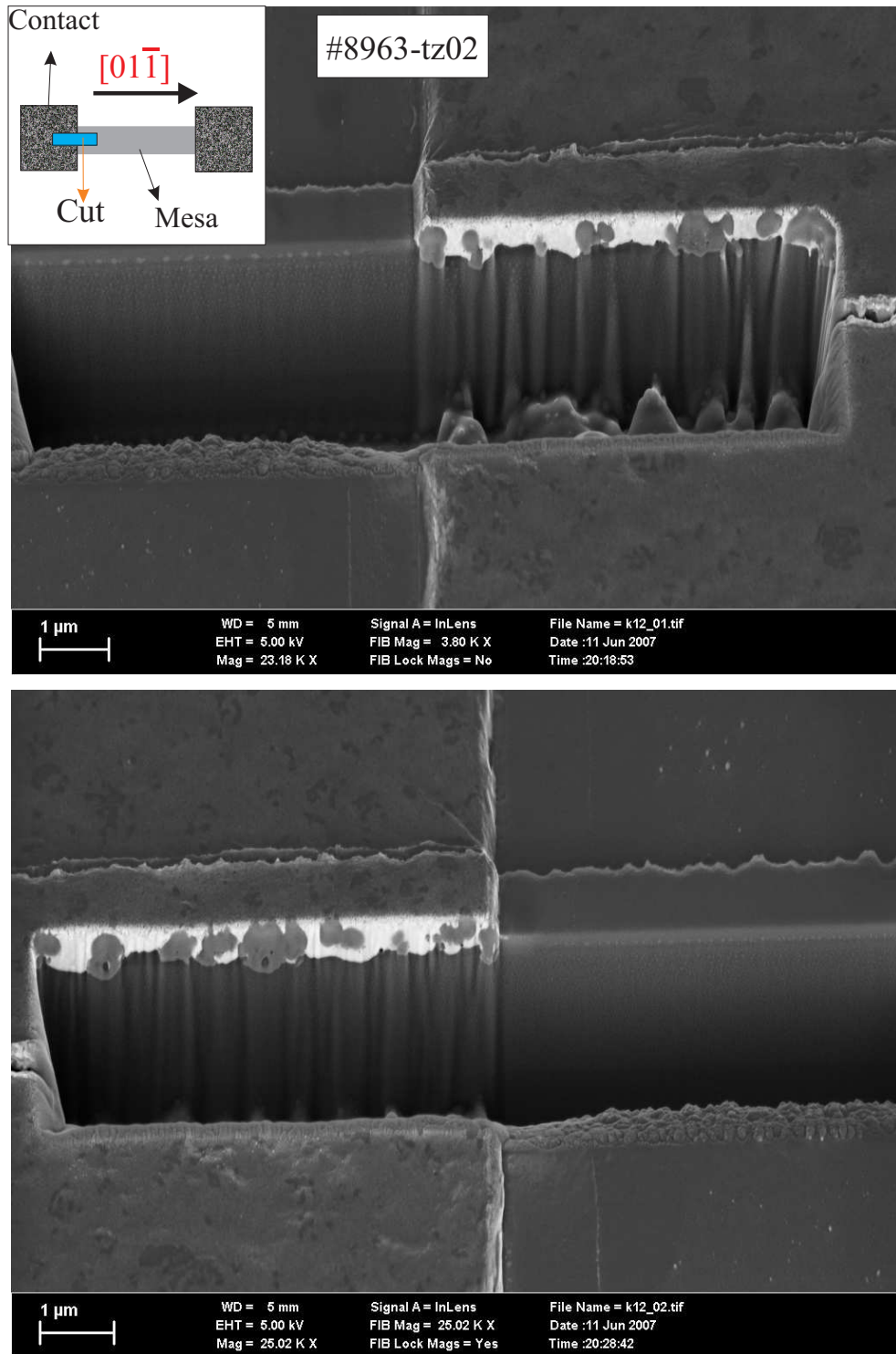


Figure D.5: Cross sectional SEM images of the alloyed contacts in bad contacting orientation

Appendix E

Additional TOF-SIMS images of the alloyed contacts

In this section the result of the TOF-SIMS experiments in the contact defined on wafer #81763 are presented. The depth of the 2DES is 86 nm for this wafer.

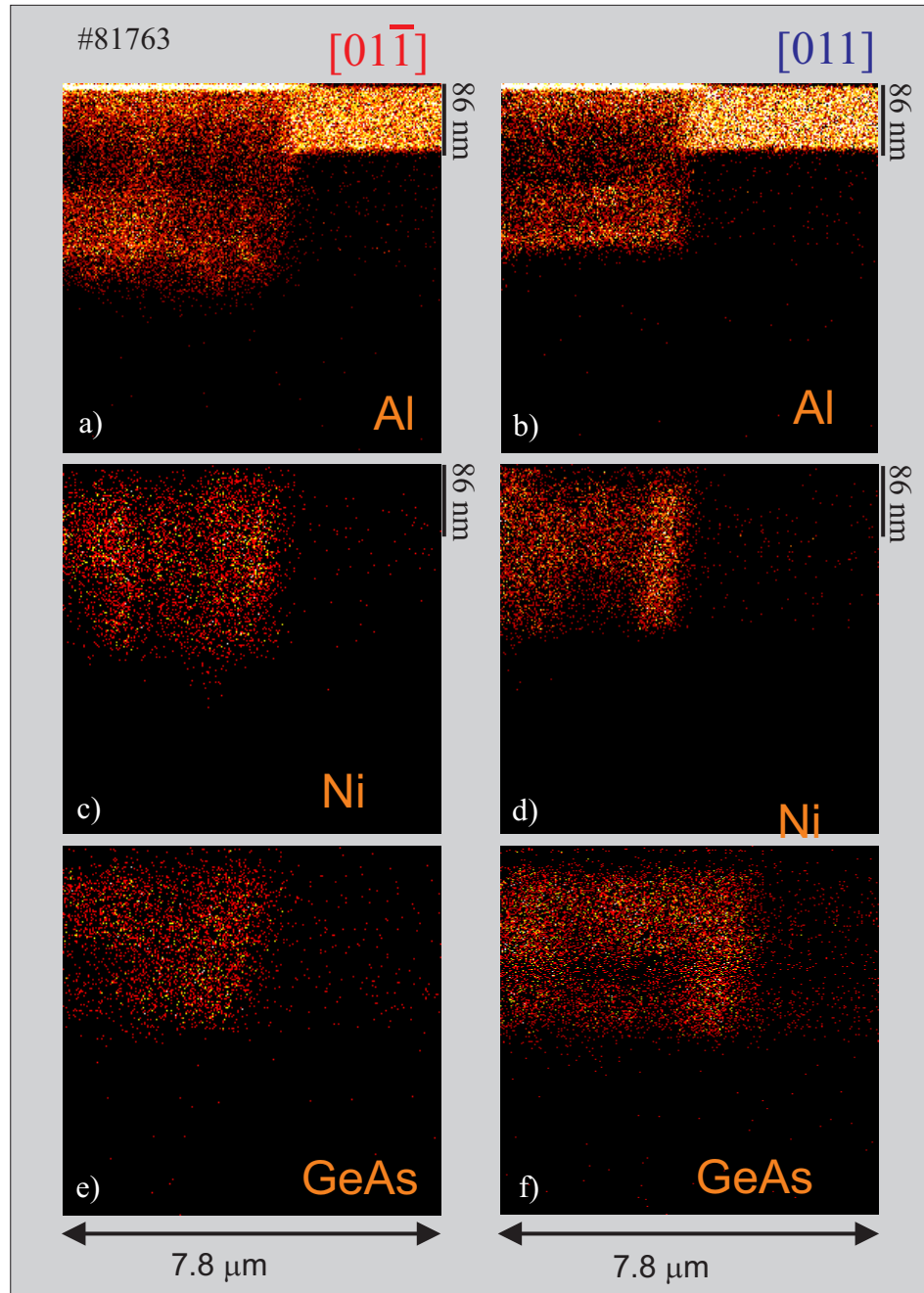


Figure E.1: TOF-SIMS investigation of the contacts defined in wafer #81763.

Appendix F

Additional TEM images of the alloyed contacts

In this section additional STEM and EDX analyzes are presented. The necessary information is provided in the figure captions. In Fig. F.1, Fig. F.2 and Fig. F.3 the point analyzes at the different position on the contact side and heterostructure side are presented. The atomic percentage of the element are given in the table next to the STEM images. The dash in the table means the element is not detected in the detection limit of the measurement apparatus. In Fig. F.4 and Fig. F.5 STEM images of two contacts are given. The EDX line scans are also given.

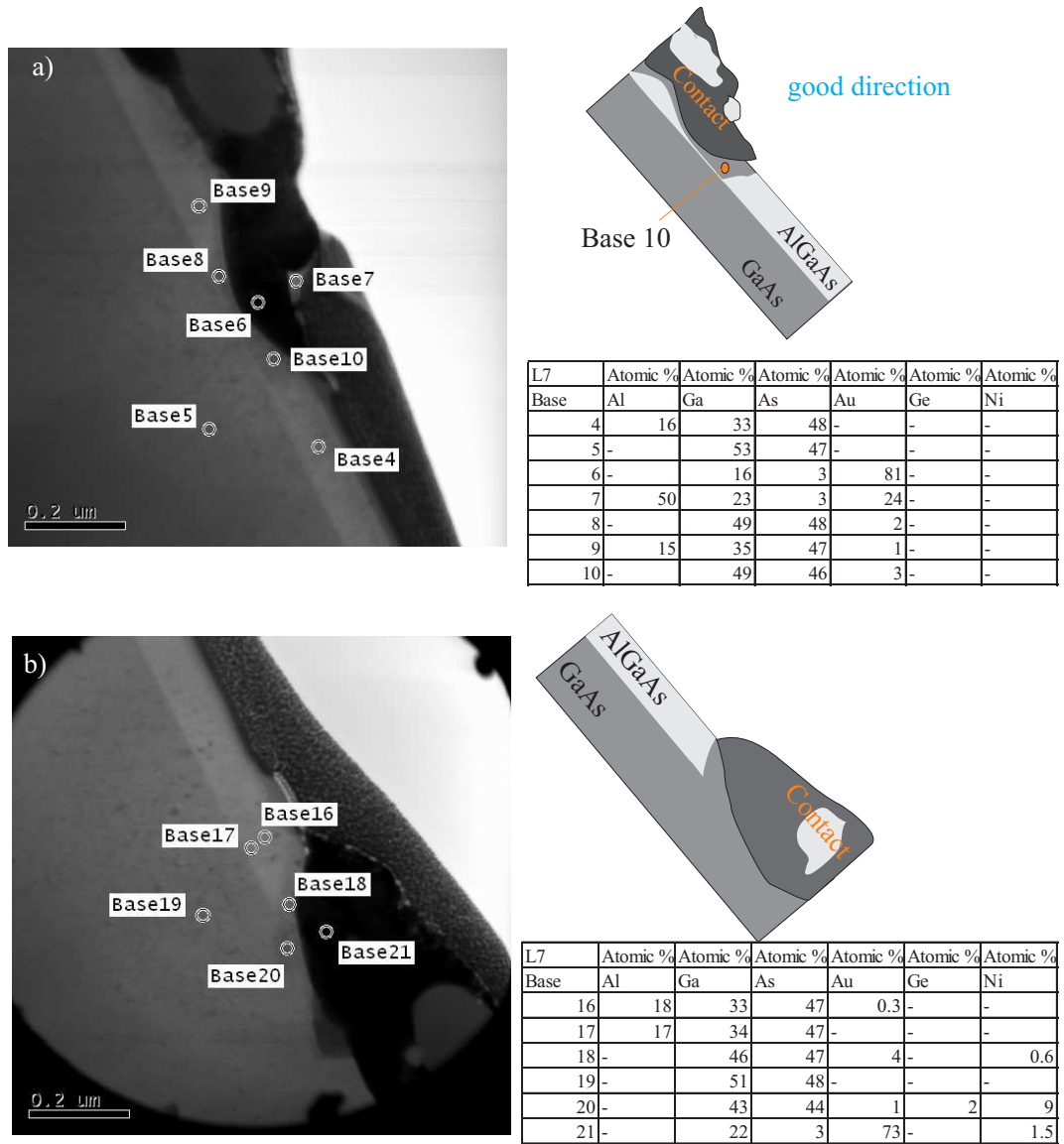


Figure F.1: (a) EDX point analyzes at different positions on a contact and heterostructure (in good contacting direction). The position of the points are indicated. (b) The similar analyzes for another contact.

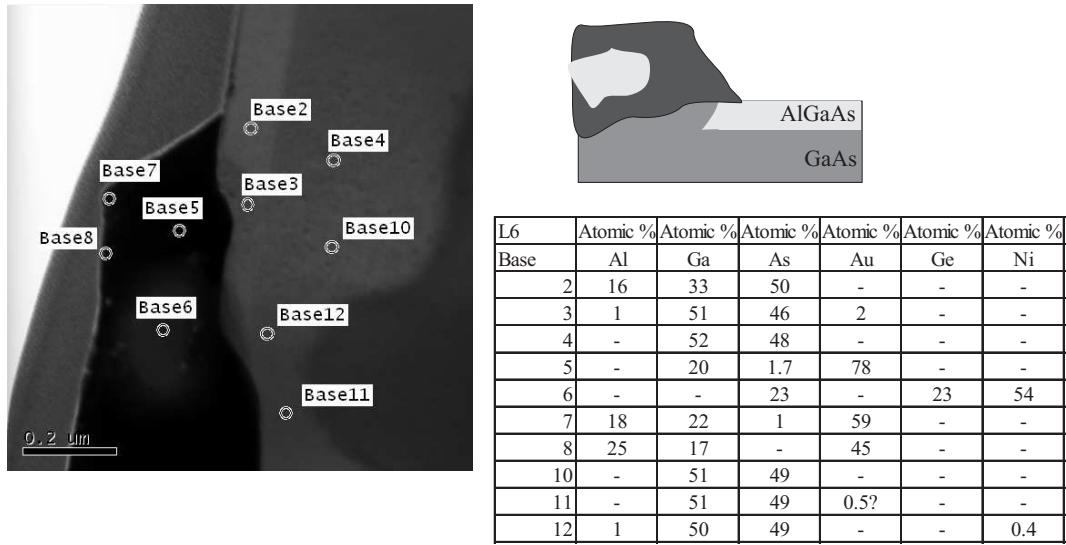


Figure F.2: (a) EDX point analyzes at different positions on a contact and heterostructure (in bad contacting direction). The position of the points are indicated. The metal grain at the interface is Au rich.

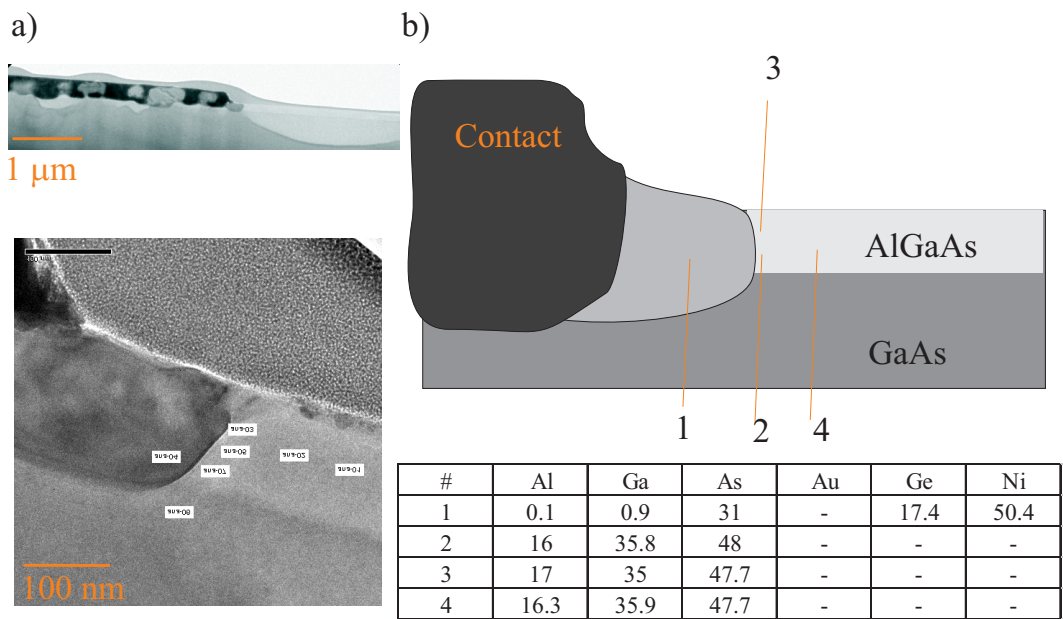


Figure F.3: (a) Low magnification and high magnification STEM images of a contact in good contacting direction. (b) The sketch of the contact is shown. Position of the EDX point analyzes are indicated. The metal grain at the interface is Ni rich.

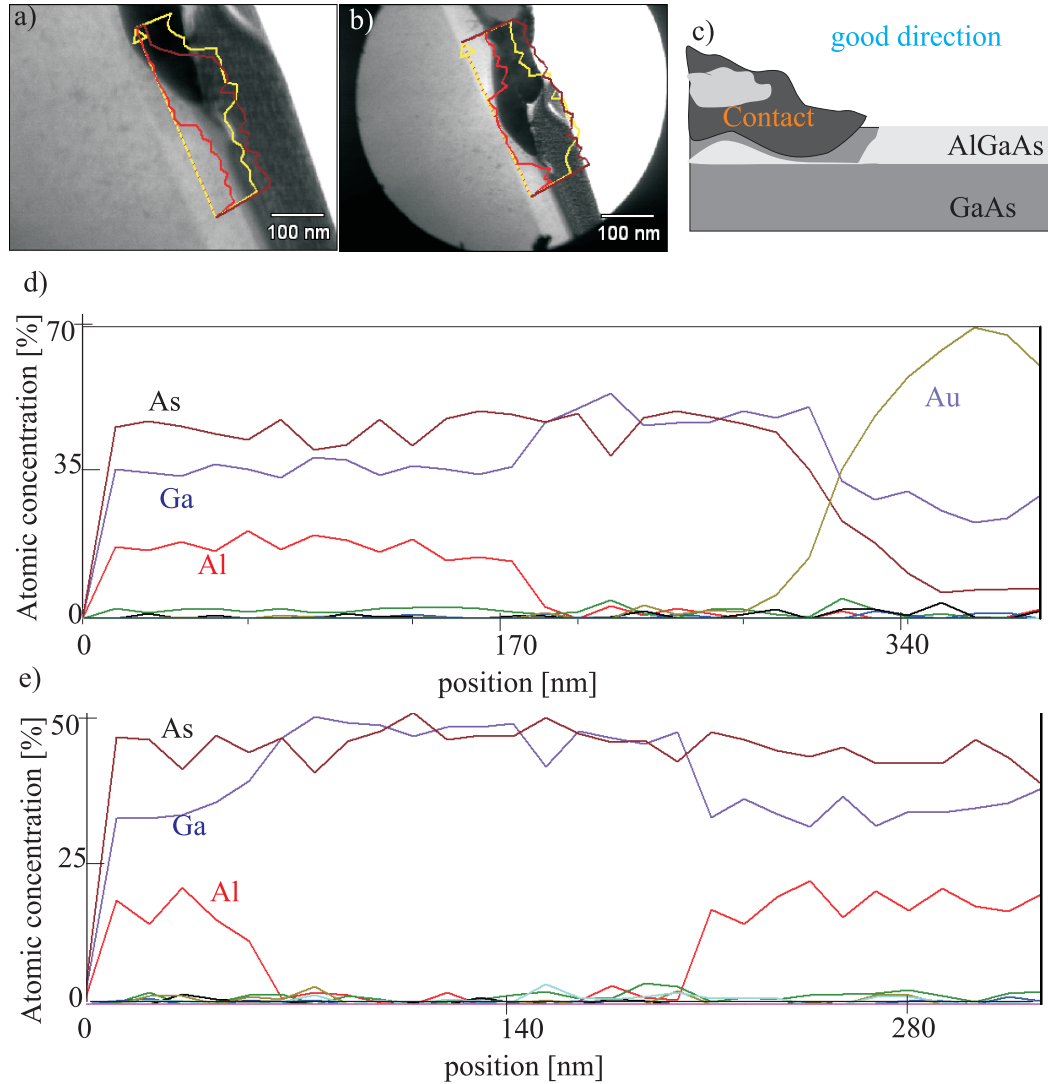


Figure F.4: STEM image of a contact in good contacting direction. The metal grain at the metal/ $\text{Al}_\delta\text{Ga}_{1-\delta}\text{As}$ interface is a Au rich grain. The position of the line scan is shown. (b) Another STEM image for the same contact. (c) The schematic of the contact. (STEM images are rotated) (c) EDX analysis along line shown in (a). The atomic percentage of Al, Ga, As, Ni, Ge and Au along the line is plotted versus position. (d) EDX analysis along the orange line shown in (b)

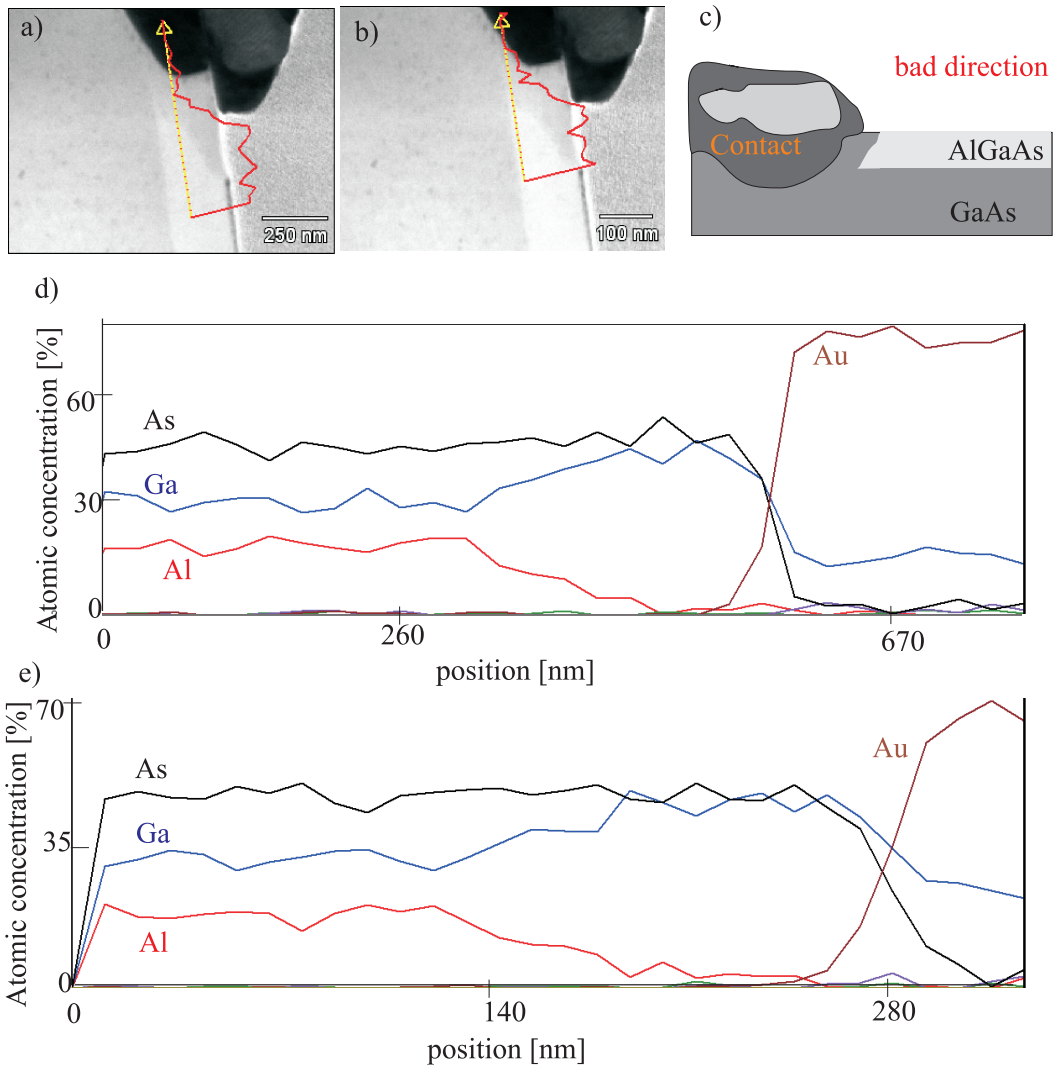


Figure F.5: (a) and (b) STEM images of a contact in bad contacting direction. The metal grain at the metal/ $\text{Al}_\delta\text{Ga}_{1-\delta}\text{As}$ interface is a Au rich grain. The position of the line scans is shown. (c) The schematic of the contact. (STEM images are rotated) (d) EDX analysis along line shown in (a). The atomic percentage of Al, Ga, As, Ni, Ge and Au along the line is plotted versus position. (e) EDX analysis along the orange line shown in (b)

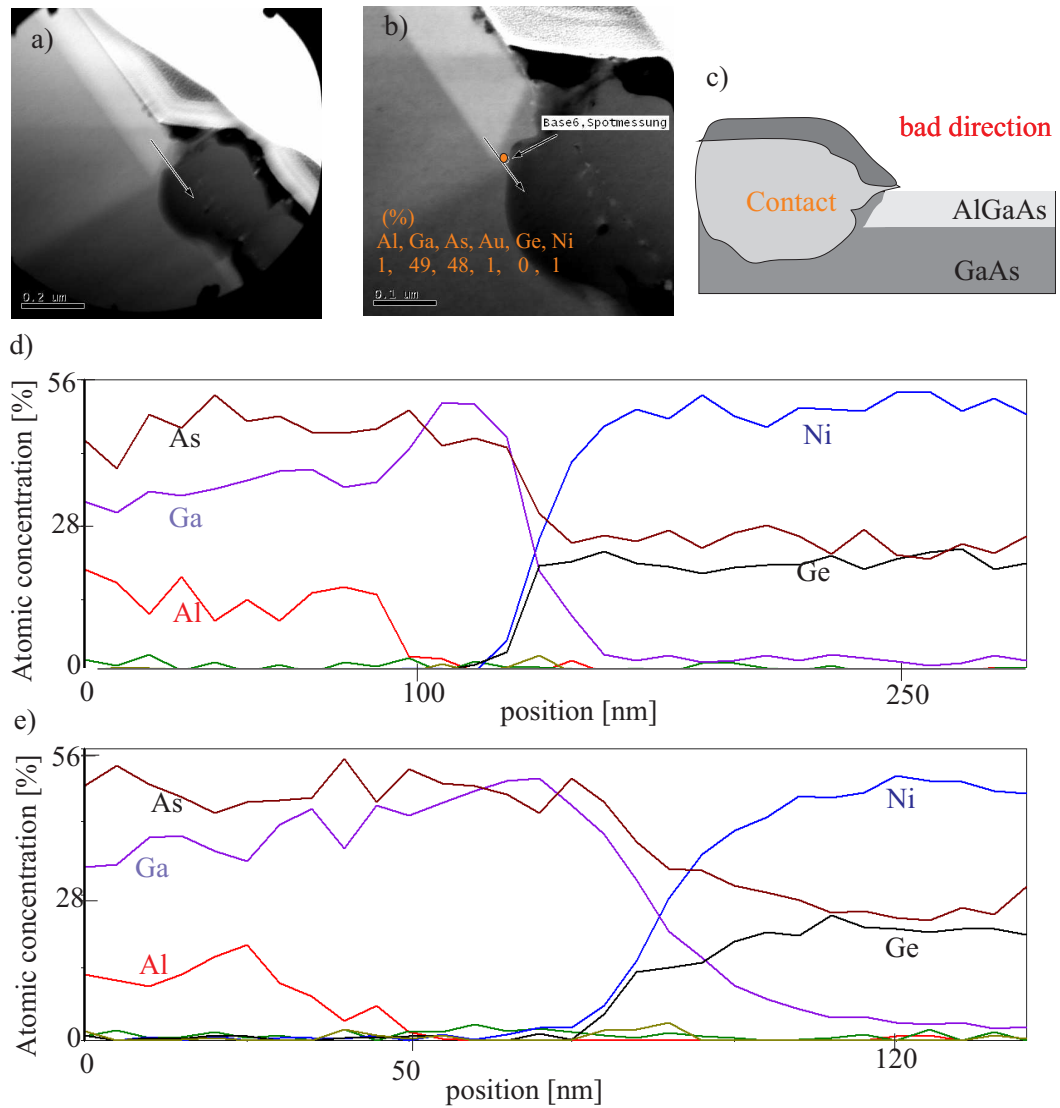


Figure F.6: (a) and (b) STEM images of a contact in bad contacting direction. The metal grain at the metal/ $\text{Al}_\delta\text{Ga}_{1-\delta}\text{As}$ interface is a NiGe rich grain. The position of the line scans is shown. (c) The schematic of the contact. (STEM images are rotated) (d) EDX analysis along line shown in (a). The atomic percentage of Al, Ga, As, Ni, Ge and Au along the line is plotted versus position. (e) EDX analysis along the line shown in (b). The atomic percentage of the elements at the position of the orange point in (b) is indicated (orange writing).

Appendix G

Clean room process for the ohmic contacts using EBL lithography

In this section the process for the preparation of the small ohmic contacts by EBL will be given. The contact recipe is the same as already described in Appendix A. Therefore, for the common processes we refer to the description in the Appendix A.

Defining ohmic contacts

1. Cleaning of the heterostructure as described in (1a) in Appendix A.
2. Spin-coating of the e-beam resist : Double layer resist is used
 - (a) First layer
 - Take sample out of propanol and put sample on the platter, dry with nitrogen
 - Put three drops of PMMA 200K 7% (E-Beam resist AR-P641.07 thinned to 7% solid contents using chlorobenzene as solvent)
 - Spin coat sample as follow
 - i. 5 seconds at 3000 rpm (put another drop of resist at this phase)
 - ii. 30 seconds at 8000 rpm
 - Clean the back side of the sample to remove resist; resist on the back side gives usually trouble (charging or tilting sample and resulting focus problems)
 - Bake at 160 °C for 1 h in an oven
 - (b) Second layer
 - Take sample out of oven and place on the platter

- Put three drops of PMMA 950K 1.5% (E-Beam resist AR-P671 thinned to 1.5% solid contents using chlorobenzene as solvent)
 - Spin coat sample as follow
 - i. 5 seconds at 3000 rpm (put another drop of resist at this phase)
 - ii. 30 seconds at 8000 rpm
 - Clean the back side of the sample to remove resist.
 - Bake at 160 °C for 1 h in an oven
- (c) Measure thickness by making a scratch at the one corner of the sample and measure by a profilometer. Total thickness should be around 400 nm

3. E-Beam exposure with e-Line system (Raith) with Software version 4.0

- (a) Sample is loaded into the system
- (b) EHT=10 kV; App=10 μm ; $I \approx 0.015 \text{ nA}$; $z=29 \text{ w} = 7.4$
- (c) Alignment: Use the corner of the sample; perform a n origin and angle correction for sample to chip(design) alignment(Adjust UVW window)
- (d) Focus and astigmatism correction : Make a rough focus and astigmatism correction using one of the corners; then expose a point somewhere in the resist in high magnification and use this point to make a good focus and astigmatism correction (you should be able to burn a circular point of 20 to 30 nm)
- (e) Set exposure parameters in the exposure window menu:
 - Area basic step size: 5 nm
 - Step size : 5 nm (or 10 nm)
 - Area dose: 120 $\mu\text{As}/\text{cm}^2$
 - Beam speed: 2 to 3 mm/s
 - Settling time: 5 ms
 - Flyback factor: 1
- (f) Write field alignment: burn a point; Set write field to 200 μm^2 ; Perform a manual mark scan process (start from large marks like 50 μm^2 then smaller like 5 μm^2 or 2 μm^2)
- (g) Drag and drop design chip into position list Align.pls from GDSII editor. Right click on the chip, from the Exposure properties window choose working areas to be exposed, choose layers to be exposed, get positions (U and V of the center of working area), check exposure parameters, current and write field area. Calculate time to see how long it takes (if

something is wrong you can see from the exposure times, very short or very long if you set wrong parameters)

(h) Start exposure (Scan)

4. Develop 160 sec:

Developer is isobutyl methyl ketone: propanol (1:3 volume ratio) (developing time= $[30 + 30 \cdot (d/100)]$ seconds; d is the thickness of the resist)

5. Evaporation of Au/Ge/Ni ohmic contacts:

Follow the steps in (3) in Appendix A.

6. Lift-off

(a) Put sample into remover (AR300-70 from Allresist GmbH) at 55 °C for 1.5 h

(b) Take out of remover and splash strongly with acetone (sample should not get dry)

(c) Put into acetone for 2 min

(d) Then take out of acetone and splash strongly with acetone

(e) Put into propanol

(f) Have a look under light microscope

(g) If lift-off did not work very well one can put sample into acetone again

7. Annealing:

Follow the steps in (5) in Appendix A.

Defining bond pads

8. Cleaning of the heterostructure as described in the (1a) in Appendix A.

9. Spin-coating of the e-beam resist :

(a) Take sample out of propanol and put sample on the platter, dry with nitrogen

(b) Put three drops of PMMA 950K 5% (E-Beam resist AR-P671 thinned to 5% solid contents using chlorobenzene as solvent)

(c) Spin coat sample as follow

i. 5 seconds at 3000 rpm (put another drop of resist at this phase)

ii. 30 seconds at 8000 rpm

- (d) Clean the back side of the sample to remove resist.
- (e) Bake at 160 °C for 1.5 h in an oven.
- (f) Measure thickness of the resist layer (should be about 400 nm).

10. E-Beam exposure

- (a) Sample is loaded into the system
- (b) Alignment: Use the corner of the sample perform an origin and angle correction for sample to chip (design) alignment (Adjust UVW window). Then use some marks which is exposed in the previous e-beam step to make a fine alignment; perform a origin and angle correction for sample to chip (design) alignment (Adjust UVW window)
- (c) Focus and astigmatism correction : Make a rough focus and astigmatism correction using one of the corner; then expose a point somewhere in the resist in high magnification and use this point to make a good focus and astigmatism correction
- (d) Set exposure parameters in the exposure window menu:
 - EHT=10 kV ; App=10 μm ; I \approx 0.015 nA ; z=29 w \approx 7.4
 - Area Basic step size : 5 nm
 - Step size : 10 nm
 - Area dose : 120 $\mu\text{As}/\text{cm}^2$
 - Beam speed : 2 to 3 mm/s
 - Settling time : 5 ms
 - Flyback factor : 1
- (e) Write field alignment: use manual and automatic mark scan procedure using marks defined in the ohmic contacts process
- (f) Drag and drop design chip into position list Align.pls from GDSII editor. Right click on the chip, from the Exposure properties window choose working areas to be exposed, choose layers to be exposed, get positions (U and V of the center of working area), check exposure parameters, current and write field area. Calculate time to see how long it takes (if something is wrong you can see from the exposure times, very short or very long if you set wrong parameters)
- (g) Start exposure (Scan)

11. Develop 160 sec

12. Evaporation of Cr/Au pads

(a) Cr 20 nm at a rate 1.5 Å/s

(b) Au 200 nm at a rate 3 Å/s

13. Lift-off as in (6)

Appendix H

Additional SEM images of small alloyed contacts

In this section the cross-sectional SEM images of alloyed contacts are shown. The wafer is #81628. These contacts are prepared by EBL lithography.

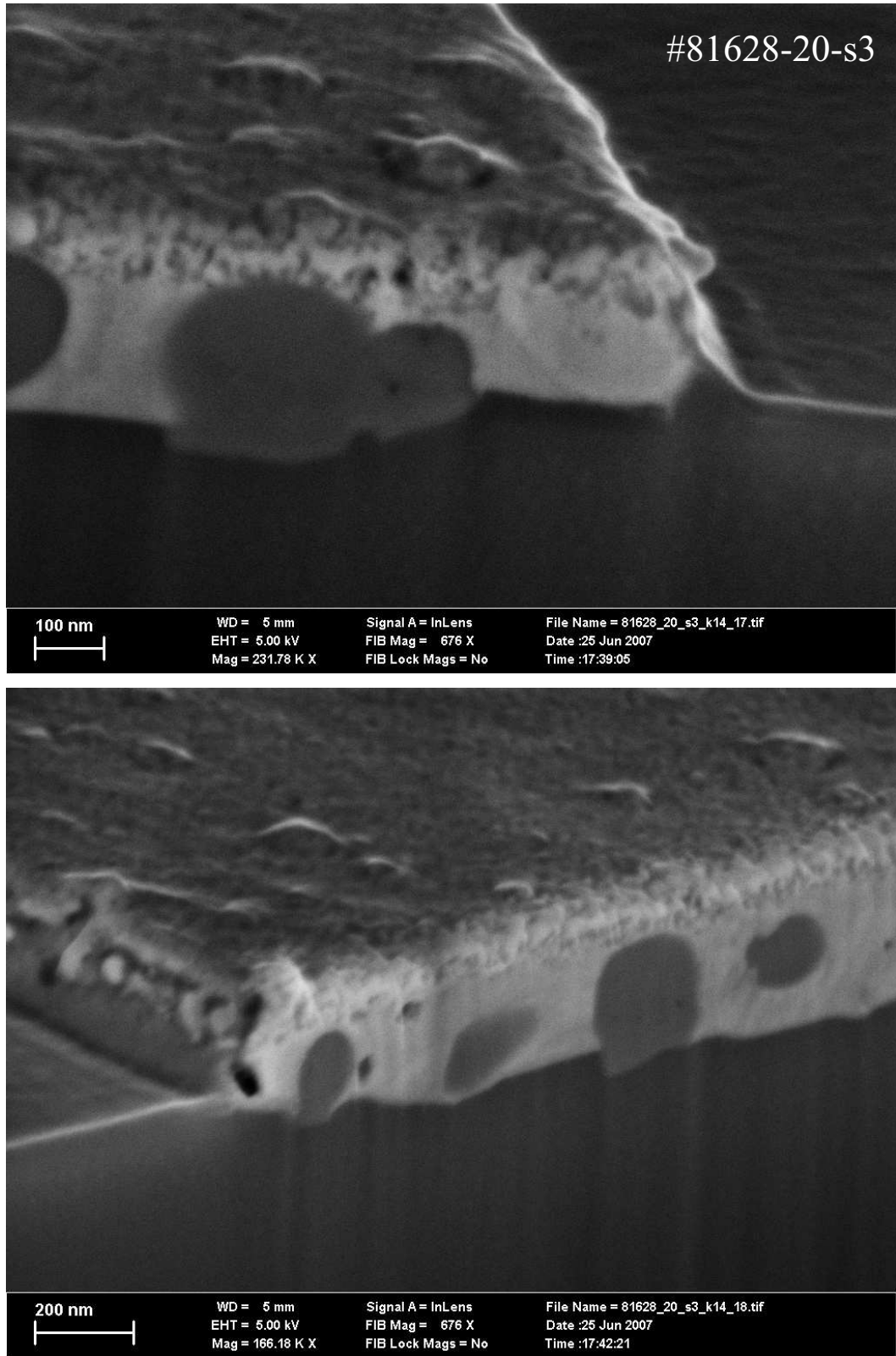


Figure H.1: Cross sectional SEM images of a circular alloyed contacts in different orientation. Wafer is #81628.

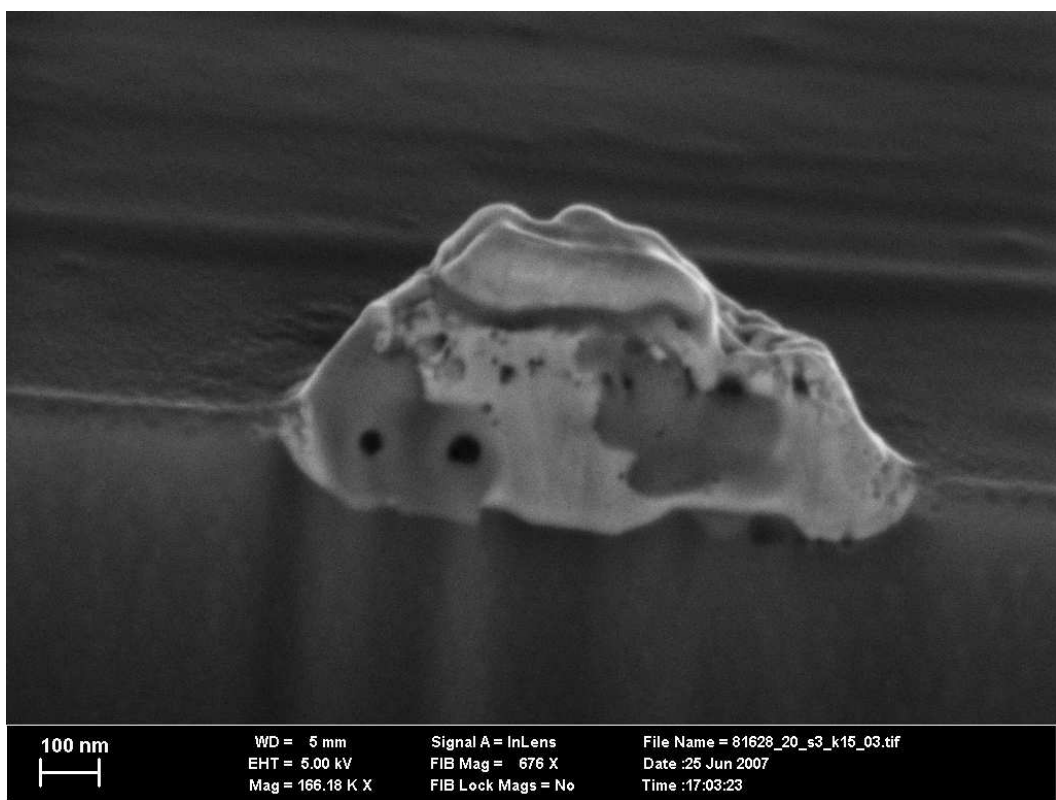
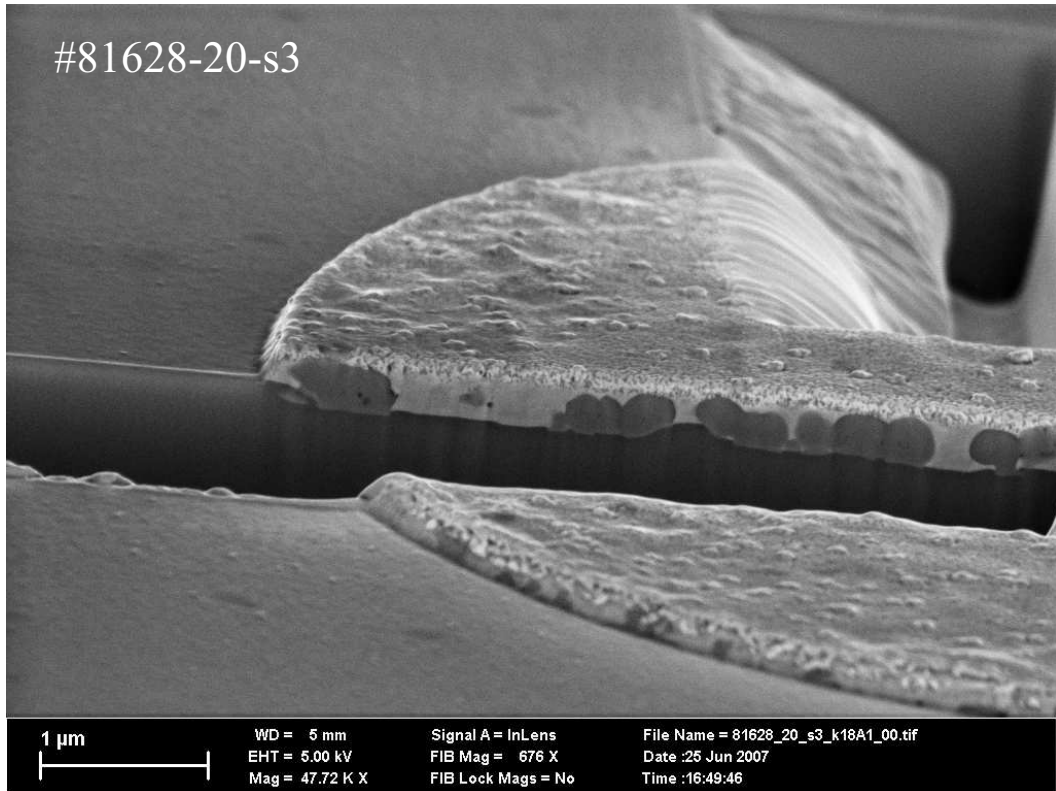


Figure H.2: Cross sectional SEM images of a circular alloyed contacts and a small contact. Wafer is #81628.

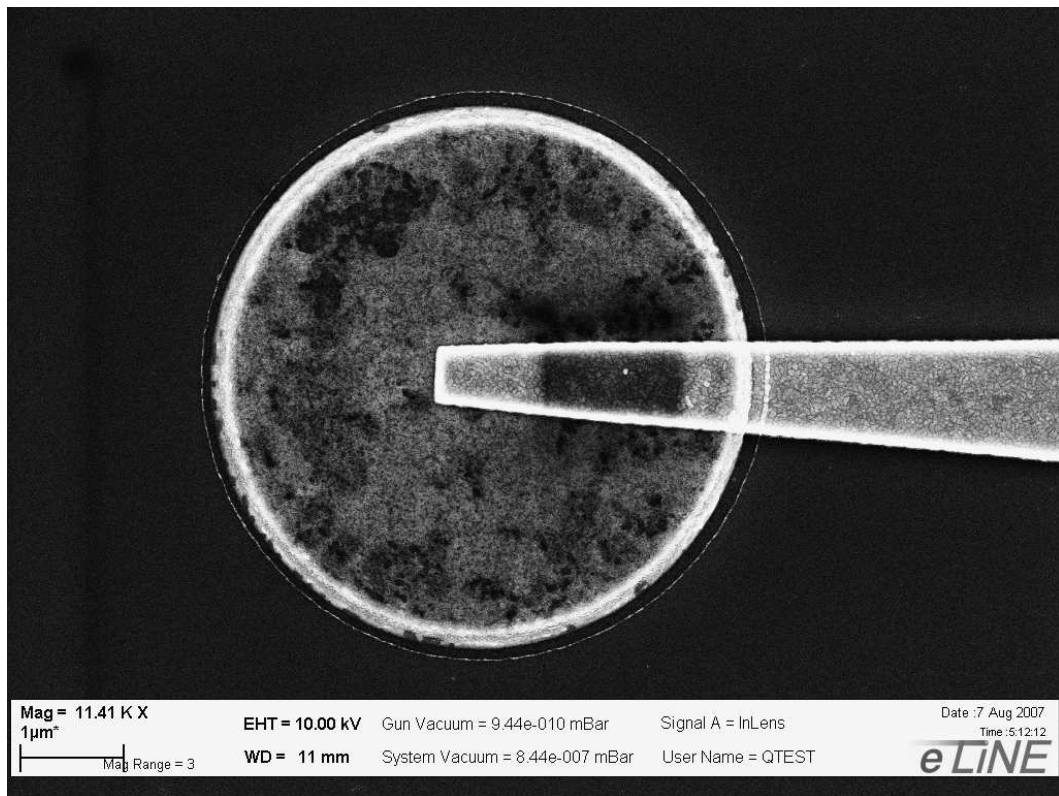


Figure H.3: A top view SEM image of a circular alloyed contact. The edge of the contact is very well defined. The circular ring like structure around the contact is due to etching during the cleaning process (Semico Clean 23 and HCl). Wafer is #81628.

Appendix I

Clean room process for the Corbino devices

In this section the clean room process for the preparation of the Corbino devices will be presented. The contact recipe is the same as already described in Appendix A. Therefore, for the common processes we refer to Appendix A is referred. EBL lithography for ohmic contacts has already been described in Appendix G. Therefore, we refer this section for the common process. Inner and outer ohmic contacts of Corbino are defined in separate steps. The reason is that when the outer contact is exposed, due to the proximity effect the inner part is already exposed quite a lot, i.e. for exposing the inner contact even a very small dose result in an overexposure of the whole area of the device. Therefore, we defined the ohmic contacts in two EBL steps. We have used a method that has been developed in Weizmann Institute of Science in Israel to make a suspended thin layer of metal-air bridges [76, 77]. The bridges and bond pads are exposed in the same EBL step. However, exposure parameters and write field size for the bridges and the bond pads are different. Parameters for bridges and bond pads are given separately.

Defining inner ohmic contacts

1. Cleaning of the heterostructure as described in (1a) in Appendix A.
2. Spin-coating of the e-beam resist for the inner contacts and marks: Double layer resist is used as described in (2) in Appendix G.
3. E-Beam exposure with e-Line system (Raith) with Software version 4.0 as described in (3) in Appendix G.
4. Develop as described in (4) in Appendix G.

5. Evaporation of Au/Ge/Ni for ohmic contacts:
Follow the steps in (3) in Appendix A.

6. Lift-off as described in (6) in Appendix G.

Defining outer ohmic contacts

7. Follow steps (1) to (6). For the alignment marks the marks which are defined with the inner contacts are used. We have used cross like marks with a width of 200 nm and length of 5 μm . For a good alignment first a manual mark scan should be performed. Then automatic mark scan should be performed. It is useful to perform auto mark scan two times for a good alignment.

8. Lift-off as described in (6) in Appendix G.

9. Annealing: Follow the steps in (5) in Appendix A.

Bridges and bond pads

10. Three layer resist is processed as follows:

(a) Spin PMMA 950K A5 for 60 s at 7000 min^{-1}

(b) Bake in an oven for 60 min at 180°C

(c) Spin MMA(17.5%) - MAA EL9 for 60 s at 4000 min^{-1}

(d) Bake in an oven for 60 min at 180°C

(e) Spin PMMA 200K A3 for 60 s at 4000 min^{-1}

(f) Bake in an oven for 60 min at 180°C

(g) The thickness of the first layer is about 280 nm. Total thickness is about 700 nm.

(h) After each spin step clean the back side of the sample. Resist on the back side on the sample causes some difficulties during the EBL exposure (charging or tilting sample and resulting focus problems).

11. E-Beam exposure

(a) Sample is loaded into the system

(b) Alignment: Use the corner of the sample perform an origin and angle correction for sample to chip (design) alignment (Adjust UVW window). Then use some marks which is exposed in the previous e-beam step to make a fine alignment; perform a origin and angle correction for sample to chip (design) alignment (Adjust UVW window)

(c) Focus and astigmatism correction : Make a rough focus and astigmatism correction using one of the corner; then expose a point somewhere in the resist in high magnification and use this point to make a good focus and astigmatism correction. Exposure of the bridges and bonds are done with different parameters. Follow the description given in 7 for the mark scan and alignment

(d) Parameters for exposure of the bridge and foots:

- Write field size: 100 μm
- EHT=30 kV ; App=10 μm ; $I\approx 0.025$ nA
- Area Basic step size : 5 nm
- Step size : 5 nm
- Area dose : 200 $\mu\text{As}/\text{cm}^2$ (Dose factor is 1 for the inner foot of the bridge (orange area in Fig. I.1) and is 0.45 for the bridge (green area in Fig. I.1)
- Beam speed : 2 to 3 mm/s
- Settling time : 5 ms
- Flyback factor : 1

(e) Parameters for exposure of the bond pads (blue regions in Fig. I.1):

- Write field size: 1000 μm
- EHT=30 kV ; App=120 μm ; $I\approx 6.9$ nA
- Area Basic step size : 20 nm
- Step size : 200 nm
- Area dose : 200 $\mu\text{As}/\text{cm}^2$.
- Beam speed : 17 mm/s
- Settling time : 5 ms
- Flyback factor : 1

12. Develop 240 sec

13. Evaporation of Cr/Au pads

- (a) Cr 25 nm at a rate 1.5 $\text{\AA}/\text{s}$
- (b) Au 300 nm at a rate 3 $\text{\AA}/\text{s}$

14. Lift-off as described in (6) in Appendix G.

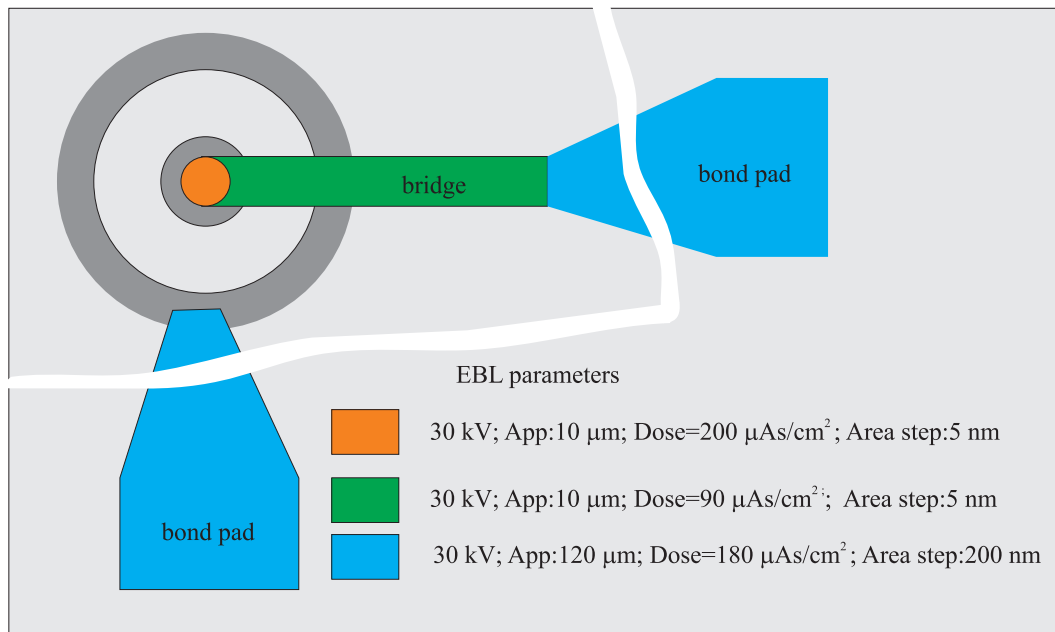


Figure I.1: (a) The schematic representation of Corbino device. Gray regions are alloyed Au/Ge/Ni contacts. The EBL exposure parameters for the bridge and bond pads are given. Acceleration voltage is 30 kV. 10 μm of aperture and 100 μm write field are used for the bridges. For the bond pads 120 μm of aperture and 1000 μm write field are used. The width of the bridge is about 200 nm. The length up to 3 μm was successful defined

Appendix J

Additional transport data for zero bias anomaly

In this section we present the supportive data for the Chapter 6. The figures are cited in the chapter were they are needed.

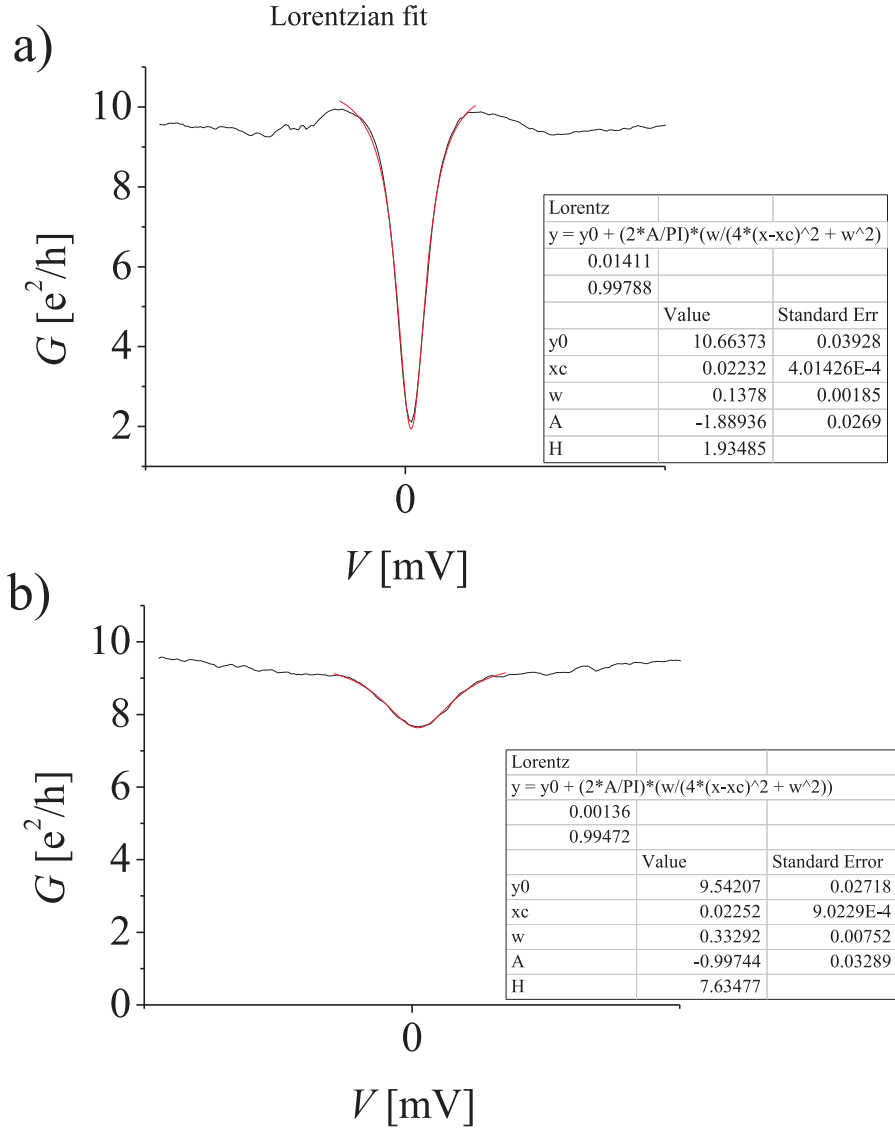


Figure J.1: The Lorentzian fit to zero bias dip measured on s#3. (a) For T=50 mK. (b) For T=480 mK

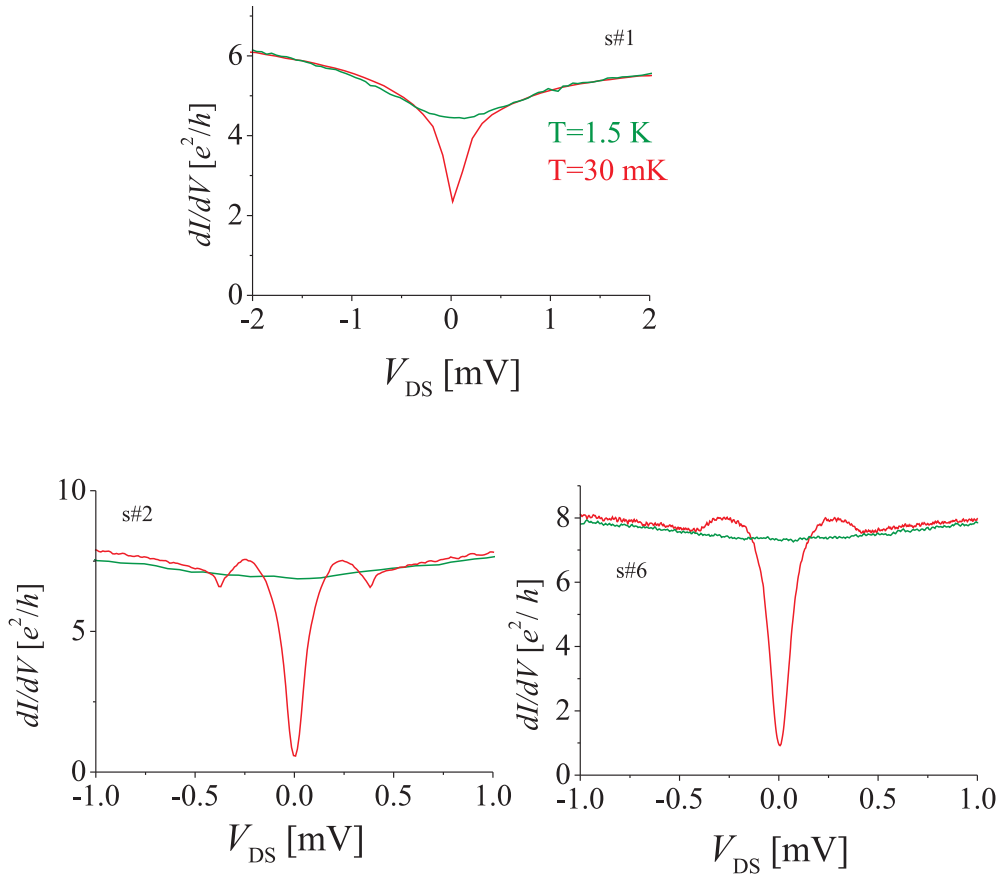


Figure J.2: The measured differential conductance at $B = 0$ T (blue) and at $B = 12$ mT (red).

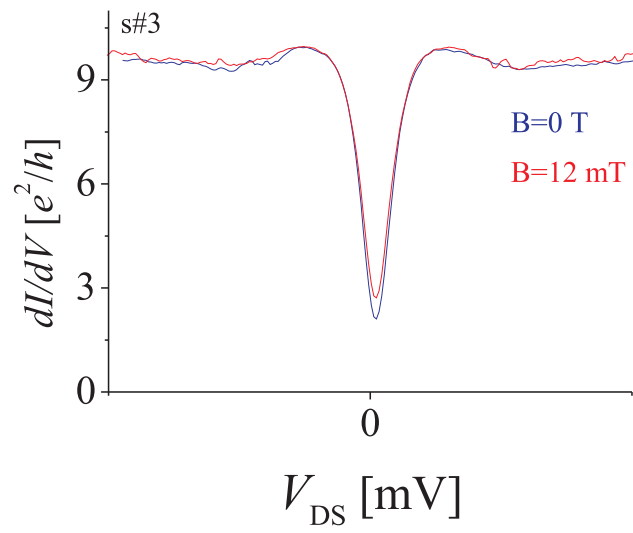


Figure J.3: The differential conductance versus bias voltage taken at $B = 0$ T and $B = 12$ mT.

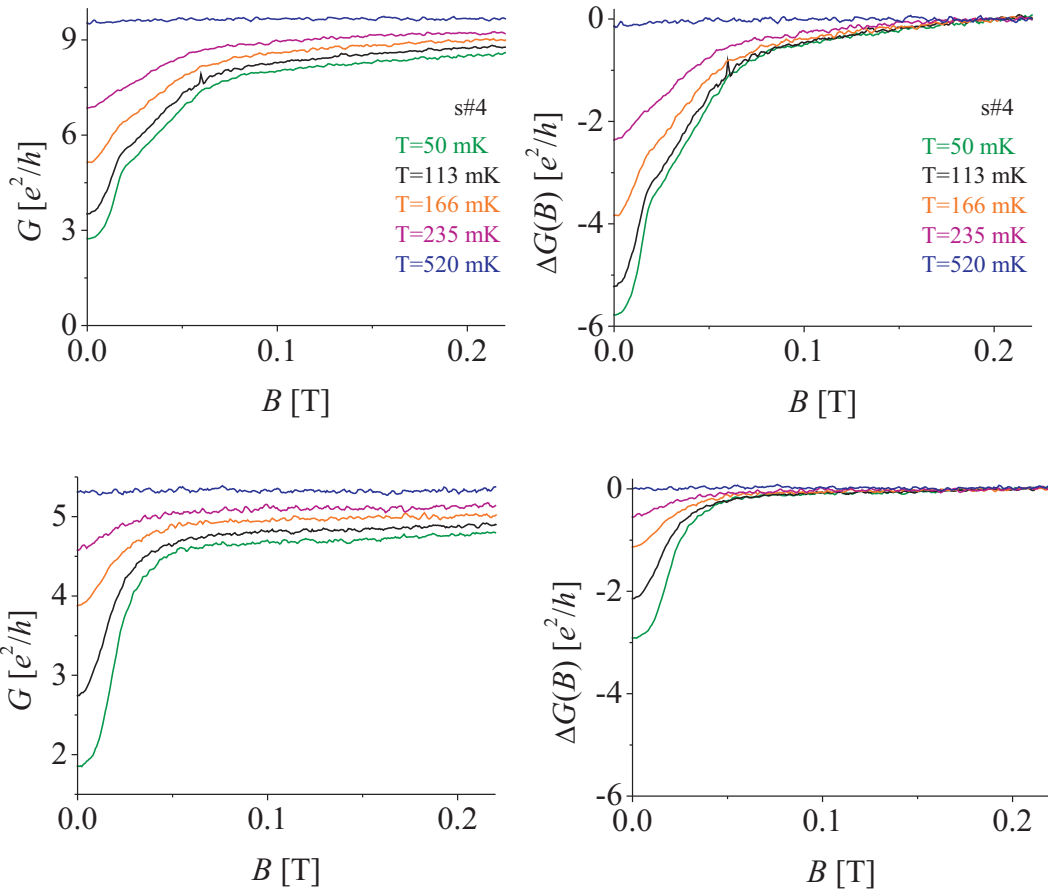


Figure J.4: Temperature dependence of the magneto conductance dip for Corbino devices s#4 and s#5

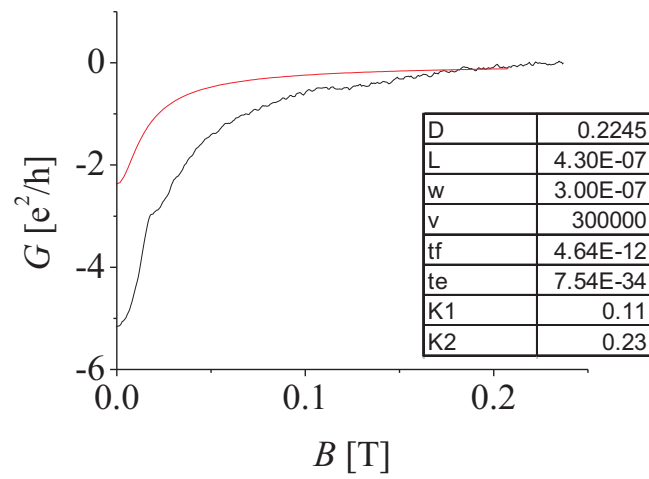


Figure J.5: Fit of relation (6.4) and (6.5) to data of s#3 for diffuse boundary scattering.

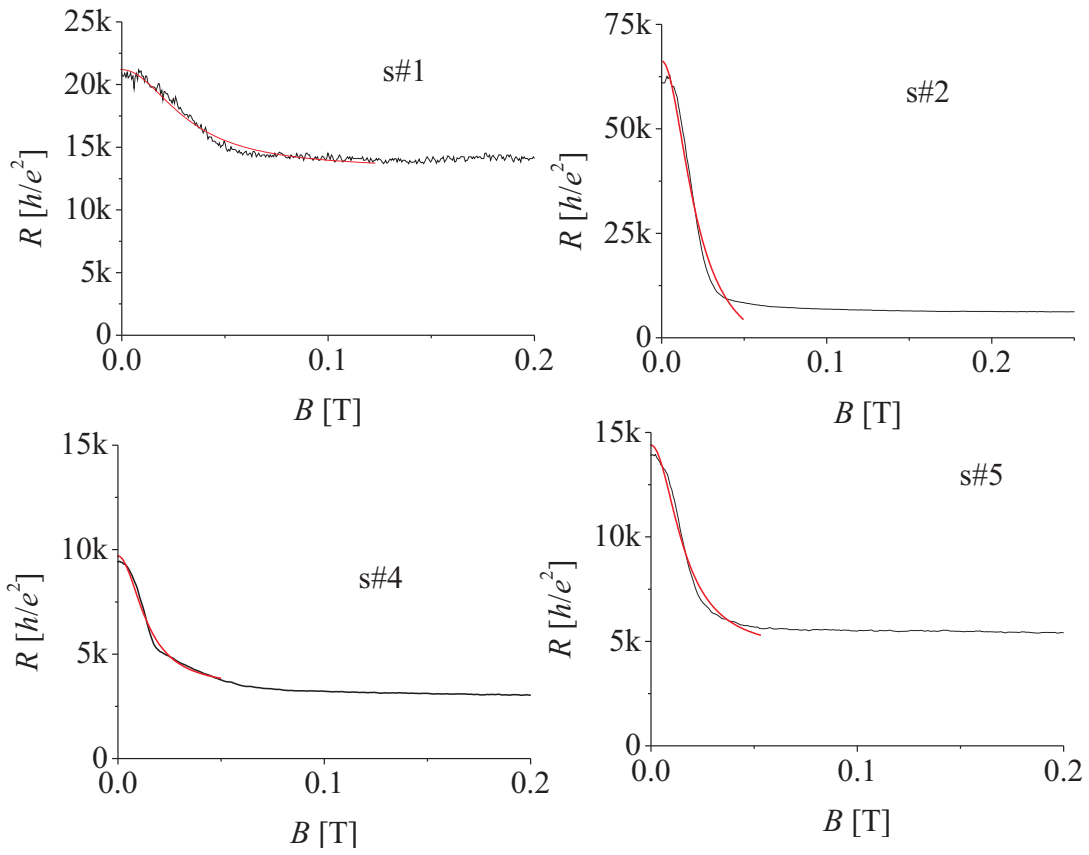


Figure J.6: Best fit of (6.6) to data for Corbino devices. The extracted parameters from the fits are presented in Table 6.4.

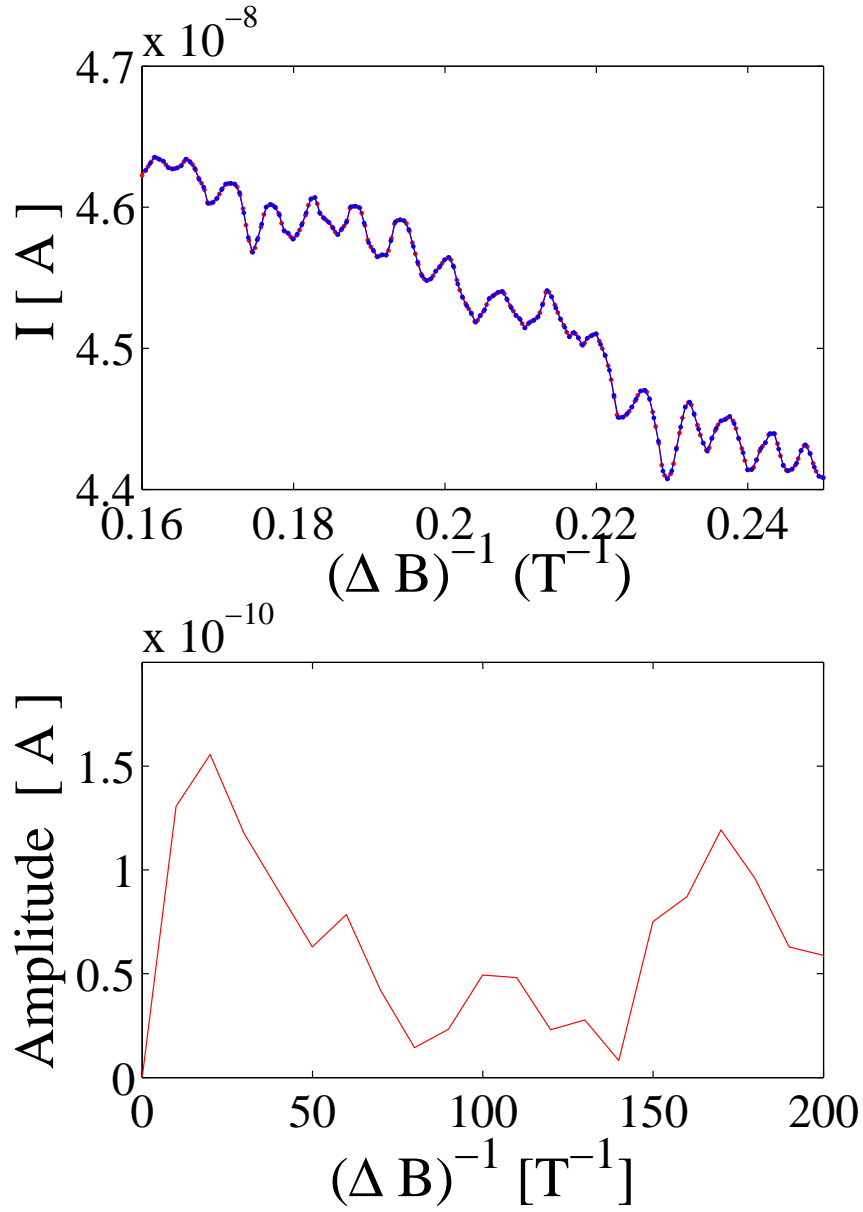


Figure J.7: FFT results on the data measured on Corbino device s#6. The peaks correspond to period of 6 mT and 50 mT. The data is taken for the $V_{DS} = 0.2$ mV.

Appendix K

Additional transport data of submicron Corbino devices under high magnetic field

In this section additional transport data supporting the experiments presented in Chapter 7 are presented.

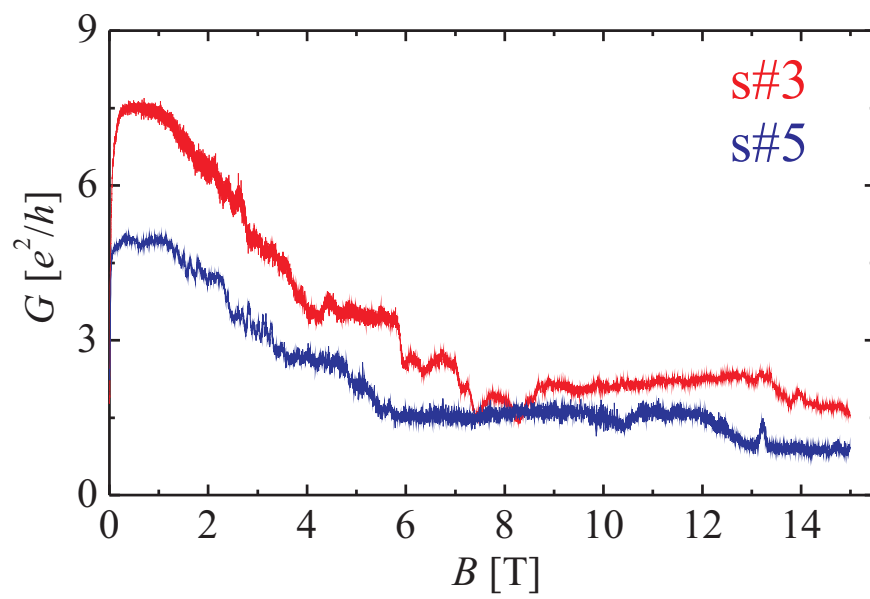


Figure K.1: Magneto-conductance measured on Corbino devices s#3 and s#5.

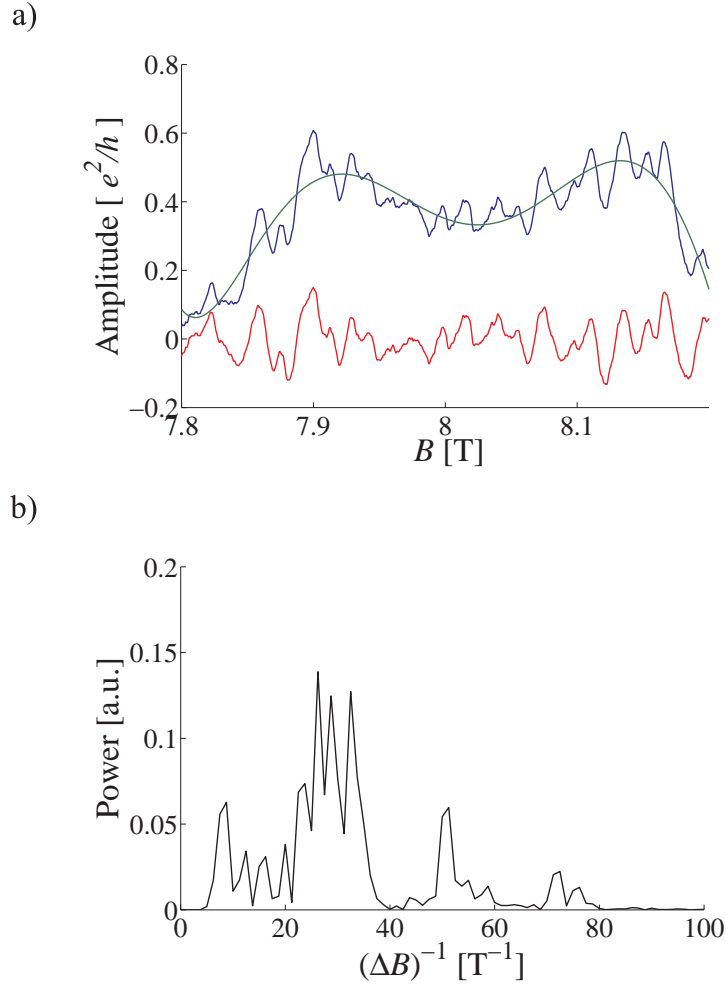


Figure K.2: (a) Magnetic field periodic conductance oscillations measured on Corbino device s#1. The blue line is the measured data. The green line is the polynomial best fit to data to get rid of the smooth back ground. The red curve shows the data after subtracting the smooth background. (b) FFT of red curve in (a).

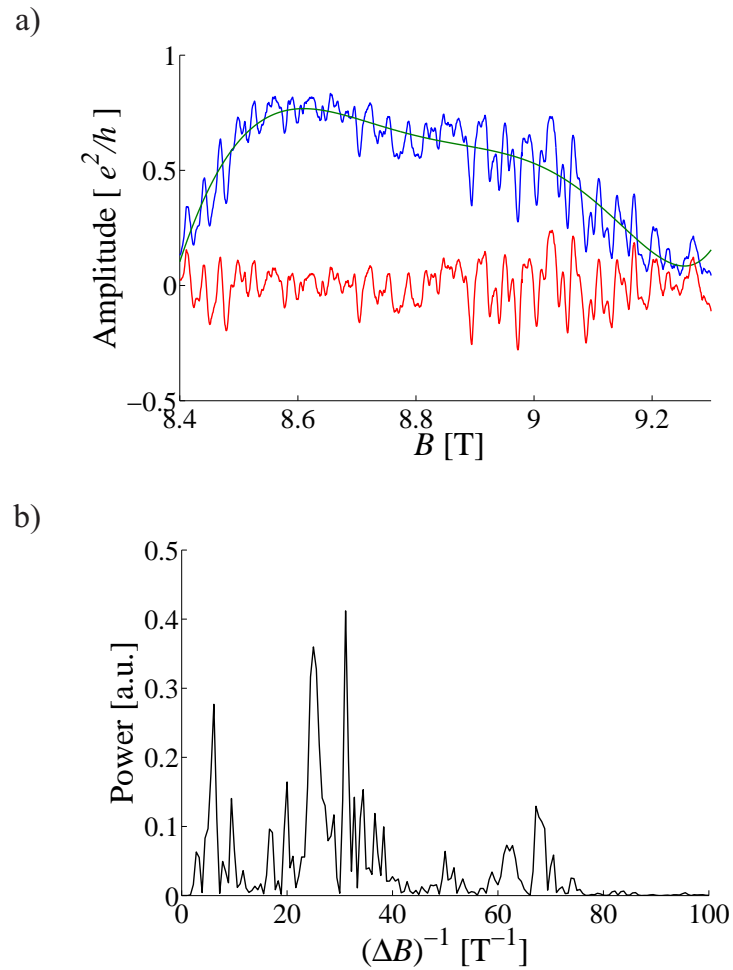


Figure K.3: (a) Magnetic field periodic conductance oscillations measured on Corbino device s#1. The blue line is the measured data. The green line is the polynomial best fit to data to get rid of the smooth back ground. The red curve shows the data after subtracting the smooth background. (b) FFT of red curve in (a).

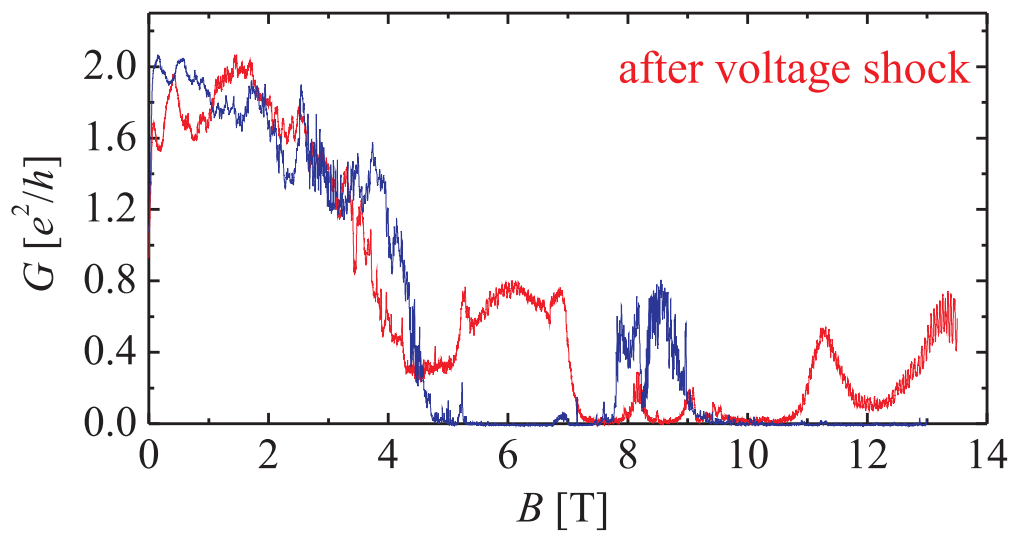


Figure K.4: Magneto-Conductance of Corbino device s#1 before and after voltage shock. The device had a voltage shock accidentally.

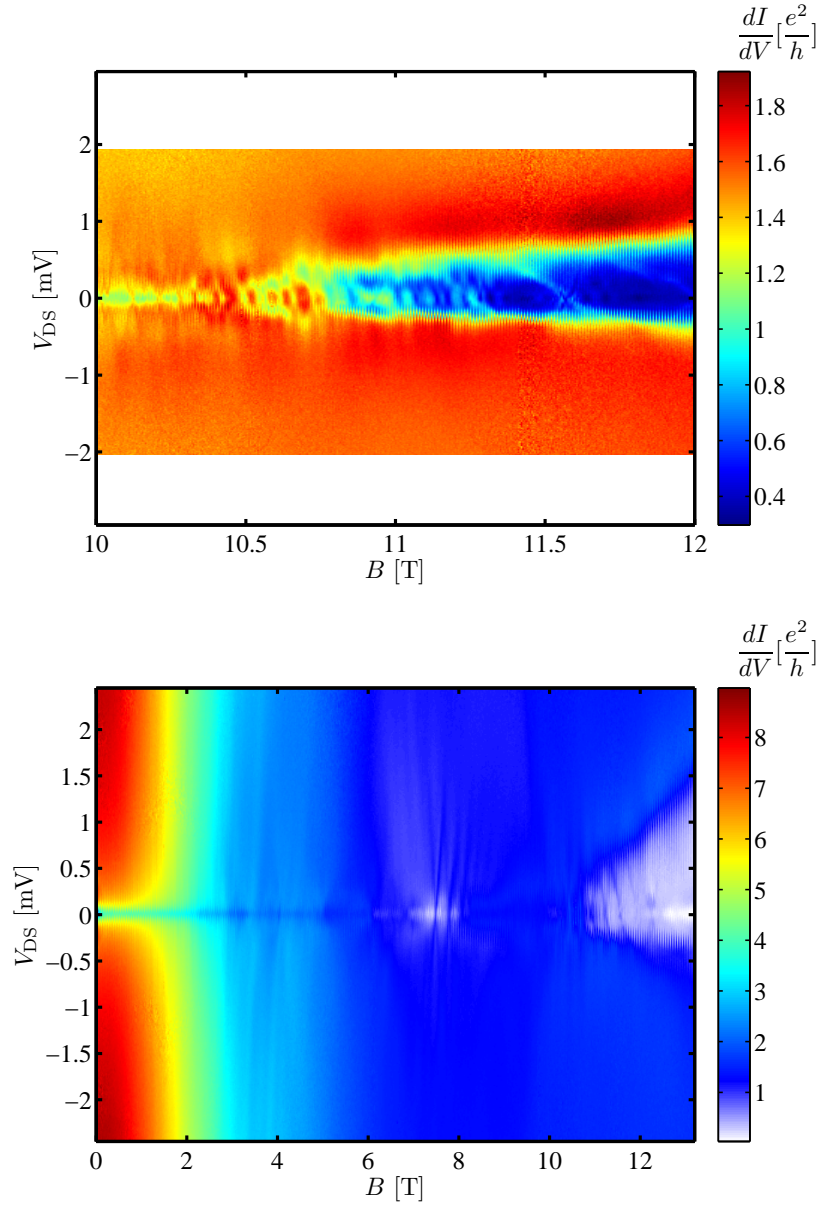


Figure K.5: (a) Differential conductance versus bias voltage and magnetic field for $s\#2$ measured around the peaks on $\nu = 1$ plateau. (b) Differential conductance versus bias voltage and magnetic field for $s\#2$ measured for the wider range of magnetic field.

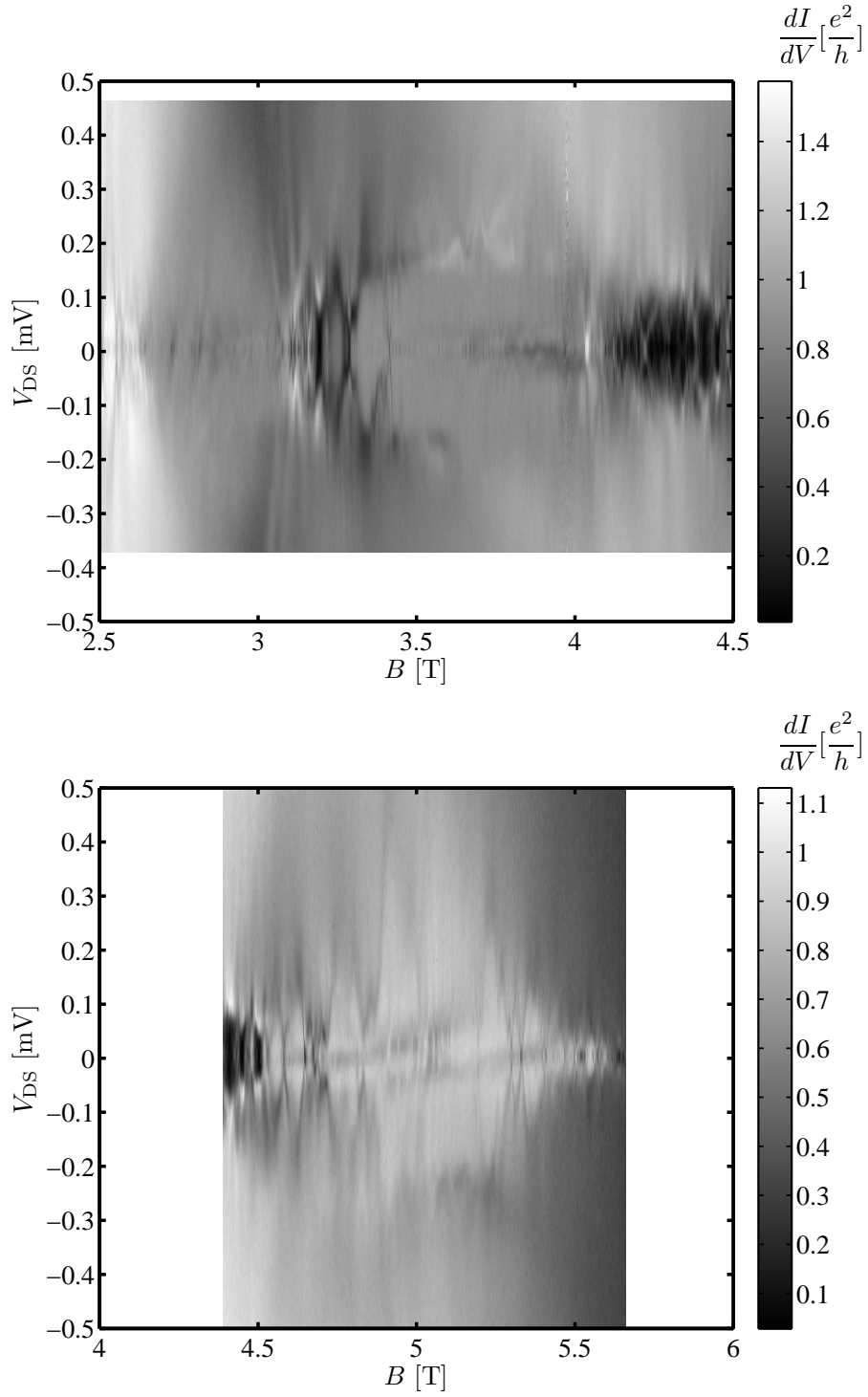


Figure K.6: Differential conductance versus bias voltage and magnetic field for s#6 measured around the peaks on $\nu = 4$ plateau (upper one) and $\nu = 5$ plateau (lower one).

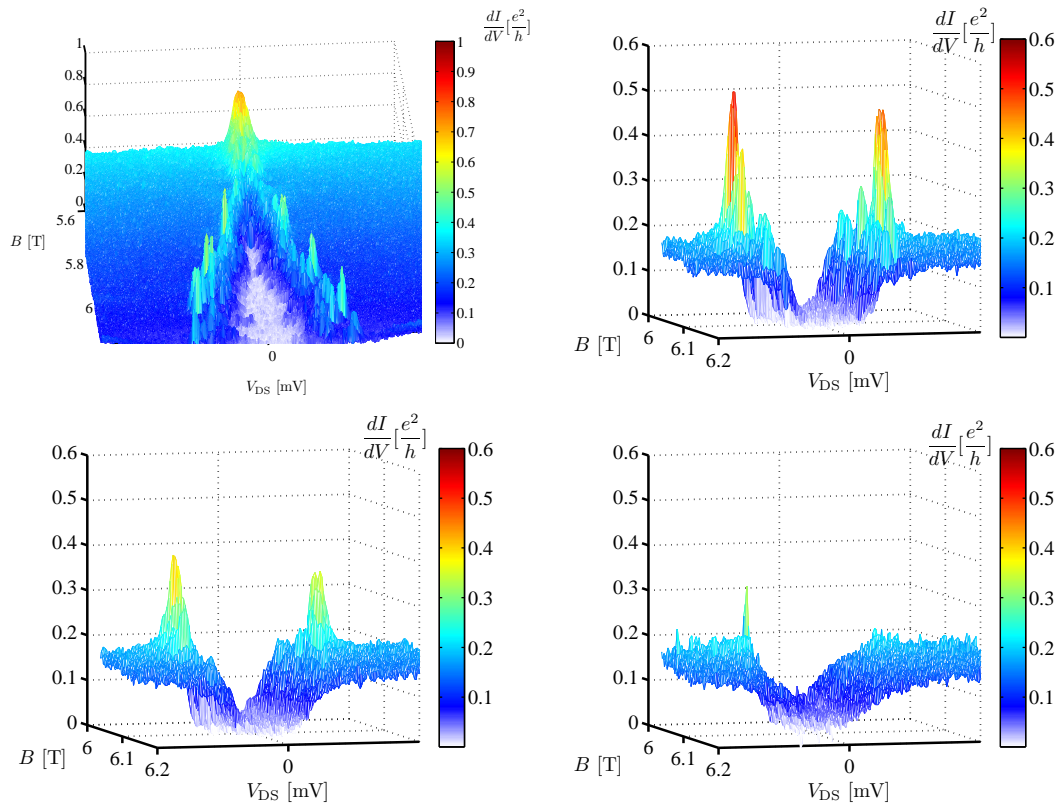


Figure K.7: (a) Differential conductance versus bias voltage measured as a function of magnetic field in s#6 shown in a mesh plot. (b), (c), and (d) temperature dependence of the peaks. (b) $T=30$ mK. (c) $T=90$ mK. (d) $T=160$ mK.

Bibliography

- [1] K. v. Klitzing, G. Dorda, and M. Pepper. New method for high-accuracy determination of the fine-structure constant based on quantized Hall resistance. *Phys. Rev. Lett.*, 45(6):494–497, Aug 1980.
- [2] R. Dingle, H. L. Störmer, A. C. Gossard, and W. Wiegmann. Electron mobilities in modulation-doped semiconductor heterojunction super-lattices. *Appl. Phys. Lett.*, 33(7):665–667, 1978.
- [3] Frank Stern and Sankar Das Sarma. Electron energy levels in GaAs – Ga_{1-x}Al_xAs heterojunctions. *Phys. Rev. B*, 30(2):840–848, Jul 1984.
- [4] Neil W. Ashcroft and N. David Mermin. *Solid State Physics*. Holt-Saunders International Editions, 1976.
- [5] B. I. Halperin. Theory of quantized Hall conductance. *Helvetica Physica Acta*, 56(4):75–102, 1983.
- [6] Klaus von Klitzing. The quantized Hall effect. *Rev. Mod. Phys.*, 58(3):519–531, Jul 1986.
- [7] B. Jeckelmann and B. Jeanneret. The quantum Hall effect and its application in metrology. *Recent Advances In Metrology And Fundamental Constants*, 146:263–290, 2001.
- [8] R. B. Laughlin. Quantized Hall conductivity in two dimensions. *Phys. Rev. B*, 23(10):5632–5633, May 1981.
- [9] R. E. Prange. Quantized Hall resistance and the measurement of the fine-structure constant. *Phys. Rev. B*, 23(9):4802–4805, May 1981.
- [10] M. Büttiker. Absence of backscattering in the quantum Hall effect in multi-probe conductors. *Phys. Rev. B*, 38(14):9375–9389, Nov 1988.
- [11] D. B. Chklovskii, B. I. Shklovskii, and L. I. Glazman. Electrostatics of edge channels. *Phys. Rev. B*, 46(7):4026–4034, Aug 1992.

- [12] Kaan Güven and Rolf R. Gerhardtts. Self-consistent local equilibrium model for density profile and distribution of dissipative currents in a Hall bar under strong magnetic fields. *Phys. Rev. B*, 67(11):115327, Mar 2003.
- [13] J. Weis. Hall potential profiles in quantum Hall samples measured by a low-temperature scanning force microscope. *Int. J. Mod. Phys. B*, 21:1297–1306, 2007.
- [14] B. I. Halperin. Quantized Hall conductance, current-carrying edge states, and the existence of extended states in a two-dimensional disordered potential. *Phys. Rev. B*, 25(4):2185–2190, Feb 1982.
- [15] R. Landauer. Spatial variation of currents and fields due to localized scatterers in metallic conduction. *IBM Journal of Research and Development*, 1(3):223–231, 1957.
- [16] R. Haug. Edge-state transport and its experimental consequences in high magnetic-fields. *Semiconductor Science and Technology*, 8(2):131–153, 1993.
- [17] C. W. J. Beenakker. Edge channels for the fractional quantum Hall effect. *Phys. Rev. Lett.*, 64(2):216–219, Jan 1990.
- [18] A. Chang. A unified transport-theory for the integral and fractional quantum Hall-effects - phase boundaries, edge currents, and transmission reflection probabilities. *Solid State Communications*, 74(9):871–876, 1990.
- [19] Karlheinz Lier and Rolf R. Gerhardtts. Self-consistent calculations of edge channels in laterally confined two-dimensional electron systems. *Phys. Rev. B*, 50(11):7757–7767, Sep 1994.
- [20] J. H. Oh and Rolf R. Gerhardtts. Self-consistent Thomas-Fermi calculation of potential and current distributions in a two-dimensional Hall bar geometry. *Phys. Rev. B*, 56(20):13519–13528, Nov 1997.
- [21] Afif Siddiki and Rolf R. Gerhardtts. Incompressible strips in dissipative Hall bars as origin of quantized Hall plateaus. *Phys. Rev. B*, 70(19):195335, Nov 2004.
- [22] J. Weis. Single-electron transistor probes two-dimensional electron system in high magnetic fields. *Physica. E, Low-dimensional systems and nanostructures*, 3(1-3):23–29, 1998.
- [23] S. W. Hwang, D. C. Tsui, and M. Shayegan. Experimental evidence for finite-width edge channels in integer and fractional quantum Hall effects. *Phys. Rev. B*, 48(11):8161–8165, Sep 1993.

-
- [24] N. B. Zhitenev, R. J. Haug, K. v. Klitzing, and K. Eberl. Time-resolved measurements of transport in edge channels. *Phys. Rev. Lett.*, 71(14):2292–2295, Oct 1993.
- [25] Y. Y. Wei, J. Weis, K. v. Klitzing, and K. Eberl. Edge strips in the quantum Hall regime imaged by a single-electron transistor. *Phys. Rev. Lett.*, 81(8):1674–1677, Aug 1998.
- [26] A. Yacoby, H. F. Hess, T. A. Fulton, L. N. Pfeiffer, and K. W. West. Electrical imaging of the quantum Hall state. *Solid State Communications*, 111(1):1–13, 1999.
- [27] E. Ahlswede. Potential-und stromverteilung beim Quanten-Hall-Effekt bestimmt mittels Rasterkraftmikroskopie. *Promotionarbeit, Max-Planck-Institut für Festkörperforschung, Universität Stuttgart*, 2002.
- [28] E. Ahlswede, P. Weitz, J. Weis, K. von Klitzing, and K. Eberl. Hall potential profiles in the quantum Hall regime measured by a scanning force microscope. *Physica. B, Condensed matter*, 298(1-4):562–566, 2001.
- [29] F. Dahlem. Adiabatic transport in the quantum Hall regime: Comparison between transport and scanning force microscopy investigations. *Promotionarbeit, Max-Planck-Institut für Festkörperforschung, Universität Stuttgart*, 2002.
- [30] Eric D. Marshall and Masanori Murakami. Ohmic contacts to GaAs and other III – V compounds: Correlation of microstructure with electrical properties. In L.J. Brillson, editor, *Contacts to Semiconductors: Fundamentals and Technology*. Noyes, 1993.
- [31] O. Göktas, J. Weber, J. Weis, and K. von Klitzing. Alloyed ohmic contacts to two-dimensional electron system in GaAs/Al_δGa_{1-δ}As heterostructures down to submicron length scale. *Physica E*, 40(5):1579–1581, 2008.
- [32] Ahlswede E., Weis J., von Klitzing K., and Eberl K. Hall potential distribution in the quantum Hall regime in the vicinity of a potential probe contact. *Physica E*, 12(1-4):165–168, 2002.
- [33] Klaus von Klitzing, Rolf Gerhardtts, and Jürgen Weis. 25 Jahre Quanten-Hall-Effekt. *Physik Journal 4 (2005) Nr. 6*, 4(6):37–44, 2005.
- [34] R. Knott, W. Dietsche, K. v. Klitzing, K. Eberl, and K. Ploog. Imaging of the dissipation in quantum-Hall-effect experiments. *Zeitschrift für Physik B*, 82(3):351–354, 1991.

- [35] R. Knott, W. Dietsche, K. v. Klitzing, K. Eberl, and K. Ploog. Electrooptic imaging of potential distributions in the quantum Hall regime. *Semiconductor Science and Technology*, 10(2):117–126, 1995.
- [36] H. Grabert and M. H. Devoret, editors. *Single Charge Tunneling: Coulomb Blockade Phenomena in Nanostructures*, volume B 294 of *NATO ASI series*. Plenum Press, New York, 1992.
- [37] J. Weis. Single-electron devices. *Lecture Notes in Physics*, 658:87–121, 2005.
- [38] M. A. Kastner. The single-electron transistor. *Rev. Mod. Phys.*, 64(3):849–858, Jul 1992.
- [39] U. Meirav and E.B. Foxman. Single-electron phenomena in semiconductors. *Semiconductor Science and Technology*, 11(3):255–284, 1996.
- [40] J. Weis. *Elektrischer Transport durch Quantendot-Systeme*. Habilitationsschrift, Stuttgart University, Stuttgart, 2002.
- [41] Jörg Schmid, Jürgen Weis, Karl Eberl, and Klaus v. Klitzing. A quantum dot in the limit of strong coupling to reservoirs. *Physica. B, Condensed matter*, 258:182–185, 1998.
- [42] M. Keller, U. Wilhelm, J. Schmid, J. Weis, K. v. Klitzing, and K. Eberl. Quantum dot in high magnetic fields: Correlated tunneling of electrons probes the spin configuration at the edge of the dot. *Phys. Rev. B*, 64(3):033302, Jun 2001.
- [43] L. P. Kouwenhoven, D. G. Austing, and S. Tarucha. Few-electron quantum dots. *Reports on Progress in Physics*, 64(6):701–736, 2001.
- [44] V. Fock. Bemerkung zur Quantelung des harmonischen Oszillators im Magnetfeld. *Zeitschrift für Physik A*, 47:446–448, 1928.
- [45] C. G. Darwin. The diamagnetism of the free electron. *Proc. Cambridge Philos. Soc.*, 27:86, 1930.
- [46] Thomas Heinzl. *Mesoscopic Electronics in Solid State Nanostructures*. WILEY-VCH, 2007.
- [47] S. J. Tans, M. H. Devoret, H. J. Dai, R. E. Thess, A. Smalley, Geerligs L. J., and C. Dekker. Individual single-wall carbon nanotubes as quantum wires. *Nature*, 386(6624):474–477, 1997.

- [48] C. J. B. Ford, P. J. Simpson, I. Zailer, D. R. Mace, M. Yosefin, M. Pepper, D. A. Ritchie, J. E. F. Frost, M. P. Grimshaw, and G. A. C. Jones. Charging and double-frequency Aharonov-Bohm effects in an open system. *Phys. Rev. B*, 49(24):17456–17459, Jun 1994.
- [49] A. Fuhrer, S. Luescher, T. Ihn, T. Heinzel, K. Ensslin, W. Wegscheider, and M. Bichler. Energy spectra of quantum rings. *Nature*, 413(6858):822–825, 2001.
- [50] T. Ihn, A. Fuhrer, M. Sigrist, K. Ensslin, W. Wegscheider, and M. Bichler. *Advances in solid state physics*, volume 43, chapter Quantum mechanics in quantum rings, pages 139–153. Springer, 2003.
- [51] M. Büttiker, Y. Imry, and R. Landauer. Josephson behavior in small normal one-dimensional rings. *Physics letters. A*, 96(7):365–367, 1983.
- [52] W. C. Tan and J. C. Inkson. Electron states in a two-dimensional ring - an exactly soluble model. *Semiconductor Science and Technology*, 11(11):1635–1641, 1996.
- [53] J. K. Jain and S. A. Kivelson. Quantum Hall effect in quasi one-dimensional systems: Resistance fluctuations and breakdown. *Phys. Rev. Lett.*, 60(15):1542–1545, Apr 1988.
- [54] H. S. Sim, A Kataoka, and Ford C. J. B. Electron interactions in an antidot in the integer quantum Hall regime. *Physics Reports*, 456(4):127–165, 2008.
- [55] M. Kataoka, C. J. B. Ford, M. Y. Simmons, and D. A. Ritchie. Kondo effect in a quantum antidot. *Phys. Rev. Lett.*, 89(22):226803, Nov 2002.
- [56] M. Kataoka, C. J. B. Ford, G. Faini, D. Mailly, M. Y. Simmons, D. R. Mace, C.-T. Liang, and D. A. Ritchie. Detection of coulomb charging around an antidot in the quantum Hall regime. *Phys. Rev. Lett.*, 83(1):160–163, July 1999.
- [57] Y. Aharonov and D. Bohm. Significance of electromagnetic potentials in the quantum theory. *Phys. Rev.*, 115(3):485–491, Aug 1959.
- [58] B. L. Altshuler, A. G. Aronov, and B. Z. Spivak. Significance of electromagnetic potentials in the quantum theory. *JETP Lett.*, 33:94, 1981.
- [59] N. Braslau, J. B. Gunn, and J. L. Staples. Metal-semiconductor contacts for GaAs bulk effect devices. *Solid-state electronics*, 10(5):381–, 1967.

- [60] A. G. Baca, F. Ren, J. C. Zolper, R. D. Briggs, and S. J. Pearton. A survey of ohmic contacts to III-V compound semiconductors. *Thin Solid Films*, 308:599–606, 1997.
- [61] M. Kamada, T. Suzuki, F. Nakamura, Y. Mori, and M. Arai. Investigation of orientation effect on contact resistance in selectively doped AlGaAs/GaAs heterostructures. *Appl. Phys. Lett.*, 49(19):1263–1265, 1986.
- [62] H.J. Bühlmann and J. M. Ilegems. Characterization of AuGe/Ni/Au contacts on GaAs/AlGaAs heterostructures for low-temperature applications. *Journal of the Electrochemical Society*, 138(9):2795–2798, 1991.
- [63] R.P. Taylor, P.T. Coleridge, M. Davies, Y. Feng, J.P. McCaffrey, and J. P.A. Marshall. Physical and electrical investigation of ohmic contacts to AlGaAs/GaAs heterostructures. *J. Appl. Phys.*, 76(12):7966–7972, 1994.
- [64] U. Graumann. *Ohmische Kontakte zu zweidimensionalen Elektronensystemen*. Praktikumsarbeit, Max-Planck-Institut für Festkörperforschung, Stuttgart, 1998.
- [65] T. S. Kuan, P. E. Batson, T. N. Jackson, H. Rupprecht, and E. L. Wilkie. Electron-microscope studies of an alloyed Au/Ni/Au-Ge ohmic contact to GaAs. *J. Appl. Phys.*, 54(12):6952–6957, 1983.
- [66] N. Braslau. Alloyed ohmic contacts to GaAs. *The Journal of Vacuum Science and Technology*, 19(3):803–807, 1981.
- [67] N. Lumpkin. The role of Ni in the formation of low resistance Ni-Ge-Au ohmic contacts to n^+ GaAs heterostructures. *Journal of Materials Research*, 14(4):1261–1271, 1999.
- [68] A. Messica, U. Meirav, and H. Shtrikman. Refractory metal-based low-resistance ohmic contacts for submicron GaAs heterostructure devices. *Thin Solid Films*, 257(1):54–57, 1995.
- [69] SJ Hawksworth, Chamberlain JM, Cheng TS, Henini M, Heath M, Davies M, and Page AJ. Contact resistance to high-mobility AlGaAs/GaAs heterostructures. *Semiconductor Science and Technology*, 7(8):1085–1090, 1992.
- [70] H. Berger. Models for contacts to planar devices. *Solid-State Electronics*, 15(2):145–, 1972.
- [71] S.S. Cohen. *VLSI Electronics*, volume 13, chapter : Test structures for ohmic contact characterisation, page 87. Academic Press. Inc., New York, 1986.

-
- [72] M. Heiblum, M.I. Nathan, and C. A. Chang. Characteristics of AuGeNi ohmic contacts to GaAs. *Solid-State Electronics*, 25(3):185–195, 1982.
- [73] R. P. Taylor, R. Newbury, A. S. Sachrajda, Y. Feng, P. T. Coleridge, M. Davies, and J. P. McCaffrey. Investigation of the current injection properties of ohmic spikes in nanostructures. *Superlattices and Microstructures*, 24(5):337–345, 1998.
- [74] M. Procop, B. Sandow, H. Raidt, and Do. Son Li. The importance of the ni to ge ratio and of the annealing cycle for the resistivity and morphology of NiAuGe ohmic contacts to n-GaAs. *Physica Status Solidi. A*, 104(2):903–916, 1987.
- [75] S. Adachi. GaAs, AlAs, and $\text{Al}_\delta\text{Ga}_{1-\delta}\text{As}$ - material parameters for use in research and device applications. *J. Appl. Phys.*, 58(3):R1–R29, 1985.
- [76] Yang Ji, Yunchul Chung, D. Sprinzak, M. Heiblum, D. Mahalu, and Hadas Shtrikman. An electronic mach-zehnder interferometer. *Nature*, 422(6930):415–418, 2003.
- [77] Jörn Göres. Correlation effects in 2-dimensional electron systems - composite fermions and electron liquid crystals. *Max-Planck-Institut für Festkörperforschung, Stuttgart*, 2004.
- [78] A. Welker. A quantum dot with three leads: Tunnel spectroscopy in the kondo and the fano regime; a single-electron-transistor with current gain. *Max-Planck-Institut für Festkörperforschung, Stuttgart*, 2007.
- [79] G. Kirczenow. Quantum transport in ballistic nano-scale corbino disks. *Journal of physics. Condensed matter*, 6(39):L583–L588, 1994.
- [80] S. Souma and A. Suzuki. Effect of impurity scattering in nanoscale corbino disks. *Phys. Rev. B*, 58(8):4649–4655, 1998.
- [81] S. Souma and A. Suzuki. Interedge scattering in mesoscopic corbino disks near the ballistic regime. *Phys. Rev. B*, 60(23):15928–15936, 1999.
- [82] C. M. Marcus, A. J. Rimberg, R. M. Westervelt, P. F. Hopkins, and A. C. Gossard. Conductance fluctuations and chaotic scattering in ballistic microstructures. *Phys. Rev. Lett.*, 69(3):506–509, Jul 1992.
- [83] Harold U. Baranger, Rodolfo A. Jalabert, and A. Douglas Stone. Weak localization and integrability in ballistic cavities. *Phys. Rev. Lett.*, 70(25):3876–3879, Jun 1993.

- [84] C. W. J. Beenakker and H. van Houten. Boundary scattering and weak localization of electrons in a magnetic field. *Phys. Rev. B*, 38(5):3232–3240, Aug 1988.
- [85] P. W. Anderson, E. Abrahams, and T. V. Ramakrishnan. Possible explanation of nonlinear conductivity in thin-film metal wires. *Phys. Rev. Lett.*, 43(10):718–720, Sep 1979.
- [86] G. Bergmann. Weak localization in thin-films - a time-of-flight experiment with conduction electrons. *Physics Reports*, 107(1):1–58, 1984.
- [87] S. Chakravarty. Weak localization - the quasi-classical theory of electrons in a random potential. *Physics Reports*, 140(4):193–236, 1986.
- [88] C. W. J. Beenakker. Quantum transport in semiconductor nanostructures. *Solid state physics*, 44:1–228, 1991.
- [89] H. van Houten, C.W.J. Beenakker, B.J Van Wees, and J.E. Mooji. Boundary scattering modified one-dimensional weak localization in submicron gaas/algaas heterostructures. *Surface Sciences*, 196:144–149, 1988.
- [90] Kurdak, A. M. Chang, A. Chin, and T. Y. Chang. Quantum interference effects and spin-orbit interaction in quasi-one-dimensional wires and rings. *Phys. Rev. B*, 46(11):6846–6856, Sep 1992.
- [91] J. P. Bird, D. M. Olatona, R. Newbury, R. P. Taylor, K. Ishibashi, M. Stopa, Y. Aoyagi, T. Sugano, and Y. Ochiai. Lead-induced transition to chaos in ballistic mesoscopic billiards. *Phys. Rev. B*, 52(20):R14336–R14339, Nov 1995.
- [92] A. M. Chang, H. U. Baranger, L. N. Pfeiffer, and K. W. West. Weak localization in chaotic versus nonchaotic cavities: A striking difference in the line shape. *Phys. Rev. Lett.*, 73(15):2111–2114, Oct 1994.
- [93] V. T. Dolgoplov, A. A. Shashkin, N. B. Zhitenev, S. I. Dorozhkin, and K. von Klitzing. Quantum hall effect in the absence of edge currents. *Phys. Rev. B*, 46(19):12560–12567, Nov 1992.
- [94] G Nachtwei. Breakdown of the quantum hall effect. *Physica. E*, 4(2):79–101, 1999.

Acknowledgment

I like to thank Klaus von Klitzing for giving me the opportunity for a PhD in his department. I also want to thank to him for all the very helpful discussions and suggestions.

I like to thank Jürgen Weis for his helpful comments and suggestions during this PhD work. He read this thesis very carefully and made very useful suggestions which improved the structure of the thesis very much.

Thanks to Werner Dietsche and Mike Hauser for providing heterostructures.

Several people have helped me during my PhD. I start with clean room crew. Monika Riek, Ulrike Weizmann, Achim Güth, Thomas Reindl were always ready for help for any kind of problem in the clean room. Thanks for their help.

Thanks to Jochen Weber for his help on the FIB.

Bernhard Fenk did a great job while preparing lamellas for STEM investigations. Thanks for his help.

I like to thank Wilfried Siegle for most of the STEM investigations presented in this thesis. He was very generous to give time for measurements and discussions. He was so kind to read the sections of this manuscript about STEM investigations and made very good suggestions. Kersten Hahn and Viola Duppel have also contributed on the STEM investigations. Thanks for their help. Thanks to Peter Kopold for the HRTEM images.

Thanks to Tolga Acartürk for the SIMS measurements. Ulrich Stärke gave us the opportunity to perform SIMS investigations in his research group and made very helpful comments on the results.

Benjamin Stuhlhofer was very fast for bonding. Thanks.

I like to thank both of our young scientist Yvonne Boose and Nefta Kanilmaz. Yvonne helped for some of the measurement on TLM structures. Nefta spent a lot of time to characterize submicron scale ohmic contacts at room temperature and at low temperatures which is a very time consuming work. With her help I was able to do lot of work in parallel.

I like to thank Franck Dahlem for very helpful discussions.

Thanks to Frank Ospald for the help on german text.

Thanks to two of my office mates Gerardo and Alexander for very nice times

BIBLIOGRAPHY

and conversations.

I like to thank to all the members of J. Weis group and all the member of von Klitzing department for the nice environment.

The list of the things to thank Eleonora is very long; to keep it short I like to thank her for her nice friendship. I also like to thank to Mark for very nice times we spent together.

Nebile, thanks for all of the help. Without you it would have been a very boring life. I cannot stop mentioning all of these incredibly delicious dishes, especially baklava, dilber dudagi, and asure. It was a good motivation to write faster.

I like to thank my mother and father for their understanding and accepting my excuses that I was busy with my PhD and did not go to see them very frequently. My special thanks goes to Bese, Kismet and Suna who were so generous to allow me stay with them in their house every now and then during my secondary and high school education period. Without them it was not possible to continue my education and to come to present situation to write this PhD. Thanks to all of the friends that I did not mention here but were helpful at any stage of this work.

Curriculum Vitae

Oktay Göktaş

- 02.01.1974 : born in Hozat,Tunceli/Turkey as the son of Emirali and Hüsniye Göktaş
- 1979-1984 : Tavuklar Köyü İlkokulu (Elementary school)
- 1984-1985 : Harput Ortaokulu , Harput (Secondary school 1st year)
- 1985-1987 : Gürçeşme Ortaokulu , İzmir (2nd and 3rd years)
- 1987-1988 : Gürçeşme Lisesi , İzmir (High school 1st year)
- 1988-1989 : Elazığ Atatürk Lisesi , Elazığ (High school 2nd year)
- 1989-1990 : Gürçeşme Lisesi , İzmir (High school 3rd year)
- 1993-1995 : Dicle University, computer programming , Diyarbakır
- 1996-2000 : Ege University, Bachelor in Physics , İzmir
- 2001-2004 : Izmir Institute of Technology, MSc in Physics , İzmir
- since January 2005 : Dissertation at Max-Planck-Institute, Stuttgart